Probing and controlling ion Coulomb crystals by optical cavity fields

Steps towards a quantum memory for light

Rasmus Bogh Linnet

PhD Thesis

Danish National Research Foundation
Center for Quantum Optics – Quantop
Department of Physics and Astronomy
The University of Aarhus

April 2014

Probing and controlling ion Coulomb crystals by optical cavity fields

Steps towards a quantum memory for light

Rasmus Bogh Linnet

PhD Thesis

Danish National Research Foundation
Center for Quantum Optics – Quantop
Department of Physics and Astronomy
The University of Aarhus

April 2014

This Thesis is submitted to the Faculty of Science at Aarhus University, Denmark, in order to fulfill the requirements for obtaining the PhD degree in Physics. The studies have been carried out under the supervision of Prof. Michael Drewsen in the Ion Trap Group at the Department of Physics and Astronomy at Aarhus University from January 2010 to April 2014.

Probing and controlling ion Coulomb crystals by optical cavity fields
- Steps towards a quantum memory for light

Rasmus Bogh Linnet,
Aarhus, April 2014

Preface

This thesis is a summary of my work done as a Ph.D. student at the Department of Physics and Astronomy at Aarhus University, Denmark. It contains the recent progress made within the ion-based cavity QED project over the last four years in the Ion Trap Group at the University of Aarhus. Prior to my Ph.D. employment I also did my bachelor project in the group on measuring frequency drifts of a reference cavity using Doppler-free spectroscopy of Cs atoms. Through this work my interest for optical and atomic physics started as I was introduced to the ongoing experiments in the group and the overwhelming complexity of the physical phenomena that was studied. When I was offered the opportunity to continue working in this exciting field of research I had no doubt in accepting the contract.

In this context, I would like to thank my supervisor Michael Drewsen for giving me the possibility to further develop the experimental project and hereby improve my physical intuition, ability to solve experimental and theoretical issues and get an impression of the entire field of research in which we are operating. I have been challenged to work both in cooperation with colleagues in the group and individually, and I think the balance between the two has been close to optimal for me.

At the beginning of my work on the project, the cavity trap had already been running for several years giving great breakthroughs in the field of cavity quantum electrodynamics. These results are to a great extent the achievements of my predecessors Peter Herskind, Magnus Albert, Joan Marler and Aurélien R. Dantan, to whom I am very grateful. I have been pleased to get the chance to continue developing the complexity of the system to achieve the new goals that were set for the studies. In the projects that I was involved in, I have been working mainly together with the post docs Aurélien R. Dantan and Ian D. Leroux, who at the same time served as my mentors, answering every question I might have had.

In the beginning of my time in the group I also worked closely together with Magnus Albert in continuing the work he had performed as a PhD student in the group. Towards the end of my study I have been working with post doc Thomas Lauprêtre and the PhD student Olivier Legrand who are going to continue the open projects and hopefully succeed in obtaining great results. Of other people with whom I have been working, I have to mention the master students Niels H. Nielsen, Kasper R. Zangenberg and Martin Larsen. I would like to use the opportunity to thank all these people for their help and for the exciting discussion we have had throughout the last four years. In addition, I would like to thank all the other people in the ion trap group for creating a friendly and constructive environment in which collaborations across projects and goals has been working seamlessly.

I also acknowledge all the help and support from the staff from the electronics

department, the construction group and the mechanical workshop.

Moreover, I would like to thank my family for their support and encouragement during the past four years. I have tried to distribute my time between work and taking care of my wife and children, but sometimes it has been hard to balance the focus between the two. I appreciate your understanding.

Finally, I would like to gratefully thank Aurélien R. Dantan and Ian D. Leroux for useful discussions during the writing process of this thesis together with the major effort of proof-reading it. Their remarks and comments improved the thesis substantially.

Rasmus Bogh Linnet, April 2014.

Resumé - English

This PhD thesis deals with the interaction between light fields in optical resonators and cold, trapped ions. The studies reported here have been carried out in an existing cavity ion trap setup in the Ion Trap Group at the University of Aarhus. Experiments are performed using ensembles of Ca^+ ions, trapped in a linear Paul trap and laser-cooled into a spatially ordered structure called an ion Coulomb crystal, with temperatures in the mK range. The ions in the crystal can couple strongly to the light field of an optical cavity integrated into the trap and resonating with the D-P transition in Ca^+.

The first experiments described in this thesis are an investigation of the temperature of large ion Coulomb crystals, by a non-invasive spectroscopy method which exploits the coupling between the cavity field and the atomic levels of the ions. By recording resonance spectra from the combined cavity-ion system probed at the single photon level we make use of the modification of the crystal-light coupling in order to infer the temperature of the crystals. In the specific experiments we observe ion crystal temperatures in the range from 10 mK to > 600 mK. These measurements will be checked against the results of independent molecular dynamics simulations. The information about the thermodynamical state of ion Coulomb crystals gained in such studies are relevant both for cold charged plasma physics as well as for ion-based cavity quantum electrodynamic studies.

In a second set of experiments we develop a technique for determining the absolute center of the optical cavity. Two optical fields, separated with a specific detuning, are resonantly injected into a linear Fabry-Pérot cavity and the spatial beating pattern between them is observed by using an ion crystal as the imaging medium. We demonstrate how this simple technique allows for finding the absolute center of a 11.8 mm-long cavity with a precision of ~ 100 nm.

The last experiments of this thesis represent a study of the localization of ions in a standing wave optical potential inside the cavity. A strong intra-cavity laser field (lattice), far detuned from an atomic transition of the ions, imposes a dipole force on the ions in the crystal that forces them to be localized at either nodes or anti-nodes of the lattice field, depending on the sign of the detuning. We first show that a single ion can be captured in a single well of a 34 mK-deep optical lattice with over 97% probability. We also show that the coupling between an ion and a second resonant intra-cavity probe field can be enhanced substantially, from 50%, for a free ion, to $> 80\%$ for an ion in the deepest lattice. Furthermore, we also show that ion crystals with up to 8 ions and in several multidimensional structures can be localized in such a lattice potential.

We also discuss the prospects and preparations for implementing a protocol for quantum storage and retrieval of light using ion Coulomb crystals in a cavity. This protocol uses the so-called cavity electromagnetically induced transparency mechanism, which has been demonstrated in our system, in order to convert photonic excitations at the single photon level into collective excitations in the ions.

Resumé - Dansk

Denne ph.d.-afhandling beskæftiger sig med vekselvirkningen mellem lys-felter i optiske kaviteter og kolde, fangede ioner. Studierne der gennemgås er blevet udført i det eksisterende kavitets ionfælde eksperiment i Ion-fælde gruppen ved Aarhus Universitet. Eksperimenter udføres her ved hjælp af ensembler af Ca^+-ioner, der er fanget i en lineær Paul fælde og laser-kølet til en rumligt vel-ordnet struktur kaldet en ion Coulomb-krystal, med temperaturer i størrelsesordenen mK. Ionerne i krystallen kan koble stærkt til feltet i en optisk kavitet som er integreret i fælden og som er resonant med DP overgangen i Ca^+.

De første forsøg, der er beskrevet i denne afhandling, er en undersøgelse af temperaturen af store ion Coulomb-krystaller vha. en metode der bruger ikke-invasiv spektroskopi, ved at udnytte koblingen mellem kavitets-feltet og de atomare niveauer af ionerne. Ved at optage resonans-spektre fra det kombinerede kavitets-ion-system målt på enkelt foton niveau, kan vi gøre brug af ændringen af krystal-lys koblingen til at udlede temperaturen af krystallen. I de specifikke eksperimenter observerer vi ion krystal temperaturer i intervallet fra 10 mK til $>$ 600 mK. Disse målinger vil blive sammenlignet med resultater fra uafhængige molekylære dynamik simuleringer. Oplysningerne om den termodynamiske tilstand for ion Coulomb-krystaller, opnået i sådanne undersøgelser, er relevante både for kold plasmafysik med ladede partikler, samt for ion-baserede kavitets kvante elektrodynamiske studier.

I et andet sæt af eksperimenter, udvikler vi en teknik til bestemmelse af det absolutte centrum af den optiske kavitet. To optiske felter, adskilt med en specifik frekvensforskel, kobles resonant ind i kaviteten, hvorved et beat-mønster mellem felterne kan observeres ved hjælp af en ion-krystal som afbildningsmedie. Vi viser, hvordan denne enkle teknik giver mulighed for at finde det absolutte centrum for en $11,8$ mm lang kavitet med en præcision på ~ 100 nm.

De sidste eksperimenter i afhandlingen er et studie af lokaliseringen af ioner i et optisk potentiale fra en stående bølge i kaviteten. Et stærkt intra-kavitets laser felt (gitter), med en frekvens langt fra en atomar overgang for ionerne, skaber en dipol kraft på ionerne i krystallen, der tvinger dem til at være lokaliserede på enten noder eller anti-noder i gitteret, afhængigt af fortegnet på frekvensforskydningen. Vi viser først, at en enkelt ion kan fanges i en enkelt brønd i et 34 mK dybt optisk gitter med over 97% sandsynlighed. Vi viser også, at koblingen mellem en ion, og et andet resonant intra-kavitets felt kan forøges betydeligt, fra 50% for en fri ion, til $>$ 80% for en ion i det dybeste optiske gitter. Endvidere viser vi også, at ion-krystaller med op til 8 ioner og i flere fler-dimensionelle strukturer kan lokaliseres i et sådant optisk gitter potentiale.

Vi diskuterer også udsigterne og forberedelserne til gennemførelse af en protokol for kvante lagring og genudlæsning af lys ved hjælp ion Coulomb-krystaller i en kavitet. Denne protokol bruger den såkaldte kavitets elektromagnetisk inducerede gennemsigtighed (EIT), som er blevet påvist i vores system, til at konvertere fotoniske excitationer på enkelt foton niveau til kollektive excitationer i ionerne.

List of publications

1. R. B. Linnet, I. D. Leroux, M. Marciante, A. Dantan, M.Drewsen, *"Pinning an Ion with an Intracavity Optical Lattice"*, Phys. Rev. Lett. **109**, 233005 (2012)

2. R. B. Linnet, I. D. Leroux, A. Dantan, M.Drewsen, *"Sub-Micron Positioning of Trapped Ions with respect to the Absolute Center of a Standing Wave Cavity Field"*, Appl. Phys. B **114**, 295 (2014)

3. T. Lauprêtre, R. B. Linnet, I. D. Leroux, A. Dantan, M.Drewsen, *"Localization of ions within one-, two- and three-dimensional Coulomb crystals by a standing wave optical potential"*, Manuscript in preparation.

Contents

Chapter 1

Introduction

The control of quantum mechanical interactions between light and matter systems have been a central issue in an understanding of physics for decades [1, 2]. Major developments have been made in quantum optics labs around the world, by trapping and coherently manipulating photons and atoms down to the single particle level. If special boundary conditions are imposed to the electromagnetic field, for example, by placing a resonator around the atoms, the light-matter coupling can be significantly enhanced. Such interactions are at the focus of the field of Cavity Quantum Electrodynamics (CQED) [3]. A prototypical system in CQED considers the interaction of a single mode of the electromagnetic cavity field with a single quantum mechanical system. A two-level regime arises in that case when the coherent coupling rate (g) between the quantum system and the field mode exceeds the dissipative rates arising from the coupling of the quantum system and the cavity field with the other modes of the electromagnetic fields (γ, κ) [4]. In this so-called strong coupling regime, single quanta can be exchanged coherently between the two-level system and the cavity field, thus making the emission of a photon from e.g. an atom a reversible process. Studies of this regime has been performed in many different systems, including single atoms in both microwave and optical cavities [5, 6], quantum dots [7, 8] and superconducting Josephson junctions [9, 10]. Using ultrahigh-finesse cavities with a small mode-volume, the strong coupling regime has been reached for single neutral atoms [11, 12]. With charged particles, reduction of the mode-volume is limited by the perturbation of the trapping potentials induced by the cavity mirrors [13, 14] and thus, the regime has yet to be reached with ions. Nevertheless, studies of single ions in optical cavities have successfully demonstrated e.g. probing of spatial structures in cavity fields [15], the generation of single photons [16, 17], studies of cavity sideband cooling [18], experiments exploiting optical fiber cavities [19–22] and the single ion laser [23].

For an ensemble of N identical two-level particles that simultaneously interact with a single photon in the cavity, the coherent coupling is enhanced by a factor of $\sqrt{N}$ [1]. For this system, an interesting regime is the *collective* strong coupling regime, where the collective coupling rate for the ensemble, $g_N = g\sqrt{N}$, is larger than both γ and κ. The regime was first entered using Rydberg atoms in microwave cavities [24], and has later been exploited with optical fields using e.g. atomic beams [5], Bose-Einstein condensates [25, 26], and recently in our group, ion Coulomb crystals [27, 28]. This

collective interaction, enhanced by the presence of the cavity, has been applied to many different studies, e.g. establishment of strong nonlinearities [29], the generation of non classical states [30–32], QND measurements [33, 34], observations of cavity optomechanical effects [35–38], and cavity cooling [39, 40].

Studies of the collective coupling are in particular very relevant for the fields of quantum information and computation [41, 42], which exploit quantum mechanical effects to reduce the complexity of computational classically unsolvable problems [43, 44]. Many of the schemes developed in these fields of research are based on the use of so-called qubits, consisting of quantum mechanical two-level systems. By performing unitary operations on the considered qubit system, it is possible to process quantum information as part of a quantum computation protocol. Often, photons are used to transport this quantum information from one computational unit to another [45], while static qubits, like an atomic system, are used for processing and storing of this information [41, 42]. In addition to atoms, many other systems are studied in this context, e.g. quantum dots [46], nuclear spins [47] and superconducting Josephson junctions [48]. Trapped laser-cooled ions are considered as one of the most promising systems for realizing scalable quantum information devices because of the high controllability of external and internal degrees of freedom that can be achieved [49–53]. Because of their charge ions can be trapped in e.g. a linear Paul trap confining them using static and RF-frequency electrical fields. By laser cooling the ions it is possible to get very stable configurations of one ion or many ions and this diversity makes ion traps a very useful system to apply in different parts of a quantum computation process. Further advantages for ions is long storage/coherence times, individual and high efficiency addressing and direct readout using optical fields.

The qubit processor is one part of a quantum computer. Another important basic component is the quantum memory [54, 55] where the information carried by e.g. photons can be temporarily stored and at a later time be retrieved from the system with the possibility to proceed in further quantum computations. Successful implementation of storage and retrieval of light have been performed with atomic ensembles [54–56]. Many factors can be used to evaluate the performance of a quantum memory, depending on the application of interest [56]. Three parameters are particularly relevant for our studies: i) the efficiency of storage and retrieval of the photonic state; ii) the storage time, which should be long compared to other timescales involved in the process; iii) a multi-mode capacity, i.e. a possibility to store several quantum states simultaneously. Quantum memories have been implemented, e.g. using atomic vapors to store single photons from free-propagating fields [57–60], but these typically have low efficiencies. The efficiency of the quantum memory can be significantly improved if the atomic medium is placed inside an optical cavity, where, as mentioned above, the interaction between the medium and a specific cavity mode can be much stronger than in free space. The realization of an efficient cavity-based quantum memory is based on the collective strong coupling regime introduced above [61–63].

Our implementation of a quantum memory for light is based on a large ion ensemble (ion Coulomb crystal) trapped within a moderate finesse ($\mathcal{F} \approx 3000$) optical cavity. This is likely to be a system with good prospects of fulfilling the three criteria mentioned above. The collective strong coupling regime has been reached for the system [28, 64] and substantial effective optical depths have been achieved, which is promising for improving the quantum storage efficiency. Furthermore, the enhanced

light-matter coupling can be used as a diagnostic tool for studying properties of ion Coulomb crystals like e.g. vibrational modes of the crystals [65] or their temperature (see sec. 6.1). Cavity electromagnetically induced transparency (EIT) [66, 67] has also been achieved in this system [68, 69], which is another requisite for realizing a quantum memory [61–63]. EIT is a quantum interference effect experienced by a light field propagating through a medium illuminated by another intense *control* field, in which a reduction in the group velocity of the light causes the pulse to be slowed down or even stopped. This coherent process can be used to convert photonic excitations into collective atomic ones, and conversely. This has been demonstrated in a number of systems [56, 70–72]. The demonstrated coupling strengths and coherence times in our ion-cavity system [61] should allow for achieving high efficiency ($> 90\%$) and long storage time ($\sim$ms). In addition, we have the possibility to store photons in multiple cavity modes in order to meet all the criteria of [56]. This could be achieved e.g. by coupling large ion Coulomb crystals strongly to different transverse modes of the cavity field [73, 74]. Another application, proposed for this quantum memory system, is a photon number detector [75–77].

Preparing the implementation of an ion Coulomb crystal-based quantum memory in an optical cavity is the goal of the project that I have been a part of. In this thesis we focus on preliminary experimental studies of the quantum memory implementation, the results of which should be useful for improving the performance of the quantum memory once it is realized.

First, we make use of the coherent coupling between the ion crystals and a weak cavity field at the single photon level to determine the temperature of large ion Coulomb crystals. In these experiments, the cavity reflection spectrum is modified by the strong interaction with the ions in the crystal in a way that depends on their temperature [28]. By changing the cooling conditions of the ions, one can study crystals with various thermodynamical properties, such as their temperature or heating rate, in a non-invasive manner. With respect to realizing a quantum memory for light based on ion Coulomb crystals, these experiments will be important in quantifying the crystal heating-rates at different trap parameters. A related study has already been performed in order to investigate the vibrational mode spectrum of large ion crystals [65]. This non-invasive spectroscopy technique was applied to the measurement of the frequencies and temperatures of electrically excited normal modes of the crystals. The good agreement observed between the experiments and the predictions of the cold charged liquid model seems to indicate that the simple CQED model of the interaction, including the effect of the motion of the ions, is reliable [65, 78]. This prompted us to try tackling the difficult task of measuring the temperature of large ion Coulomb crystals.

Secondly, we developed a technique for determining the position of the absolute center of a linear Fabry-Pérot cavity using an ion Coulomb crystal as an imaging medium [79]. Due to the boundary conditions for the fields imposed by the cavity, all longitudinal modes of the *same* parity (even or odd) have overlapping nodes and anti-nodes at the center of the cavity. This means that an in-phase relation is imposed at the center for two different modes, regardless of their frequency. For two fields with *different* parity, one with even and one with odd number of nodal planes in the cavity, similarly an out-of-phase relation will be obtained. In this study we use an ion Coulomb crystal as an imaging medium to visualize the beat pattern between

two different fields, both resonant with the cavity but at different longitudinal modes. More specifically, we inject into the cavity a probe field which is close to resonance with an atomic frequency, and an off-resonant lattice field which provides a periodic AC Stark shifting potential for the ions, and which induces a spatial modulation of the scattering rate of the probe field. By using different detunings of the lattice field we determine the center of an 11.8 mm-long cavity with about 100 nm precision [79]. This technique of positioning single or ensembles of ions with respect to the absolute center of the cavity may find several applications for ion-based CQED. It is relevant for studies of trapping ions in localizing optical potentials [80–82] and within the context of coherent atom-ion interaction studies [83–85]. Besides ions in cavities, the technique could also be applied to cold neutral atoms trapped in optical dipole or magnetic traps, used e.g. in single atom dynamics studies [86–88]. It could also apply to CQED studies with ensembles, e.g. with cold atoms in cavity-generated optical potentials [89] or for the interaction with multiple standing-wave fields [68, 90].

Thirdly, a study of localization of ions in a far detuned standing-wave optical potential inside the cavity has been performed and can be seen as an important step towards controlling structural properties of Coulomb crystals and to enhance the coupling strength between ions and a cavity field. For many years, optical lattices have been used to confine ultra-cold neutral atoms in optical-wavelength-scale potentials [91, 92], while ions are traditionally trapped in electrical potentials of much greater size [93]. In the experiments reported in this thesis we show that it is possible to combine the two techniques to also confine ions on the wavelength-scale [81], which is a topic of current interest for several groups in the world [80, 82, 94]. The prospects of such novel trapping conditions for ions are, among others, quantum simulations of many-body physics [95–97] and examination of the Frenkel-Kontorova model for friction [98, 99]. In the experiments reported here, an optical lattice formed by a standing-wave field in the cavity is applied to $^{40}Ca^{+}$ ions trapped in a linear Paul trap. The lattice induces an AC Stark shift of the atomic energy levels, which provides a dipole force confining the ions within less than half a wavelength of the standing wave potential. Since sub-wavelength imaging resolution is extremely challenging to achieve we measure the localization effect of the lattice by detecting the spatially dependent fluorescence from inelastic photon scattering by the lattice itself. Using this detection method we first demonstrate sub-wavelength localization of a single ion and subsequently prove that the lattice induced localization can increase the coupling strength of the ion to another cavity probe field to about 81%, compared to a non-localized ion (50%). Next, we demonstrate simultaneous localization of up to 8 ions in the optical lattice potential. This provides the setting for investigating interesting physical phenomena involving a competition between the lattice potential and inter-ion Coulomb interactions [98, 99]. Another potential application of these results would be to control the position of the ions with respect to the standing wave probe field in quantum memory experiments in order to increase the light-matter coupling and, thereby, the quantum storage efficiency [27].

The contents of the thesis is organized as follows:

Chapter 2 describes trapping and laser cooling of ions in a linear Paul trap and focuses on the different ion structures that can be achieved. Especially, the thermodynamics of ion Coulomb crystals will be reviewed within the context of cold charged plasmas.

Chapter 3 introduces atom-cavity field interactions, with emphasis on an ensemble of N two-level atoms coupled to a single cavity mode.

Chapter 4 describes a possible quantum memory for light using an ion Coulomb crystal placed inside an optical cavity. We outline the theoretical aspects and give a possible implementation for our experimental system.

Chapter 5 sketches the experimental setup, the laser systems and the various detection schemes.

Chapter 6 describes and discusses two different techniques for characterizing large Coulomb crystals in the cavity. First, a method for non-invasively measuring the temperature of ion Coulomb crystals using the coupling to the cavity field and, second, a method for finding the absolute center of a linear symmetric Fabry-Pérot cavity using an atomic ensemble as an imaging medium.

Chapter 7 presents a detailed study of the sub-wavelength localization of individual ions in ion Coulomb crystals in a far-detuned intracity standing wave potential.

Chapter 8 presents some future aspects of the study, including preparations and considerations for the implementation of an ion Coulomb crystal-based quantum memory in an optical cavity.

Chapter 9 summarizes the thesis and gives a brief outlook.

Chapter 2

Trapping and laser cooling of ions in a linear Paul trap

This chapter provides a basic theoretical description of ion trapping and laser cooling. We introduce the principles of the linear Paul trap and its mathematical description in sec. 2.1. In sec. 2.2 laser cooling of single $^{40}Ca^{+}$ ions is described, by introducing the Doppler cooling technique. In the last part of the chapter (sec. 2.3) we describe some general structural and thermodynamical properties of ion Coulomb crystals. Furthermore, we discuss the effect of the so-called micromotion in the ion system and how to possibly minimize it.

2.1 Trapping ions in a linear Paul trap

As ions are charged particles they can be influenced by electrical forces. Trapping ions using only static electrical fields is not possible though, as Laplace's law prevents us from obtaining an extremum for the electric potential, $\phi(x, y, z)$, in all three dimensions at the same time. To overcome this obstacle other methods are therefore used, e.g. either combinations of static electrical and magnetic fields (Penning traps) or a combination of static and time-varying electrical fields (Paul traps). For an introductory description of different trapping techniques see e.g. [93]. In all experiments presented in this thesis ions are confined in a so-called linear Paul trap combining static and radio frequency (RF) electrical fields, to create a time-averaged three-dimensional harmonic potential. The present form of this trap was invented around 1989 [100], but is closely related to its predecessor, the quadrupolar mass filter, invented by Wolfgang Paul in 1958 [101,102]. Other related types of traps include the hyperbolic Paul trap [103] and the race-track trap [104].

The linear Paul trap used in the experiments consists of four rods each segmented into three parts (see fig. 2.1, where the relevant coordinate systems are defined) [27, 73]. The axial confinement (along the z-axis) is produced by applying a static voltage (U_{DC}) to the end-electrodes, giving rise to an electrical potential along the

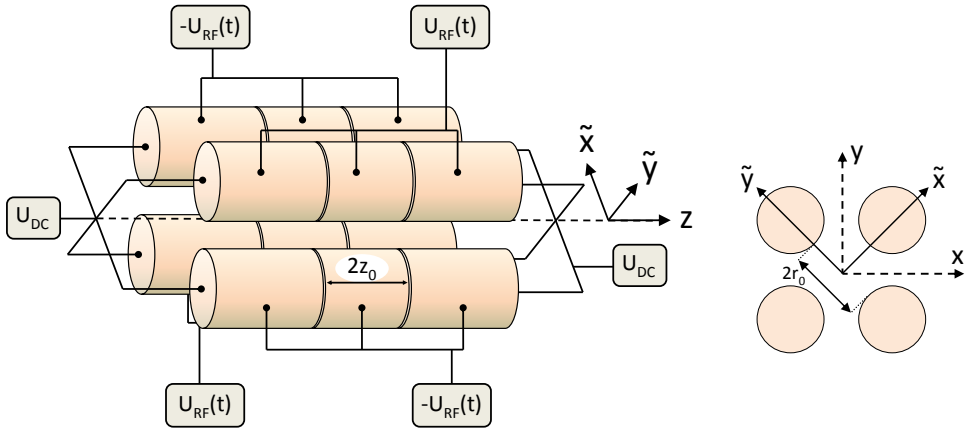

(a) (b)

Figure 2.1: (a) Schematic drawing of the Linear Paul trap electrode configuration with the applied voltages U_{RF} and U_{DC}. The center electrode length is $2z_0$. The trap axis is referred to as z (dotted line). (b) End-view of the trap showing the definitions of the $\tilde{x}$ and $\tilde{y}$ axis used in this section. The inter-electrode distance is $2r_0$. In the rest of the thesis, the x and y axis, which are tilted by 45°. with respect to the $\tilde{x}$ and $\tilde{y}$ axis, will be used.

z-axis, well described close to the center of the trap by

$$\phi(z) = \eta U_{DC} \frac{z^2}{z_0^2} \ , \tag{2.1}$$

where $2z_0$ is the length of the center electrode and η is a constant depending on the geometry of the trap, typically found through numeric simulation of the trap potentials (see [27]). The rods are placed in a quadrupolar configuration and radial confinement (xy-plane in fig. 2.1) is produced by applying sinusoidally modulated voltages, which are 180 degree out of phase, to pairs of diagonally opposite rods as

$$\pm\, U_{RF}(t) = \pm \frac{1}{2} U_{rf} \cos(\Omega_{RF} t) \ , \tag{2.2}$$

where U_{rf} is the amplitude of the applied RF-voltage and Ω_{RF} is its frequency. A requirement of Laplace's law is that the confinement along the z-axis induced by the DC field will cause a defocussing effect in the radial plane. Thus, the total radial potential takes the form

$$\phi(\tilde{x}, \tilde{y}) = -\frac{1}{2} U_{rf} \cos(\Omega_{RF} t) \frac{\tilde{x}^2 - \tilde{y}^2}{r_0^2} - \frac{1}{2} \eta U_{DC} \frac{\tilde{x}^2 + \tilde{y}^2}{z_0^2} \ , \tag{2.3}$$

where $2r_0$ is the inter-electrode distance between diagonal rods (see fig. 2.1). Sectioning the electrodes allows in addition for applying individual DC-offsets shifting the ion both radially and axially compared to the trap minimum. In the rest of the thesis, the x and y axis, which are tilted by 45° with respect to the $\tilde{x}$ and $\tilde{y}$ axis, will be used.

The equation of motion in the radial plane is found by combining eq. (2.3) and Newton's second law for a particle with mass M and charge Q, $M\ddot{\mathbf{r}} = -Q\nabla\phi(\mathbf{r})$, where $\phi(\mathbf{r}) = \phi(z) + \phi(\tilde{x}, \tilde{y}, t)$ is the total potential. Rewriting this second order differential equation with dimensionless parameters results in the so-called Mathieu equations (see e.g. [49, 102])

$$\frac{\partial^2 u}{\partial \tau^2} + [a - 2q_u \cos(2\tau)]u = 0 \ , \qquad u = \tilde{x}, \tilde{y} \tag{2.4}$$

where we introduced

$$\tau = \frac{\Omega_{RF} t}{2} \ , \quad a = -4\frac{\eta Q U_{DC}}{M z_0^2 \Omega_{RF}^2} \ , \quad q = q_{\tilde{x}} = -q_{\tilde{y}} = 2\frac{Q U_{rf}}{M r_0^2 \Omega_{RF}^2} \ . \tag{2.5}$$

A particle placed in such a potential can exhibit either stable motion, where the solutions to the Mathieu equations correspond to non-diverging trajectories, or unstable motion with diverging trajectories. This means that the particle can be either radially confined inside or expelled from the trap. The stability depends on the parameters defined in eq. (2.5), see e.g. [49, 105] for a diagram of stable motion in (a, q)-space. Generally, stable motion in the radial plane can be achieved both for positive and negative values of a, but as the work described here only considers positively charged particles and positive U_{DC}, a is limited to negative values. The region of stable motion depends linearly on the charge-to-mass ratio, Q/M, through the a and q parameters and, as a result, different atomic species can be trapped simultaneously as long as their charge-to-mass ratio is not too different. In general, the trap is operated in the regime $|a|, |q| \ll 1$, in which the Mathieu equations (2.4) have the following approximate solutions

$$u(t) = u_0 \left[1 - \frac{q_u}{2}\cos(\Omega_{RF} t)\right] \cos(\omega_r t) \ , \qquad u = \tilde{x}, \tilde{y} \ \ , \tag{2.6}$$

where u_0 is a constant and we have introduced the secular frequency

$$\omega_r = \frac{\sqrt{q^2/2 + a}}{2} \Omega_{RF} \ . \tag{2.7}$$

The radial motion of the ion is a combination of a high frequency motion at the applied rf-frequency, Ω_{RF}, and a slower motion at the secular frequency $\omega_r \ll \Omega_{RF}$. The high-frequency motion is called *micromotion* and its amplitude depends on q_u. Consequently, the fast motion is small and only acts as a small oscillatory perturbation to the larger amplitude, slow *secular motion*. By averaging over the fast micromotion, a particle close to the Paul trap center, can be described by only considering the secular motion in a radial harmonic *pseudo-potential*:

$$\Phi_r(r) = \frac{1}{2} M \omega_r^2 r^2 \ , \tag{2.8}$$

where

$$\omega_r^2 = \frac{Q^2 U_{rf}^2}{2 M^2 r_0^4 \Omega_{RF}^2} - \frac{\eta Q U_{DC}}{M z_0^2} \ . \tag{2.9}$$

From eq. (2.1) it follows that the axial motion (along the z-axis) of a single charged particle is that of a simple harmonic oscillator with a frequency ω_z, determined by the

amplitude of the end-electrode DC voltage. The harmonic potential along the trap axis, z, can thus be rewritten in the form

$$\Phi_z(z) = \frac{1}{2} M \omega_z^2 z^2 \ , \tag{2.10}$$

where

$$\omega_z^2 = \frac{2\eta Q U_{DC}}{M z_0^2} \ . \tag{2.11}$$

Notice from eq. (2.8)-(2.11), that the radial pseudo-potential contains a term which is inversely proportional to the mass of the trapped ion while the axial potential is independent of the mass. This causes heavier species to be confined less tightly in the radial plane than lighter species, which is relevant when trapping multi-component ion Coulomb crystals [106]. The final trapping potential is now given by the sum of the radial pseudo-potential and the axial DC-potential

$$\Phi_{trap} = \Phi_z(z) + \Phi_r(r) \ . \tag{2.12}$$

2.2 Laser cooling of $^{40}Ca^+$ ions

Here, we are going to describe laser cooling of $^{40}Ca^+$ ions. First, we introduce the concept of Doppler cooling in general and later apply it to the case of trapped calcium ions.

2.2.1 Doppler cooling

To lower the kinetic energy and the entropy of trapped ions, one can use laser cooling. Laser cooling of atoms and ions is a widely used technique, described in many different contexts. An outline of different cooling techniques for trapped ions is found in e.g. [107–109]. In the experiments described in this thesis, we only use the *Doppler-cooling* technique and will here mainly focus on aspects relevant for $^{40}Ca^+$ ions.

The principle of this cooling technique is based on the velocity dependent absorption probability of photons experienced by moving atoms illuminated by near resonant monochromatic light due to the Doppler-effect. When applying two counter-propagating laser beams to an atomic medium the Doppler-effect will cause absorbers moving in one direction to see the light shifted differently than absorbers moving in the opposite direction. The frequency of the light seen by absorbers (atoms or ions) moving with velocity $\vec{v}$ is hence shifted according to the Doppler formula: $\omega_\pm = \omega_l(1 \pm \frac{v}{c})$, where ω_l is the laser frequency and c the velocity of light. Here, the positive (negative) sign applies to absorbers moving towards (away from) the laser beam, and the description is kept to one dimension but can easily be expanded to all three dimensions.

If the laser frequency is less than the atomic resonance frequency (red detuned) atoms moving towards the laser beam are shifted into resonance and will have a higher absorption probability than those moving away from the laser beam. Assuming relatively low laser intensities, after each absorption, the ion will undergo spontaneous photon emission in a centrosymmetric distribution (equal emission probability for opposite directions), whilst the absorption process occurs in a specific direction. This leads to a friction force and an effective deceleration of the atomic motion in one direction because of the decrease in kinetic energy after each scattering event.

We consider a free two-level atom interacting with a near-resonant monochromatic field, having a detuning, $\Delta_l = \omega_{at} - \omega_l$, with respect to the atomic transition frequency and an intensity much lower than the saturation intensity for the atomic cooling transition ($I \ll I_{sat}$)[1]. The net force exerted on the atom can be found as [27, 107]

$$F = F^{+} + F- \tag{2.13}$$

$$= \frac{\hbar k \Gamma}{2} \frac{I}{I_{sat}} \left[\frac{1}{1 + (2(\Delta_l + kv)/\Gamma)^2} - \frac{1}{1 + (2(\Delta_l - kv)/\Gamma)^2} \right] \approx \beta v \ . \tag{2.14}$$

Here, F^{+} is the force from the co-propagating beam while F^{-} is for the counter-propagating beam. $k = \omega_l/c$ is the laser field wave-vector and $\Gamma = 2\gamma$ is the spontaneous decay rate of the two-level system, with γ being the decoherence rate of the atomic dipole. The force can be expressed through a friction coefficient, β, times the atomic velocity, by performing a 1st order expansion in kv, as indicated in eq. (2.14). To work as a friction force β needs to be negative, requiring $\Delta_l > 0$, corresponding to a red detuning. The scheme can be easily extended to three dimension using three sets of counter-propagating beams to cool a free atom.

The centrosymmetric spontaneous photon re-emission is causing a diffusion process, rather than a net-force on the atoms, and this limits the reachable temperature when using Doppler cooling. In steady state, an equilibrium arises as a balance between friction and diffusion in the simple picture described above, and for an optimal detuning choice ($\Delta_l = \Gamma/2$) the so-called *Doppler temperature* can be reached:

$$T_D = \frac{\hbar \Gamma}{2 k_B} \ . \tag{2.15}$$

The minimum temperature obtainable by Doppler laser cooling is thus set by the width of the transition Γ.

2.2.2 Doppler cooling of $^{40}Ca^{+}$ ions

The previous description assumes a free particle whereas our ions are trapped. However, as we will discuss shortly, for the parameters used for trapping and cooling in the experiment this picture still holds. In all experiments presented in this thesis $^{40}Ca^{+}$ ions were used and in fig. 2.2 the relevant energy levels are shown.

The laser cooling beams are slightly red detuned from the $4S_{1/2} \leftrightarrow 4P_{1/2}$ transition around 397 nm, illustrated as a thick blue arrow. An excited ion in the $4P_{1/2}$ state can spontaneously decay back to the ground state $4S_{1/2}$ or to the metastable $3D_{3/2}$ state. The branching ratio of these two decays is $\sim 1 : 12$, but since the lifetime of the metastable state is about 1 second, ions ending up in this state will leave the cooling cycle long enough to prevent effective cooling. To actively pump these ions back into the cooling cycle, an additional *repumping* laser, resonant with the $3D_{3/2} \leftrightarrow 4P_{1/2}$ transition around 866 nm, must be applied, illustrated in fig. 2.2 (a thick red arrow). Note here, that decay from $4P_{1/2}$ has a total rate of $\Gamma_{P_{1/2}} = 2\pi \times 22.4$MHz. Consequently, the time associated with the cooling absorption/emission process is much less than the timescale of the secular ion motion in the harmonic trap potential

[1]The saturation intensity is defined as $I_{sat} = \frac{\hbar \omega_0 \Gamma}{2\sigma(\omega_0)}$, where $\sigma(\omega_0)$ is the resonant absorption cross section

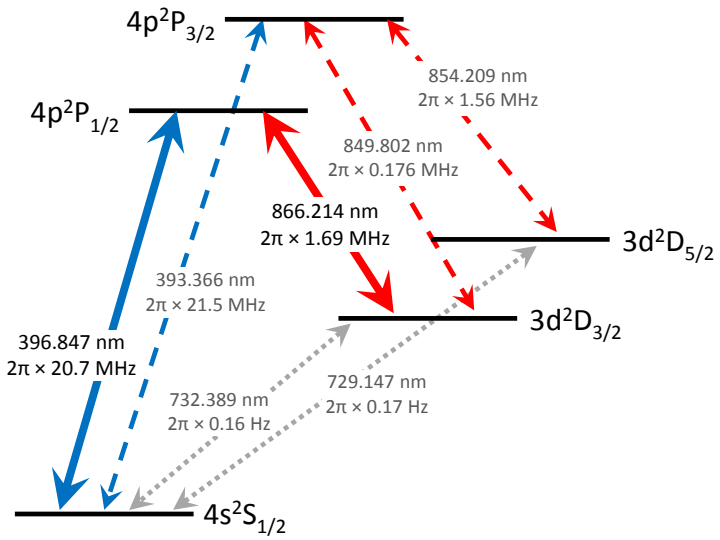

Figure 2.2: Energy level scheme for $^{40}Ca^+$ with transition wavelengths in air and decay rates ($\Gamma = 2\gamma$) for the dipole allowed transitions (taken from [110, 111]). The solid lines indicate relevant transitions for the Doppler cooling used in this thesis, i.e. the $4S_{1/2} \leftrightarrow 4P_{1/2}$ cooling transition (blue) and the $3D_{3/2} \leftrightarrow 4P_{1/2}$ repumping transition (red).

(see sec. 2.1). Typical trapping frequencies in the experiments described are in the few $10 - 100$ kHz range, so the ions in the trap can effectively be considered as free particles for the Doppler cooling process. Actually, from a frequency perspective, the ion motion adds sidebands to the absorption spectrum at the trap frequency, but since the linewidth of the cooling transition is much broader than the trap frequencies, these sidebands are not resolved. As the ion's momentum is much greater than the photon's, many scattering cycles are needed to cool down the $^{40}Ca^+$ ion close to the Doppler limit, $T_D \approx 0.5$ mK.

In general, three sets of counter propagating laser beams are needed to perform Doppler cooling of atoms, but in the confining potential from the linear Paul trap, cooling only from three directions is necessary as the ion motion reverses direction after each half-period of its axial or radial oscillation [109]. Actually, cooling can be accomplished using a single laser beam, provided that this beam has a component of its k-vector along each of the normal modes of the trap, and that the three trap frequencies (ω_x, ω_y, ω_z) are non-degenerate. The laser systems used for Doppler cooling and the optical setup will be presented in sec. 5.5, including the description of the isotope-selective loading of Ca^+-ions from neutral Ca atoms.

2.3 The physics of ion Coulomb crystals

In this section we describe the properties of ion Coulomb crystals. First, we introduce the different ion structures that we will encounter in the thesis. Afterwards, we describe the thermodynamics of ion Coulomb crystals in which the different phase

transitions will be introduced besides the zero temperature charged liquid model. In the end we discuss micromotion and temperature effects.

2.3.1 Ion structures

A deterministic isotope selective ionization process is used to load Ca^+ ions into our trap system, by using a two-photon process enhanced by the first resonant absorption stage (see sec. 5.5.5). After (or while) loading a cloud of ions into the trap, laser cooling can be used to lower the kinetic energy of the system. As the cloud gets colder and denser, Coulomb interactions between the ions get more and more important. At very low temperatures, when the mean Coulomb energy is much larger than the mean kinetic energy, the ions organize in well-ordered configurations in space. The configuration of the ion structures can be controlled by varying the DC and RF electrical voltages. Choosing to trap a single ion, there is a great freedom in choosing the possible potentials, and the ion thermal position distribution can be shaped almost at will [102, 112]. With high electrode voltages the ion position can be pinned in

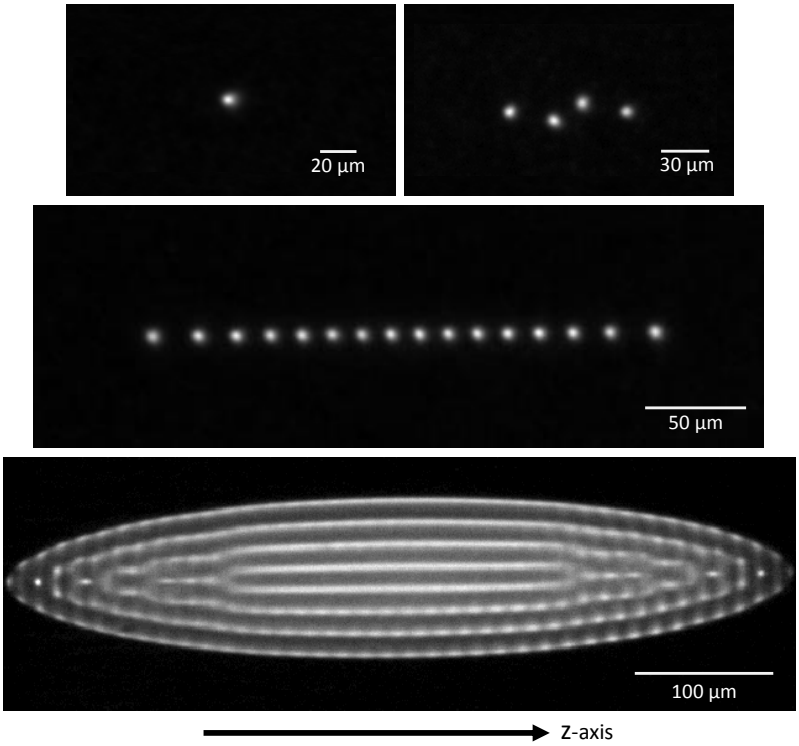

Figure 2.3: Projected images of four different types of trapped ion structures ($^{40}Ca^+$), obtained by collecting the 397nm fluorescence light emitted during cooling: a single ion, a 1D string of 16 ions, a 2D "ZigZag" crystal of 4 ions and a 3D ion Coulomb crystal of ~ 1000 ions. The three-dimensional crystal shape can be visualized by rotating the crystal around the z-axis. Relative length scales are defined on the figures. For more detail about the imaging and detection system see sec. 5.6.

a very deep potential of several tens of eV ($> 10^5$ K) and a spatial extent much lower than the optical wavelength scale can be obtained, e.g. turning the ion into a nanoscopic probe of an optical field [15]. For lower electrode voltages the position distribution of the ion can extend over a much larger area (see fig. 2.3 where the ion position extends over several microns). By adding DC-potentials to the electrodes individually or in combinations the ion position distribution minimum can be moved around in the trap deterministically. An ion placed off the trap-axis will undergo micromotion, potentially leading to additional heating and spectral broadening [113] (for more details on micromotion see sec. 2.3.4).

When more than one ion are simultaneously trapped, the Coulomb interaction between the ions has to be taken into account. In a cloud of trapped ions, the particles are subjected to both the trapping potential and the Coulomb potential arising from the other ions. The repulsion between the particles will couple their individual motional degrees of freedom. For a radial confinement much stronger than the axial, small ensembles of ions will arrange in a string configuration along the RF field-free trap axis, coupling the axial vibrational modes of the ions (see fig. 2.3). As a consequence, the axial and radial motion are in principle uncoupled and Doppler cooling along both axial and radial directions is still necessary. Such strings of ions can be used for many applications including quantum computing, where the individual ions work as so-called quantum bits and the large ion separation arising from the Coulomb interaction makes it easier to perform individual addressing and detection (for more detail see e.g. [49, 50]). By either lowering the axial or raising the radial electronic potentials, stable 2D structures of ions can be designed, e.g. the ZigZag pattern shown in fig. 2.3 [114, 115], or the pancake-shaped crystals obtained in [116].

For a large ion ensemble, lowering the radial confinement arranges the ions in a three dimensional spheroidal structure [78, 117], where some ions are situated off the RF field-free trap axis. As a consequence, it is never possible to avoid micromotion effects in the ensembles. Furthermore, the Coulomb interaction leads to a coupling of radial and axial motions, whereby it is sufficient to only apply cooling light along the longitudinal axis and still get efficient three-dimensional cooling. As a cooling beam along the radial direction can drive the jittery micromotion it is actually preferable, especially with large ensembles, to only apply the cooling light along the RF-field free trap axis. For a description of the experimental laser cooling beam directions in the different configurations, see sec. 5.5.

In the experiments described in this thesis, we will encounter a variety of ion structures, from single ions, through ion strings and ZigZag patterns, to large so-called ion Coulomb crystals, which will be described in more detail in the next section (see fig. 2.3) [118].

2.3.2 Thermodynamics of ion Coulomb crystals

For many purposes a large ensemble of ions, confined in the linear Paul trap, can be well-described as a non-neutral plasma and characterized in terms of collective parameters such as temperature and density. Later, we will introduce the zero-temperature charged liquid plasma theory, but to sketch the background for the model, we start by introducing some concepts and parameters from plasma physics.

Consider a plasma of identical charged particles, each with charge Q and mass

M, trapped in a linear Paul trap, thus experiencing the pseudo-potential defined in eq. (2.12). In a static situation, corresponding to zero temperature ($T = 0$), the equilibrium force on a single particle has to vanish, hence causing the total potential to be constant [119]:

$$\mathbf{F} = -Q\nabla\Phi_{tot}(\mathbf{r}) = 0 \quad \Rightarrow \quad \Phi_{tot}(\mathbf{r}) = \Phi_{trap}(\mathbf{r}) + \Phi_{pl}(\mathbf{r}) = const. \tag{2.16}$$

The total potential is defined here as the sum of the trapping potential, Φ_{trap} from eq. (2.12), and the mean electrostatic plasma potential from the charge distribution of the particles, Φ_{pl}. In this case, the charge distribution and, hereby the atomic density ρ_0, is constant throughout the ensemble. The density can be related to the trap potential by using Poisson's equation on the plasma potential, $\nabla^2\Phi_{pl}(\mathbf{r}) = -Q\rho_0/\epsilon_0$, giving:

$$\nabla^2\Phi_{trap}(\mathbf{r}) = \frac{Q\rho_0}{\epsilon_0} \ . \tag{2.17}$$

Now, inserting the explicit expressions of the trap potential (eq. (2.8) and eq. (2.10)) and taking the Laplacian, an expression for the average equilibrium density of the ion system can be found as

$$\rho_0 = \frac{\epsilon_0 U_{rf}^2}{M r_0^4 \Omega_{RF}^2} \ . \tag{2.18}$$

Notice that ρ_0 does not depend on the axial DC voltage and for a fixed RF-frequency, Ω_{RF}, it can be controlled by exclusively varying the RF voltage applied to the electrodes of the Paul trap. By knowing the density of the ion plasma we can deduce the mean distance between neighboring particles. This is found by assuming that each particles occupies a certain spherical volume with a so-called Wigner-Seitz radius, a_{WS}:

$$\frac{4}{3}\pi a_{WS}^3 = \frac{1}{\rho_0} \ , \tag{2.19}$$

where ρ_0 can be inserted from eq. (2.18).

Image a plasma of some density, ρ_0, and consider a one-dimensional displacement, δx, of a sheet of charge within the plasma. The sheet experiences a field associated with its own displacement corresponding to: $|\mathbf{E}| = Q\rho_0\delta x/\epsilon_0$. The potential energy associated with the displacement, U, can be found from the force $\mathbf{F} = Q\mathbf{E}$ as

$$U = \int F dx = \frac{Q^2\rho_0\delta x^2}{2\epsilon_0} \ . \tag{2.20}$$

The potential that the sheet experiences can be approximated by a harmonic potential: $U = \frac{1}{2}M\omega^2\delta x^2$, from which the oscillation frequency can be extracted as

$$\omega_{pl}^2 = \frac{Q^2\rho_0}{M\epsilon_0} \ . \tag{2.21}$$

This is generally referred to as the plasma frequency, which sets the fundamental time scale for motions in the plasma and the dynamics of the charge redistribution after external perturbations. From this, the related typical length scale of the plasma, called the Debye length λ_D, can be defined using the Virial theorem $\langle U\rangle = \langle E_{kin}\rangle$. By

inserting the harmonic potential energy $\langle U \rangle = \frac{1}{2} M \omega_{pl}^2 \lambda_D^2$ and the thermal equilibrium kinetic energy in one dimension $\langle E_{kin} \rangle = \frac{1}{2} k_B T$, we find:

$$\lambda_D = \sqrt{\frac{k_B T}{M \omega_{pl}^2}} = \sqrt{\frac{\epsilon_0 k_B T}{\rho_0 Q^2}} \ . \tag{2.22}$$

The Debye length can be interpreted as the length scale at which an external field perturbation is shielded by rearrangement of the space charge inside the plasma. Also, an ensemble of charged particles can only be considered a plasma if the complete spatial extend of the ensemble is much larger than the Debye length. Considering the ion ensembles used in our experiments with typical temperatures of ~ 10 mK and densities of $\sim 10^8 - 10^9$ cm^{-3}, we obtain $\lambda_D \sim 300$ nm. This is much less than the typical inter-ion spacing of ~ 10 μm and, consequently, even small Coulomb crystals in our system can be described using plasma theory.

Another useful thermodynamical parameter, used to describe an ion Coulomb crystal, is the plasma coupling parameter Γ_p. It is given as the ratio of the mean Coulomb interaction energy to the mean thermal energy. For a one-component plasma with particles of charge Q at a temperature T, Γ_p is defined as [120]

$$\Gamma_p = \frac{Q^2}{4\pi\epsilon_0 \ a_{WS} k_B T} \ . \tag{2.23}$$

Knowing Γ_p for a plasma system it is possible to estimate its thermodynamical state. From molecular dynamics simulations it has been found that an infinitely large plasma will undergo a phase-transition from gas to liquid at $\Gamma_p \simeq 2$ as short-range ordering occurs [117], and a phase-transition from liquid to solid state around $\Gamma_p \simeq 170$ with the establishment of long-range ordering throughout the plasma [121, 122]. The hot ion cloud will get denser and denser as it is cooled down and undergoes a phase transition into a liquid state (typically at ∼K temperatures). Cooling the plasma even more, (at ∼mK temperatures) will make the ions crystallize in a spatially well-ordered structure, forming a so-called Coulomb or Wigner crystal [123–125].

For infinite plasmas at zero temperature, the simulations predict crystalline structures in a body-centered cubic (bcc) arrangement. For crystals with finite size, surface effects have to be taken into account. These cause the ions to distribute in concentric shells with a two-dimensional hexagonal structure within each shell and a constant radial inter-shell spacing, δr, throughout the whole crystal [118]. They can be seen e.g. in fig. 2.3 showing a crystal with ~ 1000 $^{40}Ca^+$ ions. Varying the RF and DC trapping voltages, the crystal shape can be controlled as it depends on the radial and axial trapping frequencies. Shell-structured crystals were observed in linear Paul traps briefly after the invention of the trap, using buffer gas cooled aluminum particles of micron size [126], and after the introduction of Doppler cooling, atomic ion Coulomb crystals was produced in both linear Paul traps [123, 124] and Penning traps [127].

The simulations predict that, for infinitely long crystals having parallel shells in the center, the inter-shell spacing is proportional to the Wigner-Seitz radius (defined in eq. (2.19)) as: $\delta r = 1.48 a_{WS}$ [118]. In our group, shell structures have been experimentally confirmed for ion Coulomb crystals in a linear Paul trap [125] and the above relation of δr has been shown to be in good agreement with the expected value from MD simulations [128]. Measuring the exact value of the DC and RF voltages

is not trivial for technical reasons, but from knowledge of δr the crystal density can be determined and this provides a method to calibrate the trap voltages seen by the ions through eq. (2.18) [27, 128].

2.3.3 Zero temperature charged liquid model

A convenient plasma description of ion Coulomb crystals can be constructed using the so-called *zero temperature charged liquid model* [119, 120, 129], that derives explicit expressions for the plasma potential of the crystal in the linear Paul trap. The trapping potential of the linear Paul trap is cylindrically symmetric (as defined in eq. (2.12)) and, as a consequence, the equilibrium shape of the plasma is a spheroid with constant density. The spheroids are defined by the aspect ratio between their radius, R, and length, L, as

$$\alpha = \frac{2R}{L} \ . \tag{2.24}$$

The model distinguishes between three system shapes: prolate ($\alpha < 1$), oblate ($\alpha > 1$) and spherical ($\alpha = 1$). An outcome of the model is a relationship between the ratio of trap frequencies, ω_z/ω_r, and the aspect ratio, incidentally providing a calibration tool for the trap RF-voltages.

An explicit form of the electrostatic potential within the plasma, which arises from the charge distribution and depends on the charge, Q, the plasma zero-temperature density ρ_0 and the crystal aspect ratio, can be found in [119]. By taking the sum of the plasma potential and the trapping potential (eq. (2.12)) and applying Poisson's law, the potential separates in a radial and an axial part. The trap frequencies in the radial and axial directions, ω_r and ω_z, can then be expressed as (see [119])

$$\omega_r^2 = \frac{\rho_0 Q^2}{2M\epsilon_0} R^2 L \ f(R,L) \ , \tag{2.25}$$

$$\omega_z^2 = \frac{\rho_0 Q^2}{2M\epsilon_0} R^2 L \ g(R,L) \ , \tag{2.26}$$

where the two shape-related function $f(R,L)$ and $g(R,L)$ are calculated from the zero temperature charged liquid model, accounting for the difference between prolate and oblate systems (see [27, 119]). The ratio between the trap frequencies in the model can thus be written as

$$\frac{\omega_z^2}{\omega_r^2} = \frac{g(R,L)}{f(R,L)} = -2 \begin{cases} \frac{\sinh^{-1}\left(\alpha^{-2}-1\right)^{1/2} - \alpha\left(\alpha^{-2}-1\right)^{1/2}}{\sinh^{-1}(\alpha^{-2}-1)^{1/2} - \alpha^{-1}(\alpha^{-2}-1)^{1/2}} & \text{, for } \alpha < 1 \ , \\ \frac{\sin^{-1}\left(1-\alpha^{-2}\right)^{1/2} - \alpha\left(1-\alpha^{-2}\right)^{1/2}}{\sin^{-1}(1-\alpha^{-2})^{1/2} - \alpha^{-1}(1-\alpha^{-2})^{1/2}} & \text{, for } \alpha > 1 \ , \end{cases} \tag{2.27}$$

where the explicit expressions for the f and g functions have been inserted. This relationship has been shown to be in good agreement with experiments performed with ion Coulomb crystals with a moderate size aspect ratio ($\alpha \lesssim 1$) [106, 128, 130]. Furthermore, we can take the ratio of the trap frequencies found in eq. (2.9) and (2.11), which directly relates the applied trap voltages as

$$\frac{\omega_z^2}{\omega_r^2} = \left[\frac{Q U_{rf}^2 z_0^2}{4\eta M r_0^4 \Omega_{RF}^4 U_{DC}} - \frac{1}{2} \right]^{-1} \ . \tag{2.28}$$

Consequently, from the two expression of the relative trap frequencies (eq. (2.27) and eq. (2.28)) the trap voltages, U_{DC} and U_{rf}, can be calibrated, by experimentally measuring the aspect ratio, $\alpha(R, L)$, of a trapped ion Coulomb crystal for varying RF and DC voltages (for more detail see [27, 73]).

Finally, we note that as long as the ion length and radius are much larger than the distance between neighboring ions (i.e. $L, R \gg a_{WS}$) the zero temperature charged liquid model provides a good description of the ion ensemble. This also implies, that 1D string [110, 131] and 2D planar [114, 115] structures are special cases, in which the liquid model can not be considered as a good description of the shape [116]. Here, other approaches (e.g. MD simulations) have to be implemented in order to obtain detail structural information.

2.3.4 Micromotion and temperature effects

Describing the ion Coulomb crystals we have only considered the secular motion in the time-averaged pseudo potential (eq. (2.8)), and hence ignored effects of the micromotion. For a complete description of the ion motion in the trap, we would have to include the time-varying forces from this RF-field that causes the ion kinetic energy to vary dramatically, but periodic on the associated timescale. The velocity distribution is position and time dependent, and, as a consequence, the atomic transitions can be inhomogeneously broadened or unwanted heating can be introduced to the system.

The axis of the linear Paul trap is a desirable position to place single ions as the micromotion effects here can be put to a minimum. From eq. (2.6) we can write the micromotion amplitude for an ion on the axis as

$$A_{micro} = \frac{1}{2} u_0 q \ , \tag{2.29}$$

where u_0 is the amplitude of the slow secular motion. In principle, placing an ion on the trap axis and cooling it, i.e. decreasing the secular motion amplitude, thus minimizes the micromotion amplitude. As a consequence, experiments with ions placed on the trap axis can be done with almost no detectable Doppler broadening of the atomic transitions from micromotion effects.

Adjustment of the DC voltages of the individual electrodes can be used to position the ion on the RF field-free axis, thus minimizing radial micromotion. Even so, in practice, there can still be some excess micromotion due to slight asymmetries in the trapping potentials. This might come from small asymmetries in electrode geometry or alignment, patch potentials, asymmetry in the RF-voltage provided to the individual electrodes, etc. Moreover, even if the RF-field is intentionally designed to only affect the radial trapping potential, a small axial component can also be present.

RF-signal can be coupled directly into the axial direction through the voltages applied to the electrodes. As seen on fig. 2.1 the RF-signal is sent to all 12 electrodes in the quadrupolar configuration. The phase of the voltages sent to each of the electrode segments needs to be well controlled and small phase differences may cause inhomogeneities in the electrical potential seen by the ions. In particular, one could imagine a phase difference between the four electrodes in one end compared to the other end, in the axial direction. This phase difference would introduce axial micromotion to the

system, which has a big effect on the single ion level. In our setup, capacitative loads are placed between the voltage supplies and the trap electrodes, making it possible to carefully adjust the offsets and phases of every electrode [27, 128], minimizing the voltage-related excess micromotion (see sec. 5.7).

In addition, the system used for our experiments incorporates the two mirrors of the optical cavity parallel to the trap axis. The dielectrics of the cavity mirrors might cause the RF-field lines to bend and introduce axial micromotion. Simulations performed by Anders Mortensen [14] revealed that the effect of the cavity mirrors would be reduced by adding (at the extremity of the mirrors) a flat dielectric coat filling the region between the mirrors and the electrodes almost entirely (see sec. 5.4).

The techniques for detecting and minimizing the excess micromotion of single ions in our trap will be presented in chap. 7 in the context of the localization of ions in optical potentials, for which control of the micromotion is a crucial prerequisite.

Considering three dimensional ion Coulomb crystals, there are always ions off the axis and, as a consequence, there is always intrinsic micromotion in the system. Ions placed radially off the RF nodal-line will experience micromotion of the same form as shown by eq. (2.29), but with the ion mean distance from the trap axis replacing u_0, and hence a much larger amplitude. Thus, the atomic transitions can be inhomogeneously broadened [113]. The micromotion can of course be minimized by placing the crystal symmetrically with the trap axis. Moreover, performing laser spectroscopy only in the axial direction also minimizes the effect of the micromotion, as it is mainly radial (although one can expect a small axial component arising from the coupling between the different motional degrees of freedom of the ions induced by the Coulomb interaction).

In addition, in Coulomb crystals the ions are not only affected by the RF-field, but they also affect each other. The RF-motion will cause collisions from the Coulomb interaction between the ions and heat the crystal, as the RF-driven kinetic energy is coupled into the secular motion. This effect is often referred to as RF-heating [132]. The heating effectively raises the temperature of the whole crystal and is more important for crystals with high aspect ratio, having many ions away from the axis, and for high RF-voltage amplitudes. For large ion Coulomb crystals, with many ions in regions of large micromotion, it has been observed in both simulations and experiments that the RF-heating can increase the crystal temperature well above the Doppler limit [27, 73, 129, 133].

In some of the experiments reported in this thesis (sec. 6.1) we study the coupling between large ion Coulomb crystals and the cavity field . In this context, the Doppler broadening of the atomic transitions is relevant (see chap. 3) and can be found by measuring the crystal-cavity coupling, from which we can estimate the temperature of the ions.

Chapter 3

Atom-Cavity field interactions

In this chapter we will introduce the theoretical concepts necessary to describe the ion-cavity QED system. In the first section (3.2) we describe the dynamics of a single mode of the electromagnetic field confined in an *empty* optical cavity. We will introduce the different longitudinal and transverse cavity modes (sec. 3.2.1) before describing the dynamics of the cavity field close to a cavity resonance and deriving the steady state cavity reflection and transmission spectra (sec. 3.2.2). In sec. 3.3 we describe how an ensemble of two-level atoms interacts with a single mode of the cavity field. In doing so, the Tavis-Cummings model is introduced (sec. 3.3.1), after which equations of motion for the atom and cavity field observables will be derived in a semi-classical picture. Last, we will consider a situation where the atom-cavity system is weakly probed at the single-photon level (low saturation), initially without considering atomic motion (sec. 3.3.2) and, subsequently, with atomic motion in one dimension (sec. 3.3.3).

3.1 Introduction

The interaction between a single mode cavity electromagnetic field and a system of atoms, at the quantum level, can be described within the frame of CQED, see e.g. [1, 3, 134]. CQED has the past decades had a major impact in the fields of quantum mechanics and, atomic and optical physics. A huge progress is currently being made in developing different experimental systems exploiting CQED concepts and techniques, e.g. within quantum information processing (QIP) [135] or quantum metrology [136].

Cold trapped ions in optical cavities is one of the most promising systems currently investigated in this context. For a system containing a single two-level atom interacting with a single photon in the cavity mode, it is necessary to describe the dynamics purely quantum mechanically, and effects that depends on the exact number of photons in the cavity, can be studied. Strong coupling between a single ion in an optical cavity has not yet been achieved, but these systems has still been used to e.g. probe the spatial structure of a cavity field [15], generate single photons [16, 17, 137], and demonstrate a single ion laser [23]. In this thesis, we describe a special semi-classical case of CQED, that does not require having exactly one photon in the system. In stead we are working with a few photons (classically), but the dynamics will be the

same as in the quantum case, as long as the number of photons are much smaller than the number of interacting atoms in the ensemble [28].

3.2 A linear Fabry-Pérot optical cavity

In this section, we introduce the mathematical description of a light field confined in a single mode optical cavity. First, we introduce the concept of cavity modes, both transverse and longitudinal, after which, we derive the dynamical field equations of the empty cavity, together with the reflectivity and transmittance spectra.

3.2.1 Spatial cavity modes

In an empty cavity the mirrors impose boundary conditions for the electromagnetic field and light can build up only in certain cavity modes. We consider a cavity of two flat mirrors, M_1 and M_2, separated by the distance L (see fig. 3.1). The cavity resonance condition requires that the phase of the field changes by an integer multiple of 2π after one round trip. This imposes that resonant modes in the longitudinal (axial) direction will be be standing waves, and their wavelength has to satisfy: $\lambda_q = 2L/q$, where $q \in N$ is the longitudinal mode number. The resonance frequencies, when only considering the longitudinal direction, are thus

$$\nu_q = \frac{c}{\lambda_q} = \frac{qc}{2L} \ , \tag{3.1}$$

where c is the speed of light. Fig. 3.1 shows the longitudinal standing wave modes inside the cavity for four different mode number ($q = 1, 2, 3, 20$). It is clear that

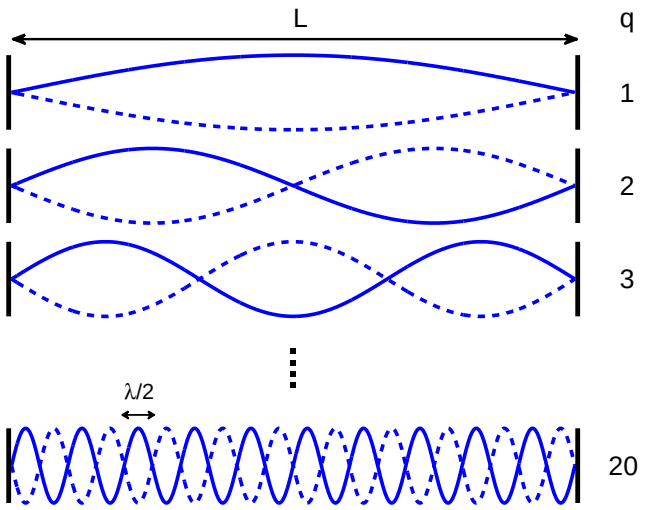

Figure 3.1: Sketch of the longitudinal standing wave modes for a laser field inside a cavity of length L, shown for resonances with mode numbers $q = 1, 2, 3, 20$. Each loop of the standing wave envelope has the width of half the laser wavelength, $\lambda/2$

increasing q by one adds an extra loop to the standing wave, corresponding to half the wavelength of the resonant laser field ($\lambda/2$). Considering the wavelength and cavity dimensions used in the experiments ($\lambda = 866$ nm and $L = 11.8$ mm) we obtain a mode number of $q \approx 2.7 \times 10^4$, thus a huge number of standing wave envelopes will be present in the cavity at all times. Furthermore, we remark that the phase of the standing wave has a specific parity in the center of the cavity. i.e. modes with an odd q have maximum amplitude and modes with an even q have minimum amplitude in the center. The standing wave nature of the field inside the cavity will become important later in the thesis, when we describe a beat mechanism between two different longitudinal field modes in sec. 6.2, as well as when describing the interaction between ions and a far detuned intracavity lattice field (see sec. 7). Now, we can introduce the free spectral range (FSR) of the cavity, i.e. the frequency spacing between two subsequent longitudinal modes: $\nu_{FSR} = c/(2L)$.

Due to the unstable nature of the flat mirror cavity, we change our description to a cavity of spherical mirrors with a radius of curvature r_M (fig. 3.2). Consequently, we have to also take into account the transverse components of the intra-cavity electromagnetic field. It can be shown that the frequency of a so-called TEM_{nm} mode (Transverse Electric and Magnetic mode), resonant with a spherical mirror cavity of length L, must satisfy [138, 139]

$$\nu_{nmq} = \nu_{FSR} \left[q + \frac{1}{\pi}(n + m + 1) \arccos\left(1 - \frac{L}{r_M}\right) \right] . \tag{3.2}$$

ν_{nmq} now depends on the two transverse mode indices, m and n, in addition to the longitudinal mode number q as before.

These TEM_{nm} modes also have a well-defined spatial distribution and in the so-called paraxial approximation (small angles) they are called the Hermite-Gaussian modes (see e.g. [138, 140]), for which the spatial field distributions is expressed as

$$E_{nm}(\mathbf{r}) = E_0 \Psi_{nm}(\mathbf{r}) = E_0 \Psi_n(x, z) \Psi_m(y, z) \Phi(x, y, z) , \tag{3.3}$$

where E_0 is the amplitude of the electric field. The transverse mode function are

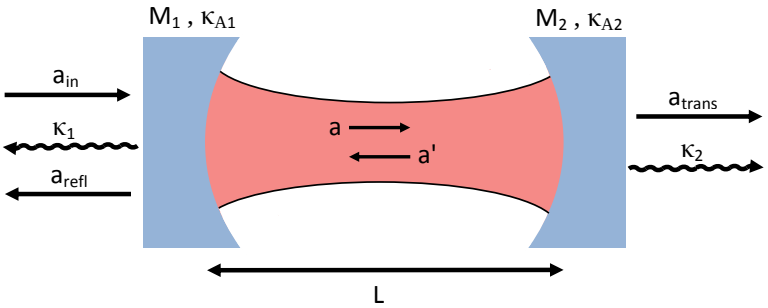

Figure 3.2: Schematics of a symmetric linear Fabry-Pérot cavity of length L consisting of two curved mirrors, both with radius of curvature r_M. The light field amplitudes, a_j, are marked at different locations and specified in the text together with the cavity loss rates κ_j.

given by ($u = x, y$):

$$\Psi_n(u,z) = \sqrt{\frac{\omega_0}{\omega(z)}}\, H_n\left(\frac{\sqrt{2}u}{\omega(z)}\right)\, \exp\left(-\frac{u^2}{\omega(z)^2}\right)\ , \tag{3.4}$$

where $H_n(\xi)$ is the n-th Hermite polynomial with $n > 0$, $\omega(z) = \omega_0\sqrt{1+(z/z_R)^2}$ is the position depending beam waist, ω_0 the minimum waist and $z_R = (\pi\omega_0^2)/\lambda$ is the Rayleigh range. The longitudinal (complex) field mode, that also depends on the transverse indices n and m, is defined as

$$\Phi(x,y,z) = \sin\left(kz - (m+n+1)\arctan\left(\frac{z}{z_R}\right) + \frac{k(x^2+y^2)}{2R(z)}\right)\ . \tag{3.5}$$

Here we introduced the wavenumber $k = 2\pi/\lambda$ and the radius of curvature of the wavefronts $R(z) = z\left[1+(z_R/z)^2\right]$.

In eq. (3.3) all possible modes are included, but often (as long as these modes are well-separated in frequency), one can restrict the analysis to a single mode. In the experiments described here we work mostly with the fundamental TEM_{00} mode. The expression for this lowest order mode is relatively simple as it is cylindrically symmetric with a Gaussian field distribution along the transverse axis (note that $H_0(\xi) = 1$):

$$\Psi_{00}(x,y,z) = \frac{\omega_0}{\omega(z)}\exp\left(-\frac{x^2+y^2}{\omega(z)^2}\right)\ \sin\left(kz - \arctan\left(\frac{z}{z_R}\right) + \frac{k(x^2+y^2)}{2R(z)}\right)\ . \tag{3.6}$$

The phase difference between a cavity mode wave and a plane wave with the same frequency is defined as the *Gouy* phase shift, $\phi_G(z) = -(m+n+1)\arctan(z/z_R)$, which can also be used to characterize the considered mode.

In sec. 3.3 we are going to describe the interaction between a single cavity mode and an atomic ensemble. Several different cavity modes can be chosen and the difference in coupling strength for higher order modes, compared to the fundamental TEM_{00} mode, can be significant. For more detail see [73, 74]. Coupling an ion Coulomb crystal to different cavity modes can be interesting when considering multi-mode storage of quantum information, a possibility that we will discuss in the next chapter.

3.2.2 The dynamics of the cavity field close to a resonances

In this section we consider the linear optical Fabry-Pérot cavity, as sketched in fig. 3.2. For now, the cavity contains no medium, and a monochromatic light field a_{in} is injected through mirror 1 with a frequency close to a cavity resonance. We wish to find expressions for the steady state cavity spectrum, i.e. a relation between the incoming field and the reflected and transmitted fields, as function of the input field frequency and the cavity parameters. The two mirrors are charactered by their (intensity) transmission, reflection and loss coefficients, T_j, R_j and A_j, respectively ($j = 1, 2$). On fig. 3.2 a is the intracavity field amplitude at the incoupling mirror and a' is the field amplitude after one round trip in the cavity. Furthermore, a_{trans} and a_{refl} are the transmitted and reflected field amplitudes coupled out of the cavity.

We inject a monochromatic input field of frequency ω_l into the cavity through mirror 1, as specified above. The mirror transmission, reflection and loss coefficients related to the field amplitudes, t_j, r_j and α_j (j=1,2), can be related to the corresponding intensity coefficients by: $t_j = \sqrt{T_j}$, $r_j = \sqrt{R_j}$ and $\alpha_j = \sqrt{1 - A_j}$. By conservation of energy, we require that $T_j + R_j + A_j = 1$. The intracavity field amplitude after the first mirror, M_1, is given by

$$a(t) = t_1 a_{in}(t) + \alpha_1 r_1 e^{i\pi} a'(t) \ , \tag{3.7}$$

where $e^{i\pi}$ is the phase shift arising from the reflection on the mirror. The field amplitude after a reflection on M_2 can be found as

$$a'(t) = \alpha_2 r_2 \ a(t-\tau) \ e^{-i\phi} e^{i\pi} \ , \tag{3.8}$$

where $\tau = (2L)/c$ is the round trip time, $\phi = \Delta_c \tau = (\omega_c - \omega_l)\tau$ is the phase change of a field with frequency ω_l after one round-trip, while $\omega_c = 2\pi\nu_{nmq}$ is the cavity mode resonance frequency closest to ω_l [140] (see eq. (3.2) for ν_{nmq}). As mentioned, the frequency spacing between two subsequent longitudinal modes (FSR) is defined as the inverse round trip time $\nu_{FSR} = 1/\tau$. To produce a self-consistent solution for the intracavity field we substitute eq. (3.8) into eq. (3.7):

$$a(t) = t_1 a_{in}(t) + \alpha_1 \alpha_2 r_1 r_2 \ a(t-\tau) \ e^{-\Delta_c \tau} e^{i2\pi} \ . \tag{3.9}$$

By subtracting $a(t-\tau)$ on both sides and dividing by τ we get

$$\frac{a(t) - a(t-\tau)}{\tau} = \frac{t_1}{\tau} a_{in}(t) + \frac{\alpha_1 \alpha_2 r_1 r_2 e^{-i\Delta_c \tau} - 1}{\tau} a(t-\tau) \ . \tag{3.10}$$

In order to simplify the expression we can insert the decay rates defined on fig. 3.2. κ_1 and κ_2 are cavity loss rates as a result of the finite mirror reflectivity, whereas κ_{A1} and κ_{A2} give the loss rates originating from absorption and scattering processes on the mirrors. The transmission, mirror loss and reflection coefficients can be related to their relative decay rates as

$$\kappa_j = \frac{T_j}{2\tau} = \frac{t_j^2}{2\tau} \qquad j = 1, 2 \ , \tag{3.11}$$

$$\kappa_{A_j} = \frac{A_j}{2\tau} = \frac{1 - \alpha_j^2}{2\tau} \qquad j = 1, 2 \ , \tag{3.12}$$

$$r_j = \sqrt{1 - T_j - A_j} = \sqrt{1 - 2\tau(\kappa_j + \kappa_{A_j})} \qquad j = 1, 2 \ . \tag{3.13}$$

For a so-called high-finesse cavity (see eq. (3.19)) the cavity decay and loss rates are very small compared to the inverse round trip time, hence $\kappa_j \tau \ll 1$ and $\kappa_{A_j} \tau \ll 1$. Furthermore, as we are only interested in the field around a resonance, where the light field frequency is close to the cavity resonance, $\omega_l \approx \omega_c$, we can assume $\Delta_c \tau \ll 1$. Substituting the rates of eq. (3.11)-(3.13) into eq. (3.10) and letting $\tau \to 0$, we can restrict ourself to linear terms in κ_j, κ_{A_j} and Δ_c, and obtain

$$\dot{a}(t) = \sqrt{\frac{2\kappa_1}{\tau}} a_{in}(t) - (\kappa_1 + \kappa_2 + \kappa_A + i\Delta_c) \, a(t) \ , \tag{3.14}$$

where the loss rates has been combined to $\kappa_A = \kappa_{A_1} + \kappa_{A_2}$. This is the equation of motion for the intracavity field amplitude. It contains passive loss terms due to the mirrors, a phase shift depending on the cavity detuning, Δ_c, and a source term from the input field, $a_{in}(t)$. In a later section we will see how the introduction of an atomic medium inside the cavity modifies the dynamics of the field. In steady state ($\dot{a}(t) = 0$) the field amplitude becomes

$$a = \frac{\sqrt{\frac{2\kappa_1}{\tau}}}{(\kappa_1 + \kappa_2 + \kappa_A + i\Delta_c)} a_{in} \ . \tag{3.15}$$

From this, the steady state intracavity intensity can be found as

$$I = |a|^2 = \frac{\frac{2\kappa_1}{\tau}}{\kappa^2 + \Delta_c^2} |a_{in}|^2 \ , \tag{3.16}$$

where we defined the total cavity field decay rate $\kappa = \kappa_1 + \kappa_2 + \kappa_A$. The reflected and transmitted cavity output field amplitudes can be defined from: $a_{refl} = \sqrt{2\kappa_1\tau}a - a_{in}$ and $a_{trans} = \sqrt{2\kappa_2\tau}a$, where the same first order expansion as with eq. (3.14) has been performed.

The cavity reflectivity $\mathcal{R}$ and transmittance $\mathcal{T}$ are defined as the ratio of the reflected and transmitted intensities to the input intensity as

$$\mathcal{R} = \left| \frac{a_{refl}}{a_{in}} \right|^2 = \frac{(\kappa - 2\kappa_1)^2 + \Delta_c^2}{\kappa^2 + \Delta_c^2} \ , \tag{3.17}$$

$$\mathcal{T} = \left| \frac{a_{trans}}{a_{in}} \right|^2 = \frac{4\kappa_1\kappa_2}{\kappa^2 + \Delta_c^2} \ . \tag{3.18}$$

$\mathcal{R}$ and $\mathcal{T}$ are Lorentzian functions of the cavity detuning Δ_c with a full width at half the maximum (FWHM) of 2κ (see fig. 3.3). To describe the quality of the cavity the so-called *finesse*, $\mathcal{F}$, can be used, given by the ratio of the free spectral range FSR and the FWHM as

$$\mathcal{F} \equiv \frac{\nu_{FSR}}{\delta_{FWHM}} = \frac{2\pi}{T_1 + T_2 + A} \ , \tag{3.19}$$

where $\delta_{FWHM} = (2\kappa)/(2\pi)$. We see that a cavity with a high finesse requires low transmission and loss coefficients, and will in general have a narrow linewidth ($\delta_{FWHM} \ll \nu_{FSR}$).

3.3 Ensemble of N two-level atoms interacting with a single mode cavity field

In this section we examine the situation in which an ensemble of N two-level atoms is trapped (e.g. using an ion trap) inside an optical cavity, and interacts with a single mode of the cavity field. The interaction of a single atom with a single cavity field mode can be described using the Jaynes-Cummings model (JC) [141,142], which derives the dynamics of the atomic and field observables in a fully quantized picture. Later, this model was extended to N atoms and named the Tavis-Cummings model (TC) [143,144], which we will describe in the following subsection.

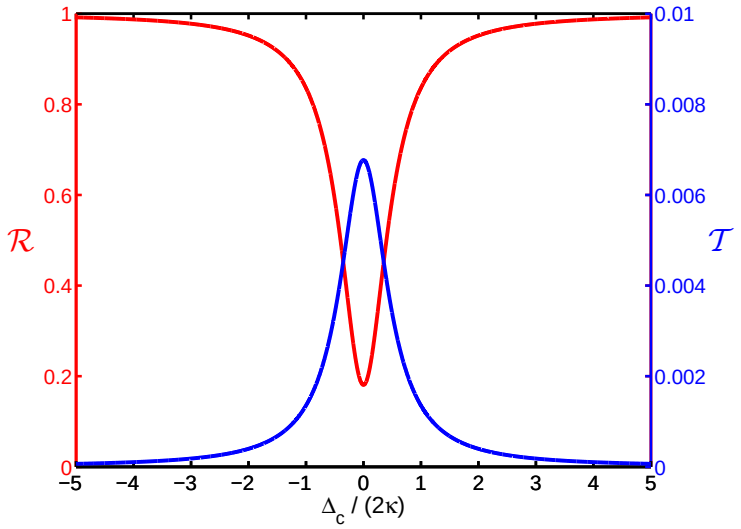

Figure 3.3: Cavity transmittance and reflectivity spectra around a resonance, plotted as function of the cavity detuning relative to the FWHM. The plot represents a cavity similar to the one used in our experiments, whose transmission coefficients for the mirrors are $T_1 = 1500ppm$, $T_2 = 5ppm$, while the total absorption loss coefficient is $A = 600ppm$. The FSR is $\nu_{FSR} = 12.7GHz$ and with these parameters the cavity finesse is $\mathcal{F} \approx 3000$. Note that the scale of $\mathcal{T}$ is 100 times smaller than for $\mathcal{R}$.

3.3.1 The Tavis-Cummings model

We consider N two-level atoms (ground state $|g\rangle$, excited state $|e\rangle$) interacting with a single mode of the electromagnetic field in a cavity. The Hamiltonian of the system can be written as

$$\hat{H} = \hat{H}_{at} + \hat{H}_{cav} + \hat{H}_{int} \ . \tag{3.20}$$

The atomic Hamiltonian is defined from the excited state population $\hat{\Pi}^e = \sum_{j=1}^{N} \hat{\pi}_j^e = \sum_{j=1}^{N} |e\rangle \langle e|_j$ as

$$\hat{H}_{at} = \hbar \Delta_l \hat{\Pi}^e \ , \tag{3.21}$$

where $\Delta_l = \omega_{at} - \omega_l$ is the atom-laser detuning. The second term of eq. (3.20) describes a single mode of the quantized cavity field (omitting the zero-point energy of the vacuum field)

$$\hat{H}_{cav} = \hbar \Delta_c \hat{a}^\dagger \hat{a} \ . \tag{3.22}$$

Here, $\Delta_c = \omega_c - \omega_l$ is the cavity detuning and $\hat{a}$ and $\hat{a}^\dagger$ are the photon annihilation and creation operators. The interaction Hamiltonian in the dipole approximation can be written as a scalar product of the electrical field and the atomic dipole operator, $\hat{H}_{int}(t) = -\sum_{j=1}^{N} \mathbf{D}_j \cdot \mathbf{E}(t)$. In the rotating wave approximation (RWA), i.e. excluding non-energy conserving terms, we can write:

$$\hat{H}_{int}(t) = -\hbar \sum_{j=1}^{N} g_j \left(\hat{\sigma}_j \hat{a}^\dagger + \hat{\sigma}_j^\dagger \hat{a} \right) \ , \tag{3.23}$$

where $\hat{\sigma}_j = |g\rangle \langle e|_j$ is the atomic coherence of the j'th atom. The coupling parameter of the j'th atom has been defined as

$$g_j = g\Psi_{nm}(\mathbf{r}_j) \ , \tag{3.24}$$

where the maximum single ion coupling rate is found as the projection of the transition dipole matrix element $\mathbf{d}^j_{eg} = \mathbf{d}^j_{ge} \equiv \mathbf{d}^j$ onto the electric field amplitude $\hat{\mathcal{E}}_0$ as

$$g = \frac{\left|\mathbf{d}^j\right| \mathcal{E}_0}{\hbar} = \frac{\left|\mathbf{d}^j\right|}{\hbar}\sqrt{\frac{\hbar\omega_l}{2\epsilon_0 V}} \ , \tag{3.25}$$

where V is the cavity mode volume. The ions in the ensemble do not a priori see the same cavity field amplitude, and in eq. (3.24) we have thus taken into account the cavity field distribution $E_0\Psi_{nm}(\mathbf{r}_j)$, describing a single cavity Hermite-Gaussian mode (see eq. (3.3)). This weights the contribution to the atom-field interaction for each single atom by taking into account the field amplitude at the atom position [64, 73].

The dynamics of the coupled atom-field system is found by using Hamilton's equations of motion: $d\hat{Q}/dt = i/\hbar \left[\hat{H}, \hat{Q}\right]$, where $\hat{Q}$ is an operator [145]. A full set of equations gives the time evolution of all observables and is known as the Heisenberg-Langevin equations [146]. In this thesis we are only interested in the expectation values of the atomic and field operators. Their equations of motion can be found by using eq. (3.20) and taking the mean value of the Hamilton equations, yielding:

$$\dot{a} = -i\Delta_c a + i\sum_{j=1}^{N} g_j\sigma_j \tag{3.26}$$

$$\dot{\pi}^g_j = ig_j\left(\sigma_j a^\dagger - \sigma^\dagger_j a\right) \tag{3.27}$$

$$\dot{\pi}^e_j = -ig_j\left(\sigma_j a^\dagger - \sigma^\dagger_j a\right) \tag{3.28}$$

$$\dot{\sigma}_j = -ig_j a\left(\pi^e_j - \pi^g_j\right) - i\Delta_l\sigma_j \ , \tag{3.29}$$

where an expectation value for an operator $\left\langle \hat{Q} \right\rangle$ is written as Q.

The system can be described in a semi-classical framework by phenomenologically adding dissipation processes. We add the effect of a spontaneous emission rate of the excited state, Γ, in the equations for the state populations $\dot{\pi}^g_j$ and $\dot{\pi}^e_j$, and the decoherence rate of the atomic dipole $\gamma = \Gamma/2$ is inserted in the equation for the atomic coherence, σ_j. Furthermore, we combine the equation of motion for the empty cavity system, defined in eq. (3.14) from sec. 3.2.2, with the field equation of the TC model of eq. (3.26). Hence, the equations of motion now takes the form:

$$\dot{a} = \sqrt{2\kappa_1}a^{in} + i\sum_{j=1}^{N} g_j\sigma_j - (\kappa + i\Delta_c)a \tag{3.30}$$

$$\dot{\pi}^g_j = ig_j\left(\sigma_j a^\dagger - \sigma^\dagger_j a\right) + \Gamma\pi^e_j \tag{3.31}$$

$$\dot{\pi}^e_j = -ig_j\left(\sigma_j a^\dagger - \sigma^\dagger_j a\right) - \Gamma\pi^e_j \tag{3.32}$$

$$\dot{\sigma}_j = -ig_j a\left(\pi^e_j - \pi^g_j\right) - (\gamma + i\Delta_l)\,\sigma_j \ . \tag{3.33}$$

Here, the field amplitude of the electrical field has been substituted with the input photon flux per round trip, $a_{in} \rightarrow \sqrt{\tau}a^{in}$. Notice, that the three lower equations, (3.31)-(3.33), are commonly referred to as the optical Bloch equations; for more detail see e.g. [139].

If we assume an equal coupling strength for all atoms, the total atomic coherence in steady state ($\dot{\sigma}_j = 0 \ \forall j$) can be found from eq. (3.33) as

$$P = \sum_{j=1}^{N} \sigma_j = -\frac{i\Omega}{\gamma + i\Delta_l}(\Pi^e - \Pi^g) \ , \tag{3.34}$$

where we inserted the total ground and excited state populations, Π^g and Π^e, together with the Rabi frequency $\Omega = 2ga$ assuming the same coupling strength for all atoms in the system. By inserting eq. (3.34) into the steady state excited state population obtained from eq. (3.32) with $\dot{\pi}_j^e = 0 \ \forall j$, we can write:

$$\Pi^e = \frac{1}{2}\frac{s}{1+s} \ , \tag{3.35}$$

where s is the saturation parameter, defined as

$$s = \frac{2\left|\Omega\right|^2}{\left(\Gamma/2\right)^2 + \Delta_l^2} = \frac{s_0}{1 + \left(\frac{2\Delta_l}{\Gamma}\right)^2} \ , \tag{3.36}$$

and where s_0 is the on-resonance saturation parameter given by

$$s_0 = 2\frac{\left|\Omega\right|^2}{\left(\Gamma/2\right)^2} \equiv \frac{I}{I_{\text{sat}}} \ . \tag{3.37}$$

Here $I_{\text{sat}} = \frac{\hbar\Gamma\omega_{\text{at}}^3}{12\pi c^2}$ is the saturation intensity and the spontaneous emission rate can be specified as $\Gamma = \frac{\omega_{\text{at}}^3\left|\mathbf{d}^j\right|^2}{3\pi\epsilon_0\hbar c^3}$ [139, 147]. The steady state population of eq. (3.35) can give us information about the atomic state for a specific light field interacting with an atomic medium. This will be important in chap. 7 where we impose a spatially varying standing wave light field from the cavity onto the ions, besides another *far detuned* standing wave field spatially confining the atoms. In the description of the interactions in the current chapter we assume that the light field frequency is close to the atomic transition and the cavity resonance frequency.

3.3.2 Low saturation and motionless atoms

The dynamical equations (3.30)-(3.33) describe the whole coupled atom-cavity system, but in the limit where only single or few photons are in the cavity, one can further simplify the description (low saturation limit). To describe the interaction of the atomic ensemble with a single cavity photon one can restrict the analysis to a basis of the three lowest-lying Dicke states [148]:

$$\left|g,n\right\rangle_N = \left|g\right\rangle^{(1)}\left|g\right\rangle^{(2)}\cdots\left|g\right\rangle^{(N)}\left|n\right\rangle \qquad \text{, for } n = 0,1 \tag{3.38}$$

$$\left|e,0\right\rangle_N = \frac{1}{\sqrt{N}}\sum_{j=1}^{N}\left|g\right\rangle^{(1)}\left|g\right\rangle^{(2)}\cdots\left|e\right\rangle^{(j)}\cdots\left|g\right\rangle^{(N)}\left|0\right\rangle \ . \tag{3.39}$$

Here $|g\rangle^{(j)}$ and $|e\rangle^{(j)}$ denote the ground and excited state of the j'th atom respectively. $|g,n\rangle_N$ describes a state with all the atoms in the ground state and n photons in the cavity, while the state $|e,0\rangle_N$ is a superposition of states having one atom in the excited state, no photons in the cavity and the remaining atoms in the ground state.

In the low saturation limit, thus almost all ions are in the ground state and it can be assumed that $\pi_j^g \approx 1$ and $\pi_j^e \approx 0\ \forall j$ [27, 73]. The dynamical equations of (3.30) and (3.33) simplify significantly and in steady state they can be solved to give

$$\sigma_j = \frac{ig_j a}{\gamma + i\Delta_l} \tag{3.40}$$

$$a = \frac{\sqrt{2\kappa_1}a^{in}}{\kappa' + i\Delta_c'} \ , \tag{3.41}$$

where an effective cavity field decay rate, κ', and an effective cavity detuning, Δ_c', have been introduced:

$$\kappa' = \kappa + \frac{g_N^2\gamma}{\gamma^2 + \Delta_l^2} \ , \tag{3.42}$$

$$\Delta_c' = \Delta_c - \frac{g_N^2\Delta_l}{\gamma^2 + \Delta_l^2} \ . \tag{3.43}$$

We also defined the collective coupling rate of the atom-cavity system:

$$g_N^2 = \sum_{j=1}^{N} g_j^2 \ \Rightarrow \ g_N = g\sqrt{N_{eff}} \ , \tag{3.44}$$

where we have expressed g_N as function of the maximum single ion coupling, g (see eq. (3.25)), times the square root of the effective number of ions interacting with the cavity field [28, 64]. This effective number is defined as the sum over all ions in the crystal weighted by the squared modulus of the field mode function, Ψ_{nm}, of the TEM_{nm} mode considered (see eq. (3.24) or app. B):

$$N_{eff} = \sum_{j=1}^{N} \Psi_{nm}^2(\mathbf{r}_j) \ . \tag{3.45}$$

In the simple ideal case where all ions couple with equal strength to the cavity field mode, the effective number of interacting ions equals the total ion number, $N_{eff} = N$. In general, for randomly distributed ions in the cavity field mode-volume, the effective number of ions is given by the overlap between the mode-function considered and the ion medium [74].

A situation of special interest arises when the collective coupling rate between the N atoms and the cavity field exceeds the dissipative rates in the system. This regime is called the *collective strong coupling regime* [1] and corresponds to

$$g_N > (\gamma, \kappa) \ . \tag{3.46}$$

In 1983 the regime was entered with neutral atomic ensembles using microwave fields [24], in the 1990's the limit was reached in the optical domain using thermal

atoms [5,149] and later with Bose-Einstein condensates [25,26]. Only a few years later (2009) our system of an ion Coulomb crystal coupled to a moderate finesse cavity was able to operate in the collective strong coupling regime, as successfully demonstrated experimentally in [28]. In these experiments $^{40}Ca^{+}$ ions were made to interact with a cavity light field on the $3D_{3/2} \leftrightarrow 4P_{1/2}$ transition (see fig. 2.2), where the decay rate of the $4P_{1/2}$ level is $\gamma = 2\pi \times 11.2$ MHz. The cavity field decay rate was measured to $\kappa = 2\pi \times 2.1$ MHz [27,73] and the maximum single ion coupling rate can be found from atomic parameters and the cavity geometry as $g_{theory} = 2\pi \times 0.53$ MHz (see appendix B or [27]). From these rates we can infer that an effective number of ~ 500 ions is enough to get into the regime of $g_N > (\gamma, \kappa)$. Our system can somewhat exceed this limit and coupling of crystals with $N_{eff} > 1500$ ions has been achieved [28]. In the case of cavity ion traps operating with single ions the (single-ion) strong coupling regime still remains to be achieved, although recent experiments exploiting optical fiber cavities, are moving close to the limit [19–22,150,151]. These have the advantage of a small cavity mode volume, boosting the coupling strength (eq. (3.25)) and at the same time reducing the disturbance on the trap potential.

Returning to eq. (3.42) and (3.43) we see that the effective cavity decay rate and detuning reflect the atomic absorption and phase shift. We can predict the steady state cavity response by considering the equation for the field amplitude (eq. (3.41)), which reveals that the cavity reflectivity and transmittance are still given by eq. (3.17)

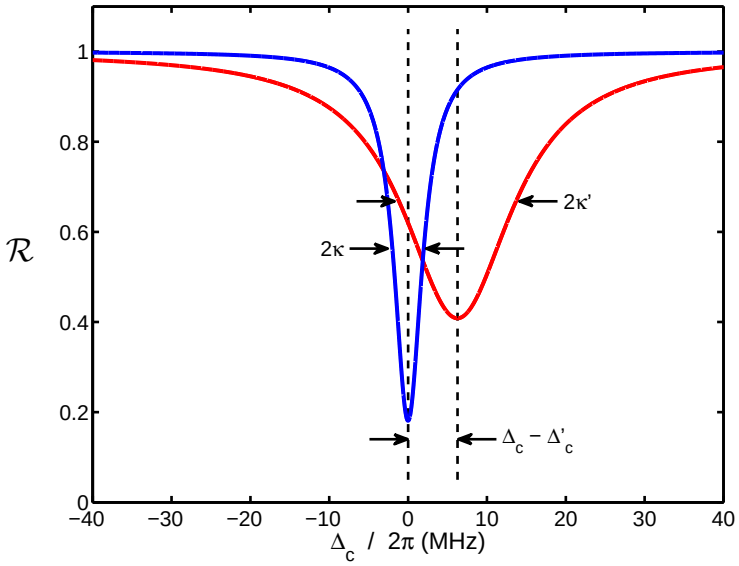

Figure 3.4: Calculated cavity reflectivity spectra as function of cavity detuning, Δ_c, for an empty cavity (blue line) and for 500 ions coupled to the cavity mode (red line). In the plot the laser detuning is set to $\Delta_l = \gamma$, while κ is defined in the text. We see that coupling ions to the cavity field changes the resonance width from κ to κ' and induces a shift of the resonance frequency, $\Delta_c - \Delta'_c$.

and (3.18), but with the substitution $\kappa \to \kappa'$ and $\Delta_c \to \Delta'_c$:

$$\mathcal{R}_{\text{atom-cav}} = \frac{(\kappa' - 2\kappa_1)^2 + \Delta'^2_c}{\kappa'^2 + \Delta'^2_c} \ , \tag{3.47}$$

$$\mathcal{T}_{\text{atom-cav}} = \frac{4\kappa_1\kappa_2}{\kappa'^2 + \Delta'^2_c} \ . \tag{3.48}$$

This means that the line shape is still a Lorentzian, but it is broadened to κ' and the detuning is shifted by $\Delta_c - \Delta'_c$. In figure 3.4 the cavity reflectivity can be seen for an empty cavity (blue line) and a cavity containing a crystal with an effective number of ions $N \sim 500$ (red line). Typical values for our system have been used as before: $\gamma = 2\pi \times 11.2$ MHz, $\kappa = 2\pi \times 2.1$ MHz and $g = 2\pi \times 0.53$ MHz [27, 73, 110]. Furthermore, the laser detuning is set to $\Delta_l = \gamma$, to make the resonance shift more evident. The effect that we are primarily going to use later in this thesis is the broadening of the cavity spectrum through κ'. In sec. 6.1 we are thus going to study experimentally how the effective cavity linewidth change as we vary the temperature of the ion ensemble coupled to the cavity. To give the required theoretical background this issue will thus be treated in the next section.

The broadening of the linewidth is maximum on atomic resonance ($\Delta_l = 0$), where the absorption from the medium is maximum, and hence from eq. (3.42) we can write

$$\kappa' = \kappa(1 + 2C) \ , \tag{3.49}$$

where the cooperativity parameter has been defined as

$$C = \frac{g_N^2}{2\gamma\kappa} \ . \tag{3.50}$$

Reconsidering eq. (3.43) we can see that the phase-shift of the detuning has a maximum value at $\Delta_l = \pm\gamma$, where in fact we get: $\Delta_c - \Delta'_c = \kappa C$. Thus, we notice that the cooperativity naturally appears as a relevant parameter to describe the strength of the light-matter interaction in our system, and we will return to its importance in chap. 4 when discussing the quantum memory.

3.3.3 Low saturation and moving atoms (along axis)

So far we have considered ions at rest inside the cavity, but after Doppler cooling the ions are moving around in the trap with a certain velocity distribution. If we consider an ion with a velocity component v_j along the cavity axis the standing-wave structure of the cavity field and the Doppler shifts due to the nonzero velocity of the ion have to be taken into account. We define the atomic dipole operators arising from the interaction between the ion and the two counter propagating components of the standing wave cavity field as

$$\sigma_{j\pm} = \frac{1}{2}\sigma_j \exp(\pm ikz_j) \ , \tag{3.51}$$

where z_j is the position of the j'th ion along the z-axis (cavity axis). In the low saturation regime and taking into account opposite Doppler shifts, the equations of

motion for the ion-cavity system from eq. (3.30) and (3.33) become [64, 73]:

$$\dot{a} = \sqrt{2\kappa_1}a^{in} - (\kappa + i\Delta_c)a + i\sum_{j=1}^{N}\frac{g_j}{2}\left(\sigma_{j+} + \sigma_{j-}\right) \ , \tag{3.52}$$

$$\dot{\sigma}_{j\pm} = ia\frac{g_j}{2} - \left[\gamma + i\left(\Delta_l \pm kv_j\right)\right]\sigma_{j\pm} \ . \tag{3.53}$$

The typical timescale of the ion motion is slow compared to the timescales for the coupled dynamics of the cavity field and the atomic dipole. The ions in the ensemble have a certain velocity distribution, $f(v)$, and the steady state mean value of the intracavity field is found by averaging the contributions of the dipole mean values (eq. (3.53)) over $f(v)$.

We consider a velocity distribution with average velocity v_D. For the model to be valid a conservative estimate is that the mean Doppler-shift has to be smaller than both effective rates of the coupled system on resonance ($\Delta_c = \Delta_l = 0$); i.e. $kv_D \ll min[\kappa + g_N^2/\gamma \ , \ \gamma + g_N^2/\kappa]$. The first effective rate describes the cavity decay, modified by the presence of the atomic ensemble, while the second effective rate describes the decoherence rate of the atomic dipole broadened by the interaction with the cavity field. In this regime the intracavity field mean value has the same form as for the motionless ions (eq. (3.41)), but the effective cavity field decay rate and detuning found in eq. (3.42) and (3.43) are modified [64, 73]:

$$\kappa' = \kappa + g_N^2\int \gamma\ \xi(\Delta_l, v)\ f(v)\ dv \ , \tag{3.54}$$

$$\Delta_c' = \Delta_c - g_N^2\int (\Delta_l - kv)\ \xi(\Delta_l, v)\ f(v)\ dv \ , \tag{3.55}$$

where

$$\xi(\Delta_l, v) = \frac{\gamma^2 + \Delta_l^2 + (kv)^2}{(\gamma^2 + \Delta_l^2)^2 + 2(\gamma^2 - \Delta_l^2)(kv)^2 + (kv)^4} \ . \tag{3.56}$$

By assuming a thermal atomic ensemble with temperature T, $f(v)$ is given by a Maxwell-Boltzmann distribution

$$f(v) = \sqrt{\frac{m}{2\pi k_B T}}\exp\left(-\frac{mv^2}{2k_B T}\right) \ , \tag{3.57}$$

where m is the atomic mass, T is the considered temperature, k_B is the Boltzmann constant and we can define the average Doppler velocity as $v_D = \sqrt{\frac{k_B T}{m}}$. From this we get

$$\kappa' = \kappa + \frac{g_N^2\gamma}{\sqrt{2\pi}\gamma_D}\int \xi(\Delta_l, v)\ e^{-\frac{(kv)^2}{2\gamma_D^2}}\ dv \ , \tag{3.58}$$

where $\gamma_D = k\sqrt{\frac{k_b T}{m}}$ is the Doppler width. The variation of κ' with Δ_l is no longer a Lorentzian, but rather given by a Voigt profile; a convolution between a Gaussian and a Lorentzian profile. The temperature of an ion Coulomb crystal can be determined

e.g. by measuring κ' as function of Δ_l and fitting to eq. (3.58), which, if κ, γ and g_N are known, allows for extracting T from γ_D. For $\Delta_l = 0$ eq. (3.58) reduces to

$$\kappa'(\Delta_l = 0) = \kappa + \sqrt{\frac{\pi}{2}} \frac{g_N^2}{\gamma_D} \mathrm{erfc}\left(\frac{\gamma}{\sqrt{2}\gamma_D}\right) e^{\frac{\gamma^2}{2\gamma_D^2}} \ , \tag{3.59}$$

where $\mathrm{erfc}(x) = 1 - \mathrm{erf}(x)$ is the complementary error function. In sec. 6.1 measurements of the resonance width of the coupled atom-cavity system is presented and the above equations can be used to extract the temperature of ion Coulomb crystals under different cooling conditions.

Chapter 4

Quantum memory for light based on an ion Coulomb crystal

In this chapter we introduce the general concept of a quantum memory for light and discuss its possible realization with ion Coulomb crystal in an optical cavity. We start by giving a short introduction to the concept of a quantum memory (sec. 4.1) and define the important factors which characterizes it. Then, we introduce a quantum memory protocol making use of a Λ-type medium in a cavity (sec. 4.2). In doing so, the so-called dressed and dark states for the system are introduced (sec. 4.2.2), followed by a discussion of the dynamical evolution of the system in a cavity STIRAP process (sec. 4.2.3). In sec. 4.3 we focus on the implementation of an ion Coulomb crystal-based quantum memory in our present experimental system. Based on previous observations of cavity electromagnetically induced transparency (EIT) with this system, we discuss two technical issues and present the results of some numerical simulations for this implementation (sec. 4.3.1-4.3.2). In the last part of this chapter (sec. 4.4) we briefly discuss the possibility for realizing multi-mode storage.

4.1 The concept of a quantum memory

Many protocols in quantum information science are based on the manipulation of so-called quantum bits (qubit), which are quantum analogues of the classical bits. A qubit is a two-state quantum-mechanical system ($|1\rangle$, $|2\rangle$) and, in contrast to the classical bit, its state can be a superposition of both logical states at the same time, $|\psi\rangle = \alpha\,|1\rangle + \beta\,|2\rangle$. To be able to perform quantum logical operations on a qubit system it might be necessary to store the qubit states temporarily, while other operations are being performed. In this context quantum memories are important and an essential ingredient for many quantum information processing applications such as quantum networks [42], quantum repeaters [152] and linear optics quantum computing [153]. In quantum optics, a quantum memory is a device in which quantum states of light can be stored and retrieved on demand. Such a quantum optical memory can be based

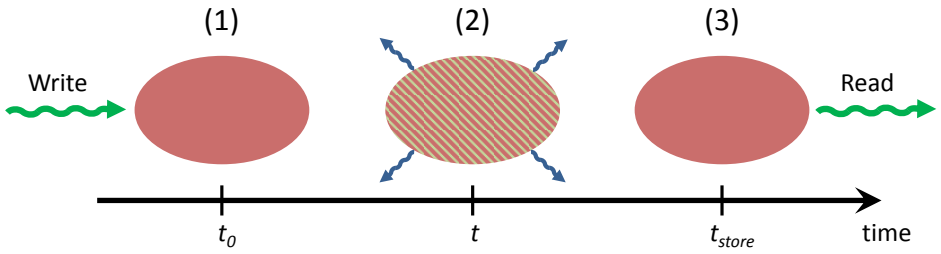

Figure 4.1: Simple illustration of the quantum memory storage and retrieval process. (1) At time t_0 a photon (green arrow) is written into the memory medium, represented by an atomic ensemble (red ellipse). (2) The quantum state of the photon is stored in the memory medium, potentially losing coherence due to decoherence mechanisms in the medium (represented as blue arrows). (3) At time t_{store} the stored state is read out as a photonic excitation, which if the quantum memory is efficient is similar to the incident quantum state.

on for example a single atomic system, but it can also be an atomic ensemble, like an ion Coulomb crystal, which is the main focus here.

A very simple illustration of the operation of a quantum memory is shown on fig. 4.1. (1) A photonic state is incident on the quantum memory medium at a time t_0 and is coherently written into the medium. (2) During storage, the quantum memory system keeps the quantum state preserved for some time, limited by the decoherence mechanisms inside the physical system. (3) After some time, at t_{store}, the excitation stored into the medium is read out, i.e. coherently converted back into a photonic excitation, which can be used in further quantum information processes.

The quantum memory, which we will describe, is based on the storage and retrieval of single- or few-photon excitations in the collective pseudo-spin state of an atomic ensemble placed inside an optical cavity. An important requirement for obtaining an efficient quantum memory is the ability of the atomic medium to absorb a single cavity field photon with a high probability. This can be achieved by operating in the collective strong coupling regime introduced in the previous chapter, i.e. by making the collective coupling rate, g_N, larger than the spontaneous emission rate, γ, and the cavity field decay rate, κ (eq. 3.46). The *efficiency* of the quantum memory, η, i.e. the ratio between the retrieved and the incident photons, depends on the cooperativity parameter $C = g_N^2/(2\kappa\gamma)$. C was introduced in sec. 3.3.2 as a measure of the effective optical depth of the system. One can show that, for the protocol that we will use, the optimal efficiency of the write *or* the read phase scales as $\eta = 2C/(1+2C)$, thus approaching unity for large C. The total efficiency of the memory is the product of the efficiencies in these two phases, times the efficiency of the storage, which depends on the possible decoherence in the system. To further evaluate the quality of a quantum memory one can also consider the *fidelity*, which is the overlap between the incoming and the outgoing state [56]. The optimal fidelity is also generally found to increase with the cooperativity.

Another important measure of the quality of a quantum memory is its storage time. Here, the important factor is the coherence time of the quantum system. Different decoherence channels will be present in any system and the fastest of these sets the

limit of the final quantum memory storage time. Consider a system of two-level atoms, mapping a photonic excitation by means of an interaction on a ground-to-excited state transition, such as the one introduced in sec. 3.3. This will result in a storage time which is limited by spontaneous emission decay from the excited state, and thereby the lifetime of the excited state. This lifetime is often short, e.g. if the transition is also used for Doppler cooling, and hence, it is naturally more interesting to use two long-lived atomic states for the mapping. We will thus consider in the next section a three-level Λ-system.

4.2 Λ-type quantum memory in a cavity

In this section we will theoretically describe a three-level Λ-system inside a cavity and its use as a quantum memory. The first sections introduce the energy-levels of the system, its Hamiltonian and a useful basis for describing the dynamic evolution of the quantum memory states. In the last part we discuss the concept of Stimulated Raman Adiabatic Passage (STIRAP) and its application in a quantum memory protocol.

4.2.1 A three-level atomic Λ-system in a cavity

We consider an atomic ensemble of N identical 3-level atoms in a Λ-configuration, illustrated on fig. 4.2(a). The system contains two long-lived ground states, $|b\rangle$ and $|c\rangle$, and an excited state $|a\rangle$ which can decay to the two ground states or other external states at a rate 2γ. The ensemble is placed inside an optical cavity and interacts with two monochromatic fields. The atoms are coupled on the $|c\rangle \leftrightarrow |a\rangle$ transition with a strong control field with Rabi frequency Ω_c (treated classically). They also couple on the $|b\rangle \leftrightarrow |a\rangle$ transition to a weak (single photon level) intra-cavity probe field having Rabi frequency Ω_p [66]. We assume that initially all the atoms are in $|b\rangle$. A single probe photon can, through the strong control field, couple the states $|b\rangle$ and $|c\rangle$ in a two-photon process called a Raman transition.

For the sake of simplicity, we assume that the cavity is resonant with the $|b\rangle \leftrightarrow |a\rangle$ transition and the control and probe fields are resonant with the atomic transitions. Using a frame rotating at the probe field frequency and applying the dipole approximation, the interaction Hamiltonian of the system will be given by

$$H_{int} = \hbar g \sum_{j=1}^{N} \Psi_{nm}(\mathbf{r}_j) \left(\sigma_{ba}^j \hat{a}^\dagger + \sigma_{ab}^j \hat{a} \right) + \hbar \Omega_c(t) \sum_{j=1}^{N} \left(\sigma_{ca}^j + \sigma_{ac}^j \right) \ , \qquad (4.1)$$

where the annihilation and creation operators of a single photon in the cavity mode are denoted $\hat{a}$ and $\hat{a}^\dagger$ respectively, while the spin operator of the j'th atom is $\sigma_{\alpha\beta}^j = |\alpha\rangle\langle\beta|$ $(\alpha, \beta = a, b, c)$. As we assumed that all atoms where initially prepared in state $|b\rangle$, the eigenstates spanning the Hamiltonian subspace are the collective symmetric

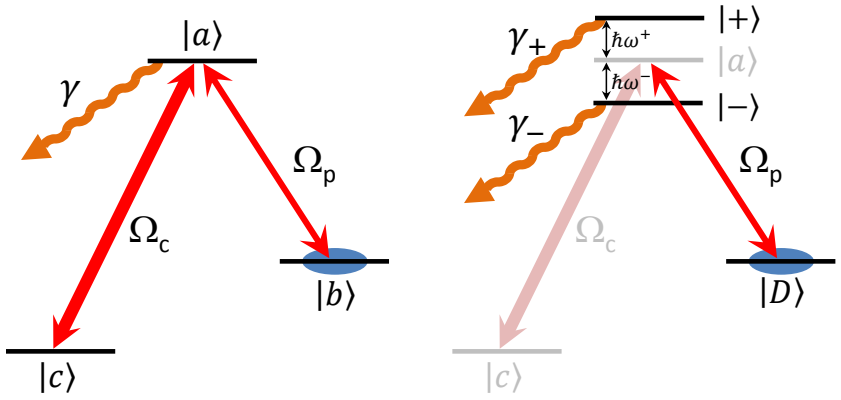

Figure 4.2: (a) A Λ configuration formed by the long-lived ground states $|b\rangle$ and $|c\rangle$ and the excited state $|a\rangle$. The ground states couple to the excited state through the weak probe field and the strong control field with Rabi frequencies Ω_p and Ω_c, respectively. The excited state can decay to the two ground states or other external levels at a total rate 2γ. As indicated with the blue ellipse the atomic population is initially in $|b\rangle$. (b) The system in the dressed state picture where the excited state splits into a doublet ($|\pm\rangle$) and the dark state becomes a superposition of the two bare ground states. The situation is shown here for a strong control field, $\Omega_c \gg \Omega_p$, for which $|D\rangle \approx |b\rangle$.

Dicke-like states [14, 154]:

$$
\begin{aligned}
|\mathbf{b}\rangle &= |b_1, b_2, \ldots, b_N\rangle \ , \\
|\mathbf{a}\rangle &= \frac{1}{\sqrt{N}} \sum\nolimits_{i=1}^{N} |b_1, \ldots, a_i \ldots, b_N\rangle \ , \\
|\mathbf{c}\rangle &= \frac{1}{\sqrt{N}} \sum\nolimits_{i=1}^{N} |b_1, \ldots, c_i \ldots, b_N\rangle \ , \\
|\mathbf{aa}\rangle &= \frac{1}{\sqrt{2N(N-1)}} \sum\nolimits_{i\neq j=1}^{N} |b_1, \ldots, a_i \ldots, a_j \ldots, b_N\rangle \ , \\
|\mathbf{ac}\rangle &= \frac{1}{\sqrt{N(N-1)}} \sum\nolimits_{i\neq j=1}^{N} |b_1, \ldots, a_i \ldots, c_j \ldots, b_N\rangle \ , \quad \text{etc.}
\end{aligned}
\tag{4.2}
$$

where, to ease the notation, N represents the effective number of interacting atoms. The simplest non-trivial case has one photon in the cavity mode and all the atoms in state $|\mathbf{b}\rangle$. This state will be denoted by the combined state $|\mathbf{b}, 1\rangle$, where the second index denotes the photon number. In this case, the interaction Hamiltonian (eq. (4.1)) couples $|\mathbf{b}, 1\rangle$ to two other states of the combined atom-cavity system: $|\mathbf{b}, 1\rangle \overset{H}{\leftrightarrow} |\mathbf{a}, 0\rangle \overset{H}{\leftrightarrow} |\mathbf{c}, 0\rangle$.

By inserting the cavity field mode function, $\Psi_{nm}(\mathbf{r}_j)$, into eq. (4.1), the atom-cavity interaction of the probe is weighted with the field amplitude at each atom position (as in sec. 3.3.1). The effective number of atoms interacting with the cavity probe field is defined in eq. (3.45), as $N_{eff} = \sum_{j=1}^{N} \Psi_{nm}^2(\mathbf{r}_j)$. For most purposes

the fundamental TEM_{00} cavity mode is used. In the next section, for simplicity, we will assume that the control field Rabi frequency, $\Omega_c(t)$, is equal for all atoms, but later we will discuss the experimentally relevant situation where the control field is also applied through the cavity, making it necessary to take into account the spatial variation of the control field amplitude.

4.2.2 Dressed and dark states

The Hamiltonian of the Λ-system (eq. (4.1)) can be diagonalized in a basis of so-called dressed states, which are related to the collective Dicke-like states of eq. (4.2). Of particular interest here is the state [154]

$$|\mathbf{D},1\rangle = \cos\theta(t)\,|\mathbf{b},1\rangle - \sin\theta(t)\,|\mathbf{c},0\rangle\,, \tag{4.3}$$

$$\tan\theta(t) = \frac{g\sqrt{N_{eff}}}{\Omega_c(t)}\,, \tag{4.4}$$

where the mixing angle $\theta(t)$ has been introduced. $|\mathbf{D}\rangle$ and two other dressed states ($|+\rangle$ and $|-\rangle$) are illustrated on fig. 4.2(b), in the case of a strong control field. The dressed state $|\mathbf{D},1\rangle$ is a combination of the ground states only and has zero eigenenergy. A system initially prepared in $|\mathbf{D},1\rangle$ can never be excited to the spontaneously decaying state, $|\mathbf{a},0\rangle$, and thus $|\mathbf{D},1\rangle$ is often called the *dark state*. The states $|\pm\rangle$ involve in general all 3 bare states and their energy is shifted by $\hbar\omega^{\pm} = \pm\hbar/2\sqrt{g^2N_{eff}+\Omega_c^2}$ [66], as indicated on the figure.

From eq. (4.3) we see that the mixing angle θ controls the relative weight of states $|\mathbf{b},1\rangle$ and $|\mathbf{c},0\rangle$ in the dark state. When the control field is strong compared to the probe field $\theta \ll 1$ and the dark state becomes $|\mathbf{D},1\rangle \approx |\mathbf{b},1\rangle$. For a vanishing control field, the mixing angle is $\theta \approx \pi/2$, turning the dark state into $|\mathbf{D},1\rangle \approx |\mathbf{c},0\rangle$. This implies that adiabatically changing the mixing angle θ the population of the dark state can be coherently transferred between the two original ground-states of the bare system.

4.2.3 Cavity STIRAP quantum memory

A simple approach for storing single photons in collective atomic systems is to use a Stimulated Raman Adiabatic Passage (STIRAP) technique. With this technique a coherent reversible mapping of the photonic state onto the atomic energy states is performed. To increase the absorption probability the atomic system can be placed inside a cavity opening the possibility to enter the strong coupling regime, as discussed before. A dissipation-free method of the photon storage can be performed, by adiabatically transferring the atom-cavity dark state from a cavity-like state (photonic cavity excitation) to an atom-like state (collective atomic state excitation) [14,61,155]. The method is based on cavity electromagnetically induced transparency (EIT), in which the optical properties of the atoms can be manipulated by varying the external classical control field, as introduced above. For a resonant control field, the absorption of a resonant probe field is reduced as a result of quantum interference in the absorption amplitudes of the probe photons to the bare states. In other words, the absorption between the states $|b\rangle$ and $|a\rangle$ occurs either directly or via the coherent indirect path $|b\rangle \to |a\rangle \to |c\rangle \to |a\rangle$. If the Rabi frequency of the control field is strong compared

to the probe field ($\Omega_c(t) \gg g\sqrt{N_{eff}} \rightarrow \theta(t) \sim 0$), the probability amplitude of the indirect path is comparable to the direct. On two-photon resonance these amplitudes are of opposite sign, though, and will interfere destructively, thereby rendering the medium transparent for the probe field [66,67]. When the Rabi-frequency of the control field is decreased the absorption probability of the probe photons in the system increases, rendering the medium completely absorbing for the probe photons in the strong coupling regime.

The equations of motion for the amplitude functions describing the atomic and cavity operators can be derived from the Hamiltonian (4.1) (see e.g. [61,73]). In the adiabatic limit in which the control field Rabi frequency is varied slowly enough so that the dynamics of the observables follow the slow collective spin operator associated with the ground state coherence between states $|b\rangle$ and $|c\rangle$, one can define an effective atomic decay rate [156,157]:

$$\tilde{\gamma}_{bc}(t) = \gamma_{bc} + \frac{\Omega_c^2(t)}{\gamma + g^2 N_{eff}/\kappa} = \gamma_{bc} + \frac{\Omega_c^2(t)}{\gamma(1+2C)} \ , \tag{4.5}$$

where γ_{bc} is the decoherence rate between the two bare ground states (not shown on fig. 4.2) and, in order to follow the adiabatic requirement, eq. (4.5) needs to satisfy

$$\gamma_{bc} \ll \tilde{\gamma}_{bc} \ll \kappa, \gamma \ . \tag{4.6}$$

We remark that the time evolution of the effective decay rate follows the control field Rabi frequency, thus, actively varying $\Omega_c(t)$ will modify $\tilde{\gamma}_{bc}(t)$. This gives us the freedom to control the dynamics of the ground state population transfer. At the same time eq. (4.6) shows that in order to stay adiabatic the strength of $\Omega_c(t)$ is restricted to a certain magnitude.

In a simple picture the atomic quantum memory evolution can be modeled by considering an empty cavity. Rather than having a time-varying control field, $\Omega_c(t)$, modifying the atomic absorption inside the cavity, we describe an empty cavity having

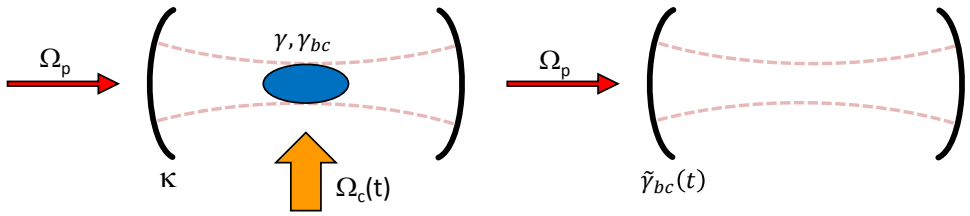

Figure 4.3: (a) The physical situation of the Λ-system quantum memory in a cavity. The probe field, Ω_p, is coupled into the cavity mode, where the interaction with the atomic system is modified by a uniformly applied control field, $\Omega_c(t)$. The cavity decay rate is κ, the spontaneous emission decay rate is γ and the decoherence rate between the two ground states is γ_{bc}. (b) A probe field is coupled into an empty cavity with a controllable cavity decay rate (variable incoupling mirror transmission). In the adiabatic limit, discussed in the text, the two situations are analogous, and the cavity containing an EIT medium can be described by an empty cavity with a variable incoupling transmission.

a controllable transmission coefficient, $\mathcal{T}(t) = 2\tilde{\gamma}_{bc}(t)\tau$ [156]. This is illustrated on fig. 4.3. The formalism of the two systems can be made identical and the transfer efficiency, the field emitted during read-out and the detection is similar.

When a probe photon is incident on the empty cavity, the transmission can be increased by raising the effective cavity decay rate, $\tilde{\gamma}_{bc}(t)$, making the cavity-EIT medium transparent for the probe light (to a degree fulfilling eq. (4.6)). Once the photon is coupled into the cavity, the effective decay rate can be lowered (still fulfilling eq. (4.6)), thus "closing" the cavity and trapping the probe photon for storage [156]. Read-out of the stored photon is performed by re-raising the cavity field decay rate, by which the transmission out of the cavity is increased again.

4.2.4 Impedance matching

Turning back to the actual physical system, a specific dynamical sequence for the probe and control fields as depicted in fig. 4.4, can be used to store photons in the three level Λ-system described above. In the ideal storage process, the incoming photon wave is completely coupled into the cavity and transferred into the atomic medium, maximizing the dark state amplitude (∼1) and the writing efficiency. To optimize the process, any reflection of the probe light during the writing process has to be minimized. This leads to an *impedance matching condition* between the incoming probe field shape, $\Phi_{in}(t)$, and the mixing angle, $\theta(t)$, ultimately set by the control

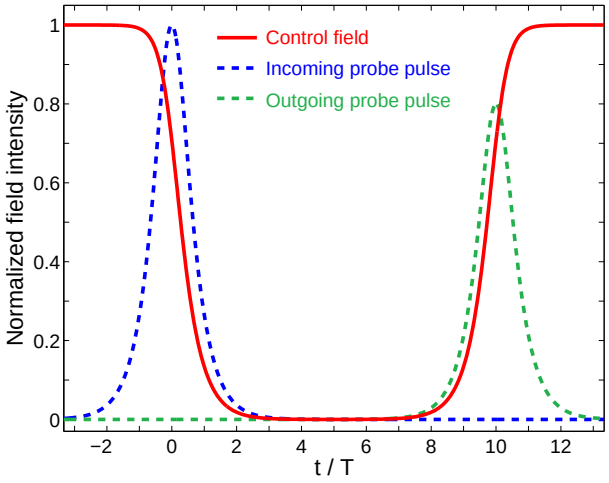

Figure 4.4: Exemplary storage sequence as a function of time. The control field intensity is decreased with a specific shape as the incoming probe pulse arrives ($t = 0$) with a sech-shape of width T. From this process the photon state is mapped onto a collective excitation in the atomic medium and thereafter stored within it. Later ($t = 10T$), the control field is turned on again with the time-reversed temporal shape and the collective atomic excitation is transferred back to the field, exiting the cavity.

field strength (see eq. (4.4)) [61] as

$$-\frac{d}{dt}\ln\left(\cos\theta(t)\right)+\frac{d}{dt}\ln\left(\Phi_{in}(t)\right)=\frac{\gamma}{2}\cos^2\theta(t)\ . \tag{4.7}$$

This relationship allows for composing sets of probe and control field shapes that will optimize the quantum storage process. We can specify a particular form of the input probe pulse (e.g. a hyperbolic secant function) [61] as

$$\Phi_{in}(t)=\sqrt{\frac{1}{T}}\mathrm{sech}\left(\frac{2t}{T}\right)\ , \tag{4.8}$$

where T is the pulse length. On fig. 4.4 this shape has been plotted at the incoming time $t=0$ (dashed blue line) together with the control field Rabi frequency found using eq. (4.7) (full red line). Note that the intensities have been normalized to their respective maximum values, but, in reality, the probe field intensity is at the single photon level, whereas the control field contains many photons. Slowly turning off the control field amplitude decreases the transmission of the cavity-medium system and the photon state is mapped onto the collective state of the atoms without being reflected at the incoming mirror. At a later time, here $t_{store}=10T$, the adiabatic evolution of the control field is reversed and the stored photon is released with a similar shape as the incoming photon. The storage efficiency of the quantum memory, η_{stor}, is defined above as the ratio between the outgoing number of photons to the incoming photon number and depends strongly on the coupling strength between the atoms and the probe field, and on the decay channels in the system.

4.3 Quantum memory in a $^{40}Ca^{+}$ ion Coulomb crystal

To implement this protocol in our experimental setup with $^{40}Ca^{+}$ ions, the Λ-system will be formed by two metastable Zeeman-substates of the $\left|3d^2D_{3/2}\right\rangle$ level as the two ground states and one Zeeman-substate of the $\left|4p^2P_{1/2}\right\rangle$ level as the excited state, as shown in fig. 4.5 (see also fig. 2.2 showing the energy levels relevant for Doppler cooling). This means that

$$|a\rangle=\left|4p^2P_{1/2},m_J=+1/2\right\rangle\ , \tag{4.9}$$

$$|b\rangle=\left|3d^2D_{3/2},m_J=+3/2\right\rangle\ , \tag{4.10}$$

$$|c\rangle=\left|3d^2D_{3/2},m_J=-1/2\right\rangle\ . \tag{4.11}$$

A magnetic field along the quantization axis (z-direction) is added, creating the Zeeman-splitting of the energy-levels. The transitions are addressed with the probe field around 866 nm and we define the frequency of the $|b\rangle\leftrightarrow|a\rangle$ transition as ω_{ab} and for the $|c\rangle\leftrightarrow|a\rangle$ transition $\omega_{ac}=\omega_{ab}+\omega_B$. The frequency shift ω_B is set by the applied B-field through the Zeeman effect (see app. A.4). The excited state $|a\rangle$ has a spontaneous decay rate to the ground states or other states of $\Gamma=2\gamma=2\pi\times22.4$ MHz. Furthermore, there is a possible decoherence between the two ground states $|b\rangle$ and $|c\rangle$, which is introduced phenomenologically as the decay rate γ_{bc} [73] (see fig. 4.5).

The considered physical system is a large ion Coulomb crystal trapped inside a linear optical cavity with a total loss rate, $\kappa=2\pi\times2.1$ MHz [27,73] (as described in

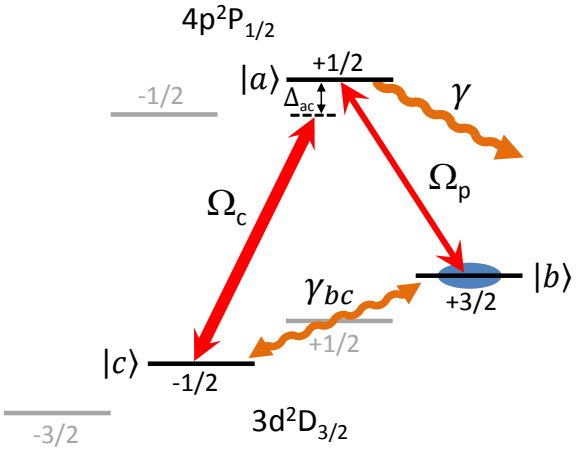

Figure 4.5: Level scheme for the realization of a quantum memory with $^{40}Ca^{+}$ ions. The Λ-system is formed by the $m_J = +1/2$ Zeeman substate of the $|4p^2P_{1/2}\rangle$ level and the metastable $m_J = +3/2$ and $m_J = -1/2$ states of the $|3d^2D_{3/2}\rangle$ level. Besides the definitions from fig. 4.2, Δ_{ac} is the control field detuning and γ_{bc} is the decoherence rate between the two ground states.

chap. 3 and 5). The probe beam is applied as a weak σ^- circularly-polarized field with a frequency, ω_p, close to the $|b\rangle \leftrightarrow |a\rangle$ transition. It is injected into the cavity trough mirror M_1 after having passed a polarizing beam splitter (PBS) and a $\lambda/4$ wave plate (see fig. 4.6). In the fundamental case the probe is coupled to the TEM_{00} mode of the cavity. The strong control field has a frequency ω_{crtl} (opposite circular polarization) and couples the states $|c\rangle$ and $|a\rangle$ with a detuning $\Delta_{ac} = \omega_{ac} - \omega_{crtl}$ (see fig. 4.5).

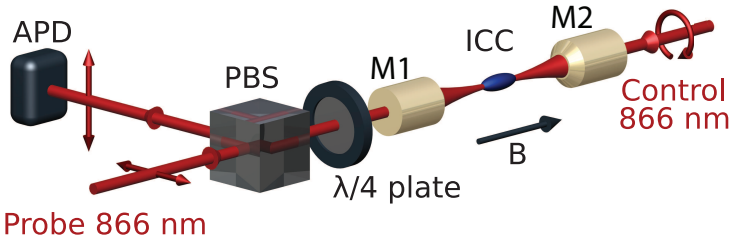

Figure 4.6: Geometry for quantum memory experiments. The 866 nm probe beam passes a polarizing beam splitter (PBS) and a $\lambda/4$-wave plate, making it σ^- circularly-polarized. It is injected into the cavity through mirror M_1, where it interacts with an ion Coulomb crystal (ICC). The reflected probe light is detected after the PBS using an avalanche photo detector (APD). To control the transparency of the medium a σ^+ circularly-polarized 866 nm control field is injected into the cavity through mirror M_2. The figure originates from [68].

In typical quantum memory experiments with cold atom ensembles a control field beam with a waist larger than the atomic ensemble extent is applied, ensuring that the control field Rabi frequency is equal for all atoms in the medium [56]. In the case of a large ion Coulomb crystal, applying the control field in the radial direction will make it impossible to achieve the two-photon resonance condition for all atoms. This is due to the large Doppler-shifts induced by the micromotion of ions away from the longitudinal axis of the trap (see sec. 2.3.4). Consequently, for our system, the control field has to be injected into the cavity as well. As shown in fig. 4.6 the control field is coupled into the cavity through mirror M_2 and has a σ^+ circular polarization. As a result, effects of the transverse profile and the longitudinal standing wave structure of the control field have to be taken into account, and we will discuss this later. Detection of the out-going probe field is performed on an avalanche photo detector (APD) placed in cavity reflection.

As previously mentioned, operating in the collective strong coupling regime should ensure in principle a high efficiency of the quantum memory. Cooperativities of ~ 8 have been achieved on the relevant transitions [28, 64, 73] and somehow higher values can probably be achieved in this setup by e.g. increasing the effective number of ions [27]. Moreover, the coherence time of collective Zeeman coherences has been measured to be in the ms range [28, 64], which is also promising for achieving reasonably long storage times. In addition, full control of the transparency of the ion crystal-cavity system using steady-state EIT has been demonstrated experimentally [68]. In these experiments the geometry of fig. 4.6 was used and the steady state reflection spectra of a probe field at the single photon level, interacting with an ion Coulomb crystal in the collective strong coupling regime, have been measured. These experiments demonstrated the possibility to fully control the transparency of an otherwise opaque ion crystal-cavity system, which is an excellent preliminary step to the implementation of the store and retrieve protocol described earlier. As a concluding remark, experiments using a radially applied control field, instead of an intracavity control field, have also been performed [73] (see. fig 4.7), but, as expected, no EIT effect could be observed, as a consequence of the micro-motion induced Doppler-shifts. Accordingly, in the quantum memory experiments the control field should also be applied through the cavity.

4.3.1 Effects of the intracavity control field

As introduced above, in our quantum memory implementation the control field is injected into the cavity trough mirror M_2. This means that the transverse and longitudinal profiles of the cavity mode have to be taken into account. As the frequency difference between the two transitions $|b\rangle \leftrightarrow |a\rangle$ and $|c\rangle \leftrightarrow |a\rangle$ is not very big we can assume that the wave vectors corresponding to the probe and control field are equal ($k \equiv k_p \simeq k_c$). The modified interaction Hamiltonian of the system now has to include both the mode function of the probe field, $\Psi_{nm}(\mathbf{r}_j, k_p)$, and of the control field, $\Psi_{nm}(\mathbf{r}_j, k_c)$ (see sec. 3.2.1), and becomes

$$H_{int} = \hbar g \sum_{j=1}^{N} \Psi_{nm}(\mathbf{r}_j, k) \left(\sigma_{13}^j \hat{a}^\dagger + \sigma_{31}^j \hat{a} \right) + \hbar \Omega_c(t) \sum_{j=1}^{N} \Psi_{nm}(\mathbf{r}_j, k) \left(\sigma_{23}^j + \sigma_{32}^j \right) \ . \tag{4.12}$$

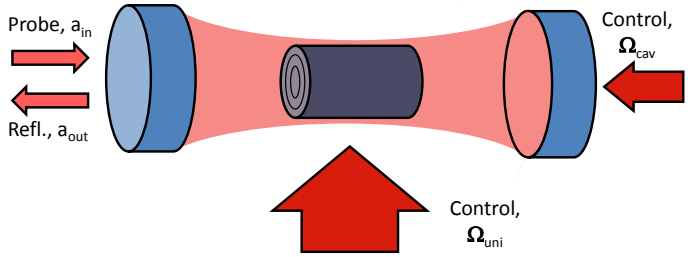

Figure 4.7: Illustration of a cylindrically symmetric Λ-type atomic medium inside a linear optical cavity. The medium interacts with a probe field and a control field in an EIT situation, as shown in sec. 4.2.1. To different scenarios are shown: one in which the control field is incident from the side with a constant uniform intensity profile over the whole ensemble, and one in which the control field is coupled to the same cavity mode as the probe. These two situations have been compared in the numerical simulations described in the text [158, 159].

The equations of motion for this system are more complicated than in the uniform control field case, but can readily be solved as e.g. in [73]. The difference in coupling strength for the uniform case and the intra-cavity case has importance both for the steady state EIT spectra measured in [68, 69] but also for the quantum memory performance considered here. Fig. 4.7 shows an illustration of a cylindrically symmetric atomic medium (of Λ atoms) enclosed by a linear optical cavity where it interacts with the probe and the control field. Two configurations can be chosen: one with both fields coupled into the same cavity mode (same field waist) and one where the control field is sent from the side with the same intensity over the whole atomic ensemble [158, 159].

The storage of single photon fields in our system, using the protocol described earlier, has been theoretically investigated by master student Kasper Rothe Zangenberg. Based on the parameters relevant for our system extensive numerical simulations were performed by Kasper in order to optimize the expected performance of such a quantum memory [158, 159]. The two scenarios introduced before were investigated simultaneously and compared (ignoring micro-motion effects).

The atomic medium was assumed to be cylindrically symmetric with concentric shells (as in fig. 4.7) and all the appropriate physical constants of our experimental system was applied. The shape of a single-component ion Coulomb crystal in a linear Paul trap is not cylindrical, but rather ellipsoidal, however, making this assumption simplifies the numerical simulations and is also relevant for prolate two-component ion crystals, whose inner component can be shaped in this way.

While the optimization of the efficiency in the all-cavity geometry generally follows that of the standard geometry [62, 63, 156], an essential difference is the dependence of the efficiency with the radial dimensions of the ensemble. A key result of this numerical study is shown on fig. 4.8 where the probe and control field shapes were defined as in sec. 4.2.4 and on fig. 4.4 ($\mathrm{sech}(t/T)$), with the pulse width $T = 2$ μs. The optimized efficiency is evaluated as function of the radius, R, and length, L, of the ion crystal (cylinder), for an ion density of $\rho = 6.1 \times 10^8$ cm^{-3}. On the figure the length is expressed in mm which is within the range of the maximum obtainable stable ion crystals for our trap. The radius is given in units of the cavity TEM_{00} mode waist,

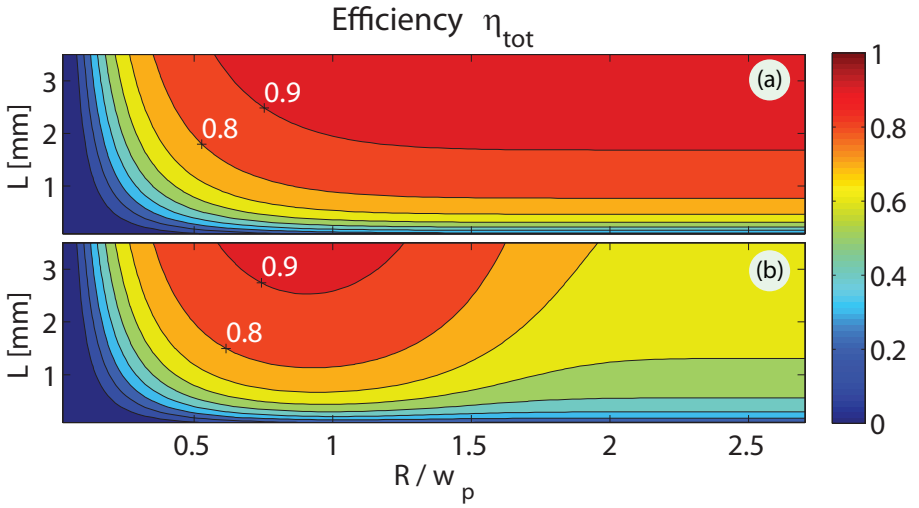

Figure 4.8: From [159]. The simulated efficiency of the quantum memory is plotted as function of the length, L, and radius, R, of the ion Coulomb crystal medium. (a) Shows the variation for the uniform control field situation. (b) Shows the variation where the control field is coupled into the cavity. $w_p = 37$ μm is the cavity mode waist, the crystal density is $\rho = 6.1 \times 10^8$ cm^{-3} and the probe and control field shapes were as defined in sec. 4.2.4 (sech(t/T)) with the pulse width $T = 2$ μs.

$w_p = 37$ μm. Graph (a) shows the results when applying the control field uniformly on all ions e.g. from the side of the cavity. The distribution is found to agree with the predicted analytical model of [62, 63, 156] and shows an increasing function with the crystal radius for any length. We see that efficiencies of more than 90% may be obtainable with large crystals. Graph (b) shows the results using a control field coupled into the same cavity mode as the probe field. The efficiency variation with radius is no longer simply increasing but rather has a maximum value at a certain radius for every choice of length. However, the simulations reveals that, for a long crystal ($L \gtrsim 2.5$ mm) choosing an appropriately crystal radius ($R \simeq 0.95 w_p$), the quantum memory efficiency can still reach $> 90\%$ [159]. The highest efficiencies are reached with $R \sim w_p$, where the crystal fills as much of the cavity mode volume as possible. The simulations serve as a reliable background estimate of the crystal dimensions needed in the actual experiments in order to obtain a reliable quantum memory device.

4.3.2 Bi-crystal Ca^+ ion system

In the previous paragraph simulations where performed using a cylindrical system (as shown on fig. 4.7) rather than the actual single-component ion Coulomb crystal shape (ellipsoidal). For very prolate single-component crystals, the cylinder shape is still a good approximation, but in practice a crystal having a length of several mm and $R \sim w_p$ will be very unstable, because it can not be cooled very efficiently. As an alternative, it is possible to use bi-component crystals for the quantum memory

medium. According to the Mathieu equations from sec. 2.1 two different ion species can be trapped in the linear Paul trap at the same time, as long as the charge-to-mass ratio is not too different. The cavity field can couple to the lighter (inner) species, while the heavy (outer) species can be laser cooled. Sympathetic cooling occurs between the two species, as a result of their mutual Coulomb interaction, and cooling only the outer component can be sufficient [27, 160, 161].

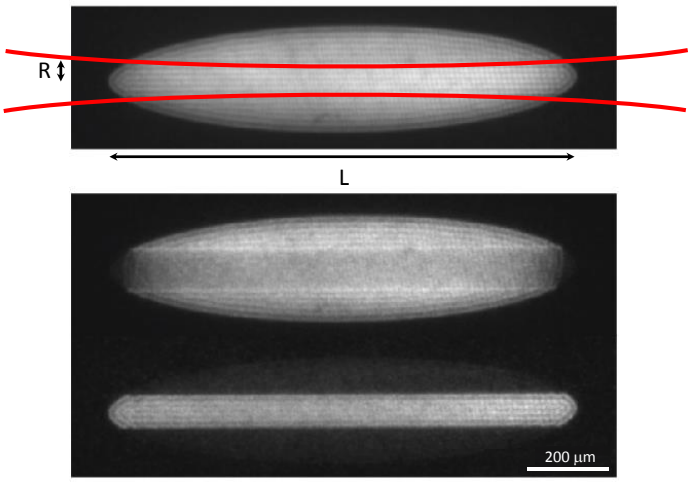

Figure 4.9: Projection images obtained during cooling of a two-component ion Coulomb crystal of ~ 2000 $^{40}Ca^{+}$ ions (inner component) and ~ 13000 $^{44}Ca^{+}$ ions (outer component). On the top image both components are being cooled simultaneously. On the lower images, only one species is cooled (middle image: $^{44}Ca^{+}$, bottom image: $^{40}Ca^{+}$). The inner part of the crystal resembles the cylindrical shape used in the previous paragraph, with a radius R and length L. The red lines illustrate the applied cavity field mode (the curvature of the Gaussian mode is very exaggerated). The images comes from [27].

On fig. 4.9 images of a two-component crystal containing ~ 2000 $^{40}Ca^{+}$ ions and ~ 13000 $^{44}Ca^{+}$ ions are shown. The lighter $^{40}Ca^{+}$ ions form the inner cylindrical core, which is surrounded by a crystal of the heavier $^{44}Ca^{+}$ ions. In the top figure both isotopes are being cooled at the same time and a cavity field mode is illustrated along the crystal as two red lines (not drawn to scale). On the two lower images laser cooling is only applied to one of the two species (first $^{44}Ca^{+}$ and then $^{40}Ca^{+}$), while the other is being sympathetically cooled [27]. The 3-dimensional shape of the crystals can be visualized by rotating the crystal around the long axis.

Using this two-component system the ion-cavity coupling resembles the situation used in the numerical simulations performed on the quantum memory efficiency. Comparing the lowest image of fig. 4.9 to fig. 4.7 the radius and length can be defined in the same way as in the simulations. A small discrepancy between the idealized shape and the inner-crystal shape arises in the ends, where the cylinder is flat opposed to a round crystal shape, but for long crystals this effect is negligible.

The inner part of the bi-component system clearly has a bigger overlap with the cavity mode and can be shaped so as to optimize the quantum memory efficiency. The essential property that maximized the collective coupling strength is the number

of effectively coupling ions. In the bi-crystal system, the inner part can be made more stable with a higher effective number of ions, compared to a single-component crystal with the same aspect ratio as the inner component. This is a result of the outer component cooling, which can in principle be performed continuously. Ultimately, this cooling can help decreasing heating effects in the central component, which can potentially increase the final storage time of the quantum memory.

4.4 Multi-mode storage implementation

For a quantum memory to be a part of a quantum information process, like e.g. a linear optics quantum computer [153], it needs to be able to store quantum information. As opposed to single atoms, atomic ensembles allow in principle for storing more than one photon, and thereby increases the capacity of a quantum memory. The quantum states of photonic qubits can be encoded in various degrees of freedom of the photons, such as their polarization or their frequency. For example, the qubit can be represented by the superposition of vertically and horizontally polarized photons, $|\psi\rangle = \alpha |V\rangle + \beta |H\rangle$. In our case, one can also exploit the spatial degree of freedom of the cavity photons by considering e.g. different transverse cavity modes (see sec. 3.2.1). Indeed, ion Coulomb crystals have a uniform density and therefore crystals with a radius larger than the cavity waist will couple equally strongly to the different transverse modes, as the collective coupling between the ions and the cavity mode depends on the overlap between the modefunction and the crystals. This has been

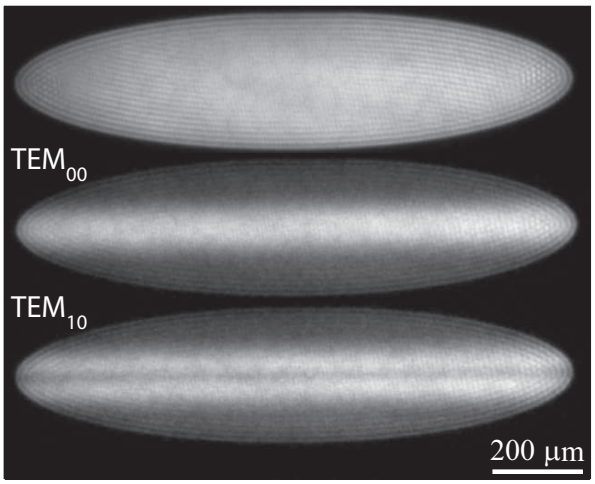

Figure 4.10: Projection images of a 1.2 mm long ion Coulomb crystal, repumped with an 866 nm field in three different ways: *Top*: from the side illuminating the whole crystal, *Middle*: injected into the TEM_{00} cavity mode, *Bottom*: injected into the TEM_{10} cavity mode. In [74] the two cavity modes was shown to couple equally strongly to a large ion crystal.

verified in prior experiments for the TEM_{00}, TEM_{01} and TEM_{10} modes [74].

On fig. 4.10 projection images of an ion Coulomb crystal (1.2 mm long, $\rho = 5.4 \times 10^8$ cm^{-1}) is shown during normal laser cooling with the 866 nm repumper from the side (along the x-axis) (*top*), with repumping predominantly performed trough the cavity mode TEM_{00} (*middle*) or TEM_{10} (*bottom*). In this way the two different cavity modes get apparent in the fluorescence pattern on the ion crystal. Numerical simulations of the efficiency of the store and retrieve protocol for different transverse modes, was also performed in [159] and show similar qualitative variations. Thus, implementing a multi-mode storage of several quantum states simultaneously seems possible, and is a natural step after having successfully achieved the fist experiments of single photon storage. This will hence, establish this system as a promising tool for implementing in a quantum information protocol.

4.5 Conclusion

In this chapter we introduced the dynamical cavity STIRAP process, based on the EIT effect, which makes it possible to store and retrieve photonic states using an atomic medium. We described a possible implementation with a large ion Coulomb crystal inside an optical cavity, for which the basics ingredients required for implementing this protocol have already been demonstrated (collective strong coupling [28], long coherence time, EIT resonances [68] and coupling to different transverse cavity modes). To successfully implement the storage process in our system, a specific all-cavity geometry scheme has to be used, together with a two-component crystal medium.

In the chapter describing future aspects of my studies (8), we are going to return to this quantum storage process. First, we describe an experimental system incorporating two electronically controlled acousto-optic modulators (AOMs) producing the relevant pulse-shapes of the probe and control fields, and show a few tests that has been performed on the system. Second, we introduce some considerations on the specific photon detection scheme for our system during quantum memory read-out, which becomes slightly complex because of the all-cavity implementation.

Furthermore, the experiments described in this thesis serves as preparatory improvements of our insight to the thermodynamic properties of the ion system, together with a study of increasing the coupling strength to the cavity mode, by placing the ions at positions of maximum field intensity. The obtained results may give us the possibility to improve the efficiency of the quantum memory, once this device is functioning.

Chapter 5

The experimental setup

This chapter presents the experimental setup used in my work as a PhD student. In the first section a short historical background is given (sec. 5.1). Then, we give an overview of the setup inside the vacuum chamber and define the different laser beams going into the cavity trap (5.2). In sec. 5.3 the trap is described, referring to chapter 2. In sec. 5.4 a description of the optical cavity is given. In sec. 5.5 we describe how the different lasers are applied to the system and what purpose they have in the measurements. In sec. 5.6 the CCD-imaging system is described together with the detection system of the cavity fields. In the last section (5.7) we discuss the calibration of the trap potentials relative to the cavity field. For a more extensive description, the reader is referred to [27, 73].

5.1 Experimental setup: historical background

In this chapter the setup used in the thesis will be presented. Most of the setup was already built and had been operating for some years when I started working on my project. The main purpose of this experimental setup is to build an efficient quantum memory consisting of a large ion Coulomb crystal in an optical cavity. A description of a quantum memory for light using cold trapped ions together with numerical simulations estimating the fidelity of single photon storage can be found in Anders Mortensen's PhD thesis [14]. To implement this scheme a first version of a linear Paul trap incorporating an optical cavity was built by Anders Mortensen in 2002-2005. Unfortunately, this trap never succeeded in trapping ions. In another trap, not including a cavity, Anders Mortensen performed experimental studies of the loading rate of ions into the trap [162], electron transfer experiments between different isotopes and general structure studies of ion Coulomb crystals both single-component and bi-component [106, 163].

Around 2005 the project was continued by Peter Herskind and Aurélien Dantan who developed and constructed a second trap, which is the one described in this thesis. An extensive description of the trap, the cavity and the majority of laser systems used in the current setup is found in Herskind's PhD thesis [27].

Trapping charged particles close to dielectric objects like cavity mirrors is very challenging, as the dielectrics modify the boundary conditions set by the electrodes and can substantially alter the field lines of the confining potentials. One of the

fundamental requirements in order to obtain a quantum memory in an ion system is the achievement of the strong coupling regime [61], introduced in sec. 3.3. To enter the strong coupling regime with single ions the cavity mode volume has to be small (see eq. (3.25)) making it very difficult. Thus, only a few groups in the world has so far obtained strong interaction between single ions and a cavity field mode (e.g. using optical fiber cavities [19–21]), although not in the single-ion strong coupling regime yet.

Our cavity trap was designed to operate with large ion Coulomb crystals, where the effective coupling rate with the cavity field is enhanced by $\sqrt{N}$, where N is the number of ions effectively coupling to the cavity field, introduced in sec. 3.3.2 (see eq. (3.44)). In 2008-2009 operation in the collective strong coupling regime, in which the collective coupling rate $g\sqrt{N}$ exceeds the decay rates of the system, γ and κ, was demonstrated in this trap [28]. Collective strong coupling was subsequently achieved for various transverse cavity modes [74], and, recently, observations of cavity electromagnetically induced transparency (EIT) and all-optical switching [68] in this system have been major advances towards the realization of an ion Coulomb crystal-based quantum memory [61]. In this context, the experiments reported in this thesis contribute to the preparation of the ion-cavity system to work as a quantum memory for photons. Only minor changes to the original optical setup have thus been performed and these will be introduced in the relevant sections.

5.2 Overview

The ion trap used in this project is a segmented linear Paul trap formed by cylindrical electrodes equivalent to the trap introduced in sec. 2.1. Integrated into the trap is a moderately high finesse optical cavity having its axis parallel to the symmetry axis of the quadrupole trap (see sec. 5.4). The whole setup is placed inside a vacuum chamber with a diameter of 40 cm, pumped to a pressure of a few 10^{-10} mbar.

Outside the vacuum chamber three sets of Helmholtz coils are mounted. Two coils produce magnetic fields in the x- and y-direction to compensate for the residual earth magnetic field. The third coil produces a magnetic field in the z-direction to create a well-defined quantization axis parallel with the trap axis. This splits the atomic energy levels into Zeeman states and these can be addressed by narrow linewidth laser fields. More detail about the considered substates will be given in the relevant sections describing the experiments.

The vacuum chamber is provided with 7 view-ports, anti-reflex coated for the appropriate wavelengths, giving optical access to laser fields from all sides. On fig. 5.1 this is illustrated together with the main applied laser beams. Cooling light is primarily provided along the trap axis (z) and, optionally, in the radial direction (x) depending on the ion structure in each of the experiments (see 2.3.1). The cooling light (397 nm) does not couple to the optical cavity because of the chosen coating on the mirrors, but is transmitted through the mirrors almost unaffected. A repump beam (866 nm) and an optical pumping beam (866 nm) is applied in order to cool the ions and prepare the internal states of the ions. In addition, a probe (866 nm) and a reference (894 nm) beam are applied along the cavity axis coupling light resonantly into the cavity mode. To load ions into the trap an ionization laser (272 nm) is applied orthogonally to a beam of neutral Ca atoms provided from an oven and some skimmers

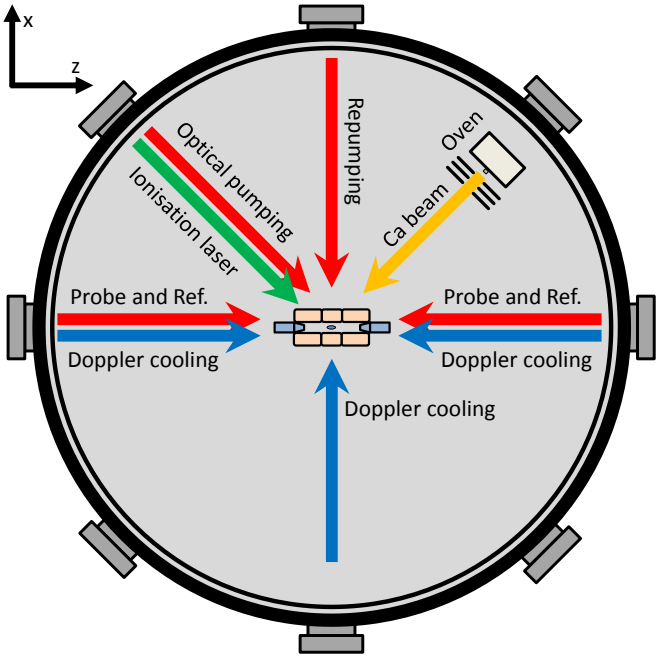

Figure 5.1: Sketch of the vacuum chamber (top-view), showing the cavity-ion trap (center), the main laser beams and their direction relative to the trap. The inner diameter of the chamber is 40 cm. The x- and z-directions has been defined on the figure in accordance to the definitions of sec. 2.1.

shaping the atomic beam. More details on the isotope selective loading procedure are given in sec. 5.5.5. The vacuum chamber is placed on an optical table containing all the necessary optics distributing the laser beams to the correct directions into the system. For more detail on the different applied lasers see sec. 5.5. All laser systems are placed on different optical tables and brought to the trap table through single-mode optical fibers. This minimizes vibration and noise interactions between the trap and laser systems and more importantly ensures stability in the beams directions on the trap table. More details about the trap design, assembly and characterization can be found in the Ph.D. thesis of Anders Mortensen [14], Peter Herskind [27] and Magnus Albert [73].

5.3 The linear Paul trap

A central part of our experimental setup is the ion trap; a linear Paul trap of four cylindrical rods, each segmented into three individual electrodes. On fig. 5.2 a photograph (sideview) of the actual trap and cavity system are seen, while fig. 5.3 shows a sketch defining the length scales. A description of a linear Paul trap is given in sec. 2.1 together with equations for the confining potentials. All electrodes have a radius of $r_e = 2.6$ mm and the distance between diagonal electrodes is $2r_0 = 4.7$ mm. The end-electrodes have a length of $z_e = 5.9$ mm while the center electrode length is

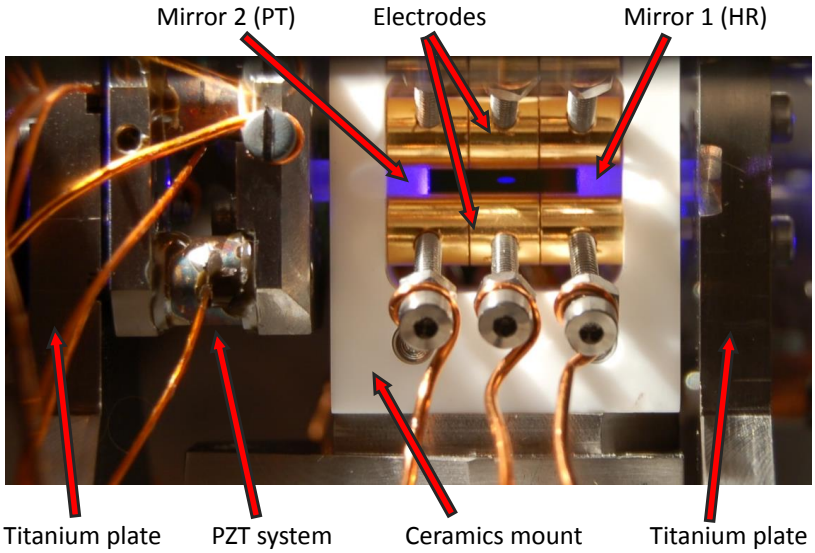

Figure 5.2: Photo of the cavity trap inside the vacuum champers seen through a view port. The cylindrical electrodes, made from copper with a gold coating, are mounted to a monolithic ceramic mount. The two cavity mirrors are hidden inside the mirror coats, here shining blue. Mirror 1 (high reflector (HR)) is mounted to a titanium plate on one side, while mirror 2 (partial transmitter (PT)) is mounted into a PZT system allowing for scanning or actively stabilizing the cavity length. In the trap center a large ion Coulomb crystal ($\sim$ 1 mm long) emitting 397 nm light during cooling, can be observed.

$2z_0 = 5.0$ mm. An electrical RF-field is applied to all three electrodes in each rod, in a quadrupolar configuration, i.e. with a phase difference of π between neighboring rods (see fig. 2.1). The RF-field is operated around the frequency $\Omega_{RF} = 2\pi \times 4.0$ MHz and provides a confinement in the radial direction (x and y). The axially confining potential (z-direction) is created by applying a static electrical DC potential to the electrodes on each end of the rods.

With these geometric definitions the a- and q-parameters, defined in eq. (2.5), can be expressed as: $a = -0.84 \times 10^{-3} V^{-1} \times U_{DC}$ and $q = 1.38 \times 10^{-3} V^{-1} \times U_{rf}$. Here the axial geometric constant is $\eta = 0.342$ (see eq. (2.1)). The electrodes are manufactured in copper, coated with a thin layer of gold and mounted on ultra low expansion glas rods[1]. The whole structure is held together by a monolithic ceramic mount[2]. For more detail about the trap design and assembly see the thesis by Peter Herskind [27].

The RF trap-voltages are produced by a frequency generator and amplified before being transfered to the electrodes through a resonant circuit. A homemade voltage driver is used to supply DC voltages to the electrodes. Most importantly, this allows for varying the axial potential by changing the end-electrode voltages at the same time, but it also makes it possible to alter the DC potentials of each individual electrode

[1] Made of *Zerodur*®, manufactured by the company Schott
[2] Made of a machinable ceramic material called *Macor*

segment separately. In this way the DC potential minimum can be shifted around in the trap both radially and axially opening the possibility to position the ions at will. The trap itself acts as a capacitative part of an LRC-circuit which is coupled inductively to the RF-power supply. Variable external capacitors makes it possible to either tune the phases of different RF-chains and in this way alter the resonance frequency of the circuit, while others can be used to fine tune the voltage on individual trap electrodes. This adjustment is usefully when overlapping the trap center with the cavity axis (see sec. 5.7), but also crucial for minimizing the excess micromotion in the ion system (see sec. 7.3.5).

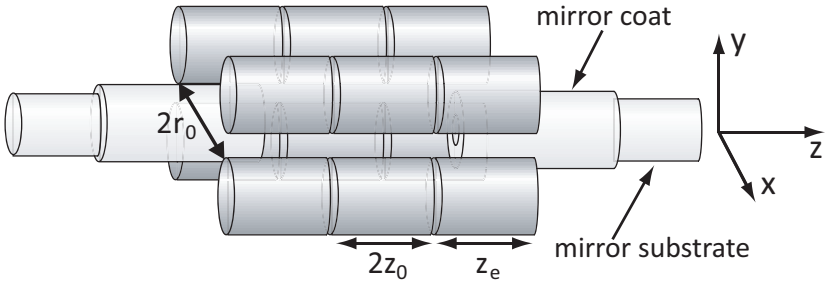

Figure 5.3: Sketch of linear Paul trap with integrated mirrors forming an optical cavity along the RF field-free axis (z). For more detail see [27].

5.4 The optical cavity

The optical cavity consists of two mirrors with a diameter of 1.2 mm and a radius of curvature of $r_M = 10$ mm. The mirrors are mounted in a nearly confocal geometry with a spacing of $L = 11.8$ mm and the cavity axis is parallel to the symmetry axis of the linear Paul trap (see fig. 5.3). The mirrors are made of fused silica and their presence could in principle cause the RF-field lines to bend and introduce excess micromotion, and thereby broaden the atomic transitions through the Doppler effect. As mentioned in sec. 2.3.4, simulations showed that this issue could be minimized by adding dielectric mirror coats around the substrates extending almost all the way to the electrodes [14]. The coats have a diameter of 4.16 mm, while the electrode separation is $2r_0 = 4.70$ mm (see fig. 5.3). On fig. 5.2 the coats appear blue arising from scattering of 397 nm cooling light.

The mirrors are coated for 866 nm and 894 nm with one mirror being a high reflector (HR) and the other being a partial transmitter (PT), having transmittances of 5ppm and 1500ppm, respectively, at 866 nm. A construction of two titanium plates holds the cavity together. The HR mirror is fixed at one plate, and on the other plate, the PT mirror is mounted in a holder containing a piezo-electric transducer (PZT) module. This allows for the cavity length to be either scanned or locked (see fig. 5.2). The choice of optical frequency-bands in the coating makes it possible to address the $3D_{3/2} \leftrightarrow 4P_{1/2}$ transition in $^{40}Ca^{+}$ with an 866 nm laser field (see fig. 2.2), while at the same time having a non-atom-interacting laser field resonant with the cavity at 894 nm, with the purpose of locking it. The cavity has a free spectral range of

$\nu_{FSR} = 12.7$ GHz and the waist of the TEM_{00} mode is $\omega_0 = 37\mu m$. The cavity decay rate is measured at 866 nm to $\kappa = 2\pi \times (2.1 \pm 0.1)$ MHz giving a finesse of $\mathcal{F} = 3000 \pm 200$ [27], whereas, the finesse at 894 nm is about 2000. Modematching the 866 nm light to the fundamental cavity mode can typically be achieved with $> 95\%$ efficiency.

5.5 Laser systems

In this section we introduce the lasers used for Doppler cooling, state preparation and ionization of the ions. A sketch of the beams entering the trap area are shown on fig. 5.1, and the optical setup for most the laser beams is shown on fig. 5.4.

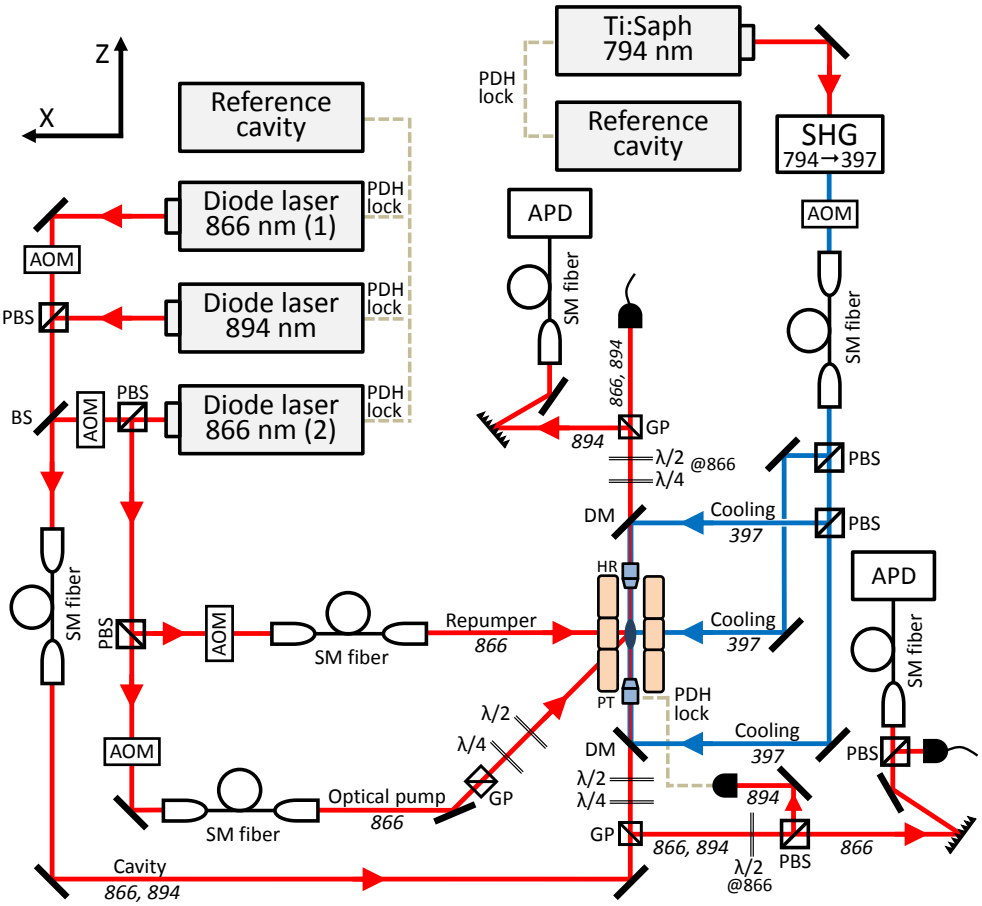

Figure 5.4: Schematics showing the cavity trap and the laser beams needed for Doppler cooling and state preparation of the ions. Along the beam paths the wavelength and purpose of the laser fields are indicated. The abbreviations are: acousto-optic modulator (AOM), second harmonic generation (SHG), Pound-Drever-Hall (PDH), single mode (SM), beam splitter (BS), polarizing beam splitter (PBS), avalanche photo detector (APD), dichroic mirror (DM), glan polarizer (GP).

5.5.1 Doppler cooling laser - 397

Light at a frequency of 397 nm is used to cool the trapped ions by driving the $4S_{1/2} \leftrightarrow 4P_{1/2}$ transition for the $^{40}Ca^{+}$ (see fig. 2.2). A Verdi V8 laser (5.5 W at 532 nm) pumps a Coherent Ti:Saph laser and produces typically $\sim$ 200 mW of 794 nm light, which is subsequently frequency doubled into 397 nm through a second harmonic generation (SHG) process in an external bow-tie cavity system containing an LBO crystal. Before the SHG a part of the 794 nm beam is taken out and used for frequency stabilization using a Pound-Drever-Hall (PDH) lock [164,165] to a temperature stabilized reference cavity. The reference cavity is formed by two mirrors on a 25 cm long quartz tube, it is mounted inside a vacuum tube and has a FSR of $\sim$ 600 MHz. The stability of the laser in lock was measured to 1 MHz/h (for more detail see [166]). Fine tuning of the laser frequency is done using a double pass acousto-optic modulator (AOM) in the locking setup, allowing for tuning the Ti:Saph laser by $\pm$100 MHz. This corresponds to a total tuning range of the doubled 397 nm light of $\pm$200 MHz. When the laser is in lock its linewidth is <MHz, hence, much narrower than the Doppler cooling transition in $^{40}Ca^{+}$ which is $\Gamma = 2\pi \times 22.4$ MHz.

The 397 nm light passes an AOM in single pass and the -1st order of diffraction is coupled into a single mode (SM) optical fiber and sent to the trap table (see fig. 5.4). This AOM has the purpose of switching the laser source on and off during the experimental process. The attenuation after the fiber is $\sim$ 55 dB and the switching has a typical rise time of $\sim$ 100 ns. At the trap table the laser beam is split into three parts. Two beams are sent to the trap along the axis (z) in opposite directions (see fig. 5.4), with σ^{+}/σ^{-} circular polarization and approximately equal intensity at the center of the trap. The third beam, linearly polarized along the y-direction, is sent perpendicular to the trap axis (x). The balance of axial to side cooling can be adjusted in order to stabilize cooling of single ions, strings of ions as well as ion Coulomb crystals.

5.5.2 Repumping and optical pumping laser - 866-2

A diode laser [167], here referred to as 866-2, provides light at 866 nm corresponding to the $3D_{3/2} \leftrightarrow 4P_{1/2}$ transition of the $^{40}Ca^{+}$ ion (see fig. 2.2). The laser uses an external-cavity, as the output coupler is a grating (1800 lines/mm) placed in a Littrow configuration. The frequency can be tuned by varying the diode current, the temperature (through a peltier element) or by a PZT changing the angle of the grating (i.e. the cavity length). The 866-2 laser is used to repump the ion population that decayed into the metastable $3D_{3/2}$ state during the Doppler cooling cycle, but also to optically pump the ion populations into a certain Zeeman sub-state of the $3D_{3/2}$ level.

Like the 397 nm laser system, the 866-2 diode laser is frequency stabilized to a temperature controlled reference cavity (25 cm long and $\nu_{FSR} \sim 600$ MHz) using a PDH lock, resulting in a laser linewidth of $\sim$ 100 kHz. As before, a double-pass AOM is used to tune the laser frequency, while a single pass AOM on each beam allows for switching the light on or off during the experimental sequence. Again, the -1st order of diffraction is coupled into a single mode optical fiber and sent to the trap table (see fig. 5.4) with an extinction $>$ 55 dB after the fiber. A third part of the 866-2 laser beam is coupled into the cavity, which is described below.

The repumper is sent into the trap along the x-direction as shown in fig. 5.4. It has a linear polarization perpendicular to the y-axis, which corresponds to a superposition of σ^+ and σ^-, in the basis of the quantization axis (z-axis). This ensures that all four Zeeman states of the $3D_{3/2}$ level are addressed and repumped into the cooling cycle. The optical pumping is performed by sending the 866-2 beam to the trap at an angle of 45^o relative to the quantization axis (see fig. 5.4). The polarization is carefully chosen to only drive π and σ^+ transitions between $3D_{3/2}$ and $4P_{1/2}$ [168]. Before entering the trap area the beam passes a glan polarizer (GP), followed by a $\lambda/4$ and a $\lambda/2$ wave plate, in order to control precisely its polarization. During the optical pumping process, the 397 nm cooling light is also present, making the $m = +3/2$ state of $3D_{3/2}$ the only un-addressed state and hence, population is pumped into this specific quantum state (more detail will be given in the appropriate experimental descriptions).

5.5.3 Cavity reference laser - 894

A diode laser, with a wavelength of 894 nm, is used as a cavity reference in the experiments (see fig. 5.4). The laser has the same design as 866-2 and is locked to the same reference cavity using the PDH technique. As with the other diode lasers the frequency can be tuned using a double pass AOM before the reference cavity.

The wavelength of 894 nm is not resonant with any transitions in the $^{40}Ca^+$ ion, but despite the narrow linewidth the laser light still contains a non-negligible amount of photons at 866 nm. These might possibly interfere with the probe field light at the single photon level, interacting close to resonance with the $3D_{3/2} \leftrightarrow 4P_{1/2}$ transition. As a consequence, the 894 nm light is spectrally filtered with a diffraction grating (1800 lines/mm) before being sent to the trap table through a SM fiber overlapped with the beams of the cavity probe lasers. The grating is not shown on fig. 5.4.

The 894 nm laser has two purposes in the experiments, depending on the measurement. By scanning the cavity length, the resonance signal of the 894 nm laser can be observed. The transmission peak is used to monitor drifts and acoustic noise by comparing its position in the scan with a resonance of the probe lasers [27], i.e. serving as a frequency reference. The second purpose of the laser is to lock the cavity length in a PDH scheme to ensure that the cavity resonance frequency is well-determined with respect to the atomic resonance frequency of interest. Note, that the 894 nm laser and the probe lasers have the same reference cavity and hence, experience (almost) the same slow drifts of the reference cavity. The detection system of all cavity fields will be described in sec. 5.6.2.

5.5.4 Cavity probe lasers - 866-1 and 866-2

In the experiments, two different lasers are used to probe the interaction of the coupled ion-cavity system, 866-1 and 866-2 (see fig. 5.4). 866-1 is a diode laser similar to 866-2. It can be frequency stabilized to the same reference cavity and tuned using a double pass AOM by ± 100 MHz. The linewidth of the 866 nm probe lasers in lock ($\sim$ 100 kHz [27]) are substantially narrower than both the cavity decay rate ($\kappa = 2\pi \times 2.1$ MHz) and the atomic dipole decay rate ($\gamma = 2\pi \times 11.2$ MHz), ensuring reliably interaction between the lasers and the ion-cavity system. A SM fiber transfers the 866 nm probe light, together with the 894 nm reference light, from the laser table

to the trap table. Before the fiber, a single pass AOM is used as a shutter for each beam, sending the -1st order of diffraction into the fiber (attenuation after fibers > 55 dB). In fig. 5.4 both 866 nm lasers enter the cavity from the PT mirror side.

Depending on the aim of the experiment, the cavity probe lasers serve different purposes:

- In measurements of the collective coupling between an ion Coulomb crystal and a cavity field, such as those depicted in sec. 6.1, the 866-1 beam is used for probing the crystal-cavity system at the single-photon level and its detection is performed by measuring the light reflected by the cavity using an APD. In this configuration the 866-2 beam is only used for repumping and optical pumping. The 894 nm, 866-1 and 866-2 lasers are all locked to the stabilized reference cavity. This makes it possible to reference the 894 nm laser to the others and prevent any relative frequency drifts.

- In sec. 6.2 and chap. 7, the 866-1 laser light is used to create a far-detuned intracavity optical lattice, while light from the 866-2 laser, close to resonance with the atomic transition, is used to probe the ions. Both lasers are resonant with the cavity but with different frequencies, i.e. resonate with different longitudinal modes of the cavity. In these experiments it is required that the standing wave lattice field (866-1) follows the vibrations of the trap cavity and thus, the laser is locked directly to the experimental cavity, and not to the reference cavity. This is done in order to minimize the intensity fluctuations of the intracavity optical lattice. The trap cavity itself is then locked to the 894 nm laser, which is locked to the stabilized reference cavity. Furthermore, locking the cavity probe (866-2) to the reference cavity keeps it resonant with the trap cavity but also on atomic resonance.

Beside the configurations described above, there is also a possibility to send one of the 866 nm laser beams through a different fiber in order to couple light into the cavity from the HR side. This beam arrangement was used when investigating cavity electromagnetically induced transparency (EIT) (see [68,73]) and this will also be the configuration used in order to realize a quantum memory for light (see chap. 4 for more detail).

5.5.5 Isotope selective loading laser - 272

Our ion loading scheme only involves an atomic beam and a single laser source, nonetheless, a specific number of ions of a particular isotope, can deterministically be loaded into the trap. The atomic calcium beam is produced from a resistively heated oven and sent through the trap center at 45° compared to the trap axis as seen on fig. 5.1. The most abundant calcium isotope is ^{40}Ca (96.9%), which is also used in all experiments presented in this thesis, however, any other stable Ca isotope can be ionized and loaded into the trap [27,169] (see app. A.1). This is important, e.g. when trapping two species simultaneously in the trap, in the context of quantum memory [106,170].

The oven is heated to ~ 400°C and the atomic beam is collimated using skimmers after which it passes the trap center. Here, a 272 nm laser beam crosses the atomic beam at 90° and photo-ionizes the calcium atoms. As shown in fig. 5.5, we

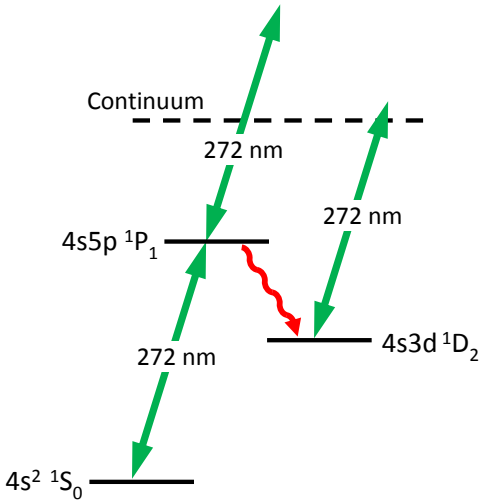

Figure 5.5: Isotope selective two-photon ionization scheme for Ca^+-ions from neutral Ca atoms, resonantly enhanced by the first 272 nm absorption. The lifetime of the $4s5p^1P_1$ and the $4s3d^1D_2$ states in Ca are 17-60ns [171] and 18ms [172] respectively.

use a two-photon ionization process enhanced by the first resonant absorption stage. Neutral calcium is resonantly excited to the $4s5p^1P_1$ state with the 272 nm laser and afterwards transferred into the ionization continuum, using the same laser field. This occurs directly from $4s5p^1P_1$ or through the metastable $4s3d^1D_2$ state, after a spontaneous decay. For the different isotopes, the resonance frequency of the first transition differs substantially, and thus, this method is isotope selective (as demonstrated in [162]), e.g. the difference between the resonances of ^{40}Ca and the closest isotope, ^{42}Ca, is 1 GHz.

The 272 nm light is produced by a fiber laser[3] at 1088 nm that is frequency doubled twice using SHG in two consecutive bow-tie cavities [173]. The first SHG stage uses a type I non-critical phase-matching in a $LiNbO_3$ crystal, which depends on temperature matching of the medium, to produce light at 544 nm, while the second stage employs type I critical phase-matching in a BBO crystal to turn the frequency into 272 nm. The frequency of the fiber laser can be scanned over a range of 5.8 GHz using a PZT or, by changing its temperature (2.3 GHz/K). The wide tuning range of the fiber laser and its narrow linewidth (<MHz) makes it possible to ionize any stable Ca isotope. During loading, the cooling and repump lasers are also present in the trap [169], and as the desired number of ions is reached, the 272 nm loading laser is blocked manually and the oven is closed. Using this method, large single- and bi-component crystals of up to 10^5 ions can be quickly loaded into the trap [169]. The same ion ensemble can be kept in the trap during many experiments and we can easily reload ions if they escape from the trap.

[3]The fiber laser is a so-called distributed feedback (DFB) laser, Koheras Boostik™

5.6 Imaging and detection system

In the experiments we use two different methods to get information on the ion-cavity system. The first method is based on the collection of fluorescence photons emitted by the ions during cooling (397 nm), while the other method is based on the measurement of the cavity reflection signal (866 nm).

5.6.1 CCD imaging

Two charge coupled device (CCD) camera systems are used to detect images of the ions in the trap by collecting the 397 nm fluorescence remitted during the Doppler cooling process. This makes it possible to determine the size and location of the ion position distribution in the trap. On fig. 5.6 the camera system is depicted together with images obtained with each of the cameras. Images of the ion Coulomb crystals are projections of the three-dimensional ellipsoidal shaped ion system into an image in two dimensions.

A camera[4] mounted above the trap can image trapped ions in the (x, z)-plane. The ion fluorescence is collected by a long achromatic imaging lens with a focal length of

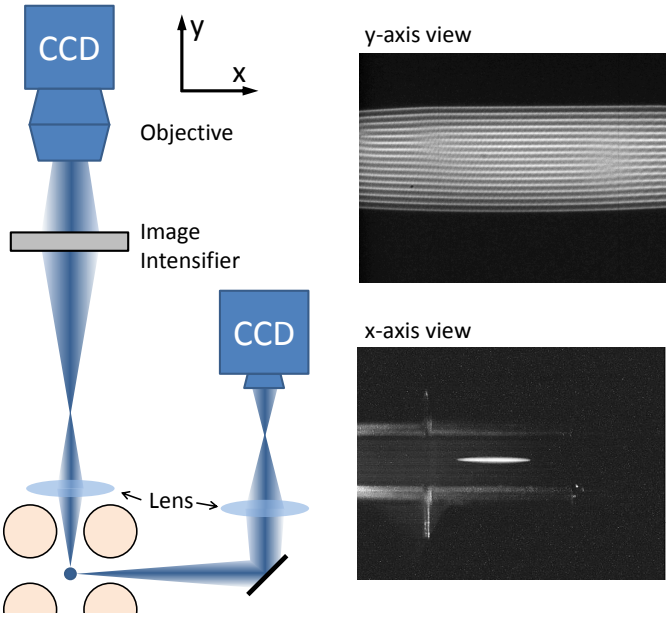

Figure 5.6: Schematics of the imaging setup. Two charge coupled device (CCD) cameras can be used to monitor the ion position by collecting the 397 nm fluorescence of the ions. The camera used in the experiments are mounted above the trap in the y-direction and an image recorded with a magnification of 10 is shown to the right (part of an ion Coulomb crystal containing $\sim$ 13000 ions). A second camera can image the ions from the side (x-direction), although with a much lower magnification, and the projection image to the right shows a very large crystal of length $\sim$ 2.5 mm.

[4] PCO sensicam

70 mm. The lens and camera are mounted in a hight above the trap leading to a magnification of ~ 10 on the CCD. The size of the camera CCD is 640×480 pixels and this leads to an image resolution on the CCD of $0.9\ {}^{\mu\mathrm{m}}/_{\mathrm{pixel}}$. In the experiments presented in sec. 6.1, where the ion-cavity coupling is measured from the cavity spectrum, the ions are imaged directly onto the camera. The image depicted in the top right of fig. 5.6 shows a projected image of an ion Coulomb crystal ($N_{tot} \approx 13000$) during cooling. In the experiments described in chap. 7 the fluorescence level is extremely low, as the experiments involve only single ions. In this case the ions are imaged onto an image intensifier[5] with a magnification of 20 and subsequently onto the CCD camera with a magnification of 1/2 using a commercial objective[6]. The resulting magnification is still ~ 10.

Inside the image intensifier, incident light from the ions is transformed into electrons using a photocathode. The electrons are accelerated and amplified through two stacked multichannel plates and produces a fluorescence image on a phosphor screen. This is detectable for the CCD camera as an amplified image of the ions. The acceleration voltage of the image intensifier can be used to gate the images in well controlled sequences with a time resolution as short as 20ns. This is of great importance especially for the experiments of chap. 7 where we are only interested in measuring scattered light from the ions at certain time-intervals in an experimental sequence. The fast gating can also be used to obtain time resolved images of the ions to e.g. visualize dynamics of the ion Coulomb crystal undergoing micromotion for example.

The side camera (x-axis view) images the ions in the (y, z)-plane and is only used under circumstances where the top-camera has a limited view. As the lens is outside the vacuum chamber (with ~ 30 cm to the trap center), its imaging resolution and magnification is considerably lower than for the top-camera. This makes it possible, though, to observe very large ion Coulomb crystals but also to determine the vertical position of the ions. Fig. 5.6 shows an image taken with the side camera containing a long ion Coulomb crystal. On the image, contours of the electrodes can also be seen indicating the length scale of the crystal (~ 2.5 mm).

5.6.2 Probing and detection of the cavity signal

As introduced above we use two possible configurations in the experiments described in this thesis. In the experiments with the high-power lattice laser of sec. 6.2 and chap. 7 detection of the reflection or transmission can be done with normal photodiodes. The ion-cavity coupling experiments (sec. 6.1) take place at the single photon level and therefore we use two avalanche photo detectors (APD) to collect the reflected and transmitted photons. A PBS placed in cavity reflection makes it possible to choose between measuring with the APD or with the normal detectors.

One APD is installed on the PT side of the cavity to record the reflected signal from the cavity probe beam (see fig. 5.7). Before arriving at the cavity, the probe (866 nm) and reference (894 nm) beams pass a glan polarizer (GP), separating the incident and reflected cavity signals. Subsequently, a $\lambda/4$ and a $\lambda/2$ wave plate ensures the appropriate circular-polarization of the laser fields, and in addition they compensate

[5] Proxitronic detector systems, MCP-Proxifier
[6] Nikon

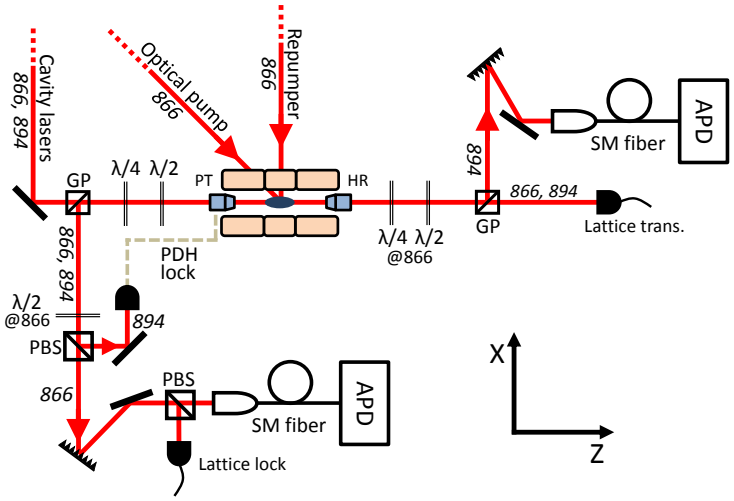

Figure 5.7: Schematics of the cavity detection system showing a segment of fig. 5.4.

for any birefringence effects imposed by the cavity mirrors or the dichroic mirror used to combine the cooling light at 397 nm with the cavity beams. The beams are then injected into the cavity through the PT mirror and the reflected beam is deflected in the GP that was passed by the incident beam. In order to separate the probe from the reference in the reflected signal a wave plate thats acts like $\lambda/2$ at 866 nm and λ at 894 nm is combined with a polarizing beam splitter (PBS) (see fig. 5.7). The 894 nm light is reflected off the PBS and sent to a photo-detector where a PDH lock can be used to stabilize the length of the experimental cavity. The 866 nm light is sent to the APD through a SM fiber, after having passed a diffraction grating (1800 lines/mm) removing any remaining 894 nm photons. The resulting detection efficiency of the reflected probe photons is $\sim$ 16% [27] (APD@866 nm $\sim$ 44%, grating $\sim$ 63%, APD fiber coupling $\sim$ 65%, optics $\sim$ 90%).

On the HR side of the cavity an APD measures the transmitted 894 nm reference light (see fig. 5.7). The light passes a combination of $\lambda/4$ and $\lambda/2$ wave plates at 866 nm, not changing the 894 nm polarization. A part of the reference light is reflected off a GP, passes a spectrally filtering diffraction grating (1800 lines/mm) and is coupled via a SM fiber to a second APD.

The standard photo-detectors present on each side of the cavity (see fig. 5.7) measures reflection and transmission signals of greater intensity, i.e. when not working on the single photon level. In experiments with the strong 866 nm lattice laser the transmitted signal is used to monitor the lattice strength by measuring the hight of the signal in lock and converting it to an intra-cavity field strength. The standard detector placed in reflection is used to lock the lattice laser to the experimental cavity (as mentioned above).

Scanning the cavity

We scan the cavity length by varying the voltage sent to the PZT system at the PT mirror. Typically we drive the voltage with a triangular shape at a rate of 30Hz and a variable amplitude allowing for a frequency span of the spectrum of up to 13 GHz. In the experiments described in sec. 6.1 the cavity reflection signal is repeatedly measured by the APD with a typical integration time of ~ 1 μs at a rate of ~ 50 kHz. Because of the extremely low photon flux ($\sim 10^6$/s), the cavity spectrum is obtained from an average over several hundreds scans. To compensate for acoustic vibrations, which are changing the cavity resonance position from scan to scan, the 894 nm reference laser is used. It is possible to overlap the cavity resonances of the two lasers in the scan (866 and 894) by slightly changing the frequency of the reference. Thus, mechanical drifts will affect both signals equally.

Since the amount of 894 nm light injected into the cavity is much higher than that of the probe, the transmitted 894 nm resonance can easily be observed with the APD in cavity transmission in a single scan. Hence, the cavity resonance frequency determined by the reference peak position in each scan can be monitored individually. This can be used to reference the probe signal to that of the cavity in different scans and perform an average which is not broadened by the cavity vibrations [27]. From this referencing technique the final resonance spectrum of the ion-cavity probe can be determined precisely in accordance to sec. 3.3.2 and 3.3.3.

Locking the cavity

Another option is to lock the cavity at a certain detuning from the atomic resonance frequency. The reflected 894 nm reference signal can be used to actively stabilize the cavity length by imposing a PDH lock feedback to the PZT system. Usually, the frequency of the reference laser is set such that the cavity resonance overlap with the atomic resonance and the reflected 866 nm probe laser is recorded with the APD.

Again, acoustic noise in the cavity makes the stabilization difficult and the measurements of the reflected probe field will be noisy [73]. To filter this noise we record the transmitted signal of the reference laser on the second APD at the same time as we record the reflected probe laser signal. On fig. 5.8(a) the reflected signal of the resonant 866 nm probe is shown (black squares) when the cavity length is locked, together with the transmitted signal of the 894 nm reference laser (red circles). It is evident that noise[7] dominates the signal, and makes it hard to get reliable data directly. We observe variation in the reflected signal from the known on-resonance count (~ 25) up close to the completely off-resonant level (~ 215). The signals are actually obtained after optimizing the electrical feedback system to react on the known vibrational frequencies, but the signals are still clearly unusable.

A way to avoid this problem is to exploit that the noise in the two signals are correlated in time. When the transmitted reference signal (894 nm) drops below a certain threshold we deduce that the cavity is no longer resonant with the laser. In the recorded data, a filtering can be performed by only keeping point for which the reference APD exceeds the threshold limit. This cleaning reduces the useful data

[7] Measurements of the mechanical spectrum revealed the dominant vibrational resonances around 400 Hz and 2000 Hz. For more detail see [27]

points and hence increases the measurement time, but eventually it ensures that the cavity was resonant for the selected data points [27, 73]. On fig. 5.8(b) we see the cleaned data for a threshold value of 305 counts and we clearly observe a signal with much less noise and much closer to the correct on-resonance level.

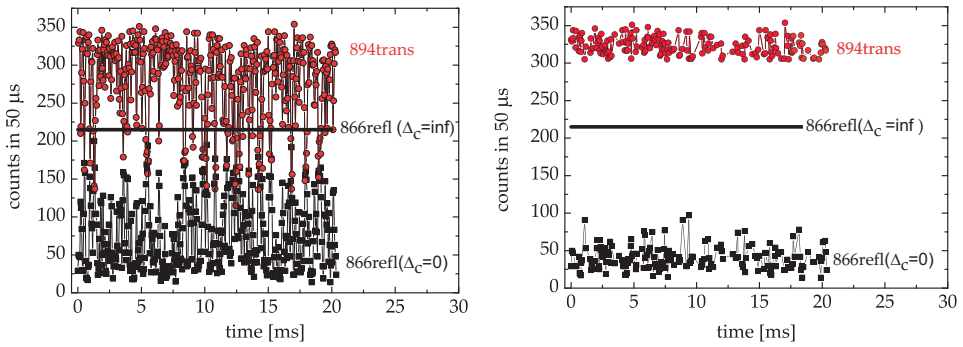

Figure 5.8: Measurements from [27]. (a) APD counts in 50 μs bins when locking the cavity to the 894 nm laser. Observed is the 894 nm signal in transmission (red circles) and the reflected signal of the 866 nm probe with another (black squares). The horizontal black line shows the level of 866 nm reflection when the cavity is completely off-resonant. (b) Corrected data. All data sets, for which the 894 nm signal is lower than the threshold (here 305 counts) is disregarded.

5.7 Calibration and overlapping of the cavity and trap axis

For the experiments performed in our setup, it is crucial that the cavity axis and the trap axis are well-overlapped. This ensures that the ions are addressed efficiently by the cavity field while being placed on the field-free nodal line of the RF potential. DC potentials added to some of the electrodes can translate an ion crystal e.g. in the radial direction, but this causes the symmetry-axis of the crystal to move away from the nodal-line. The crystal is hence moved into regions of large micromotion amplitudes (described in sec. 2.3.4) leading to unwanted RF-heating and broadening of the atomic linewidth.

Another approach is to change the RF-voltages (U_{rf}) by which the position of the radial pseudo-potential minimum can be controlled. This will move the ion crystal with respect to the geometric center but keep it centered on the field-free nodal line. Fig. 5.9(a) illustrates how lowering the 6 electrodes on one side[8] makes the ions move radially in the x-direction. The curves illustrate the RF-potential at two different times in the RF-cycle out of phase by π.

The RF-voltage is applied by a frequency generator and amplified by an RF-amplifier[9] before it is transferred to the trap electrodes. The RF power supply is applied through a ferrite toroid transformer with a single turn on the supply side

[8] Here the amplitude of the RF-field on the 6 electrodes numbered 7-8-9 and 10-11-12 is decreased
[9] Amplifier Research, 4W1000

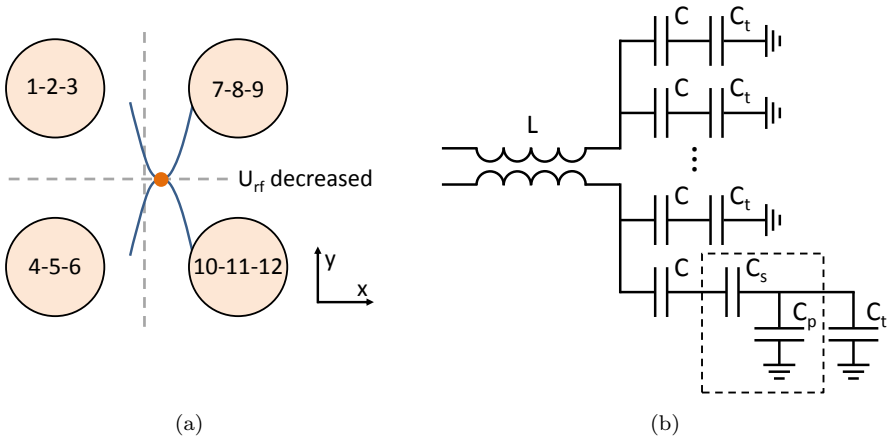

(a) (b)

Figure 5.9: (a) Illustration of moving the ions (in the x-direction) with respect to the geometric center by decreasing the RF-amplitude of the electrode rods on one side of the trap compared to the other. Electrodes number 7-8-9 and 10-11-12 are changed by varying the capacitative loads in accordance to the text. The curves represent the RF-potential at two times in the RF-cycle out of phase by π and the ions are depicted with an orange circle. (b) Schematics of the RF resonant circuit. Each electrode has a capacitance C_t and are connected to the RF power-supply through a toroidal transformer of inductance L. C represents the capacitance of the remaining circuit. By applying additional loads in serial (C_s) or parallel (C_p) the RF potential minimum can be moved radially.

and 10 turns on the trap side. The individual trap electrodes acts like a capacitative part of an LRC resonance circuit and the inductance, L, is mainly set by the transformer. In fig. 5.9(b) a schematic drawing of the circuits is shown, where the single electrodes have a capacitance C_t and the rest of the circuit is represented by the capacitance C. Without any other capacitances the voltage on the electrode is given by $U_e = U_{in}/(1 + C_t/C)$. The RF-voltage can be adjusted by changing the capacitative loads of the individual electrodes by adding extra capacitors in series, C_s, or in parallel, C_p. By modifying the individual electrode loads the ion crystal can be moved slightly in any radial direction of the trap. For a more comprehensive description see [27, 128]

After the trap was assembled, the potential minimum was displaced in this fashion by $\sim$ 90 μm in the x,z-plane and $\sim$ 80 μm in the y,z-plane [128]. By measuring projection images of ion crystals or the coherent coupling with the cavity field, it was found that the trap and cavity axis could be overlapped to within $\pm 1\mu$m. The whole electrode system acts like one resonant circuit and changing one load affects the coupling of the RF-voltage sent to any of the other electrodes. Also, the RF resonance frequency will change and this might induce unwanted phase shift in the RF-fields. Additional variable capacitors have been added in parallel to the electrode capacitance (C_t) allowing for fine tuning of the voltage on the individual trap electrodes. This option is used in the experiments described in chap. 7 where small adjustments of the loads is used to vary the RF-phase between different electrode segments. This can remove residual micromotion to which the experiments of chap. 7 are very sensitive.

Chapter 6

Techniques for characterizing large Coulomb crystals in the cavity

In preparation for the quantum memory implementation this chapter discusses two techniques for characterizing large ion Coulomb crystals in an optical cavity. The first technique (sec. 6.1) is a non-invasive measurement of the temperature of cold ion crystals, making use of the coherent coupling of the crystal with a single mode cavity field at the single photon level. In addition to directly assessing the effect of the crystal temperature on the coupling with the cavity field it may also provide an alternative temperature measurement method to the often-used comparison of fluorescence images with molecular dynamics (MD) simulations [125, 174–176]. The second technique (sec. 6.2) demonstrates the possibility of locating the absolute center of the optical cavity by using a large ion Coulomb crystal as an imaging medium to visualize the fluorescence pattern from two simultaneously resonant cavity fields. In this scheme, a probe field, nearly resonant with the ions, and a strong off-resonant field create a periodic AC Stark-shifting potential. This combination causes a spatial beat pattern in the ion fluorescence which can be used to determine the absolute position of the cavity center within less than a micron. In addition to being of general interest for CQED experiments in which absolute positioning of the atoms with respect to the cavity center may be required, this capability is needed for the localization experiments of chap. 7.

6.1 Measuring the temperature of ion Coulomb crystals by their coupling to an optical cavity

In this section, we will present a noninvasive method for measuring the temperature of ion Coulomb crystals, which uses the coherent coupling of the ions to the cavity field. When an ensemble of two-level atoms is present inside the mode volume of the cavity, the steady state cavity reflection spectrum expresses the absorption and dispersion induced by the atoms on the cavity field, as described in sec. 3.3.3. How these alter the cavity field spectrum depends on the velocity distribution of the ions and can be used to extract information on the thermodynamical state of the ions. Such a strategy has already been used successfully to investigate collective motional modes

of ion Coulomb crystals [65]. Among other things, it benefits from the collective coupling enhancement with the cavity demonstrated in [28], and, as probing with single cavity photons on the $3D_{3/2} \leftrightarrow 4P_{1/2}$ transition of $^{40}Ca^{+}$ ions essentially leaves the thermodynamical state of the crystal unperturbed, it is a non-invasive method.

The theory describing the CQED-interaction between an ensemble of N two-level atoms and a single mode cavity field is found in sec. 3.3.3, and we will apply this to the presented experiments. In sec. 6.1.1 we introduce the experiment and recapitulate the theoretical model that is relevant for the measurements. In sec. 6.1.2 we present the experimental procedure and in sec. 6.1.3 the experimental results are presented. In sec. 6.1.4 a short introduction to a method for simulating crystal pictures at different temperatures using MD simulations is given. In the future, the agreement between the temperature obtained in the simulation and the cavity measurement should be compared. If successful, this noninvasive method for measuring the temperature of ion Coulomb crystals could e.g. give insight into the complex heating processes of such crystals. Finally, in sec. 6.1.5 we provide a small discussion and give an outlook on the experiments.

6.1.1 Introduction

The thermodynamic state of a large ion Coulomb crystal, described as a non-neutral plasma (sec. 2.3.2), is determined by the the plasma coupling parameter, defined as the ratio of the Coulomb interaction energy to the kinetic energy in eq. 2.23:

$$\Gamma_p = \frac{Q^2}{4\pi\epsilon_0\ a_{WS} k_B T}\ . \tag{6.1}$$

When the temperature, T, is increased Γ decreases. As introduced in sec. 2.3.2 large one-component plasmas are in a liquid phase when $\Gamma_p \gtrsim 2$ and will undergo a liquid-solid phase transition when $\Gamma_p \sim 170$ [120]. Determining the temperature of ion systems is challenging experimentally as well as theoretically. Several methods have been used so far, e.g. fluorescence imaging of single ions or ensembles of ions, possibly in combination with molecular dynamics (MD) simulations [125, 174–176].

As opposed to using incoherent scattering, the experiments described in the current section detect the effect of ion motion through the coherent coupling to the optical cavity field. In the experiments, an ion Coulomb crystal of $^{40}Ca^{+}$ ions is trapped and Doppler-cooled to a certain temperature which can be changed by varying the detuning of the cooling laser. MD simulations of the system has shown that the velocity distribution of the ions after Doppler cooling is a Boltzmann distribution, for the experimental parameters. For the ions to act as two-level systems they are prepared in a specific Zeeman substate (here $|g\rangle = \left|3d^2D_{3/2}, m_J = +3/2\right\rangle$) and then probed by a weak cavity field at the single photon level resonant with the transition to the excited state $|e\rangle = \left|4p^2P_{1/2}, m_J = +1/2\right\rangle$.

The theoretical description of the coupled ion-cavity system is reviewed in sec. 3.3, where the dynamical equations of motion for the system observables are given together with the steady-state solutions. In the experiments we measure the reflection spectrum from the cavity, as it couples to the ion crystal, which is fitted to the model. From the measured reflection spectra and the model of sec. 3.3.3 including a thermal motion of the ions, the temperature of the crystal can be extracted. The cavity

reflectivity is given by

$$\mathcal{R}_{\text{atom-cav}} = \frac{(\kappa' - 2\kappa_1)^2 + \Delta_c'^2}{\kappa'^2 + \Delta_c'^2} \ , \tag{6.2}$$

where, κ_1 is the cavity loss rate of the incoupling mirror, and κ' and Δ_c' are the effective cavity field decay rate and detuning defined in sec. 3.3.2. As in sec. 3.3.3, if we assume a thermal atomic ensemble with a Maxwell-Boltzmann distribution, the effective cavity detuning, Δ_c', is given by eq. (3.55) and the effective decay rate can be expressed through an integral over the atomic velocity distribution:

$$\kappa'(\Delta_l) = \kappa + \frac{g_N^2 \gamma}{\sqrt{2\pi}\gamma_D} \int \xi(\Delta_l, v)\ e^{-\frac{(kv)^2}{2\gamma_D^2}}\ dv \ , \tag{6.3}$$

where κ is the total empty cavity decay rate, v is the ion velocity along the cavity axis (z-axis) and $g_N = g\sqrt{N_{eff}}$, with g being the maximum single ion coupling rate and N_{eff} the effective number of ions coupling to the cavity field. Hence, the total cavity decay rate (κ') is the sum of the empty cavity rate (κ), i.a. due to the mirror coatings, and the decay due to absorption in the ion crystal, which in general depends on the Doppler broadening. We define the Doppler width as $\gamma_D = k\sqrt{\frac{k_b T}{m}}$, where m is the atomic mass, T is the considered temperature, k_B is the Boltzmann constant and k is the wavenumber of the laser field. Furthermore, we have

$$\xi(\Delta_l, v) = \frac{\gamma^2 + \Delta_l^2 + (kv)^2}{(\gamma^2 + \Delta_l^2)^2 + 2(\gamma^2 - \Delta_l^2)(kv)^2 + (kv)^4} \ , \tag{6.4}$$

where $\Delta_l = \omega_{at} - \omega_l$ is the probe laser detuning from atomic resonance, γ is the decoherence rate of the atomic dipole.

The variation of κ' with Δ_l is given by a Voigt profile. The temperature of an ion Coulomb crystal can be determined by measuring reflectivity spectra, from which κ' can be determined, as function of Δ_l and fitted to eq. (6.3). If the values of κ, γ and g_N are known, it allows for extracting T from γ_D. For $\Delta_l = 0$ eq. (6.3) reduces to

$$\kappa'(\Delta_l = 0) = \kappa + \sqrt{\frac{\pi}{2}} \frac{g_N^2}{\gamma_D} \text{erfc}\left(\frac{\gamma}{\sqrt{2}\gamma_D}\right) e^{\frac{\gamma^2}{2\gamma_D^2}} \ , \tag{6.5}$$

where $\text{erfc}(x)$ is the complementary error function.

6.1.2 The experimental sequence

To measure the coupling between the ions and the cavity field a crystal is first loaded into the trap and Doppler-cooled to a certain temperature. In the experiments presented here, various ion Coulomb crystals are loaded with different crystal parameters; N_{eff} = 100-445 ions, radius R = 55-110 μm, length L = 515-1200 μm. The parameters were intentionally chosen not to include a very large number of ions, in order to be able to perform a tractable comparison with MD simulations. This means that we are not actually entering the collective strong coupling regime. Once a reliable connection has been established between the temperatures measured using the cavity

and the simulations, we can apply the same techniques to study to larger crystals, in order to find the optimal crystal parameters for CQED experiments with strong coupling enhancement, like e.g. the quantum memory system described in sec. 4.3.

We then use a specific laser sequence to prepare the ions by optical pumping into a given Zeeman sub-level of the metastable $3D_{3/2}$ state and subsequently probe them weakly by injecting the cavity with a σ^- circularly-polarized pulse, close to resonance with the $3D_{3/2} \leftrightarrow 4P_{1/2}$ transition and such that the mean number of intracavity photon would be at most one in an empty cavity (to make the two-level situation of sec. 3.3 applicable). After a short time (0.1 μs), allowing for the cavity field to build up and reach steady state inside the optical cavity, the reflected probe field is measured with an avalanche photo detector (APD) [27]. From numerical simulations of an ensemble of $N = 100$ ions (described in [27]) it was found that in order to probe a quasi-steady state regime of the system, the probing should last at most 2 μs to be short enough, not to cause significant depopulation of the state prepared by the optical pumping. Hence, the APD measurement is performed on this timescale. The sequence is repeated at a rate of 33.3 kHz while the cavity is slowly scanned at a frequency of 30 Hz over 1.3 GHz. In fig. 6.1(b) the sequence is shown and in fig. 6.1(a)

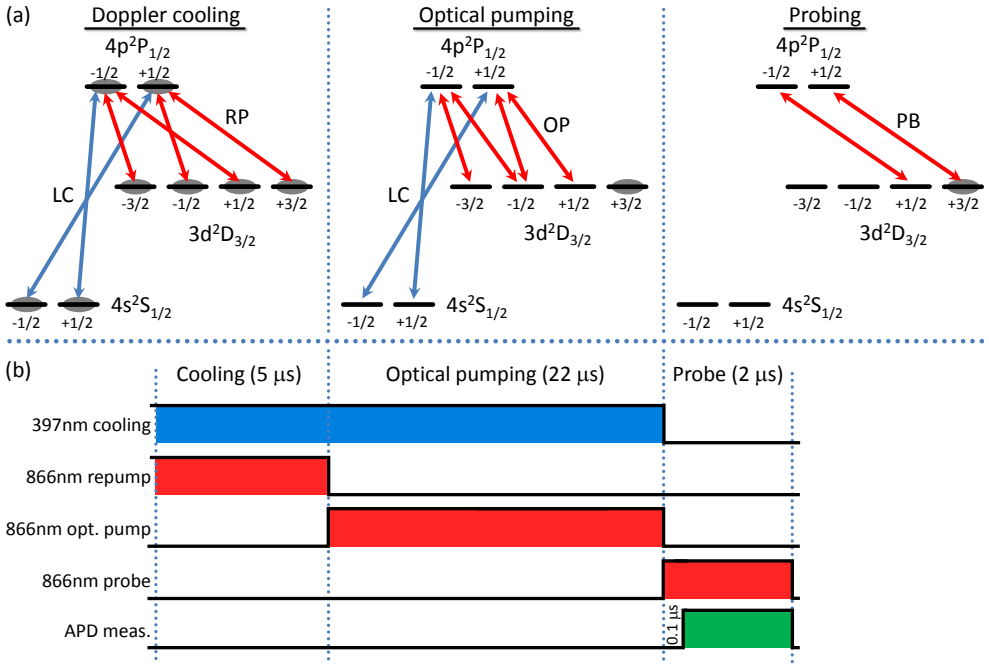

Figure 6.1: The laser sequence used in our experiments to measure the temperature of ion Coulomb crystals. (a) shows the relevant energy levels of $^{40}Ca^+$ including the addressed transitions in the three parts: Doppler cooling, Optical pumping and Probing. The acronyms are: laser cooling beam (LC), repumping beam (RP), optical pumping beam (OP), probe beam (PB). The gray shading represents the state position of the ion population in the specific sequence part. In (b) the schematics of the experimental sequence is shown, indicating the on and off timing of each laser and the probing APD.

a detailed picture of the main energy-levels are shown for the different parts of the sequence. The magnetic field (a few G) is applied along the quantization axis (z-axis). A description of the experimental setup is found in chapter 5 where the different lasers types are specified (see also [27, 73]).

Doppler cooling In the first part of the sequence (5 μs) the ions are Doppler cooled, which has been described in sec. 2.2 and 2.3. Two counter propagating 397 nm laser cooling (LC) beams are sent along the z-axis with left and right hand circular polarizations, respectively. In this way the ions are scattering photons on the $4S_{1/2} \leftrightarrow 4P_{1/2}$ transition. To avoid accumulating ions in a dark state in the metastable $3D_{3/2}$ state a 866 nm repumping laser beam (RP) is sent along the x-direction, polarized along the y-direction. With optimized cooling parameters (mostly depending on the 397 nm detuning and power) typical temperatures of the crystals of a few tens of mK can be obtained.

Optical pumping The second part (22 μs) is the optical pumping stage [168], which transfers the ion population to the $m_J = +3/2$ Zeeman sub-state of the $3D_{3/2}$ level. After turning off the RP laser an 866 nm optical pumping laser (OP) is sent onto the ions, while still having the 397 nm cooling laser (LC) on. The OP laser is resonant with the $3D_{3/2} \leftrightarrow 4P_{1/2}$ transition, but consists only of σ^+ and π polarized components. It is sent to the ions with an angle of 45° with respect to the z-axis and with a specific elliptical polarization [27]. At the same time the 397 nm laser is applied in order to pump the population decaying to the $4S_{1/2}$ ground state back to the $3D_{3/2}$ state. As the $m_J = +3/2$ state is not coupled to any light field, eventually all population is transferred to it. The efficiency of the optical pumping process can be optimized by selectively probing the population in the different Zeeman sub-levels and measuring the fluorescence on the $4S_{1/2} \leftrightarrow 4P_{1/2}$ transition (397 nm). A strong probe field is used to address the population in the $m_J = +1/2,\ +3/2$ states (with σ^- circular polarization) or the $m_J = -1/2,\ -3/2$ states (with σ^+ circular polarization). The population is thus transfered to the $4S_{1/2}$ level by a emitting 397 nm photon. Sending the probe along the x-direction with a π-polarization measures the population in the $m_J = -1/2,\ +1/2$ states. Comparing the obtained fluorescence levels after several repetitions makes it possible to ensure an optical pumping into the $m_J = +3/2$ state with an efficiency of typically $\sim 97\%$ (for more detail see [27] or sec. 7.4.2 for optical pumping measurements in the few ion case).

Probing In the final part (2 μs) we are probing the system by measuring the cavity reflection signal. An 866 nm σ^- circularly-polarized probe laser beam (PB), resonant with the $D_{3/2,m_J=+3/2} \rightarrow P_{1/2,m_J=+1/2}$ transition, is injected into the TEM_{00} cavity mode and this can be used to mimic the two-level system described earlier. In this part LC, RP and OP are turned off. From the theoretical description the $m_J = +3/2$ state now acts like the ground state and the $4P_{1/2}$ state with $m_J = +1/2$ acts like the excited state. The PB laser has sufficiently low intensity that the mean intracity photon number is less than one all the time. Because of the low intensity of the light, it is necessary to measure the reflected signal with an APD (see sec. 5.6.2). The APD is turned on after a small delay (~ 0.1 μs), letting the field build up inside the cavity and the system reach steady state.

6.1.3 Experimental results

While the sequence is repeated, the length of the optical cavity is slowly varied using the PZT (see fig. 5.2). This changes the detuning of the ion-cavity system, Δ_c. The cavity is scanned over a range corresponding to ~ 1.3 GHz at a repetition rate of 30 Hz and the reflection signal is constructed by sampling each cavity scan while repeating the sequence at a 33.3 kHz rate. The width of the reflection signal can be determined, for a given Δ_l, after averaging a number of scans (normally a few hundreds of scans). Scan-to-scan drifts of the cavity are compensated by referencing the probe signal to the transmission signal of the reference laser at 894 nm (see sec. 5.6.2 for more detail).

In fig. 6.2 (a)-(c) typical reflectivity spectra for the cavity have been plotted for different probe detunings, Δ_l, with a $^{40}Ca^{+}$ ion crystal of $N_{eff} \approx 445$ ions. The crystal (number 4 of table 6.1) has the parameters: radius $R = 100$ μm, length $L = 1200$ μm, total ion number $N_{tot} = 13000$, density $\rho = 4.3 \times 10^8$ cm^{-3} and trap frequencies $(\omega_r, \omega_z) = (475, 140) \times 2\pi$ kHz. From each of these spectra an effective decay rate of the cavity, $\kappa'(\Delta_l)$ can be found by fitting to the expected Lorentzian line-shape of eq. (6.2). As can readily be seen on the data, the reflection dip widens as the probe laser is tuned towards atomic resonance, because the coupling between the ion crystal and the cavity field gets stronger. A symmetric behavior is obtained for negative detunings.

Varying the probe laser detuning over a range around atomic resonance, allows to measure κ' as function of Δ_l. This is plotted in fig. 6.3 and the data has been fitted to the expected Voigt profile of eq. (6.3), shown as a red line. From the fit to the model one obtains: $\kappa = 2\pi \times (2.8 \pm 0.1)$ MHz, $g_N = 2\pi \times (11.2 \pm 0.2)$ MHz and $\gamma_D = 2\pi \times (2.0 \pm 0.8)$ MHz, while γ was fixed to the value given in the literature, $\gamma = 2\pi \times 11.2$ MHz [110]. In this example the effective number of ions coupling to the cavity field, found from the fit-parameter g_N, is $N_{eff} = 445 \pm 15$ and the resulting crystal temperature is found to be $T = 14^{+8}_{-6} mK$, by using the definition of the Doppler width, γ_D.

If only the temperature of the crystal is changed, keeping all other crystal and cavity field parameters fixed, then κ' changes via γ_D in eq. (6.3). This means that it is now only necessary to measure κ', and thereby γ_D, for one detuning Δ_l. When

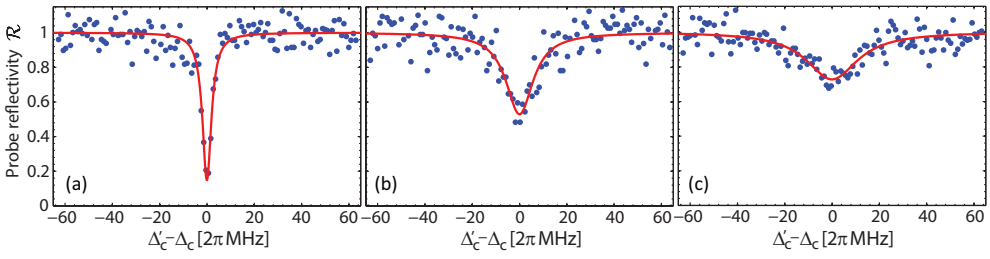

Figure 6.2: Typical reflection spectra averaged over 100 scans of the cavity containing $N_{eff} \approx 445$ ions have been plotted for three different atomic detunings: (a): $\Delta_l = 2\pi \times$ 36MHz, (b): $\Delta_l = 2\pi \times 10$MHz and (c): $\Delta_l = 2\pi \times 0$MHz. The solid red line is a Lorentzian fit which determines κ' which is seen to vary as expected with the atomic detuning.

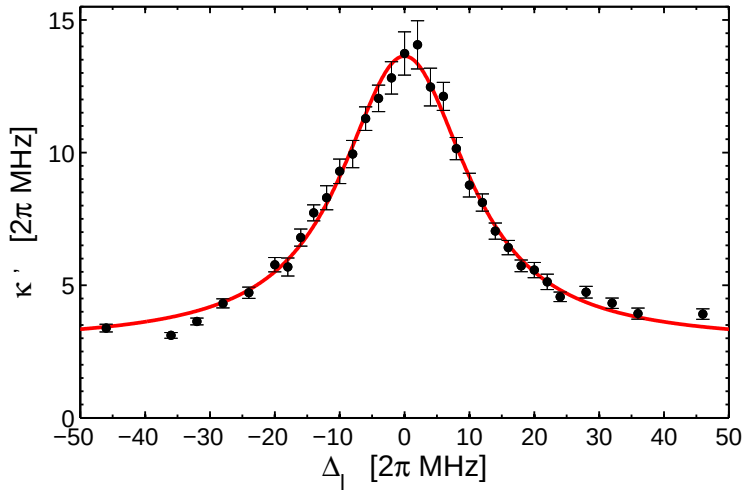

Figure 6.3: A resonance curve of κ' as function of Δ_l is shown for the same crystal as used in fig. 6.2 and shown on fig. 6.4(b) ($N_{eff} \approx 445$). A fit using eq. (6.3) is plotted as a red line, and makes it possible to extract the crystal temperature; here $T = 14^{+8}_{-6} mK$.

$\Delta_l = 0$ the ion-cavity coupling, and hence κ', is maximum and this is what we exploit in the experiments. Also, the equation for κ' is rather simple here (see eq. (6.5)).

We change the temperature of the ion Coulomb crystal by varying the detuning of the 397 nm cooling laser, Δ_{397}. If we consider the simple picture on Doppler cooling of a single two-level ion by two counter propagating beams, as described in sec. 2.2, the effect of Doppler cooling can be modeled by two forces acting on the ion moving left or right respectively. It turns out that the optimal cooling occurs when $\Delta_{397} = \Gamma/2$, where Γ is the excited state decay rate. A qualitatively similar behavior is observed with large ion Coulomb crystals, with the difference that the optimal detuning, power and resulting temperature are typically higher than for a single ion because of RF-heating. As not all ions in a large ion Coulomb crystal are positioned on the trap axis there will be a substantial micromotion in the crystal and this leads to RF-heating [120] and a resulting equilibrium temperature which can be substantially higher than the Doppler temperature (see sec. 2.3.4). When lowering the detuning of the cooling laser, from typically $\sim 2\Gamma$ towards 0, a strong increase in the temperature of the crystal can be observed as the cooling becomes less effective. A similar behavior would also be observed when increasing the detuning, but then the optical pumping efficiency would be affected, which would, first, lower the effective number of ions and, secondly, make the situation more complicated as more levels should be taken into account in the modeling of the interaction [27].

In the experiment we first load a $^{40}Ca^{+}$ ion Coulomb crystal with chosen thermodynamic properties (dimension, density, number of ions). Afterwards, we measure the Voigt profile $\kappa'(\Delta_l)$ and extract a value for γ_D for a close-to-optimal cooling detuning (low temperature). The cooling laser detuning is then lowered step by step, for which $\kappa'(\Delta_l = 0)$ is measured for a resonant probe only. We decrease the detuning towards

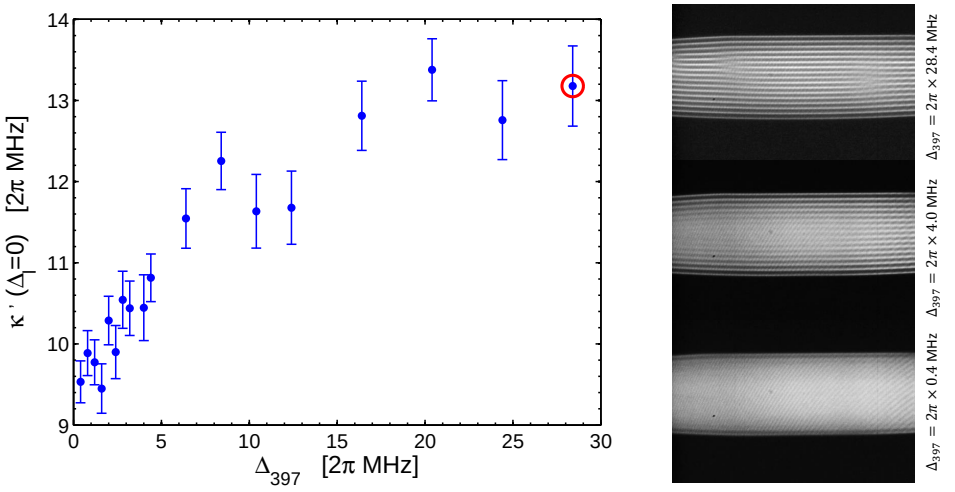

(a) (b)

Figure 6.4: (a) The variation in $\kappa'(\Delta_l = 0)$ when decreasing the cooling detuning from the optimal value towards zero. The red circle marks the detuning at which T_{ref} was measured. (b) Projected images of a $^{40}Ca^+$ ion Coulomb crystal during cooling, detected with the CCD camera. This crystal (number 4 in table 6.1) is the one used in all measurements presented in this section and it has: radius $R = 100$ μm, length $L = 1200$ μm, total ion number $N_{tot} = 13000$, density $\rho = 4.3 \times 10^8$ cm^{-3} and trap frequencies $(\omega_r, \omega_z) = (475, 140) \times 2\pi$ kHz.

resonance ($<$ MHz) until the crystal heats up too much to stay crystallized.

The final temperature variation is measured in the following way: First, a resonance curve of $\kappa'(\Delta_l)$ is measured with the optimal cooling laser detuning, Δ_{397}^{opt}. From the fit to this curve (fig. 6.3) it is possible to extract a reference Doppler width, γ_D^{ref}, which results in a reference temperature, T_{ref}. Now, all other parameters are known (κ, g_N, γ) and the rest of the measurements can be done for $\kappa'(\Delta_l = 0)$ to simplify the experiment, i.e. with the cavity on atomic resonance to maximize the atomic absorption. On fig. 6.4(a) the reflection width $\kappa'(0)$ is plotted as function of the detuning of the cooling laser. It is clear that $\kappa'(0)$ drops significantly as Δ_{397} approaches zero. On the figure, a red circle marks the cooling detuning where the complete κ' resonance has been measured (fig. 6.3), which serves as the reference for the rest of the data points. On fig. 6.4(b) projected images of a trapped $^{40}Ca^+$ ion crystal are shown at different cooling laser detunings: $\Delta_{397} = 2\pi \times 28.4$ MHz, $\Delta_{397} = 2\pi \times 4.0$ MHz, $\Delta_{397} = 2\pi \times 0.4$ MHz. This is the crystal used in the measurements presented on fig. 6.2-6.5. On the images we can see that the crystal is melting and the shell structure disappears as a result of the increase in temperature, as one approaches the atomic resonance with the cooling laser.

From each point in fig. 6.4(a) the temperature of the crystal can be found through eq. (6.5) and by using the reference parameters found from the $\kappa'(\Delta_l)$ resonance fit. This means that the correlation between the crystal temperature and the cooling detuning can be constructed and in fig. 6.5 the resulting plot of T as function of Δ_{397} is shown. Again, the reference detuning has been marked with a red circle. We

observe a large increase in crystal temperature as the cooling detuning approaches zero.

By changing the external trapping parameters for various ion Coulomb crystals it should in principle be possible to gain more insight on the temperature of different crystals. So far we have measured the temperature, with approximately the same cooling parameters, as function of Δ_{397} for a number of different crystals listed in table 6.1. We have varied the crystal radius R, length L, number of ions N and amplitude of the RF potential confining the crystals. The numbers presented in the table are found by inspecting images of the crystals, by considering their shape, the RF-potential and our knowledge on the imaging magnification [27, 73, 128].

From this analysis, complemented with MD simulations, we expect to be able to check variations of the temperature as well as investigate the heating processes taking place in ion Coulomb crystals in linear RF traps. For instance, one could study the temperature increase when varying one external parameter, while keeping the others constant, to see whether this parameter has an effect on the RF-heating and stability of the crystal. Some studies have been performed on the basis of the different ion Coulomb crystals in table 6.1. For instance one could study the temperature increase when varying one external parameter, while keeping the others constant, to see whether this parameter has an effect on the RF-heating and stability of the crystal. In fig. 6.6 a plot of the temperature dependence on the cooling detuning for four different crystals is plotted. The crystals are number 1(green), 2(blue), 3(red) and 4(black) from table 6.1 and these all have the same aspect ratio and radius, but different ion number and RF-amplitude. This keeps the the crystal size constant, but changes the density, which one could expect to have an influence on the crystal

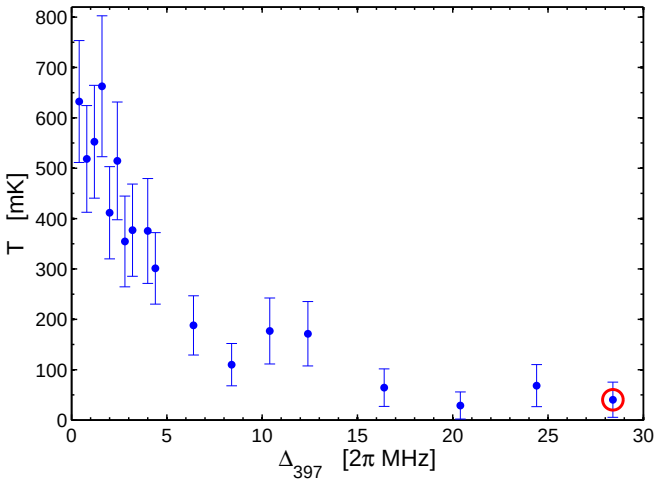

Figure 6.5: Temperature of an ion Coulomb crystal as function of the detuning of the cooling laser, Δ_{397}. It is constructed by measuring $\kappa'(\Delta_l = 0)$, referencing to T_{ref} found from the fit on fig. 6.3 and using eq. (6.5). The red circle marks the detuning at which T_{ref} was measured.

Crystal	V_{RF} [V]	V_{DC} [V]	R [μm]	L [μm]	$\alpha = R/L$	N_{tot}	N_{eff}
1	155	1,2	100	1200	0,08	4900	150
2	180	1,5	100	1200	0,08	7200	300
3	212	1,9	100	1200	0,08	9200	350
4	248	2,4	100	1200	0,08	13000	445
5	180	1,6	58	640	0,09	900	100
6	220	3,1	55	580	0,09	1100	170
7	200	2,9	58	560	0,10	1000	150
8	200	2,9	58	570	0,10	1000	150
9	220	3,1	58	580	0,10	1250	170
10	220	2,1	58	600	0,10	1550	200
11	180	2,2	60	570	0,11	900	110
12	220	3,6	56	520	0,11	1000	150
13	220	3,7	58	530	0,11	1100	150
14	220	3,6	58	540	0,11	1100	150
15	238	4,1	55	515	0,11	1200	170
16	200	3,0	58	500	0,12	800	120
17	212	1,5	108	900	0,12	9800	250
18	212	2,5	108	800	0,13	5500	200
19	212	4,0	108	660	0,16	5000	200

Table 6.1: The variation of the temperature of ion Coulomb crystals as a function of the detuning of the cooling laser has been investigated. In this table the thermodynamic properties of these crystals are listed: applied RF and DC potentials (V_{RF} and V_{RF}), the crystal radius (R), the crystal length (L), the total and effective number of ions (N_{tot} and N_{eff}) and the aspect ratio ($\alpha = R/L$).

stability in the extreme limit. From fig. 6.6 we see that this variation is not changing the heating process noticeably. Including e.g. much denser ion crystals might show thermodynamic effects, and thus a more systematic study based on the numerical simulations described in the next section is under way.

From the obtained temperatures we can calculate the resulting plasma coupling parameter (eq. (6.1)) of the specific ion crystal ($\rho = 4.3 \times 10^8 \mathrm{cm}^{-3}$). At temperatures around 12 mK, $\Gamma_p \sim 170$, corresponding to a completely solid-like crystal structure. However, already at $T = 150$ mK we get $\Gamma_p \sim 13.5$, indicating that the medium is in the liquid phase and for $T > 600$ mK, $\Gamma_p < 3.5$ and hence, approaches the liquid-gas phase transition. Comparing this information with crystal images, shows a qualitatively good agreement between the thermodynamic crystal phase and the obtained temperatures. Furthermore, comparing this information to numerical simulations could complete the thermodynamic study of the crystals.

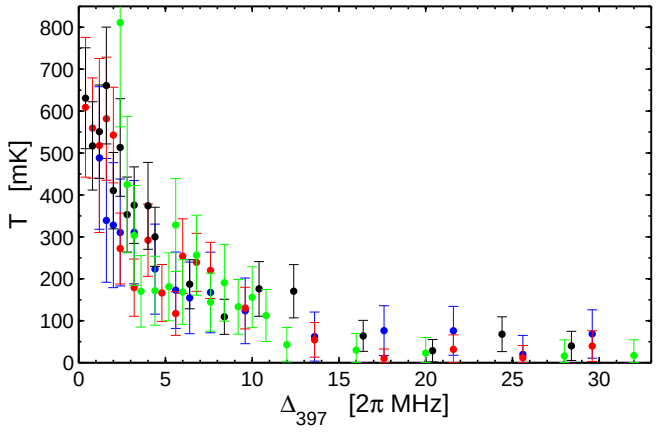

Figure 6.6: Temperature of four ion Coulomb crystals as a function of the detuning of the cooling laser, Δ_{397}. In the figure crystal 1(green), 2(blue), 3(red) and 4(black) from table 6.1 are plotted.

6.1.4 Comparing with numerical simulations

Using molecular dynamics (MD) simulations one can simulate the dynamics of the position and velocity distribution of ions in an ion Coulomb crystal for different trapping conditions and temperatures. The obtained projection images of a given crystal, simulated at different temperatures, can then be compared to images taken in an experiment and the temperature can be determined. Several ion-trap groups in the world uses this technique (see e.g. [175–177]).

This work was part of Niels Hygum Nielsens masters project [178]. The program that he created is an MD program which describes the dynamics and interactions of the system using classical mechanics. The forces used in the calculations include both the trapping forces and the Coulomb interaction between all the ions. This makes the description of the system rather complex, but instead of solving a large number of coupled differential equations the numerical calculation evolves the system in very short time steps until the desired steady state is reached. The time steps used in the integrator needs to be smaller than the shortest timescale of the ion dynamics. However, as there are actually two timescales present here (micro motion and secular motion) the total force in the system needs to be described by a slow and a fast varying part, in a multiple time step integrator [178]. The outcome of the MD simulation is a position/velocity distribution of all the ions. From the 3D position distribution, an image that mimics the projection images taken in the experiment can be produced by adding an optical blurring corresponding to the finite focal depth of the imaging system which can be calibrated independently [178].

We are under the process of simulating images for the crystals of table 6.1 at different temperatures in order to compare them with the images taken in the experiments. One could then check the agreement between the temperature extracted from the cavity measurements to that of the simulations and allow us to estimate the applicability of this method.

6.1.5 Discussion and outlook

In this section, we presented a method for measuring the temperature of trapped, laser-cooled ion Coulomb crystals from the coupling to an optical cavity field. As opposed to e.g. neutrals where the temperature can be determined from time-of-flight measurements, our method uses only *non-invasive* measurements. A general study using this method to measure temperature and heating rates for different crystal parameters could give insight into heating mechanisms and the thermodynamics of cold plasmas. Furthermore, we plan to perform a study comparing temperatures measured from the cavity signal to temperatures obtained from MD simulations. This will hopefully confirm the accuracy of the simulation method and give an alternative approach for temperature measurements. We also expect that the thermodynamic information about ion Coulomb crystals, gained by this method will be useful for realizing quantum storage of light in our system, as described in sec. 4.3.

While using the coupling with the cavity field has the advantage of being a non-invasive method it has the downside that the signal-to-noise depends om the number of ions, and is obviously highest for crystals with large effective number of ions. This can be explained by the fact that the interaction benefits from the collective coupling (eq. (3.46)) between ions and the cavity field and the larger N_{eff} gets, the larger g_N becomes. Moreover, the method essentially relies on measuring the relative broadening of the natural atomic linewidth. The linewidth of the transition used here being rather large (~ 22 MHz), the precision of the measurement could naturally be improved by using a narrower line from which smaller broadenings could be detected.

Another potential limitation of this method is the applicability of the model. In sec. 3.3.3 we gave a conservative estimate of the validity of the model by comparing the average velocity of the ion distribution, v_D, with the effective rates of the coupled system on resonance, i.e. $kv_D \ll min[\kappa + g_N^2/\gamma\ ,\ \gamma + g_N^2/\kappa]$. At very high temperatures ($\sim$K) these considered timescales no longer satisfy the slow-motion approximation made in this simple model. For the specific ion crystals considered in the presented results, the inequality start to break down at temperatures of a few hundred mK (around 600 mK the rates of kv_D and $\kappa + g_N^2/\gamma$ typically become comparable). Although our validity estimate is probably conservative, full numerical simulations of the dynamics would then be required at high temperatures.

6.2 Finding the center of an optical cavity using an atomic ensemble

In this section we present a technique for determining the center of a linear cavity by using an atomic ensemble (ion crystal) placed within it. We demonstrate that it is possible to position a trapped ion crystal with sub-micron precision with respect to the absolute center of a standing wave cavity field. In sec. 6.2.1 we describe the experiment and give a simple theoretical model (sec. 6.2.2). The experimental procedure is described in sec. 6.2.3 followed by a presentation of the obtained results (sec. 6.2.4). The last section (6.2.5) discusses the results and their relation to the rest of our studies, after which an outlook is given.

6.2.1 Introduction

As already introduced in prior chapters, the system of crystallized ions placed inside an optical cavity is a promising platform for quantum optics experiments, as e.g. multi-mode photon storage with long coherence times [74,159]. At the same time, the mechanical interactions of ion crystals with intracavity standing-wave light fields can lead to localization of the ions in finely-structured optical lattice potentials [80–82] (see chap. 7). This potentially opening the possibility of studying e.g. the behavior of particles in quantum potentials [96, 179] or the fine control of crystal ordering by weak optical forces [180, 181].

These studies all rely on carefully characterizing the combined ion-cavity system spectrally as well as spatially. For instance, the spatial relationship between different field modes changes along the cavity length, and multi-mode storage will depend on the precise position of the Coulomb crystal relative to the cavity mirrors. In the experiments described in this section we present a way to precisely determine the position of an ion Coulomb crystal relative to the cavity mirrors, by using the ions as an imaging medium in order to visualize the spatial beating between different longitudinal modes of the cavity [79]. This absolute measurement of the distance from the cavity mirrors is different from the studies of probing the longitudinal structure of the cavity field using single ions in e.g. [15, 182, 183]. These studies demonstrated the ability to measure small displacements but can not distinguish between two positions along the cavity separated by an integer multiple of the field wavelength. That is possible with the simple technique introduced here.

6.2.2 Theoretical modelling

An atomic ensemble is placed inside an optical Fabry-Pérot cavity and is driven by two cavity modes. One is near-resonant with an atomic transition and the other is detuned, essentially giving rise to an AC-Stark shift of the probed energy levels. The scattering of both light fields from the ions produces a fluorescence signal that depends on the local spatial phase between the standing-wave patterns of the two modes. Using pairs of modes separated by an odd or even multiple of the free spectral range (FSR) of the cavity allows for varying this beat pattern and unambiguously determining the absolute center of the cavity.

A full description of the applied method for Ca^+ ions would have to be based on an ensemble of multi-state atoms, including the effects of the applied magnetic and

electrical fields on the various energy levels. However, in order to provide a clear illustrative physical picture, we construct a theoretical model based on an ensembles of *two-level* atoms. More specifically, we consider an ensemble of two-level atoms with a ground state $|g\rangle$ and an excited state $|e\rangle$ positioned inside a near-confocal symmetric optical Fabry-Pérot cavity (see fig. 6.7). The atoms are trapped by some external mechanism which keeps them confined within the cavity mode-volume (in the specific experiment we consider an ion Coulomb crystal trapped in a linear Paul trap). A so-called *lattice* field, which is far-detuned from the atomic resonance, but on resonance with a longitudinal mode of the cavity, is applied. One of the cavity modes is kept on resonance with the $|g\rangle \leftrightarrow |e\rangle$ transition and hence, the lattice is detuned by a whole number of cavity free spectral ranges (ω_{FSR}) from the bare atomic resonance. The lattice field has the effect of inducing a spatially modulated AC Stark shift of the atomic transition, because of its standing wave nature:

$$\Delta_S(z) = \Delta_{S,0} \sin^2(k_l z) \ , \tag{6.6}$$

where $\Delta_{S,0}$ is the maximum Stark shift, z the spatial displacement along the cavity and trap axis, $k_l = (q_l \pi)/L$ the lattice field wavenumber, L is the cavity length and q_l is the longitudinal mode number of the lattice field (see sec. 3.2.1 for more detail).

The effect of this lattice field is monitored by a near-resonant intra-cavity *probe* field detuned by Δ_p with respect to the bare two-level transition frequency (see fig. 6.7). Both the lattice field and the probe field are simultaneously present in the cavity, but their intensities are chosen such that the scattering from the lattice field is negligible with respect to that from the probe field. The spatially dependent photon scattering rate of the probe field can be expressed through the steady state excited population of eq. (3.35), as $\Gamma_{\text{scat}} = \Pi^e(z)\Gamma$, and hence

$$\Gamma_{\text{scat}}(z) = \frac{1}{2} \frac{s(z)}{1 + s(z)} \Gamma \ , \tag{6.7}$$

where Γ is the decay rate of the excited state and $s(z)$ is the spatially dependent

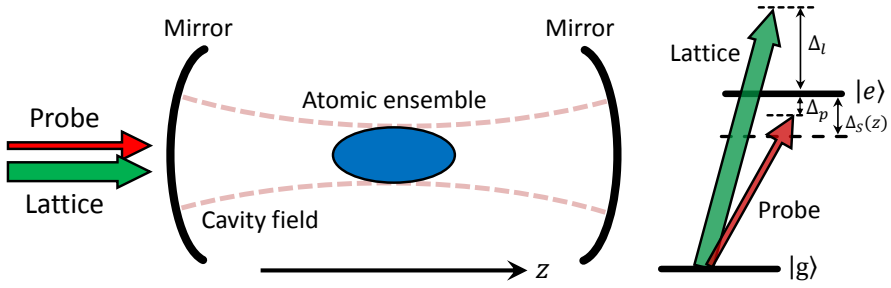

Figure 6.7: Schematics of the considered atomic two-level medium placed inside an optical Fabry-Pérot cavity, together with the energy levels and applied fields. The probe and lattice standing wave fields are detuned from the bare atomic resonance by Δ_p and Δ_l, respectively. The energy-levels are AC Stark shifted by $\Delta_S(z)$ because of the the strong lattice field.

saturation parameter of the probe standing wave field (see eq. (3.36)), defined as

$$s(z) = \frac{s_0 \sin^2(k_p z)}{1 + (2\Delta(z)/\Gamma)^2} \ , \tag{6.8}$$

with $s_0 = I_0/I_{sat}$ being the maximum on-resonance saturation parameter for the probe field, $k_p = (q_p\pi)/L$ the probe field wavenumber expressed in terms of the longitudinal mode number of the probe field, q_p, and the spatially varying effective detuning is found using eq. (6.6) as

$$\Delta(z) = \Delta_p + \Delta_{S,0} \sin^2(k_l z) \ . \tag{6.9}$$

The effect of the Stark shifting lattice field on the probe photon scattering rate (eq. 6.7) is a beating signal arising from the wavenumber difference of the probe and

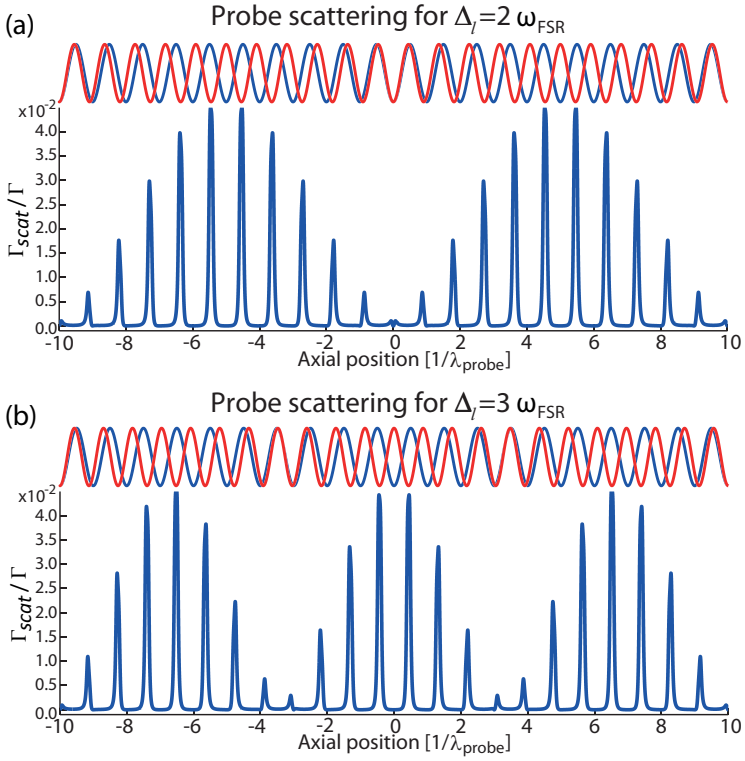

Figure 6.8: Illustration of the beating effect, using the parameters $q_p = 20$ and $q_l = (22,\ 23)$, together with $L = 10\lambda$, $\Gamma = 1$, $\Delta_{S,0} = 10$ and $s_0 = 0.1$. The real values of q_p and q_l in the experiments are around 2.7×10^4. The top part of the figures (sinusoidal curves) shows the probe standing wave (blue) and the effective Stark shifted detuning $\Delta(z)$ (red) along the cavity axis; the two sinusoidal curves in this part of the figure have been rescaled to the same amplitude in order to better illustrate the spatial beating. The lower part of the figures (blue peak structure with a wide envelope) shows the variation of the probe scattering, $\Gamma_{\rm scat}$ (from eq. (6.7)), along the cavity axis, for a lattice detuning of (a) $2\omega_{FSR}$ and (b) $3\omega_{FSR}$.

lattice fields. This is illustrated in fig. 6.8 where the parameters have been chosen to illustrate the effect ($q_p = 20$ and $q_l = 22$ in (a) and $q_l = 23$ in (b)). In the experiment the values of q_p and q_l are around 2.7×10^4. The scattering signal in Γ_{scat} shows a fine peak structure that follows the periodicity of the probe field standing wave, with a wide envelope arising as a consequence of the AC Stark shift of the energy-levels. In our experiment, the imaging system is not able to resolve the fine-structured pattern, as the individual lattice sites are typically separated by only a few hundreds of nm. The beating envelope signal, on the other hand, occurs on a much larger length scale (proportional to the inverse of the probe-lattice wavenumber difference) and can be resolved using standard imaging techniques.

At the center of the cavity ($z = 0$) the beat pattern has an extremum because of the boundary conditions imposed by the mirrors. If the lattice detuning is an even number of free-spectral-ranges (FSR) the scattering rate is minimized, as the probe and lattice fields overlap so that the transition is shifted away from the probe frequency wherever the probe field is strong. The exact shape of the beat signal depends on whether the probe field has an even or odd longitudinal mode number, but the minimum is always at the same position. A lattice detuning by an odd number of FSRs produces a maximum of the scattering rate, as the probe field is strongest where the transition is unshifted. This is illustrated in top part of fig. 6.8(a)-(b) as a sketch of the probe standing wave (blue) and the effective AC Stark shifted detuning $\Delta(z)$ of eq. (6.9) (red), along the cavity axis. From this, the beating between the two standing waves can easily be visualized and it is clear that at the center the wave extrema are overlapping.

As mentioned earlier, the two-level description cannot be expected to give a precise account of the measured scattering rates. However, around the center of the Fabry-Perot cavity, the scattering rate will always vary periodically with a spatial period set by the inverse of the probe-lattice wavenumber difference, $\lambda_{beat} \propto 1/(k_l - k_p)$, with a maximum (minimum) for $q_p - q_l$ being odd (even). The length scale of λ_{beat} for our experimental parameters is hundreds of μm.

With an exact knowledge of the center position of an applied optical cavity one can deterministically switch between having the atoms at a node or anti-node of the potential, as has e.g. been exploited in some of the experiments reported in [81]. For large atomic ensembles, it could also be interesting to be perform this with respect to a corrugated super-lattice created through the interference of two cavity modes.

6.2.3 Experimental procedure

The setup used in this experiment is described in detail in chap. 5. We load a large $^{40}Ca^+$ ion Coulomb crystal into the trap, where it is confined within the linear optical cavity. As stated in sec. 5.4 the cavity has a length of 11.7 mm which corresponds to a free spectral range of $\omega_{\text{FSR}} = 2\pi \times 12.7$ GHz, and the TEM_{00} mode waist radius is 37 μm for light at 866 nm. The $4S_{1/2} \leftrightarrow 4P_{1/2}$ transition at 397 nm is used for Doppler cooling and imaging, while the $3D_{3/2} \leftrightarrow 4P_{1/2}$ transition at 866 nm is used either for repumping during cooling or for interactions with the cavity light (corresponding to the two-level situation above). The relevant energy levels and transitions are depicted on fig. 2.2.

As before, the cooling light is applied along the axial (z) direction and the 866 nm

repump light along the radial (x) direction, but now with linear polarization along the z direction (see sec. 5.5). The ions are imaged by collecting the 397 nm fluorescence through the image intensifier and onto the CCD camera (see sec. 5.6.1). The resonant *probe* field and the off-resonant *lattice* field at 866 nm is coupled into the cavity with circular polarization from the PT mirror side. Furthermore, we apply a bias magnetic field of ~ 1 Gauss in the y-direction to ensure that the cavity fields address all four Zeeman sub-levels of the $3D_{3/2}$ state. The cavity length is stabilized by using the 894 nm reference laser, which is itself locked to the external reference cavity. The probe field is also locked to the same external reference cavity, while the lattice field is locked directly to the experimental cavity.

The cavity length is set so that one cavity mode is resonant with the unperturbed atomic transition frequency (i.e. in absence of the lattice field). The experiment is performed by continuous imaging of the ions. As the cavity probe and lattice fields are applied, the 866 nm repump beam is blocked, while keeping the 397 nm cooling laser on. Doing so, all repuming in the cooling cycle is performed through the cavity fields. Hence, we detect the 397 nm fluorescence which depends on the repumping rate of the cavity fields, and thus on the scattering rate at 866 nm. The spatially varying saturation parameter of the probe field (eq. (6.8) or (3.36)) has an amplitude of $A_S \approx 4$, while that of the lattice is more than 1000 times smaller. This was chosen in order to obtain a situation where the measured scattering signal primarily comes from the probe field and to ensure that the lattice filed only produces the spatially varying AC Stark shift.

The probe laser is set on atomic resonance ($\Delta_p = 2\pi \times (0 \pm 2)$ MHz), while the lattice Stark shift depends on the lattice field detuning and is in the range $\Delta_S = 2\pi \times (3 - 9)$ MHz. Furthermore, the 397 nm laser is red-detuned by 40 MHz to ensure that the Stark shift does not affect its scattering rate substantially and thus, that the observed fluorescence modulation is dominated by the variation in the probe repumping rate out of the $3D_{3/2}$ state.

6.2.4 Experimental results

In the experiment we used an ion Coulomb crystal containing ~ 6000 $^{40}Ca^{+}$ ions, with a length of 650 μm, a diameter of 150 μm and a density of $\sim 6 \times 10^8$ cm^{-3}. In fig. 6.9 projection images of the crystal are shown for lattice detunings of +15FSR and +16FSR, obtained in continuous imaging from 60×200 ms exposures on the CCD with 224×640 pixels. The cavity fundamental mode is clearly visible on the crystal, as only the ions contained within the cavity mode volume fluoresce. This is because only these ions participate in the cooling cycle and thus sympathetically cool the ions outside the cavity mode volume. The top figures show images obtained when applying both the lattice and probe fields and the beating variation is already visible, with a maximum at the cavity center in the first case and a minimum in the second. The middle figures show images with the probe field only, recorded as a reference, and the actual crystal shape is illustrated by the dashed ellipsoids. After background subtraction, making the ratio of the image with and without the lattice allows for correcting for inhomogeneities in the imaging system and thus isolates the fluorescence modulation pattern due to the lattice. The result of this correction is shown on the bottom image of fig. 6.9.

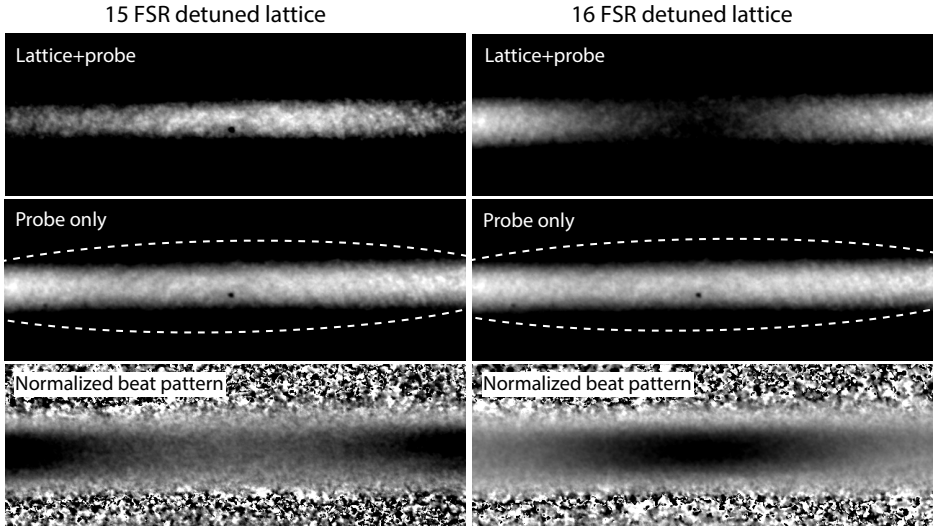

Figure 6.9: Experimental images of a $^{40}Ca^{+}$ ion Coulomb crystal with ≈ 6000 ions. Repumping during cooling is only performed by intracavity fields and, thus, only the crystal part contained in the cavity mode-volume is visible. The dashed ellipsoids outline the actual crystal shape. The top images show the ion scattering signal when applying both the probe and lattice fields, the latter being detuned by +15FSR or +16FSR, respectively. After background subtraction, making the pixel-to-pixel ratio of the top and middle (probe only) images gives the bottom image, thus isolating the fluorescence beat pattern due to the lattice field.

We perform a running average across the beat pattern image by setting the single pixel value equal to the mean of pixel values in a 10×10 square around it. By doing so, unevenness in the crystal structure (from e.g. the shell structures) will be blurred enough to smoothen the beating signal along the axial direction. We isolate the central part of the crystal in the axial direction, and sum 37 pixels (33 μm) in the vertical direction all the way along the crystal length. The resulting signal is a single curve that represents the axial beat pattern variation. On fig. 6.10 the modulated signals are shown for four different lattice field detunings: 15 FSR (blue), 16 FSR (red), 27 FSR (dashed blue) and 28 FSR (dashed red), respectively. As expected, for a lattice field detuned by an even number of FSRs from the probe field (here, 16 and 28), the fluorescence is suppressed at the cavity center and the envelope beating has a minimum. For a detuning by an odd number of FSRs (here, 15 and 27) the suppression occurs half a period away from the cavity center, while the center position shows a maximum in fluorescence.

The theoretical model introduced in sec. 6.2.2 was based on a simple two-level system, but the actual experimental system is much more complicated, as it includes in general 8 levels (all Zeeman levels), and the envelope of the beat pattern is not given by a simple analytical function. The model was meant as an illustrative picture, and in stead of fitting the full beat pattern to a numerical model, we fit the points around the center of the cavity with a parabolic function in order to establish the

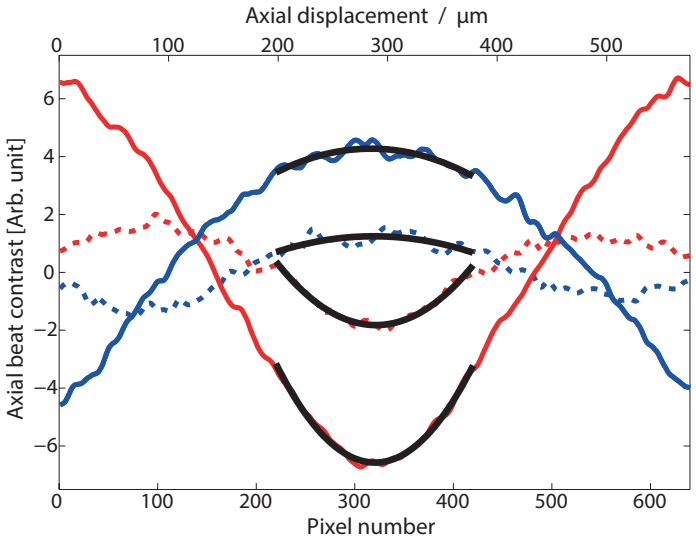

Figure 6.10: The resulting beating signals along the axis of the ion crystal. Depending on the lattice detuning from the probe the beating signal changes and this is shown for four different detunings: 15 FSR (full blue), 16 FSR (full red), 27 FSR (dashed blue), 28 FSR (dashed red). At the center of the cavity maxima and minima line up, as expected. The black parabolic fit is performed on ±100 pixels around the center.

exact cavity center position which is all we care about in this study.

The purely parabolic fits are performed including ±100 pixels around the approximate cavity center position (shown on fig. 6.10 as black lines). From these, we can determine the cavity center to be at an axial position of 320.70 ± 0.15 pixels. Considering the individual measurements, they agree with the mean value within $+1.5$ and -2.5 pixels and their errorbars are within range of the mean. The resolution of our imaging system onto the CCD is 0.9 $^{\mu m}/_{\text{pixel}}$ and hence, the fit results can be converted into a physical length. The uncertainty in the absolute positioning of the cavity center is thus of only ±135 nm. This is smaller than both the beating periods (here 400-700 μm) and the periodicity of the two standing waves (433 nm). An even better precision could be obtained in principle by using more sets of detunings, all of which should give beat patterns with an extremum at cavity center.

6.2.5 Discussion and outlook

The experimental study, described in this section, has demonstrated a simple method to accurately find the absolute center of a linear cavity using a spatially modulated fluorescence signal from an ion crystal, by probing it with two simultaneously resonating cavity fields. The measurements are based on the beating signal that arises when one of the fields (lattice) is detuned by a number of cavity free spectral ranges from the other field (probe) which is on atomic resonance. Constructing a beat pattern with only one or a few cycles within the length of the cavity can give precise position information, but does not provide a large position resolution because of the coarse

spatial structure. On the other hand, beat patterns containing many cycles within the cavity length, obtained using a far-detuned lattice field, will provide a fine resolution, but can not distinguish between positions separated by a whole number of beat periods. By combining beat patterns for several different lattice detunings, we can obtain more precise location information anywhere in the cavity without losing track of the overall position. For example, for the set of beat patterns shown in fig. 6.10, all maxima and minima line up at the cavity center, as they must. Since e.g. 15 and 28 are coprime, there is only one such location over the entire length of the cavity. Including even more beat patterns for additional detunings should further improve the precision with which we determine the cavity center position.

From the beat pattern in fig. 6.10 it is obvious that the curvature for a maximum is much wider than for a minimum, at the center position. Extending the beat patterns further, reveals that this pattern of a narrow minimum and a wide maximum continues. Performing numerical plots of our model (eq. (6.7)-(6.9)) with the real physical parameters, shows a huge amount of small peaks which together form an envelope shape qualitatively comparable to the experimental beating shape. Our model only includes two levels while the physical situation is much more complex and includes 8 levels, where e.g. the repumping process will depend on the exact laser polarization and the chosen magnetic field strength. Accordingly, the simple numerical fits will not precisely match the data, and hence, to just obtain the cavity center position, we use the parabolic shaped fits shown above. In the figure presenting the results (6.10) the amplitude of the beat pattern is given in arbitrary units, as all we care about is calibrating the horizontal axis. In order to construct a complete model and use numeric fits to the data, a careful calibration of the vertical axis would also be needed.

This method of determining the positioning of single ions or ensembles of ions with respect to the center of a linear Fabry-Pérot cavity has potential applications to a wide range of cavity QED investigations with cold ions or atoms. As mentioned, it is essential for studies of trapping ions in localized optical fields [80–82] where precise control of the ion position relative to the cavity standing wave field is crucial (see chap. 7). Localizing an ion in a standing wave cavity field also allows for a better control of the ion-cavity coupling strength, which can become important in order to increase the efficiency of a quantum memory for light using our ion-cavity based system. Additionally, this positioning technique will also be applicable to e.g. cold neutral atomic species, trapped in magnetic or optical dipole traps, and interacting with a cavity field mode. The accurate positioning would in particular be beneficial in single atom quantum dynamics studies [86–88], e.g. examining cavity cooling [184, 185]. It will also apply to cavity QED studies with ensembles, e.g. investigations of the quantum dynamics of cold atoms in cavity-generated optical potentials [89] or the simultaneous interaction with multiple standing wave fields [90].

Chapter 7

Localizing atomic ions in an intracavity standing wave field

In this chapter we will describe how an intracavity standing wave optical potential can be used to localize ions situated in the center of a cavity ion trap. The ions are, at all times, trapped in the shallow potential from the linear Paul trap, but as the far detuned intracavity optical lattice field is applied, they can also experience a finer-scale, deep optical potential. For the transitions considered here, the frequency of the lattice field is in the optical regime and this means that the spatial extent of one standing wave period (433 nm) is much smaller than the size of the external trapping potential (∼mm). As the depth of the optical lattice is increased, ions can thus be *localized* on a sub-wavelength scale in this intracavity potential.

The first section (7.1) introduces the mechanism that provides the localizing force on the ions, and puts the experiment in context with related studies. In sec. 7.2 we introduce the theoretical modeling of the system and compare it to molecular dynamics (MD) simulations. Section 7.3 describes the experiment and presents the results on the localization of a single atomic ion in the intracavity standing wave field. In the last section (7.4) we describe how ions in small Coulomb crystals with different structural configurations can be localized in the standing wave optical potential at the same time.

7.1 Introduction

Trapping *neutral* atoms in optical potentials (dipole traps, optical lattices) has been performed routinely for years, resulting in many successful studies within a wide variety of fields [186–190]. The confining mechanism provided by an optical dipole force for trapping atoms was proposed by Letokhov in 1968 [191], but a more detailed theoretical background of dipole forces was not developed until 1980 [192]. In 1986 Chu et al. accomplished the first optical trapping of neutral atoms [91] and in 1999 single atoms were trapped optically [92]. The typical depth of optical traps for neutral atoms is on the order of 10^{-3} K, while charged particles can be trapped by electrical fields, as described in sec. 2.1, which can reach depths of the order of 10^5 K. Thus, for ion trapping the use of optical trapping potentials may seem superfluous, but special

interaction conditions can be generated between the ions by including both potentials, which has lately attracted a lot of attention.

In 2010 Schneider et. al. [94] showed that is was also possible to optically trap a single ion by using a far detuned dipole field in a focal region of size $\sim 30\ \mu$m. In 2012, in parallel to the experiments reported here, this experiment was improved to achieve optical trapping of ions in a standing wave field, produced by two counter-propagating beams with individual polarization control [80]. In both cases, the deep RF-trapping potential was carefully turned off, and the trapping was achieved purely by optical means, resulting in trapping conditions quite, similar to neutral atom dipole traps in terms of both depth and trapping time. In the experiments reported here [81], the detuned dipole field is used to localize the ions in one node or antinode of an intracavity standing wave lattice, while still keeping the RF-trap on (see fig. 7.1). This makes the ions more stable during the measurements, as they can not escape the deep RF-potential, but it also adds some complexity to modeling the dynamics of the system, as well as some experimental requirements on the control of parasitic RF fields. Fundamentally though, it opens possibilities for interesting interactions between ions that are trapped in a sum of two potentials which can be independently altered with respect to each other.

In a simple description neglecting scattering forces, the dipolar force on an atom (or ion) from a far detuned optical lattice field, can be found as the gradient of the lattice potential, which is caused by the AC stark shift of the atomic energy levels [193]:

$$F_{\mathrm{dip}} = -\nabla U(z)\ . \tag{7.1}$$

Coupling an optical field resonantly into a mode of a linear Fabry-Pérot cavity, far from an atomic resonance transition, creates such a standing wave potential, which,

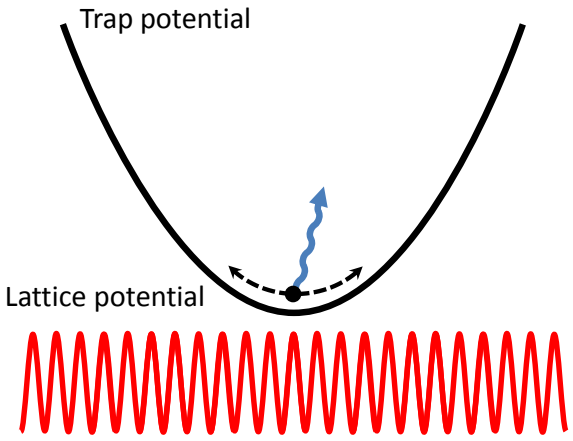

Figure 7.1: A sketch of our implementation of localizing an ion in an optical potential formed by an intra-cavity standing wave field. We trap an ion in a loose RF-trap (ion extent 4-5 μm) and laser-cool it to a thermal equilibrium close to the Doppler limit. A sinusoidal optical potential ($\sin^2(kz)$) is adiabatically turned on and can localize the ion within a fraction of the lattice period (433 nm). We probe the ion position distribution by observing its scattering as function of the lattice depth.

close to the center of the cavity, has the form

$$U(z) = \frac{\Omega_0^2}{\Delta_{\text{lat}}} \sin^2(kz) \ , \tag{7.2}$$

where Ω_0 is the Rabi frequency of the lattice field and Δ_{lat} is its detuning from the atomic transition, k is the field wavenumber and z is the distance to the center of the cavity. As the potential depends on the lattice detuning the sign of the force can be changed. For a red detuned lattice ($\Delta_{\text{lat}} < 0$) the ion will be trapped at an anti-node of the standing wave (maximum intensity) while for a blue detuned lattice ($\Delta_{\text{lat}} > 0$) the ion is trapped at a node of the standing wave (minimum intensity).

Localizing ions in such fine structured optical potentials could make it possible to perform coherent atom-ion studies with both particles in the same trapping potential [83–85]. Additionally, superposing a steep and short-scale periodic optical potential to a shallow RF-trap allows studies of structural [179–181] and dynamical phase transitions (e.g. the Coulomb-Frenkel-Kontorova model [98, 99, 194]). In cavity QED experiments the localization mechanism can also be exploited to control (e.g. enhance or inhibit) the coupling of the ions with another intracavity field (probe), compared to a non-localized situation [81]. This can be of interest for quantum information processing applications, such as single-photon generation [16, 17], quantum memory [28, 68], photon counters [77], single ion-photon interfaces [19, 195], or for cavity-mediated cooling [18].

7.2 Theoretical modelling

In this section we describe a simple analytical model that predicts the energy and position distribution of a *single* ion in the lattice potential (7.2.1). Afterwards, we present molecular dynamics simulations performed on the system with assumptions closely related to the analytical model (7.2.2).

7.2.1 Simple Analytic Models

We consider a classical particle trapped in a one-dimensional harmonic potential of frequency ω_t (corresponding to the axial trapping potential of a linear Paul trap). We assume that the particle is in an initial thermal state with mean energy $k_B T_0$, as the ion is Doppler-cooled to a specific temperature before the lattice is applied in the experiments. Adding an adjustable optical lattice potential of depth U yields the Hamiltonian

$$H = \frac{p^2}{2m} + \frac{m\omega_t^2}{2} z^2 + U \sin^2(kz) \ , \tag{7.3}$$

where z is the particle position, p its momentum, m its mass and $k = 2\pi/\lambda$ is the wavenumber of the light field used to generate the lattice potential, by which λ corresponds to twice the lattice period. Furthermore, we assume that the particle can only perform classical and conservative motion, i.e. it feels no damping forces and no work is done on the particle as the lattice potential is raised adiabatically. Based on these assumptions, we are interested in finding the energy and position distribution of the particle for different lattice depths.

The lattice field is ramped up slowly, in the sense that its rate of increase can be approximated as adiabatic for the dynamics in a single lattice site. We define, $z_{T_0} = \sqrt{k_B T_0/m\omega_t^2}$, as the typical thermal position excursion of the particle in the harmonic potential. The problem can be treated analytically in the two limits:

1. $kz_{T_0} \ll 1$: the initial particle temperature is so low that it is always localized within a single lattice site.

2. $kz_{T_0} \gg 1$: the initial particle temperature is high and causes its position distribution to spread over many lattice sites. Thus, the sinusoidal distortion to the harmonic potential is small compared to the initial thermal energy.

In these cases, we can restrict our analysis to a single lattice site, but obtain results that apply for the complete system. In case 1 this holds because the particles probability distribution is concentrated on a single lattice site from the beginning, while in case 2 this is because all the populated lattice sites behave similarly. We will in the following consider the second case, as this is the one which is relevant to the experimental situation.

Hot ion situation ($kz_{T_0} \gg 1$)

In this case, the particles initial position distribution is spread over many lattice sites and we can consider a single particle in a sinusoidal potential with periodic boundary conditions. We assume that the ion is initially delocalized and ignore the background harmonic potential. We want to evaluate the energy and position distribution of the ion as the lattice is raised and, hence, need to identify a quantity which is conserved during this process. The ion energy is not conserved, as raising the lattice does work on the ion, and neither is the ion temperature, as the ion is isolated and, hence, not in equilibrium with a heat bath. Instead, we use the conservation of the classical action $S = \oint p \, \mathrm{d}z$, which is the area enclosed by the ion's trajectory in phase space. The Hamiltonian (eq. (7.3)) is symmetric in both z and p, and therefore we can calculate the area for a quarter of an oscillation and multiply by 4:

$$\begin{aligned} S &= 4\int_0^{z_{\max}} \sqrt{2m(E - U\sin^2(kz))}\mathrm{d}z \\ &= \frac{2\pi U}{\omega_l}\sigma \ , \end{aligned} \tag{7.4}$$

where a substitution of $z_{\max}$ by $kz_{\max}$ was performed as an intermediate step. $z_{\max}$ is the turning point of the ion motion, which becomes $\pi/2k$ when the ion energy is greater than the lattice depth. E is the total energy of the ion, $\omega_l = \sqrt{2Uk^2/m}$ is the oscillation frequency at the bottom of a lattice well and σ is a dimensionless function, given by

$$\sigma = \frac{4}{\pi} \times \begin{cases} \mathcal{E}(E/U) - \mathcal{K}(E/U)(1 - E/U) & E \le U \ , \\ \sqrt{E/U}\,\mathcal{E}(U/E) & E > U \ , \end{cases} \tag{7.5}$$

where $\mathcal{K}$ and $\mathcal{E}$ are the complete elliptical integrals of the first and second kind, respectively (see app. D). In the limit $E \ll U$ the ion motion is that of a simple

harmonic oscillator and σ reduces to E/U. When $E \gg U$ the ion can be regarded as a free particle, and the trajectory in phase space is a rectangle. In this limit $\sigma = 2\sqrt{E/U}$ and the action reduces to $S = 2\pi |p| /k$. Raising the lattice slowly enough keeps the action conserved and, hence, for any lattice depth U, it is the same as in the initial thermal state case. This means that the action can be described by an appropriately scaled Gaussian distribution at any time. The probability of an ion being on a trajectory, $P(S)$, whose action is within an infinitesimal interval $\mathrm{d}S$, can be found from this Gaussian distribution. This can be turned into an expression for the energy distribution, because we know how to relate action and energy for arbitrary lattice depth U through eq. (7.4). Thus we can predict the energy distribution in the lattice to be

$$\begin{aligned} P(E)\mathrm{d}E &= P(S)\frac{\mathrm{d}S}{\mathrm{d}E}\mathrm{d}E \\ &= \frac{\mathrm{e}^{-\sigma^2\frac{U}{4k_BT_0}}}{\sqrt{\pi k_B T_0/U}}\tau\frac{\mathrm{d}E}{U} \ , \end{aligned} \tag{7.6}$$

where

$$\tau = \frac{\mathrm{d}\sigma}{\mathrm{d}(E/U)} = \frac{2}{\pi} \times \begin{cases} \mathcal{K}(E/U) & E \leq U \ , \\ \sqrt{\frac{U}{E}}\mathcal{K}(U/E) & E > U \ . \end{cases} \tag{7.7}$$

We note here that this distribution has an integrable singularity at $E = U$, which we will discuss later. From τ we can define the period of the ion orbit as

$$\begin{aligned} T &= \oint \mathrm{d}t = \oint \frac{\mathrm{d}z}{\mathrm{d}z/\mathrm{d}t} \\ &= 4\int_0^{z_{\max}} \sqrt{\frac{m}{2(E - U\sin^2(kz))}}\mathrm{d}z = \frac{2\pi}{\omega_l}\tau \ . \end{aligned} \tag{7.8}$$

Using this period, we can find the ion position distribution for a given total energy as

$$\begin{aligned} P(kz|E)\mathrm{d}(kz) &= \int_0^T \delta(kz - kz'(t))\frac{\mathrm{d}t}{T}\mathrm{d}(kz) = \frac{2}{T}\frac{\mathrm{d}(kz)}{\mathrm{d}(kz)/\mathrm{d}t} \\ &= \frac{\mathrm{d}(kz)}{\pi\tau\sqrt{E/U - \sin^2(kz)}} \ . \end{aligned} \tag{7.9}$$

This expression is only valid for $\sin^2(kz) < E/U$, otherwise the probability is zero. The average position distribution, which is of importance for the experimental study, can be found as an energy integral over the conditional position distribution just derived and the energy distribution found earlier (eq. (7.6)) as

$$P(kz)\mathrm{d}(kz) = \int_{U\sin^2(kz)}^{\infty} P(E)P(kz|E)\ \mathrm{d}E\ \mathrm{d}(kz) \ . \tag{7.10}$$

This integral can not readily be solved analytically. We therefore perform a numerical evaluation to some arbitrary precision when applying the model to the measured data.

The experimental situation

For typical experimental parameters $kz_{T_0} \sim 4$ and we are not strictly speaking in any of the limits introduced above. Nevertheless, the second limit ($kz_{T_0} \gg 1$) provides energy and position distributions close to what we believe fits our system. To test this conjecture we compare our model with MD simulation results, which we will describe in the next section.

By ignoring the background harmonic potential, we have made two assumptions. First, we assume that the harmonic potential does not appreciably distort the ions trajectory within a single lattice well. This means that the change in background potential over a lattice needs to be much less that the thermal energy, which is the case if the initial thermal fluctuations in the ions position is large compared to the lattice period. Secondly, we assume that the energy distribution for an ion at a given site is unaffected by the possibility for the ion to travel to or from another site with a different background potential. This can be understood as a balance condition, stating that there must be no net flow of ions of any given energy between lattice sites.

7.2.2 Numerical simulations

In order to make sure that our theoretical model could actually predict the ion energy and position distribution in the relevant experimental conditions, numerical MD simulations were performed by Mathieu Marciante[1]. The simulations were carried out using molecular dynamics by describing the ion as a classical particle in an initially harmonic pseudo potential (similar to our trap potential) and ramping the lattice potential to a certain optical depth. Afterwards, the ion trajectories were recorded for a large number of time-steps, from which the ion position and energy distributions could be obtained. Varying different experimental parameters (final lattice depth, ramp time, initial ion temperature ect.) we could simulate the system under several conditions and compare this to the simple analytical model introduced above.

In order to test our adiabatic lattice potential ramp model, the simulations in fig. 7.2 show the kinetic energy of the ion in the lattice potential as function of the lattice depth. These simulations builds on a single one-dimensional ion, initially trapped in a harmonic trap with frequency 490 kHz, which is subject to a lattice ramp linear in Rabi frequency (corresponding to its intensity varying as t^2). The lattice is ramped adiabatically with speed 4.7 mK/μs^2 to a certain depth, and the kinetic energy of the ion is determined for different initial velocities and positions of the ion. On fig. 7.2 the results of the simulation performed for ions with initial temperatures of 0.5 mK (red), 1 mK (blue), 2 mK (green), 4 mK (black) and 8 mK (cyan) are shown together with the model prediction. Note that the plot is double-logarithmic and that the final kinetic energy and the lattice depth after ramp-up are both scaled with the initial temperature, in order to better compare the five different cases. Good agreement is found, and this gives evidence that our model can be used to describe the experimental system in the adiabatic regime.

[1] From Aix-Marseille University in Marseille, France

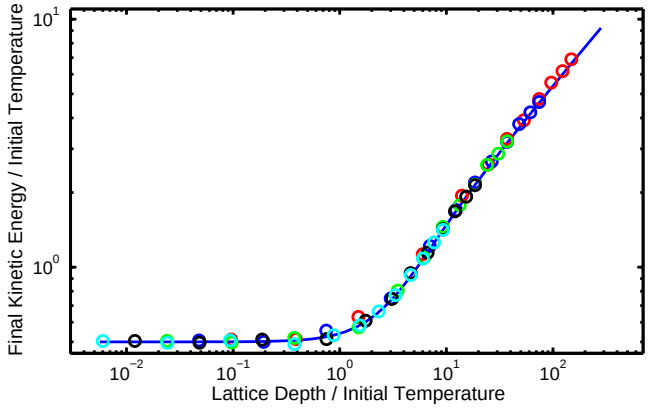

Figure 7.2: Results of molecular dynamics simulations showing the final kinetic energy of an ion in an optical lattice potential of different depths. The harmonic trap frequency is 490 kHz. The lattice potential is ramped up adiabatically (4.7 mK/μs^2) and the simulations are performed for various initial ion temperatures: 0.5 mK (red), 1 mK (blue), 2 mK (green), 4 mK (black) and 8 mK (cyan). The solid line is the no-free-parameter prediction from the analytical model of the prior section.

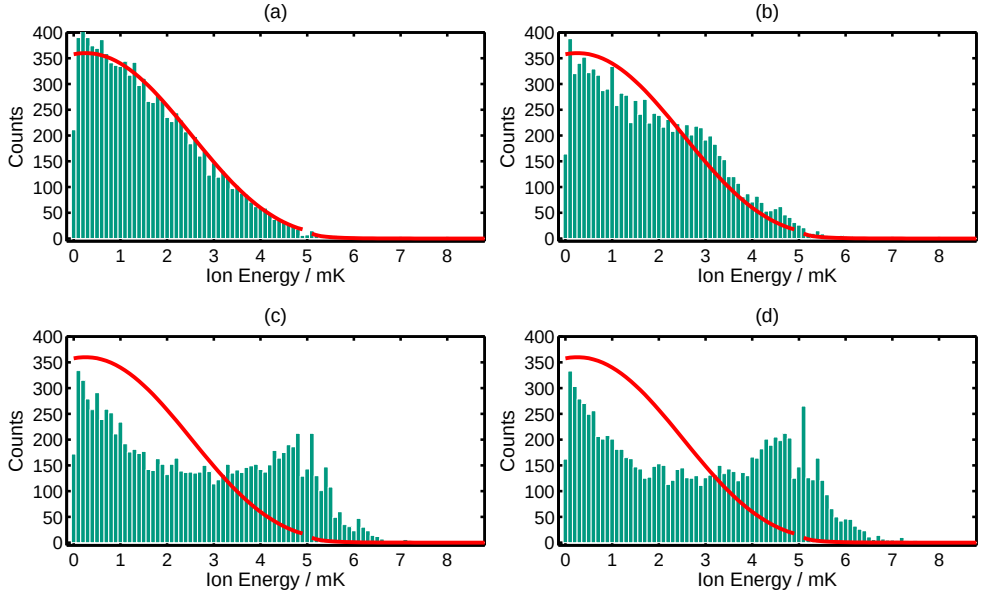

Figure 7.3: Simulations of the final energy distribution of an ion which is subject to a lattice potential ramped at different speeds. The initial ion temperature is 0.5 mK and the lattice potential is ramped to a depth of 5 mK with the ramp speeds: (a) 0.05 mK/μs^2, (b) 4.7 mK/μs^2, (c) 118 mK/μs^2, (d) 1890 mK/μs^2. The red curve shows the results of the analytical model introduced in sec. 7.2.1.

Next, we tested the limit of the adiabatic assumption and performed numerical simulations of the dynamics of a single ion subjected to a 5 mK deep lattice which was ramped up at various rates. The results could then be compared to those given by the single-site adiabatic model described above. In the simulations the initial temperature was set to 0.5 mK, the harmonic trap frequency was 78 kHz (comparable to the experimental value), the lattice field had a detuning of 63.5 GHz, and the lattice ramp was still assumed to be linear in Rabi frequency. The most significant test is to compare the final energy distribution of the ion, which becomes non-thermal in the lattice. The simulated energy distribution was obtained from 10000 simulation runs, each yielding a total energy of the ion after lattice ramp-up. Fig. 7.3 shows histograms of this final energy for different rates of lattice ramp-up. The four different ramp speeds are: (a) 0.05 mK/μs^2, (b) 4.7 mK/μs^2, (c) 118 mK/μs^2, (d) 1890 mK/μs^2. In the experiments, we typically use a 2 μs ramp and, as the lattice is ramped linearly in Rabi frequency to a size corresponding to the 5 mK lattice depth, the ramp speed is typically 1.25 mK/μs^2. The red curve in fig. 7.3 shows the model prediction described from the prior section, and we see that for the 0.05 mK/μs^2 ramp the agreement with the model is excellent. For faster ramp speeds the energy distribution becomes distorted, as the ions placed close to an anti-node are lifted up by the potential (5 mK depth) before they have time to adjust their orbit and fall into the lattice well. In the analytical model the singularity in energy ($E = U$) is seen as a hole in the red curve at the lattice depth, 5 mK. In order to fulfill the adiabaticity criterion, one needs to operate in the regime between fig. 7.3(a) and 7.3(b) or even slower.

The last simulations presented here apply directly to the parameters used in the single-ion localization experiments. The initial temperature of the ion is set to 5 mK, which is more realistic than the prior choice, and the harmonic trap frequency is taken to be 88 kHz. The lattice potential in this simulation has a final depth of 24 mK, corresponding to one of the highest values obtained in the single-ion experiments. The lattice ramp is no longer assumed to rise as t^2 in intensity (linear in Rabi frequency), but rather like $t^{1.4}$. This was inspired by the measurement of the temporal profile of the ramp used to produce the lattice potential, which is primarily dominated by the response time of the acousto-optic modulator (AOM) used to switch the lattice field on.

Fig. 7.4(a) shows the total energy distribution (green) and the lattice potential distribution (red). The circles represent the results of a histogram obtained from the simulations while the lines show the analytical model prediction. The vertical dashed line represents the top of the lattice where both the simulations and the model predict a peak in probability, as some ions can still get pushed by the lattice when it ramps up, and this increases their energy. The energy distribution (green) to the left of this point represents ions that are localized in a lattice well, while the right side shows the distribution of ions that have enough energy to pass the lattice wells. Note that the vertical axis is logarithmic. In fig. 7.4(b) the ion position distribution is shown in the initial thermal case (red) and in the final localized case (green). The circles show results from the numerical simulations while the lines give the expected analytical shapes in the two situations. This illustrates the nature of the localization process, and we remark that the global uncertainty in the ion position distribution remains as large in the final stage as in the initial (Gaussian). However, after the lattice is ramped, the ion has a high probability of being localized in a certain lattice well in

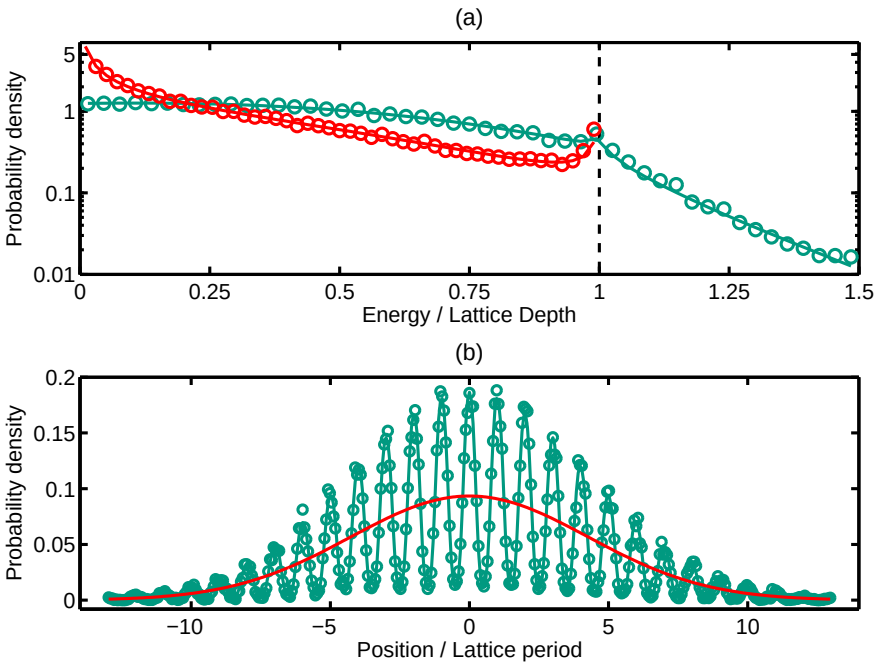

Figure 7.4: The analytical model (lines) is compared to simulations (circles) with typical experimental parameters (5 mK initial temperature and a 24 mK final lattice depth). (a) Probability distribution of the total energy (green) and lattice potential (red) relative to the lattice depth, on a semilogarithmic scale. (b) Initial thermal position distribution (red Gaussian) and final position distribution in the lattice (green).

each experimental realization, as there is a great difference in probability between a lattice well (up to 0.2) and a lattice top (typically 0.01). All the distributions shown in fig. 7.4 show an excellent agreement between the molecular dynamics simulated results, which include a finite lattice ramp time and a harmonic background potential, and our analytical model, which neglects these. This supports our assumptions and confirms that, with the tested experimental properties, the single-site analytical model assuming adiabatic ramping of the lattice indeed describes well the essential physics of the experiment.

7.3 Single-ion localization experiments

In this section we describe the experiments demonstrating the localization of a single atomic ion in an intracavity standing wave lattice. In the first part (sec. 7.3.1) we introduce the fluorescence measurements that are used to infer the localization, and which build on the analytical model described earlier. In sec. 7.3.2 the experimental setup and procedure is described including the temporal sequence used. After having described an absolute calibration method for the measured fluorescence signals (sec. 7.3.3), the experimental results are presented in sec. 7.3.4. In sec. 7.3.5 we describe how the excess micromotion can be measured and minimized, so as not to impede the localization mechanism, before we conclude in sec. 7.3.6.

7.3.1 Measuring the localization using scattering

Experimentally, we can not directly observe the full energy distribution nor the sub-wavelength features of the position distribution, as the length scale on which the localization occurs (less than half a wavelength of the lattice field) is less than our imaging resolution. Instead, we detect the scattering of the ion from the lattice, which depends on the potential energy of the ion. At every time during the lattice ramp we know the expected position distribution of the ion from the analytical model of sec. 7.2.1. For each ion position the intensity of the lattice field can be found and, from this, we can calculate a time- and position-dependent scattering rate.

To get a measure of the localization, we can compare the photon scattering probability for red- and blue-detuned lattices (as introduced in sec. 7.1). These generate identical potentials, but a red-detuned ($\Delta_{\mathrm{lat}} < 0$) lattice localizes the ion at lattice anti-nodes, which increases the scattering, while a blue-detuned ($\Delta_{\mathrm{lat}} > 0$) lattice localizes the ion at the nodes, where scattering is suppressed. The difference in scattering between the two situations can then be seen as a signature of ion localization. This is illustrated on fig. 7.5(a) where the two lattice detunings are shown in a simple two-level picture and a scattering event takes the ion from the excited state out of the two-level system.

As a second measure, a near-resonant probe field is applied in order to infer the position distribution of the ion. This is illustrated on fig. 7.5(b). Because of the boundary conditions imposed by the cavity mirrors, we know the standing wave structure of both fields at the ion location at the center of the cavity (see also sec. 6.2). Let us assume that the lattice field is blue detuned from atomic resonance. When the frequency separation between the lattice and the probe fields is an even number of cavity free spectral ranges, their standing waves overlap. In this case, localization of the ion close to a node of the lattice field suppresses the resulting scattering from both fields in the same way. When the lattice field is detuned by an odd number of free spectral ranges, the nodes of the probe field align with the anti-nodes of the lattice field and the scattering rate from the probe field is enhanced, as the ion sees a high probe intensity. Measuring the difference in scattering for the two scenarios can give information on the enhanced or inhibited coupling to the probe field as compared to the situation without lattice, in which the ion can move freely and effectively has on average half the maximum coupling strength with the probe field.

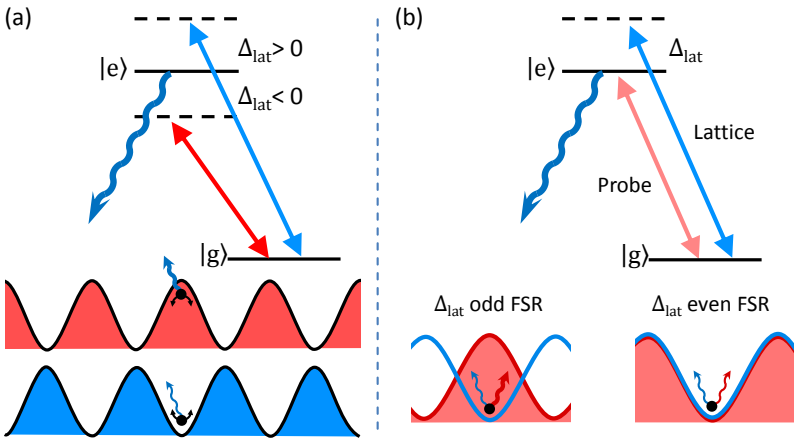

Figure 7.5: (a) A standing wave lattice field is applied detuned to the red or the blue of an atomic transition of the ion and a scattering process can occur through the excited state. The lower illustrations show the lattice field intensity pattern and indicates the difference between a red-detuned lattice ($\Delta_{\text{lat}} < 0$), from which the ion localizes at anti-nodes (high scattering) and a blue-detuned lattice ($\Delta_{\text{lat}} > 0$), localizing the ion at nodes (low scattering). (b) A near-resonant standing wave probe field is applied to the atomic system together with a far detuned standing wave lattice field (here blue detuned), and they are resonant with different longitudinal modes of the cavity. Lower illustration: lattice potential (blue curve), probe field (red shaded curve). When the detuning between the fields is an odd number of cavity FSRs the ion has a high probability to scatter from the probe field whose intensity is high at the ion's position, whereas for a detuning corresponding to an even number of FSRs the ion sees almost no probe light and has a low probability to scatter.

The optical transition, on which the lattice potential is applied, is the $3D_{3/2} \leftrightarrow 4P_{1/2}$ in $^{40}Ca^{+}$ (see fig. 7.6(a)). The scattering that we are able to measure with our imaging system is provided by 397 nm photons produced when the ion decays to the ground state, $4S_{1/2}$ (see details later in sec. 7.3.2). The expected scattering on this transition for our system is given by the product of the decay rate of the 397 nm transition, Γ_{397}, and the excited state population in steady state, Π^e. By looking at the steady state solutions for the optical Bloch equations we can obtain Π^e (see eq. (3.35)-(3.37)). We will consider the scattering from the probe standing wave field when the ion is localized by the lattice field, $\Gamma_{sc,p}$, and from the lattice standing wave directly, $\Gamma_{sc,l}$. With the spatial variation of the fields these can be written as

$$\Gamma_{sc,l}(z,t) = \Gamma_{397} \frac{(g_l(t)\sin(kz))^2}{\frac{\Gamma_{P_{1/2}}^2}{4} + 2(g_l(t)\sin(kz))^2 + \Delta_l^2}\,, \tag{7.11}$$

$$\Gamma_{sc,p}(z,t) = \Gamma_{397} \frac{(g_p\sin(kz+\delta_{lp}))^2}{\frac{\Gamma_{P_{1/2}}^2}{4} + 2(g_p\sin(kz+\delta_{lp}))^2 + (\Delta_p + 2V_L(z,t))^2}\,, \tag{7.12}$$

where $\Gamma_{P_{1/2}}$ is the total decay rate out of the $4P_{1/2}$ state, $g_l(t)$ (g_p) is the coupling strength between the ion and the lattice (probe) field and δ_{lp} can be 0 or π depending on whether the lattice field is detuned by an even or an odd number of FSRs from

the probe, respectively. Δ_p is the detuning of the probe field from atomic resonance (which is much smaller than a cavity FSR), while Δ_l is the detuning of the lattice field (typically several cavity FSRs). The time and space dependent lattice potential is defined as: $V_L(z,t) = U(t)\sin^2(kz)$, and is included in the probe scattering as a result of the ground and excited states being Stark shifted by the strong lattice field. Note that U is *positive* for a blue detuned lattice and *negative* for a red detuned lattice. The lattice coupling strength and depth have explicit time dependence because we ramp the lattice adiabatically, and during this time the scattering process has an increasing rate.

At every moment during the lattice ramp process we have a position distribution for the ion from the analytical model described in sec. 7.2.1. Using eq. (7.10) we can average the position distribution over the time- and position-dependent scattering rate of the two fields and, hence, get the scattering rate as a function of time only:

$$\langle \Gamma_{sc,i} \rangle (t) = \int_{-\infty}^{\infty} P(z,t)\ \Gamma_{sc,i}(z,t)\ \mathrm{d}z \qquad \text{where } i = p, l \tag{7.13}$$

where the time dependence in the position distribution, $P(z,t)\mathrm{d}z$ again comes from the variation in lattice depth, $U(t)$. As the oscillation frequency of the ion in the lattice is fast compared to the ramp (requirement for adiabaticity), it is a good approximation to assume that the ion sees the average scattering rate for its position distribution throughout the whole ramp.

The scattering that we measure in the experiments is the probability for the ion to leave its initial state, while being subject to a certain field strength. At every moment during this process, we will define the rate for the ion to leave the initial state $L(t)$ (see fig. 7.6(b)). First, we consider the situation of the lattice being ramped up and

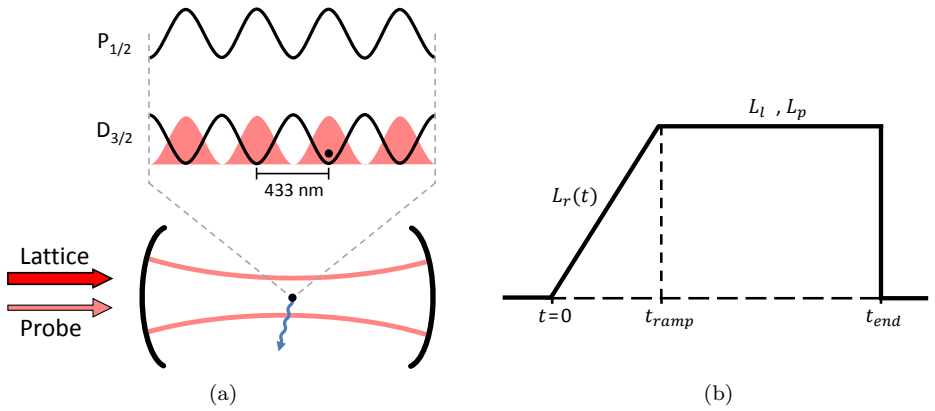

Figure 7.6: (a) Schematic of the main concepts of the experiment. A $^{40}Ca^{+}$ ion is trapped at the center of the cavity and is subject to a lattice standing wave field on the $D_{3/2} - P_{1/2}$ transition. A near-detuned probe field can probe the ion position distribution (shading). The 397 nm fluorescence from the scattering off the lattice or probe fields is measured (wavy arrow). (b) Sketch of the lattice field intensity. During the ramp-time t_{ramp} the leaving rate of the ion ($L_r(t)$) is time-dependent, while it is constant during the interval where the lattice intensity is held high (L_l or L_p depending on the experiment).

hence the "leaving" rate equals the position-averaged scattering rate of the lattice field: $L_r(t) = \langle \Gamma_{sc,l} \rangle (t)$. The probability for the ion to be in the initial state is $P(t)$ and we assume that $P(t=0) = 1$. When ramping the lattice $P(t)$ will decay as

$$\frac{\mathrm{d}P(t)}{\mathrm{d}t} = -L_r(t)P(t) \ . \tag{7.14}$$

Here we neglect the scattering back into the initial state which means that, once the ion has left the initial state, nothing more happens. We can define the integrated leaving rate after a time t, as: $S(t) = \int_0^t L(t')\mathrm{d}t'$. In terms of $S_r(t)$ the differential equation for $P(t)$ has the form

$$\frac{\mathrm{d}P(t)}{\mathrm{d}S_r(t)} = -P(t) \ , \tag{7.15}$$

the solution of which is

$$P(t) = P(0)\ \exp\left(-S_r(t)\right) = P(0)\ \exp\left(-\int_0^t L_r(t')\mathrm{d}t'\right) \ . \tag{7.16}$$

After the lattice ramp has ended, the population left in the initial state is $P(t_{ramp})$, where t_{ramp} is total length of the ramp (see fig. 7.6(b)). In eq. (7.16) the decay rate increases in time because the lattice field intensity is increased and, as the population does not have a simple analytical form, we handle the calculations numerically.

Secondly, after the ramping, the intensity of the standing wave fields are kept high for some time, during which we measure the scattering signal. This implies that the leaving rate is constant in time and, in experiments with the lattice only, $L_l = \langle \Gamma_{sc,l} \rangle$, while, in experiments with both the lattice and the probe fields, $L_p = \langle \Gamma_{sc,l} \rangle + \langle \Gamma_{sc,p} \rangle$.

What we indirectly detect in the experiments is the probability of the ion to leave the initial state (to scatter) in the time between the end of the ramp (t_{ramp}) and the end of our measurement (t_{end}). This can be found as

$$\begin{aligned} P_{measure} &= P(t_{ramp}) - P(t_{end}) \\ &= P(0)\ \exp\left(-S(t_{ramp})\right) - P(0)\ \exp\left(-S(t_{end})\right) \\ &= P(0)\ \exp\left(-\int_0^{t_{ramp}} L_r(t')\mathrm{d}t'\right)\left[1 - \exp\left(-L_i(t_{end} - t_{ramp})\right)\right] \ , \end{aligned} \tag{7.17}$$

where $i = l, p$ depending on what experiment we are performing.

As mentioned above, the initial state of the $^{40}Ca^+$ ion is the $3D_{3/2}$. When the ion sees the applied standing wave fields, the dominant scattering process is inelastic scattering to the $4S_{1/2}$ level (93% probability) emitting a 397 nm photon. In the experiments this background-free fluorescence signal can be observed with shot-noise-limited resolution by the image-intensified CCD camera. The efficiency of the detection system ($\sim 10^{-4}$) together with the 397 nm scattering probability needs to be taken into account in eq. (7.17) to obtain the correct expected fluorescence signal. Furthermore, in the next section we introduce further corrections due to the multi-level structure of the transitions when the different Zeeman substates are taken into account.

7.3.2 Experimental setup and sequence timing

In the experiment we trap a single $^{40}Ca^{+}$ ion in the linear Paul trap with radial and axial trapping frequencies of 377 and 97 kHz, respectively. The ion is placed at the absolute center of the cavity using the method of sec. 6.2 and an applied magnetic field ($\sim$ 1 G) splits the Zeeman sub-levels of the atomic states (see fig 7.7 (a)). A description of the experimental sequence is illustrated in fig. 7.7 (b)

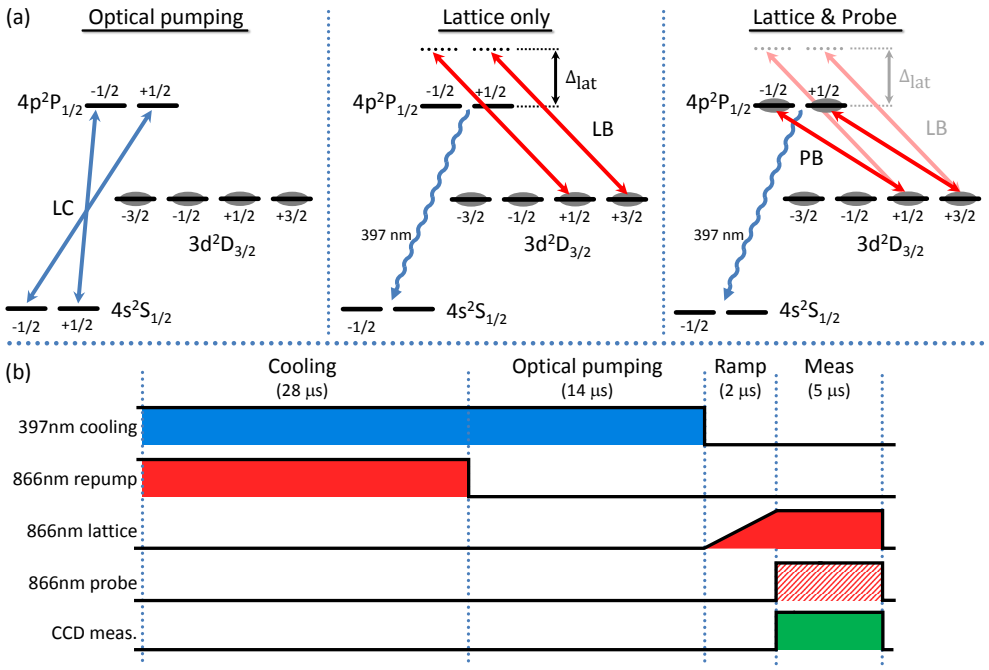

Figure 7.7: The laser sequence used in the experiments of localizing a single ion in an intracavity standing wave field. (a) shows the relevant energy levels of $^{40}Ca^{+}$ including the addressed transitions in the three parts: optical pumping, applying the lattice field only and applying both the lattice and the probe fields. Furthermore, the sequence contains a cooling part for which the energy levels can be found on fig. 6.1 (a). The acronyms are: laser cooling beam (LC), standing wave lattice beam (LB), standing wave probe beam (PB). The gray shading indicates the ion population in the specific sequence part. In (b) the schematics of the experimental sequence is shown, indicating the on and off timing of each laser and the measurement with the CCD camera. The probe beam is shaded, to indicate that it is only used in some of the measurements.

Doppler cooling The first part (28 μs) consists in Doppler cooling as described earlier (see e.g. 2.2.1 or 6.1.2). Two 397 nm laser beams (LC), applied along the longitudinal trap axis with circular polarizations, cools the ion on the $4S_{1/2} \leftrightarrow 4P_{1/2}$ transitions while an 866 nm repumper beam (RP), sent from the side of the trap axis (x) with a linear polarization (along y), returns any population lost to the $3D_{3/2}$ states. This scheme is shown on fig. 6.1 (a).

Optical pumping The second part (14 μs) is an optical pumping stage, where only the 397 nm cooling laser is present (see fig. 7.7 (a) left). From the spontaneous emission of the $4P_{1/2}$ states to $3D_{3/2}$ states, all the population is transferred into the four Zeeman sub levels of the $3D_{3/2}$ state, with roughly equal populations in each, and hence, the ion is in a statistical mixture of the 4 Zeeman substates before ramping up the lattice potential.

Lattice ramping The third part (2 μs) is where the far detuned 866 nm lattice field is applied (see fig. 7.7 (a) middle). This creates a standing wave optical potential with a period of 433 nm (see fig. 7.6(a)). The $D_{3/2}$ and $P_{1/2}$ energy levels gets a position dependence because of the AC Stark effect imposed by the strong lattice field, as shown on the figure. We ramp up the magnitude to the chosen level while keeping the ramp time constant. This time should be long enough for the temperature to evolve roughly adiabatically and to avoid unnecessary heating of the ion, which will be discussed later. The lattice beam, with the detuning Δ_{lat}, is resonantly coupled into the cavity trough the PT mirror, and is σ^- circularly-polarized. The exact ramp-shape was found by analyzing the optical lattice signal and it grows like $t^{1.4}$, as seen on fig. 7.9. Its shape is primarily affected by the response time of the acousto-optic modulator (AOM) used to switch the lattice field on.

Measuring the fluorescence The fourth part (5 μs) is where the system is probed. After ramp-up we can perform two different scattering measurements. By only having the optical lattice present (fig. 7.7 (a) middle) we measure the scattering from this field, and using our theoretical model, we can predict the measured level of localization. By adding an 866 nm *probe* standing wave field (shown as a shading on fig. 7.6(a)) we can measure the combined scattering from the probe and the lattice, which gives us additional information about the ion's position distribution and the ion-probe field coupling strength. The probe is near-detuned from the bare $3D_{3/2} \leftrightarrow 4P_{1/2}$ transition and is also σ^- circularly-polarized (fig. 7.7 (a) right). In either case, some population from the $m_j = +1/2$ and $m_j = +3/2$ sub-levels of $3D_{3/2}$ will be excited to the $4P_{1/2}$ sub-levels from which there is a $\sim 11/12$ probability of decaying to the $4S_{1/2}$ state, emitting one 397 nm photon. We measure the scattering by detecting these photons with the CCD camera, so only ions ending up in the $4S_{1/2}$ states are detected. The timing of the CCD camera is controlled using the image intensifier, which can be shut on and off on a timescale < 100 ns.

The total sequence runs for 50 μs, but we have to expose the camera for 30×10 s to collect enough statistics (i.e. in total 6×10^6 sequence repetitions). On an averaged image the total scattering signal can now be found by taking the mean pixel number within a box containing the whole ion spot (see fig. 7.8). The size and position of this box are kept fixed for every image in each experiment. In the final experiments the scattering signals are measured for different lattice field intensities. In this way the depth of the lattice is varied and we find the scattering signal as function of the lattice depth, corresponding to eq. (7.17) combined with eq. (7.13). We infer g_l and g_p from the lattice power transmitted through the cavity, P_{trans} as: $g_i = 2\pi \times 4.4$ GHz$\sqrt{P_{trans,i}/1\mu W}$ for $i = l, p$, which can be calculated from the transition strengths between the considered states of $^{40}Ca^+$ and the corresponding saturation intensities

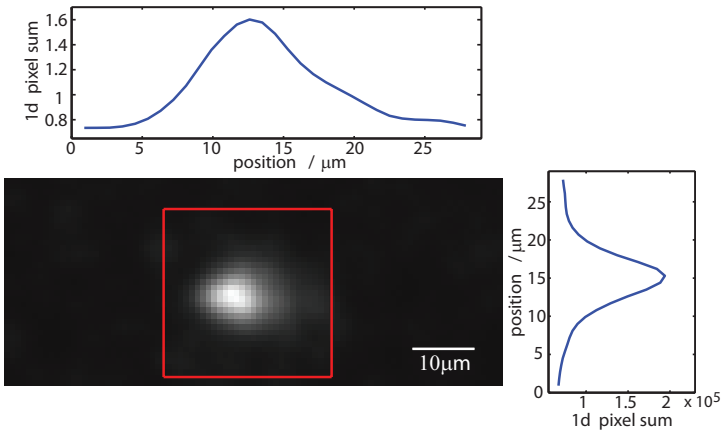

Figure 7.8: Typical image of a single ion from which we obtain the scattering probability during the localization experiment. In this example the lattice potential has a depth of ~ 20 mK. The sum of all pixels in the red box (30×30 pixels $\approx 27 \times 27$ μm), subtracted by the background, represents the scattering signal used in the data-analysis. The two graphs show the variation along the vertical or horizontal direction within the red box, constructed by summing pixels in the opposite direction.

(see e.g. [27]). The decay rate of the 397 nm transition is $\Gamma_{397} = 2\pi \times 20.7$ MHz and the total decay rate of the excited state is $\Gamma_{P_{1/2}} = 2\pi \times 22.4$ MHz.

As indicated above, after the optical pumping stage the ion population is equally distributed over all four sub-levels, and an ion in the $m_j = -3/2$ and $m_j = -1/2$ sub-levels of the $3D_{3/2}$ state does not couple to the lattice field. It can thus be ignored. Ions in the $m_j = +1/2$ and $m_j = +3/2$ sub-levels will be able to localize, as they are coupled to the $4P_{1/2}$ sub-levels by the lattice field. Ions in the $m_j = +3/2$ substate will experience the strongest transition dipole moment and see a lattice three times deeper than the ions in the $m_j = +1/2$ substate, because of their difference in Clebsch-Gordan coefficients ($\sqrt{1/2}$ and $\sqrt{1/6}$, respectively, see app. A.3). In the result section, we plot raw data obtained by observing both bright levels and analyze them taking into account the exact contributions from the two states, but report lattice depths and localization results for $m_j = +3/2$. In the experiments described in sec. 7.4, where several ions are localized in the lattice field, optical pumping into $m_j = +3/2$ actually ensures that all ions start in the same initial substate and see the same lattice potential.

Furthermore, as the lattice field is far detuned from the $3D_{3/2} \leftrightarrow 4P_{1/2}$ transition there can be a non-negligible probability for the ion to scatter on the higher lying $4P_{3/2}$ state (see fig. 2.2) and this has to be taken into account in the model used for fitting our results.

The laser locking scheme

As described in sec. 5.5 we use a specific approach to lock all lasers and the experimental cavity carefully together. Both the probe (866-2) and lattice (866-1) lasers are resonant with the cavity but with different frequencies, i.e. resonate with different

longitudinal modes of the cavity. The trap cavity is locked to the 894 nm reference laser, which is locked to a temperature stabilized reference cavity, together with the probe laser. The signal from the trap cavity is generally rather noisy (see sec. 5.6.2) and as these experiments require that the standing wave lattice field (866-1) follows these vibrations, the laser is locked directly to the experimental cavity, and not to the reference cavity. This minimizes short-term intensity fluctuations of the intracavity optical lattice during each sequence.

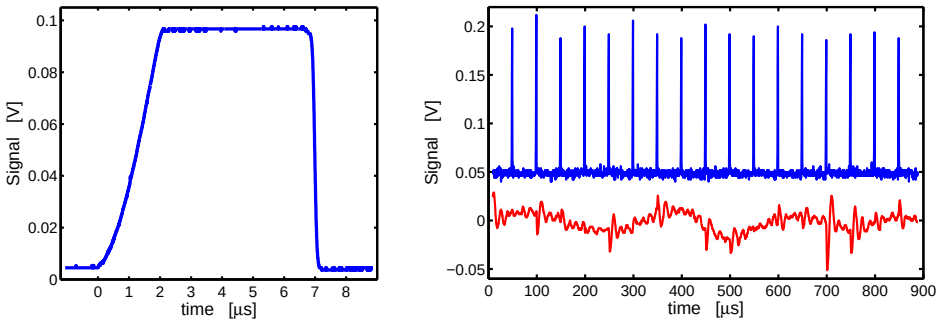

(a) (b)

Figure 7.9: (a) A lattice field profile recorded with a photo-detector in cavity transmission during the sequence. The maximum power corresponds to $\sim$ 20 mK. The lattice field is ramped for 2 μs with a shape growing as $t^{1.4}$ and is held high for 5 μs. (b) A measurement of the reflected lattice power (blue) and the lattice lock error signal (red) during 17 sequential repetitions. The lattice is locked to the low power signal and, as the lattice power is quickly ramped up, the lock does not have time to react before the lattice power is at low level again. Much of the noise in the error signal originates from the noisy trap-cavity.

As shown on fig. 5.7, after reflection from the cavity, a diffraction grating separates the 894 nm light from the 866 nm lattice light, and the latter is sent to a detector giving the signal which is used in the Pound-Drever-Hall (PDH) lock for the lattice laser. In the sequence just described we ramp the lattice field from a low to a high intensity in a short period of time, after which it is quickly dropped back to the low level (see fig. 7.9(a)). This violent variation in power (i.e. error signal amplitude) affects the lock of the laser and it can be difficult to get it reliably stable for fixed gains in the feedback loop. However, the lattice field is not held at high intensity for very long ($\sim$ 5-7 μs) in the 50 μs sequence. Accordingly, if we can keep the lattice pulses short compared to the inverse of the lock bandwidth we never see the steady state performance of the lock with the lattice on. From these considerations, we are forced to use a low overall gain to keep the lock stable during the lattice pulses and to keep fluctuations at a minimum, the error signal offset needs to be optimized to make sure that the error signal crosses zero when the gain is low[2]. In other words, all the important lock performance is at low laser power and once the lattice pulse begins the lock will have almost no time to react to the change. To make sure that this is the case, we can observe the reflected or transmitted signal of the lattice laser

[2]For more information on the PDH technique see [165]

while running the sequence, and adjust the lock parameters so that the pulse does not make the optical signal unstable. The choice of the low-power setting, to which we lock, is made by ensuring that the low-level lattice field does not affect the ion during cooling and optical pumping in the sequence. In fig. 7.9(b) the reflected lattice power (blue) and the lattice lock error signal (red) are shown during 17 sequential repetitions, and this illustrates that the lattice laser can be reliably locked during the localization experiment. We still observe some noise on the error signal, which mostly originates from the noisy trap-cavity lock (using the 894 nm reference laser).

7.3.3 Signal calibration with probe saturation

As we only have one ion which can send out at most one photon in every sequence run, and if we take into account that our imaging system has a low detection efficiency, the expected scattering measurement needs to be repeated a large number of times. By only applying the probe field, without the lattice, the highest signal can be found, whereas when the lattice is applied we typically get a lower signal.

If we set the resonant probe intensity high enough to saturate the $3D_{3/2} \leftrightarrow 4P_{1/2}$ transition, taking into account that we only address the $m_j = +3/2$ and $m_j = +1/2$ states of $3D_{3/2}$, on average we get the ion to an excited state in every second sequential run. We can measure the fluorescence signal obtained when the ion is depumped into the $4S_{1/2}$ state, and as this process occurs with 93% probability we know that in mean every run gives out exactly 0.46 photons. As a typical example, we use a box around the ion on the images of 30×30 pixels ($\sim 27 \times 27$ μm) and sum the total CCD counts within it, resulting in ~ 91000 counts after background subtraction (see fig. 7.8). The exposure time on the CCD for a single image is 10 s and the total sequence length is 50 μs, resulting in 2×10^5 cycles per image. From these numbers, we can deduce that we collect 0.99 ± 0.05 CCD counts per scattered photon (397 nm). To obtain a reasonable measured signal, we collect 30 of these images and perform the total average. In the lattice experiments we collect only a fraction of these CCD counts (as we are far from saturation), but from the calibration we can calculate exactly the corresponding photon number and then get the scattering probability for the ion. Using this calibration, the photon shot noise and the variance of the CCD signal it is possible to estimate the total quantum efficiency of the detection system, which is $\sim 10^{-4}$.

7.3.4 Experimental results and discussion

The purpose of the experiments was to prove that a single ion can be localized in the lattice potential. Prior to the results presented in this section, various calibrations and optimizations of the system were performed, some of which will be described in the following sections.

In the first experiment we only applied the lattice field and observed the scattering probability as described above. To obtain a clear evidence for localization, we compare the photon scattering probability for red- and blue-detuned lattices. As described in sec. 7.3.1 we expect the red-detuned lattice to increase the scattering above the delocalized average level, while the blue-detuned lattice is expected to produce a suppressed scattering signal. On fig. 7.10 the resulting scattering signals are shown for a lattice detuning of ± 0.19 THz (± 15 FSR). The probabilities to scatter a lattice

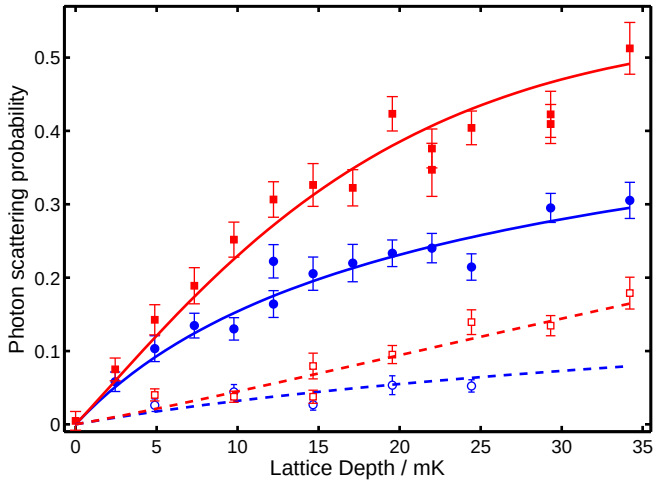

Figure 7.10: Photon scattering probability from the optical lattice as function of its depth, for red (full squares) and blue (full circles) detuned lattices. The solid lines are one-free-parameter fits of our analytical model giving $T_{ini} = 5.1 \pm 0.6$ mK. The open symbols and dashed lines shows the scattering probability during lattice ramp-up, from experiments and from the model, respectively.

photon in the 5 μs during which the lattice is kept high (after ramp-up) are shown as solid red squares and blue circles. The fact that the observed scattering is systematically higher in the red-detuned lattice case compared to the blue is a signature of localization, matching the expectations of sec. 7.3.1.

The analytical model can be used to predict the fluorescence signal, which is shown as solid lines in fig. 7.10. As seen, this simple model provides a good quantitative description of the observed scattering probabilities. The curves are fitted simultaneously with the initial temperature as the only free parameter, all other quantities being known from independent calibrations. The obtained temperature is $T_{ini} = 5.1 \pm 0.6$ mK and, although it is about ten times the Doppler limit, it appears to be consistent with the observed spread of the ion position after Doppler cooling. The model accounts for the population loss during lattice ramp-up, but as a cross-check we also measured the scattering probability (predicted by eq. 7.16 in sec. 7.3.1) during this process for both detunings (fig. 7.10, open symbols and dashed lines). Again, the model consistently reproduces the observed variations. These localization experiments require a minimization of any micro-motion in the system, and as we shall see in sec. 7.3.5 the ion can get completely delocalized by imposing a few nanometers of motion. In this case, the red- and blue-detuned curves are pushed towards each other resulting in scattering from a hot free ion (only trapped by the harmonic Paul trap). In general, increasing the initial ion temperature by any process has the same effect, and the observed scattering curves would be identical when its temperature is much larger than the highest lattice depth; hence the ion will be delocalized.

By modeling the experiment with the same initial temperature (5 mK) and final

lattice depth (34 mK) as obtained from the fit, we infer that the ion is captured in a single lattice well with over 97% probability. This is the fraction of the energy distribution which is below the lattice depth. Furthermore, this modeling reveals that we can (for the same parameters) deduce the approximate ion position spread in a lattice cite to $\Delta z \approx 190$ nm (FWHM), corresponding to sub-wavelength localization ($\lambda_{lat} = 433$ nm).

We then carried out a second experiment to consolidate the evidence of localization. Here, after ramping up a blue detuned lattice field, the near-resonant probe field is injected into the cavity, as explained in sec. 7.3.2. The boundary conditions of the mirrors determines the overlap between the probe and lattice standing waves at the center of the cavity, as described in sec. 7.3.1. The probe field will increase the scattering in a way that depends on the separation in frequency between the two fields (even or odd number of FSRs). The scattering from the probe field has an additional position dependence because of the lattice-induced AC Stark shift on the energy-levels, since the detuning of the probe from the $3D_{3/2} \leftrightarrow 4P_{1/2}$ transition changes by twice the local lattice depth. This is illustrated on fig. 7.6(a) where the application of the lattice shifts the levels in opposite directions following the sinusoidal pattern of the lattice. The probe field has in these experiments been detuned by 0.65 GHz so as to be less sensitive to this shift and to obtain a more clear splitting between the signals. In fig. 7.11 the observed photon scattering probability is shown for blue lattice detunings of 15 FSR (0.19 THz) and 16 FSR (0.20 THz) by the probe, as green squares and orange circles, respectively. There is only a 6.7% difference between the two lattice detunings but the figure clearly shows the difference in the probe field

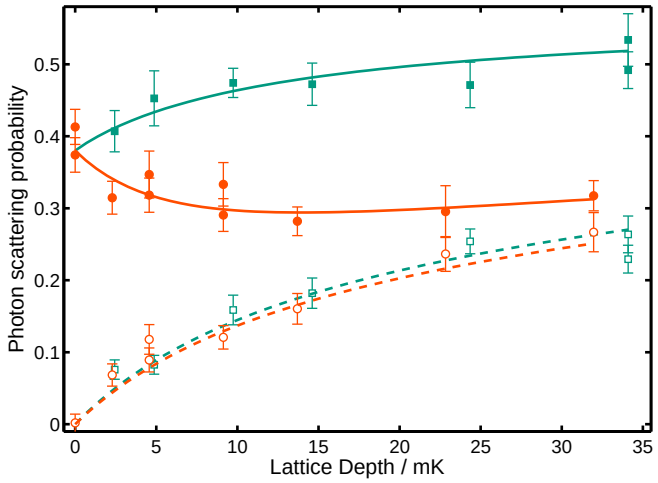

Figure 7.11: Combined scattering probability for the probe field and a blue-detuned lattice field separated by 15 (green squares) and 16 (orange circles) cavity free spectral ranges. The open symbols are scattering from the lattice field alone for both detunings. The full curves are a fit to the analytical model with two free parameters: probe power and initial ion temperature ($T_{ini} = 3.9 \pm 0.3$ mK).

scattering rate, as the ion goes from being localized near a probe node (16 FSR) to being localized near a probe anti-node (15 FSR). The open symbols show the scattering probability obtained with the lattice only for the two detunings and, as they are both on the blue side, they follow each other closely and resemble the blue curve in fig. 7.10. The model predictions are shown as full lines (probe on) and dashed lines (lattice only) on the figure, and they agree with the observed scattering. We fit all four curves simultaneously with two free parameters: probe power and initial ion temperature ($T_{ini} = 3.9 \pm 0.3$ mK). The fitted probe power is consistent with the one measured in the experiments, and corresponds to an intracavity Rabi frequency of $\Omega_p = 2\pi \times 16$ MHz. We can consider the scattering from the probe alone, by subtracting from the signals obtained with the probe on (solid symbols) the signals from the lattice only (open symbols). This reveals that changing the lattice detuning by a single FSR increases the probe scattering with more that a factor of four (for the highest lattice depth). This shows that the coupling between an ion and a cavity field mode can be increased by localizing the ion in an optical lattice with a standing wave structure of a different mode. The average coupling strength squared (related to the local cavity field intensity) increases from 50%, for a delocalized ion, to $81 \pm 3\%$ for the ion in the deepest lattice at a cavity antinode. This change in coupling does not depend on our model as the measured scattering rates are directly proportional to the cavity coupling strengths squared. The only corrections needed are the loss during ramp-up (which we have measured independently) and weighting the signals between the $m_j = +3/2$ and $m_j = +1/2$ sub-states of $3D_{3/2}$.

7.3.5 Effect of excess micro-motion on the localized ion

Localizing an ion by a standing wave lattice field while keeping it in a linear Paul trap requires the ion kinetic energy to be low as compared to the energy of the lattice confinement. In Paul traps though, excess micromotion could in principle drive the ion at the RF-frequency and heat it up (see sec. 2.3.4). The lattice potential in our system is placed along the axis of the trap and, consequently, the ion localization is very sensitive to parasitic RF-fields in the axial direction. Micromotion in an ideal linear Paul trap is normally a radial effect, i.e. arising when ions are displaced radially from the nodal line, but, in a real trap, parasitic RF-fields with a non-zero axial component cannot be excluded. As introduced in sec. 5.7 we can consider each individual trap electrode as an LRC resonance circuit and by inserting variable capacitors in each circuit we can control the relative phase of all the electrodes [128]. In particular, a phase difference between the RF-field of the four end-electrodes in one end compared to the other could induce excess micro-motion of non-negligible magnitude in the context of our ion localization. By varying the relative phase of the two ends we can control this dipolar RF-potential along the trap axis. As the oscillation frequency of the lattice potential is close to the RF-frequency ($2\pi \times 4$ MHz) the ion localization will thus be affected and can ultimately vanish.

Our analytical model can not handle the complication of adding a fast varying micro-motion field and, hence, we examine the effect through numerical MD simulations performed by Mathieu Marciante. At first, we will give some simple considerations on the problem. By including the harmonic trapping potential, the micro-motion

effect and the localizing lattice field, the ion's motion is governed by a second order differential equation:

$$\ddot{z} + \omega_z^2 z = A_M \omega_{rf}^2 \cos(\omega_{rf} t) - \frac{\nabla(U(z,t))}{m} \ , \tag{7.18}$$

where ω_z is the axial harmonic oscillation frequency, A_M is the micro-motion amplitude, ω_{rf} is the RF-frequency and m is the ion mass. The force from the micro-motion can be found as $F_{rf} = A_M m \omega_{rf}^2$. The lattice potential is $U(z,t) = U(t)\sin^2(k_l z)$, where k_l is the wavenumber of the lattice field and $U(t)$ is the lattice potential depth which is being ramped up. Note that eq. 7.18 resembles a driven pendulum equation, which is known to become chaotic when e.g. the drive amplitude is high. Solving this equation numerically makes it possible to simulate the ion trajectories, from which the average potential energy can be obtained.

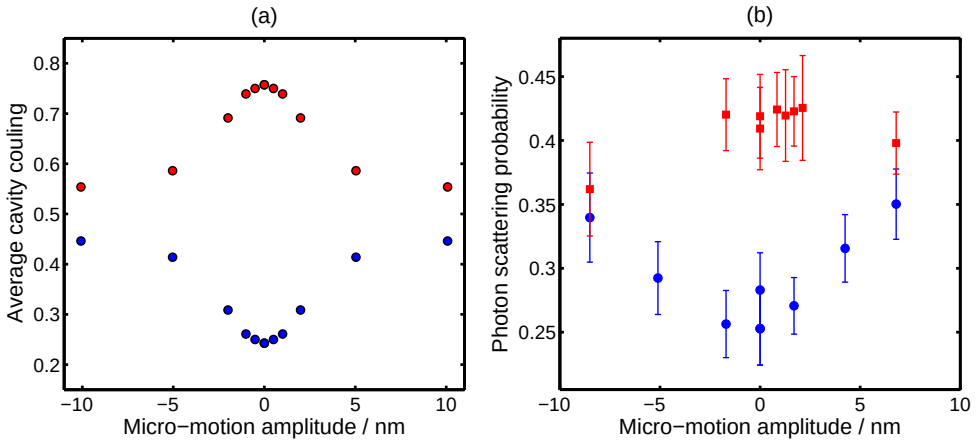

Figure 7.12: (a) Results for ion trajectory simulation in a sinusoidal lattice potential for a given micromotion amplitude, giving the average coupling to the lattice cavity field. The lattice is ramped in 2 μs to a final depth of 28 mK. The results are shown for red- and blue-detuned lattices by symmetrically mirroring horizontally and vertically. (b) Experimental results of localizing a single ion in lattice fields with red (−15 FSR - red squares) or blue (+15 FSR - blue circles) detuning and a depth of 29 mK. The photon scattering probability is plotted as function of micro-motion amplitude along the cavity axis and shows that the localizing effect is eliminated with only a few nm of axial micromotion in the system.

For a given RF force we consider the micro-motion amplitudes for a free particle, the sinusoidal lattice potential is ramped adiabatically to a certain depth U_0 and the simulation runs for a fixed time. The result of a simulation with one $^{40}Ca^+$ ion is plotted in fig. 7.12(a) with an initial temperature of $T_{ini} = 0.5$ mK, a 97 kHz harmonic trapping frequency and a 2 μs lattice ramp with intensity growing as $t^{1.4}$ to a final lattice depth of $U_0 = 28$ mK. The 4 MHz RF micro-motion force is imposed with amplitudes of 0, 0.5, 1, 2, 5 and 10 nm for a free ion. Like before, we consider the case of having a red- or a blue-detuned lattice field, but ion trajectories are not distinguishing between the sign of the detuning or the sign of the micro-motion amplitude since there is a random phase between the initial ion oscillation and the RF-motion. Hence, for each setting the simulation gives information about four points;

red- and blue- detuning, positive- and negative-amplitude micromotion. This causes the symmetry in the curves on fig. 7.12(a). The outcome of the simulations are the average energy of the ion motion in the lattice, which can be expressed as a fraction of the lattice depth $\langle U/U_0 \rangle$. For a blue detuned lattice, the average cavity coupling is $g^2_{cav,b} \propto \langle U/U_0 \rangle$, whereas for a red-detuned lattice it is the complement, $g^2_{cav,r} \propto (1-\langle U/U_0 \rangle)$. As shown above, in absence of axial micromotion, the localizing effect causes the red-detuned lattice to increase the ion-cavity coupling, whereas the blue-detuned lattice decreases the coupling. We see that only a few nm of RF-induced axial micromotion can change the coupling drastically and in the high-amplitude limit both couplings approach an un-localized situation of 50% of the maximum coupling.

In order to measure how axial micro-motion can influence the ion localization we need to calibrate the external modification into a known micro-motion amplitude. This is done by conventional correlation fluorescence measurements of the excess micro-motion in the axial direction [113] (see also app. E). In our implementation, a single $^{40}Ca^+$ ion is trapped and cooled by mostly illuminating it with a single axial 397 nm cooling beam. A Doppler effect arises between the cooling light and the ion excess micro-motion and modulates the fluorescence signal. In order to resolve this fast ($2\pi \times 4$ MHz) modulation we gate our imaging system with a $100ns$ short pulse at a rate 0.5 Hz faster than the RF frequency. This pulsed observation aliases the 4 MHz Doppler modulation down to a 0.5 Hz fluorescence fluctuation easily detectable on our CCD camera. From a Fourier transform of the signal the amplitude can be found and the noisy background is subtracted. In Fig. 7.13 the modulation power are shown

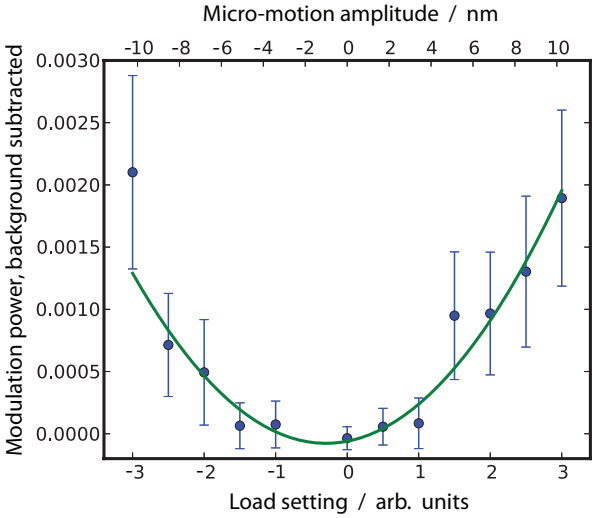

Figure 7.13: Correlation fluorescence measurements of the excess micro-motion in the axial direction [113], showing the micro-motion modulation as function of the capacitative load setting of end-cap electrodes. Gating the imaging with pulses close to the RF-frequency (4 MHz) modulates the fluorescence fluctuation down to a detectable 0.5 Hz signal. Its amplitude is directly related to the micro-motion amplitude, and hence a calibration between the load setting and the size of the micro-motion influence is established.

for a scan of end-cap electrode loads on one side of the trap. Note that changing the capacitative loads of the circuit changes slightly the RF resonance frequency, and this needs to be compensated in order for the ion to be stably trapped. The modulation power is here defined as the square of the modulation contrast. From the quadratic fit the load position can be related to the contrast signal. From simple considerations of the effect on the scattering signal obtained from a moving particle affected by an electrical field it is possible to estimate a connection between micro-motion amplitude and the contrast signal. In connection with the correlation fluorescence measurements we eventually find the relation of excess micro-motion to be 3.4 nm per load turn. With this calibration at hand the micro-motion effect on the localization signal can be estimated.

To test the effect on the experimental localization we localize a single $^{40}Ca^{+}$-ion in a lattice potential like in the prior section. The experimental sequence is run in the same way as described in sec. 7.3.2, but we only measure the scattering probability for a single lattice depth, 29 mK. As before, we compare the scattering signal obtained from a red (-15FSR) detuned lattice and a blue (+15FSR) detuned lattice, where a difference indicates that the ion is localized. By varying the electrode loads in the same way as with the correlation fluorescence measurements, we can observe the effect on the localization. On fig. 7.12(b) the localization signal are shown for red- and blue-detuned lattices, as function of the micromotion amplitude for a free ion, which was obtained from the load settings using the known calibration. We see clearly that increasing the micro-motion amplitude delocalizes the ion, as the curves approach each other. Although the kinetic energy of the ion, originating from RF-amplitudes of a few nm, is much lower than the lattice depth, we still observe that the ion delocalizes. This is a result of off-resonant excitations of the driven motion by the ramped lattice. Delocalization occurs even if the effective frequency in the lattice is lower than the RF frequency, because of the anharmonicity of the sinusoidal lattice potential. As a comparison, the oscillation frequency in a lattice well can be found trough $\omega_l = \sqrt{2Uk^2/m}$ from sec. 7.2.1, and near ~ 29 mK lattice depth it matches the RF-frequency ($\omega_l \approx \omega_{rf} = 2\pi \times 4$ MHz). Nevertheless, we still observe micro-motion induced delocalization at lower depths. Also, note that a micro-motion amplitude of $A_M = 5nm$ corresponds to a parasitic force of only $F_{rf} = A_M m\omega_{rf}^2 = 200zN$ and this makes a single ion in an optical lattice a sensitive directional probe of stray RF-field forces in the trap.

Comparing the ion localization signal to the numerical simulations in fig. 7.12 we see a qualitatively good agreement. The scale at which the micro-motion force destroys the ion localization (5-10 nm) is roughly the same for both approaches, indicating that our description of the system is somewhat correct. We have to emphasize that the vertical scales are not directly comparable, as one gives the ion coupling to the localizing cavity field while the other gives the probability for the ion to scatter on the lattice field. Actually this technique can also be used the other way around - to minimize the micro-motion by making the localization signal as large as possible. Furthermore, we have checked that moderate radial micromotion does not affect the ion localization.

7.3.6 Conclusion

This section addressed the demonstration of localization of a single $^{40}Ca^{+}$ ion by an optical wavelength-scale intracavity standing wave potential. We introduced two measurement techniques which are both based on the inelastic scattering from the $3D_{3/2}$ to the $4P_{1/2}$ level followed by a decay to the $4S_{1/2}$ ground state by emitting 397 nm photons. By only applying the lattice field, the ion scattering was obtained for red and blue lattice detunings (± 0.19 THz) and can be related through a simple analytical model to the level of localization. The only free parameter in the model is the initial ion temperature (here $T_{ini} = 5.1 \pm 0.6$ mK) which agrees with the independent estimate based on the width of the ion fluorescence spot. Furthermore, we applied both the lattice potential (blue detuned) and a standing wave probe field, and obtained additional evidence of localization. This was done for a detuning of an even or odd number of FSRs between the fields, by which the spatial relation of the fields is well defined at the cavity center, where the ion is located. The probe field is close to resonant with the $3D_{3/2} \rightarrow 4P_{1/2}$ transition and the signals obtained for a frequency separation between the fields of an even or an odd number of cavity free-spectral ranges were compared. This revealed that the coupling strength to the probe field could be either enhanced or diminished when the ion is localized in the lattice wells. The average coupling between the ion and the probe field was hence increased from 50% of its maximum value for a delocalized ion to 81% when the ion is localized.

7.4 Multi-ion localization experiments

In this section we investigate the possibility of simultaneously localizing several ions in the standing wave lattice potential. In sec. 7.4.1 we introduce some possible applications of the study and its limitations. In sec. 7.4.2 we describe the process of optimization of the optical pumping to a single Zeeman substate to which the localizing lattice field couples strongly. In sec. 7.4.3 we describe the localization of one-dimensional strings of ions, first specifying the differences in the experimental setup and sequence as compared to the single ion localization experiments, and afterwards presenting the obtained experimental results. In sec. 7.4.4 we consider localization of multi-dimensional ion crystals. In the last section (7.4.5) we discuss possible issues associated with the experimental results of localizing multiple ions and give a conclusion.

7.4.1 Introduction

The previous experiments were limited to the dynamics of single ions in an intracavity lattice potential. In this section we extend the studies to the case of ion Coulomb crystals composed of several ions. Such a system exhibits a natural competition between Coulomb and optical forces, which can be used to test cold solid-state models, such as Ising spin-models [196, 197], generalized Dicke models [198] or the Frenkel-Kontorova model of friction [98, 99, 194]. The latter model is based on a one dimensional description of friction between two crystals: a chain of atoms from one crystal sliding along the periodic potential created by the other crystal. A string of ions can be used to mimic the first crystal, while the optical lattice corresponds to the second crystal. By increasing the lattice strength, the system can undergo a transition from a regime where the ion-ion coupling dominates to a regime where the ions form a chain of independent oscillators, mimicking the friction between the two crystals. The application of light induced potentials on two- and three-dimensional crystals is furthermore interesting for e.g. the control of the crystalline structure of large Coulomb crystals [180] or for the enhancement of the ion-light coupling in cavity QED experiments [28, 68].

The experiments we describe in the following demonstrate the simultaneous localization of ions in multidimensional ion Coulomb crystals by an intracavity optical potential, and, as such, they represent an important step towards the implementation of the above mentioned applications. However, let us note that the typical inter-ion distance in our experiments is $\sim 10 - 30$ μm, and as the Coulomb force between the ions is mostly balanced by the trapping potential, the force induced from the lattice easily overcomes the Coulomb force (for small ion displacements). This limitation on the interaction-induced delocalization from Coulomb repulsion can be quantified by comparing the energy scales associated with the different types of ion motion, i.e. comparing the frequency scales involved. In order to observe a clear localization effect on the initial thermal motion of the ion, we need a lattice depth of ~ 10 mK. The oscillation frequency at the bottom of a lattice well was defined at eq. (7.4), and will here be on the order of $\omega_l = 2\pi \times 2$ MHz. For multiple ions in the trap the stiffest crystal modes possible will have frequencies on the order of the plasma frequency, which can be found from eq. (2.21) and which, for typical parameters, is on the order of $\omega_{pl} = 2\pi \times 500$ kHz. In order to observe Coulomb interactions disrupting the

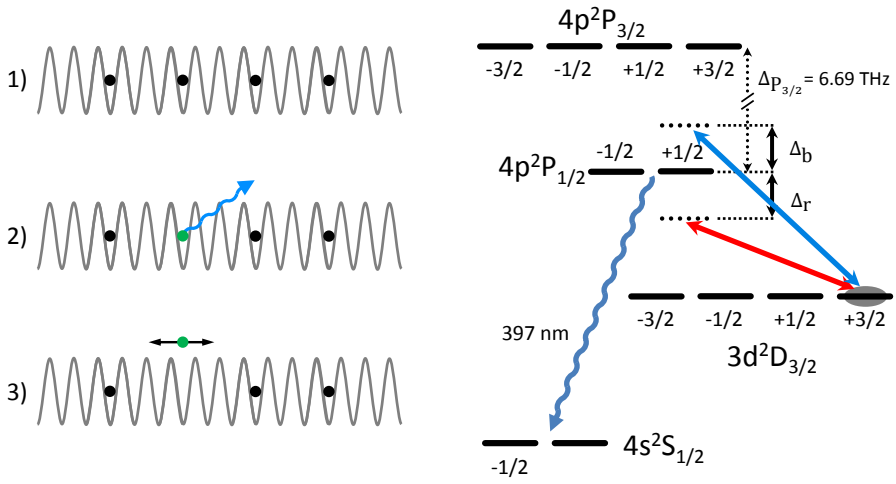

(a) (b)

Figure 7.14: (a) Illustration of the confinement of a 4 ion string in a lattice potential. 1) The ions are all localized in the lattice potential. 2) One ion scatters on the lattice field and decays to the ground state emitting a 397 nm photon. 3) The system now contains three ions in the lattice and one free ion (in the Paul trap potential), and the configuration is therefore different than in the initial system. To demonstrate simultaneous multi-ion localization, the measurement thus has to stop before more than one ion have time to scatter, which limits the total scattering rate. (b) The relevant energy-levels for $^{40}Ca^{+}$. The ions are prepared in the $m_j = +3/2$ sub-state of $3D_{3/2}$ by optical pumping and the σ^- circularly-polarized lattice field is applied with either red (Δ_r) or blue (Δ_r) detuning from the $3D_{3/2} \leftrightarrow 4P_{1/2}$ transition. We measure the lattice induced scattering by again collecting the emitted 397 nm photons. Furthermore, we indicate the frequency spacing to the $4P_{3/2}$ level, as scattering to this level can become non-negligible when the lattice detuning gets large.

localization, a conservative estimate is that the plasma frequency must be at least as large as the oscillation frequency of ions in the lattice well. As this is not the case in the present experiments the ions can be described as independently localized in the optical potential and our system is in a regime where we can describe the multi-ion localization physics with our existing single ion model. In order to observe noticeable Coulomb interaction effects one would have to change the experimental configuration in one or several of the following ways. We could create a stiffer background potential (to compress the crystal and raise the plasma frequency), but raising the trap potentials enough to get the frequencies comparable would cause the ion position distribution in the trap to be on the order of the lattice period, and our model would break down. We could also create a shallower lattice (lower depth), but this would require a lower initial ion temperature in order to still observe a localizing effect. Last, we could create a longer lattice period, which could be achieved through the interference between two counter propagating beams with carefully chosen polarizations.

As in the single ion case, we localize a number of ions in red- and blue-detuned lattice fields, and compare the scattering probability. A complexity arises though,

if one wants to demonstrate simultaneous localization of several ions. In principle, the goal of the localization measurement is to have all ions localized in the lattice potential right up until one of them scatters off the lattice and a fluorescence photon can be observed. However, as soon as one of the ions scatters it will decay with 93% probability to the $4S_{1/2}$ state and will no longer see the lattice potential (as illustrated on fig. 7.14(a)). This changes the ion configuration in the lattice and the total potential energy of the system. Thus, in order to demonstrate simultaneous multi-ion localization, the total photon number scattered by all the ions in the lattice must be much less than one. In this case, the single-ion model used in the prior section is still expected to give reliable predictions of the localization, but this quickly limits the maximum achievable scattering signal, and thereby the maximum number of ions which can be realistically investigated with this experimental configuration.

To lower the scattering probability we introduce a number of changes to the experiment. The lattice laser is detuned even further than in the single ion case and to reach comparable potential depths, the intensity of the lattice laser is also increased (the lattice depth depends on the detuning and Rabi frequency as $U = \Omega^2/\Delta$). As the lattice detuning (0.76 THz) approaches a considerable fraction of the frequency difference between the $4P_{1/2}$ and $4P_{3/2}$ states (6.69 THz), the scattering on the $4P_{3/2}$ level becomes non-negligible and has to be taken into account in the modeled scattering probability. Furthermore, in order to ensure that all the ions see the same lattice field they have to be in exactly the same state before the lattice is raised. Thus, we perform optical pumping into the $m_j = +3/2$ sub-state of $3D_{3/2}$, as this has the strongest coupling to the σ^- circularly-polarized lattice field. This is illustrated on fig. 7.14(b) and in the following section the optimization of the OP process is described.

7.4.2 Optimizing the optical pumping with few ions

In order to obtain the maximum population in the $m_j = +3/2$ sub-state of $3D_{3/2}$ a careful optimization of the optical pumping process needs to be performed. This state was chosen, as the $3D_{3/2}, m_j = +3/2 \leftrightarrow 4P_{1/2}, m_j = +1/2$ transition at 866 nm has the highest Clebsch-Gordan coefficient and will hence give rise to the largest coupling strength to the lattice field. As described in sec. 6.1.2 optical pumping has been performed on large ion Coulomb crystals with high efficiency ($\sim 97\%$) in our system (see also [27]). Now, our studies only include a few ions (up to 8 in a string) and the optical pumping parameters need to be adjusted and optimized accordingly.

As introduced in sec. 5.5 the optical pumping (OP) beam is sent onto the ions with an angle of 45° from the quantization axis with both σ^+ and π polarization components. This can e.g. be seen on fig. 6.1(a). During the optical pumping process the 397 nm cooling laser is also applied in order to empty the $4S_{1/2}$ state. Because the OP polarization has no σ^- component the only un-addressed state is the $m_j = +3/2$ sub-level of the $3D_{3/2}$ state, and hence all population will eventually accumulate in this state. In the experiments a magnetic field of ~ 2.5 G along z defines the quantization axis for the system and this results in the Zeeman splitting of the energy levels. The system is described by 8 different levels, as can e.g. be seen on fig. 7.15, and these all have different magnetic shifts. The equations for the time-evolution of the atomic state population in this system can be found through its Hamiltonian, but as the states are coupled using six different electrical fields (in the

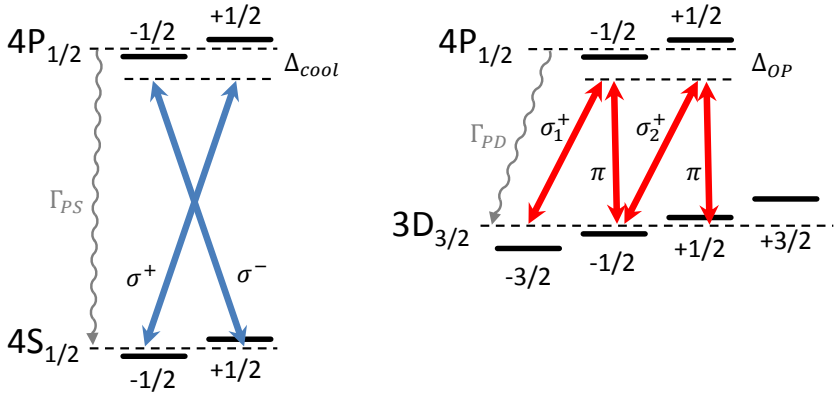

Figure 7.15: Scheme of the relevant levels and transitions for optical pumping of $^{40}Ca^{+}$. Due to the Zeeman effect, the levels are shifted from their unperturbed configuration (dashed lines). The various transitions are labeled by the polarization of the fields addressing them and the detunings of the fields from the unperturbed levels are indicated. The decay rates Γ are distributed among the substates according to the Clebsch-Gordan coefficients of those transitions and thus, as $3D_{3/2}, m_j = +3/2$ is not addressed by any field, all the population can ideally be accumulated there.

quantized picture) the calculations include in general 64 coupled first order differential equations. For numerical solutions of the system properties and a general description, see [27]. In practice there are several factors that need to be optimized explicitly in order to gain a high optical pumping efficiency. The laser intensity and detuning on the 866 nm and 397 nm transitions need to be well adjusted, together with the relative polarizations of the fields. Given the relative strength of the two transitions ($\Gamma_{PS}/\Gamma_{PD} \simeq 12$) the $4S_{1/2} \leftrightarrow 4P_{1/2}$ transition is the most critical and should be driven strongly.

During the optical pumping process the scattering from the $m_j = +3/2$ state will decrease, and ideally the state should become completely dark. To measure the efficiency of the optical pumping process, one can specifically probe the Zeeman states after the optical pumping has ended, and maximize the scattered fluorescence from the $m_j = +3/2$ state, i.e. maximize its population. We load an ion string into the trap and run a sequence in three parts: Doppler cooling (28 μs), optical pumping (variable duration), probing (5 μs). Between the optical pumping and the probing the cooling light is left on for 5 μs in order to be sure that all population is distributed on the substates of $3D_{3/2}$. The saturating probe field is applied first with σ^+ circular polarization and addresses the $m_j = -3/2$ and $m_j = -1/2$ substates and subsequently with σ^- circular polarization addressing the $m_j = +1/2$ and $m_j = +3/2$ substates. As in the localization experiments we measure the probe scattering by collecting the 397 nm fluorescence on the $4P_{1/2} \leftrightarrow 4S_{1/2}$ transition with the CCD camera, while the probe field is on. By comparing the height of the scattering signals generated by the two different probe polarizations (Γ_{σ^-}, Γ_{σ^+}) we can give an estimate for the optical pumping efficiency. The two scattering signals give the combined population of two Zeeman states as $\Gamma_{\sigma^-} \propto n_{1/2} + n_{3/2}$ and $\Gamma_{\sigma^+} \propto n_{-1/2} + n_{-3/2}$, and consequently we

have to also probe with a π-polarized field to measure the population in the $m_j = \pm 1/2$ states independently. The final optical pumping efficiency will be defined as

$$\eta_{OP} = \frac{n_{3/2}}{n_{-3/2} + n_{-1/2} + n_{1/2} + n_{3/2}} \ . \tag{7.19}$$

By varying one parameter at a time, the optical pumping efficiency is raised as much as possible, to ensure that all ions are prepared in the same state every time the sequence runs. In the setup the beam waist of the 397 nm cooling beam is ~ 0.5 mm and for the 866 nm OP beam horizontally it is $\sim$ 1.3 mm (see [27]). In all the measurements the field on the $4P_{1/2} \leftrightarrow 4S_{1/2}$ transition has a detuning of $\Delta_{cool} = 2\pi \times 28$ MHz and the Rabi frequency is $\Omega^{SP} = 2\pi \times 6$ MHz. The optical pumping field has a detuning close to zero ($\Delta_{OP} \approx 2\pi \times 0$ MHz) and the Rabi frequencies of the different components are $\Omega^{DP}_{\sigma_1^+} = 2\pi \times 5$ MHz and $\Omega^{DP}_{\sigma_2^+} = \Omega^{DP}_{\pi} = \sqrt{1/3}\Omega^{DP}_{\sigma_1^+}$, because of the difference in Clebsch-Gordan coefficients (for more detail see [27], and for the coefficients see app. A.3).

Varying the duration of the OP process is an important optimization and a result of this is shown on fig. 7.16(a). In these measurements the duration of the Doppler cooling and probing are kept fixed. The red points give the scattering probability when using a σ^- polarized probe field, while the blue points corresponds to a σ^+ polarization (as indicated in the illustration on the figure). For every set of points the sum of fluorescence corresponds to scattering one photon pr. sequence run and from an average over all the points the scattering probability can be calibrated. With no

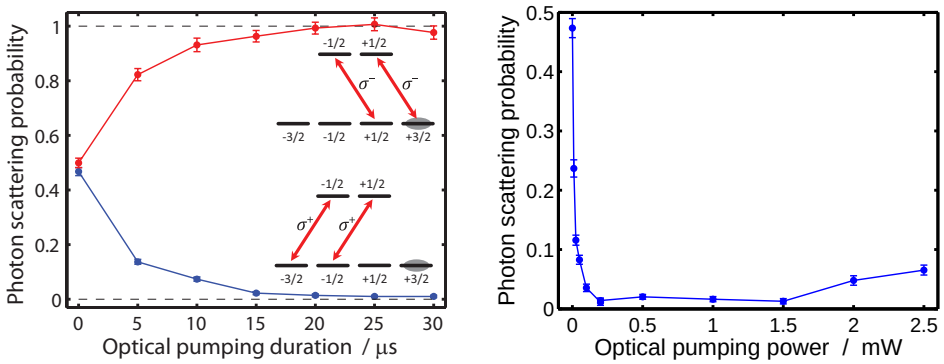

(a) (b)

Figure 7.16: Optimizing the optical pumping (OP) process using 6 $^{40}Ca^+$ ions in using the sequence described in the text. (a) Varying the OP duration in the sequence, after which the system is probed with either a σ^- (red) or a σ^+ (blue) circularly polarized probe field. The scattering probability for σ^-increases, while for σ^+ it decreased, and thus, the efficiency of the OP is raised. The insets show the probing process on the considered energy levels of $4P_{1/2}$ and $3D_{3/2}$. (b) For increasing OP power the σ^+ probed scattering probability is plotted. With low power the scattering is high, corresponding to a large population in $m_j = -3/2$ and $m_j = -1/2$, but as it increases this population is decreased. At high OP power a saturation of the process makes the population increase again.

OP, the population in all four $3D_{3/2}$ substates is practically equal (25% in each) and thus, the σ^- and σ^+ measurements give the same signal. As the OP is turned on, population is transferred into $m_j = +3/2$ state and, thus the σ^- (σ^+) probe gives higher (lower) scattering as the the duration is increased. We observe that the OP efficiency increases with the duration of the OP process until it reaches a steady state. By choosing a duration of 25 μs the optical pumping will be completed and three of the substates will be almost empty. Before stating the final efficiency we introduce a few other optimization possibilities.

With OP duration fixed, the power of the OP light could for example be varied, as shown in fig. 7.16(b). Here, we only observe a σ^+ polarized probe field, as minimizing a fluorescence signal rather than maximizing has less uncertainty. With low OP power the population in the $m_j = -3/2$ and $m_j = -1/2$ substates are large giving a high probe scattering probability. As the power increases we observe an optimal range before the probability starts to rise again. The process also depends on the power of the 397 nm cooling laser and thus, this reveals that the process is complicated and requires several iterations of the laser and timing settings in order to be fully optimized.

To ensure the right polarization of the optical pumping beam the $\lambda/4$ and a $\lambda/2$-wave-plates (see fig. 5.4) on the OP beam-path are varied. The polarization is turned into an elliptical polarization by the $\lambda/4$-plate, while the $\lambda/2$-plate are used to compensate for imperfections in the optics and birefringence in e.g. the viewport of the vacuum chamber. In fig. 7.17(a) the scattering probability for the σ^+-probe is shown as function of the $\lambda/2$-plate for a fixed $\lambda/4$ setting and shows a clear minimum at an optimum position, at which the $\lambda/2$-plate is then set. A similar variation on the $\lambda/4$-plate is performed (see 7.17(b). Though an iterative procedure, optimizing the

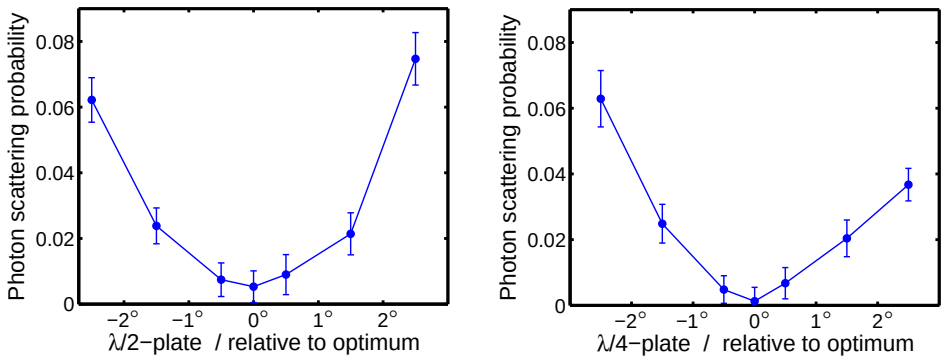

Figure 7.17: Optimizing the optical pumping process using 6 $^{40}Ca^+$ ions and probing the system using a σ^+-polarized probe field. (a) Turning the $\lambda/2$-wave-plate for a fixed $\lambda/4$-plate setting a minimum in photon scattering is observed and this is used as a temporary optimum setting. (b) The $\lambda/4$-wave-plate is turned with the $\lambda/2$ kept fixed, again showing a minimum at some position. By performing an iterative process on the wave-plate variation an absolute optimum can be reached.

plates one at a time, an absolute scattering minimum can be reached, by which the population in the unwanted Zeeman states is minimized.

At this point, what has been measured so far is the relative population in the $m_j = -3/2, -1/2$ states to the $m_j = +1/2, +3/2$ states of the $3D_{3/2}$ level. To measure the population in the $m_j = +3/2$ only we have to perform another measurement. By setting the probe field polarization to π relative to the $3D_{3/2} \leftrightarrow 4P_{1/2}$ transition we can measure the combined population of the $m_j = -1/2, +1/2$ states independently, in order to ensure that the population of the $m_j = +1/2$ state is at a minimum. On fig. 7.18(a) the π-polarized fields and the addressed transitions can be seen and we expect a low scattering signal when the OP is optimal while most of the population is in $m_j = +3/2$. With all parameters optimized through the σ^+ and σ^- circularly polarized probe measurements, we measured the probe scattering probability as function of the optical pumping duration for the π-polarized probe. This is shown in fig. 7.18(b). As in the prior measurements for σ^+, the signal is decreased when the OP duration is increased, indicating that the addressed sub-states are being emptied. For the optimal OP length of 25 μs we find that the population in the $3D_{3/2}, m_j = \pm 1/2$ states is $0.70 \pm 0.37\%$. From the σ-probe measurements we find an optimum combined population in the $3D_{3/2}, m_j = -3/2, -1/2$ states of $0.45 \pm 0.32\%$ and in the $3D_{3/2}, m_j = +1/2, +3/2$ states of $99.5^{+0.5}_{-2.5}\%$. Comparing these three measurements and assuming equal population in the minimized substates, we can estimate the total population in the $m_j = +3/2$ using eq. (7.19) to be $99.2^{+0.8}_{-1.1}\%$.

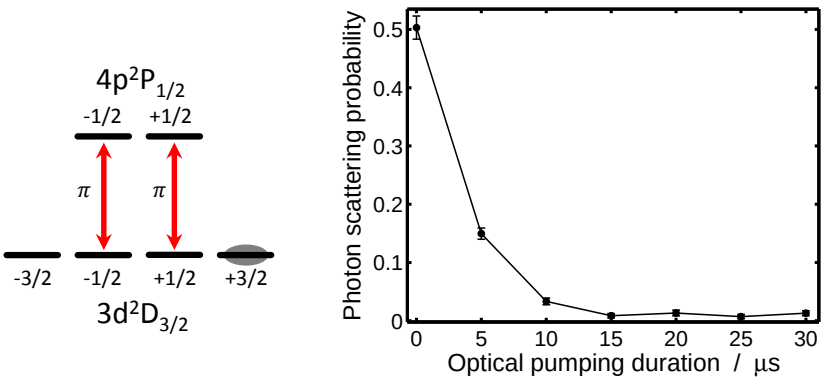

(a) (b)

Figure 7.18: (a) A sketch of the π-polarized fields and the relevant Zeeman states used when optimizing the OP process. (b) Photon scattering probability for 6 $^{40}Ca^+$ ions probed by a π-polarized field after OP. We only address states with minimum population and thus expect a low scattering signal. As we increase the OP duration the signal decreases and the resulting population in $m_j = \pm 1/2$ states is less than 1%.

7.4.3 Localization of ion strings

The natural extension of the single ion localization was to proceed with one-dimensional structures, and hence, we performed measurements on strings with 1-8 ions. In the following we consider the simultaneous sub-wavelength localization of several $^{40}Ca^{+}$ ions, with the same approach as in the single ion case (see fig. 7.7).

7.4.3.1 Experimental setup and sequence timing

A string of ions are positioned at the absolute center of the optical cavity (see sec. 6.2 [79]) and confined in a loose trapping potential with axial and radial trap frequencies $\omega_z = 2\pi \times 70$ kHz and $\omega_r = 2\pi \times 430$ kHz, respectively. In the experimental sequence the Doppler-cooling part is extended to 62 μs, and the axial and radial cooling powers are adjusted in order to minimize the temperature of the ion configuration. The optical pumping process occurs for 25 μs and as described above almost all population is transferred into $3D_{3/2}, m_j = +3/2$ state ($\sim 99\%$). After the optical pumping has ended the cooling beam is left on for 5 μs in order to assure that the $4S_{1/2}$ level is emptied completely. After cooling and optical pumping the 397 nm and OP fields are turned off, and the lattice potential field is applied with a detuning of ± 0.76 THz from the $3D_{3/2} \leftrightarrow 4P_{1/2}$ transition, corresponding to ± 60 FSRs of the cavity. After an optimization of the lattice laser and its beam path the available laser power makes it possible to reach lattice depths of up to ~ 30 mK. The optical lattice intensity is ramped up adiabatically in 2 μs and held at maximum depth for 1 μs, in order to keep the scattering signal low (as mentioned earlier). As in the single ion case, any ion that is excited to the $4P_{1/2}$ state by scattering on the lattice, has 93% probability to decay to the $4S_{1/2}$ state by emitting a 397 nm photon which is detected by the imaging system. The total sequence runs for 100 μs, but we have to expose the camera for 30×10 s to collect enough statistics, resulting in a total number of sequence repetitions of 3×10^6 per data point. In the detection we measure the signal only at maximum lattice depth after ramping, and the collected scattering signal is averaged over all ions. In order to prove the localization of the ion string we measure the scattering from red and blue detuned lattices, but the scattering needs to be kept low to fulfill the requirement of not including multi-ion excitation in the modeling.

As shown on fig. 7.14(b) the lattice detuning (0.76 THz) is now a substantial fraction of the frequency difference between $4P_{1/2}$ and $4P_{3/2}$. This causes an increased scattering probability on the $4P_{3/2}$ level and while most of the scattering processes brings the ion back to the ground state, there is a 6.8% probability to decay into the metastable $3D_{5/2}$ level which has a lifetime of ~ 0.9 s (see fig. 2.2). An ion ending here is thus *shelved* and we can compare the probability of shelving to the (measured) probability of scattering to $4S_{1/2}$ level. In doing so, we include the lifetime of the different decay channels and, the Clebsch-Gordan coefficients and the relative strengths of the transition from $3D_{3/2}$ to $4P_{1/2}$ relative to $4P_{3/2}$. The results is a shelving probability of 60-100 ppm of the probability to scatter a 397 nm photon. The 397 nm photon scattering probability is typically 5-10% at maximum lattice depth, and for an experimental cycle of 100 μs an ion is expected to shelve after $10 - 30$ s of measurement. As an experimental check, we observed a string of 4 ions with continuous imaging, but running the laser sequence for localization (i.e. we obtained mostly fluorescence from the Doppler cooling at the start of the sequence).

We observed an ion shelve (go dark) in average for every $\sim$ 10 s of measurement, when applying a red-detuned lattice. For comparison, without the lattice we observed a dark ion for every $\sim$ 25 s of measurement. Since the lifetime of the shelving state is $\sim$ 1 s and our localization measurement is based on 30×10 s exposures, the lattice-dependent signal is reduced by 4-10%. In order to avoid this signal loss, we add a 854 nm laser field which pumps all population out of the $3D_{5/2}$ level (see fig. 2.2). This does not change the probability for the ions to be excited to $4P_{3/2}$, but it ensures that after few tens of ns the ion has returned to $4S_{1/2}$ from which it can quickly re-enter the localization sequence.

7.4.3.2 Experimental results

In this experimental study we measured the localization effect on several different ion strings and all the results can be seen on fig. 7.19, where the measured scattering probability per ion is plotted as a function of the optical potential depth. The insets show fluorescence images of the different strings. Comparing the signal obtained with red- and blue-detuned latices ($\pm$60 FSR), we see a clear separation that increases with the lattice depth, for all strings. The full lines are a one-free parameter fit to the analytical model, giving the initial temperatures: (a) 1 ion $T_{ini} = 1.5 \pm 0.2$ mK, (b) 2 ions $T_{ini} = 3.2 \pm 0.5$ mK, (c) 3 ions $T_{ini} = 2.5 \pm 0.3$ mK, (d) 4 ions $T_{ini} = 3.1 \pm 0.2$ mK, (e) 6 ions $T_{ini} = 4.1 \pm 0.5$ mK, (f) 8 ions $T_{ini} = 3.7 \pm 0.7$ mK. We restricted the fits to only take into account the data with less than 10% multi-ion scattering probability as a consequence of the requirement of only scattering one ion in mean in every sequence, as discussed in sec. 7.4.1. This means e.g. for the 4 ion string (d) that we can only include data points with photon scattering probability < 0.07 and thus, we have to exclude the measurements at the two highest red-detuned lattice depths (see app. F). For 8 ions the same requirement puts a limit on the photon scattering probability of only 0.032, excluding most of the measurements for the red-detuned lattice. Comparable requirements are applied to fits for the other ion strings (see app. F).

For the strings of 1-4 ions there is a high resemblance between the data and the model, even for the data at high lattice depth which is not included in the fit, indicating that our simple single ion description might be generalized to this multi-ion case. Considering the 8 ion string, as the scattering probability per ion becomes large at high red-detuned lattice depths, deviations from the single-ion model become visible. On the contrary, the blue-detuned lattice data shows very good agreement with the theoretical expectations, indicating that sub-wavelength localization in the optical potential is achieved for all the strings. The red and blue dashed lines corresponds to the expected signal for completely delocalized ions, i.e. at very high temperatures. Even though the lattice depths are equal, the delocalized scattering probabilities are not exactly equal, as the blue-detuned lattice scattering contains a higher probability of scattering to the $4P_{3/2}$ state, as discussed.

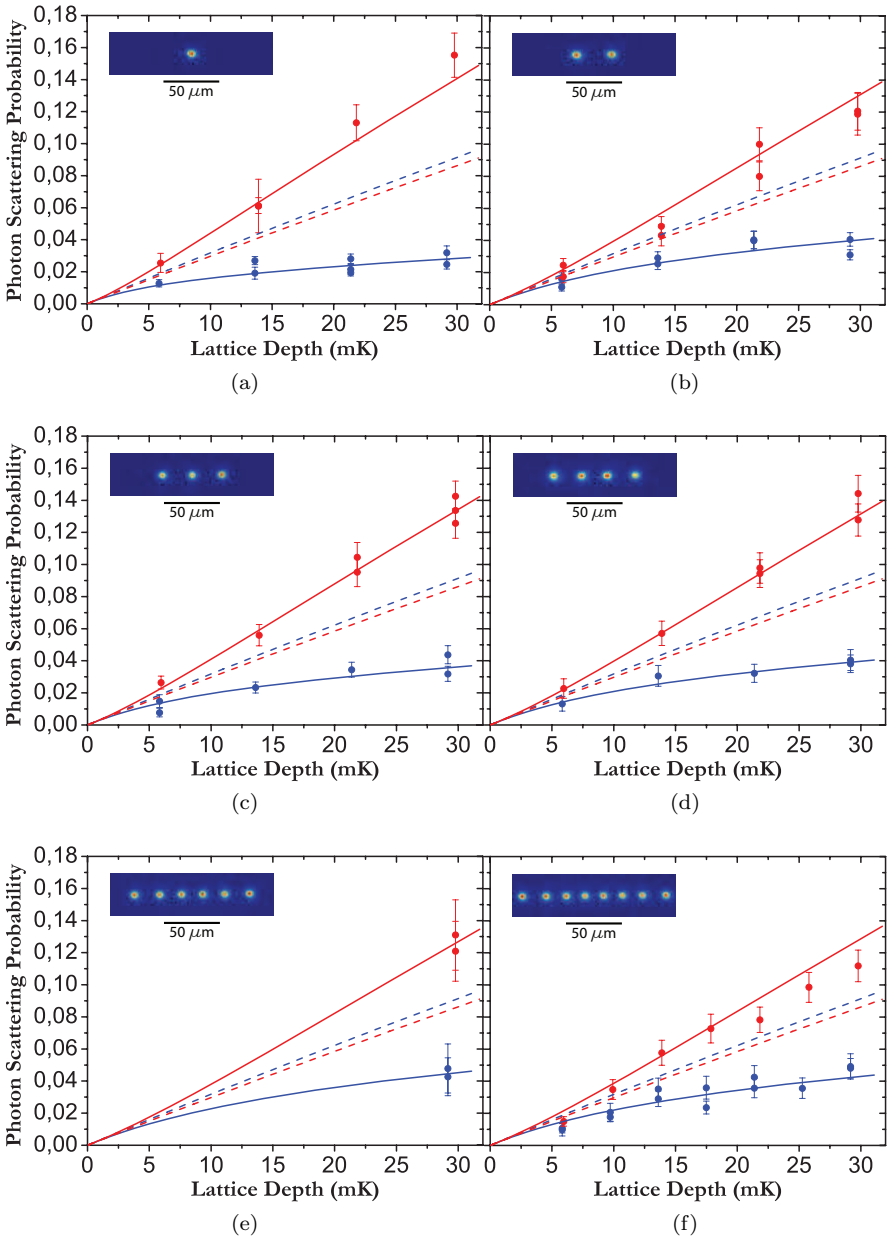

Figure 7.19: Photon scattering probability per ion as a function of the optical lattice depth for ion strings. *Circles*: measurements with a red and a blue detuned lattice, *full lines*: fit to the single ion one-free parameter analytical model of sec. 7.2.1, *dashed lines*: theoretical scattering probabilities for delocalized ions. The fits are only applied to the data with average multi-ion excitation of $< 10\%$ (see text), and reults in initial temperature of (a) 1.5 ± 0.2 mK, (b) 3.2 ± 0.5 mK, (c) 2.5 ± 0.3 mK, (d) 3.1 ± 0.2 mK, (e) 4.1 ± 0.5 mK, (f) 3.7 ± 0.7 mK. The insets show CCD images of the ion strings.

7.4.4 Localization of multi-dimensional ion crystals

The next step was to localize more complex ion structures of more than one dimension, and thus we have studied the localization of ions in a two-dimensional 4-ion ZigZag crystal and a three-dimensional 6-ion octahedron crystal (see insets of fig. 7.20).

7.4.4.1 Experimental setup and sequence timing

The experiments for multi-dimensional crystals are performed in a way similar to the ion string localization experiments. In the experimental sequence the Doppler-cooling part is extended to 112 μs in order to stabilize the ion configurations with lower total 397 nm power. The optical pumping length is still 25 μs, but was not tested and thus, it is unsure whether the efficiency of the OP process was as high as for the ion strings. The total sequence length is 150 μs, and as the camera is still exposed for 30×10 s the total number of sequence repetitions is 2×10^6. The axial and radial trap frequencies for the two-dimensional 4-ion ZigZag are $2\pi \times$ (80 and 160) kHz, respectively, and for the three-dimensional 6-ion crystal they are $2\pi \times$ (110 and 180) kHz.

For both crystal structures we applied a small voltage to one pair of diagonal electrode rods, inducing a small asymmetry in the radial trapping potential, in order to better stabilize the structures in a fixed configuration as seen by the imaging system. This small modification leaves only two configurational possibilities for the structures. The ZigZag structure aligns along one of the diagonal electrode planes ($(\tilde{x}, z)$ or $(\tilde{y}, z)$ planes in fig. 2.1) and thus, the CCD camera images these ions at an angle of 45°.

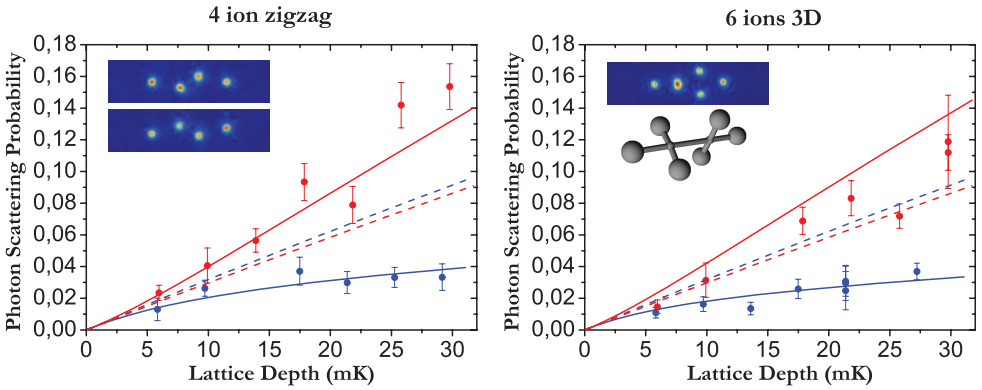

(a) (b)

Figure 7.20: Photon scattering probability per ion as a function of the optical potential depth for two configurations of $^{40}Ca^+$ ions; (a) a two-dimensional 4-ion ZigZag crystal (inset shows CCD images of the two possible orientations), (b) a three-dimensional 6-ion octahedron crystal (inset shows a CCD image and a 3d-sketch of the ions). Measured scattering from red and blue detuned lattices are plotted together with a fit to the analytical model (full lines), resulting in initial ion temperatures of: (a) 2.9 ± 0.5 mK, (b) 2.1 ± 0.5 mK. Due to un-complete optical pumping, these experiments are not completely reliable, but still shows the splitting that indicates a localized ion system. The dashed lines show the theoretical scattering probabilities for delocalized ions.

The octahedron crystal on the other hand is stable in the (x, z) or (y, z) planes (see inset of fig. 7.20(b)). Swapping between the two possible configurations typically occurs for the ZigZag at a rate of 1.3/s, while for the 3d structure it is ~ 0.5/s. If we assume that the structures relaxes quickly after a swap, it is a good approximation to assume that the ions are in a comparable configuration in almost every sequence run.

7.4.4.2 Experimental results

Fig. 7.20(a) shows the scattering probability as function of lattice depth for the ZigZag structure, while fig. 7.20(b) shows the same for the three-dimensional structure. The scattering levels are comparable to the strings, but the data is more noisy. One explanation is possibly imperfect optical pumping that could cause the unevenness seen especially on the red-detuned data. A new optimization of the OP process for these structures together with new measurements of the localization is under progress. Nevertheless, we still observe an unambiguous localizing effect on both structures, as the signals obtained with red- and blue-detuned lattices split up as the lattice depth is increased. The fits are again performed using the analytical model and only using the lower points with limited scattering signal (< 0.07 and < 0.04, respectively), and yield initial temperatures of 2.9 ± 0.5 mK (ZigZag) and 2.1 ± 0.5 mK (3d). Again the red and blue dashed lines indicate the expected level for delocalized ions.

7.4.5 Discussion and conclusion

In order to quantify the degree of localization, the splitting between the red- and blue-detuned signals are compared for the highest experimental lattice depth of 29.5 mK. Fig. 7.21 presents the scattering probability per ion vs. the number of ions, for all the different ion structures that we have studied so far. The data of the two detunings (full red and blue) are plotted together with the model predicted scattering (light red and blue). The initial temperatures, obtained from a fit to the single ion analytical model, are indicated above the figure. The combined results show that all the ion systems can be confined in an optical potential of a far detuned standing wave lattice field, as all sets of detunings clearly separate far from the delocalized level (indicated by the horizontal dashed lines).

We need to emphasize that in all the considered ion structures any excess micromotion is expected to have a detrimental effect on the localization, as described in sec. 7.3.5 for the single ion case. If anything, multi-ion structures, such as the 8 ion string of fig. 7.19(f), are expected to be more sensitive to any residual axial micromotion than single ions, as the interaction between the ions is more likely to introduce anharmonicities in the potential seen by the individual ions and as excess micromotion has to be minimized over a larger region. Multi-dimensional structures may be even more sensitive, as they contain ions that are located away from the RF field-free axis and which will always experience a driven micro-motion in the radial direction. By measuring the distance of the ions from the trap axis and assuming a driven motion in a harmonic potential, we can use the q-parameter and eq. 2.29 to estimate the micromotion amplitude and hence find its kinetic energy. The kinetic energy of the radial micro motion for the configurations of fig. 7.20 is ~ 160 mK for the ZigZag and ~ 750 mK for the octahedron crystal. This is substantially larger than the axial thermal energy (2-5 mK) and the obtained depth of the optical trap potential

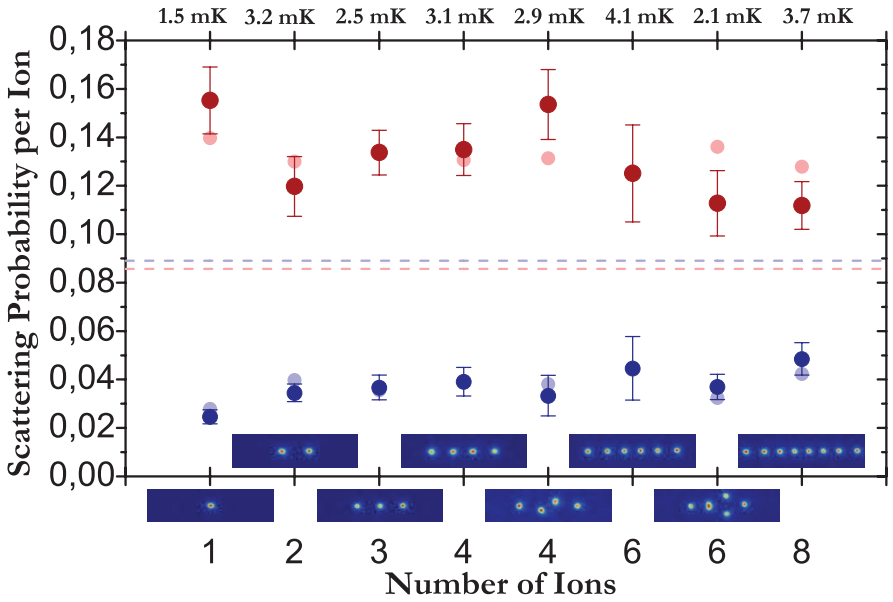

Figure 7.21: Photon scattering probability for all the ion structures that we have studied so far. The experimental results are shown for red- and blue-detuned lattices at 29.5 mK lattice depth. The light red and blue circles represents the fit results to the theoretical model for this lattice depth, and the fit-parameter of initial temperature is displayed above the graph. Dashed lines give the theoretically predicted level for completely delocalized ions.

(up to 34 mK). The fact that we still see a localizing effect under these conditions, indicates that the axial and radial motional degrees of freedom are uncoupled enough not to substantially disturb the interaction with the lattice potential.

While these experiments clearly demonstrate sub-wavelength localization, the interaction time in the lattice potential were intensionally kept short (μs) in order to demonstrate the agreement with the theoretical expectations. This time could be increased by increasing the detuning of the lattice field further (which requires more laser power) or by lowering the initial ion temperature through better cooling. An alternative scheme would consist in operating on the $4S_{1/2} \rightarrow 4P_{1/2}$ or $4S_{1/2} \rightarrow 4P_{3/2}$ transitions (see fig. 2.2). These offer a larger coupling strength between the ion and the lattice, but, more importantly, the scattering from the lattice field brings the ion back to the $4S_{1/2}$ ground-state, which is also where the lattice potential is applied. As demonstrated in [82], this would open the possibility to perform Raman cooling in the lattice and substantially suppress the diffusion of the ions. With this at hand, investigations could be performed on the dynamics of ion crystals in dissipative lattices or ion crystal-based cavity optomechanics experiments.

In conclusion, we demonstrated sub-wavelength localization of multi-dimensional ion structures in an intracavity optical lattice potential. The effect was investigated for one-dimensional strings of ions (1-8), a two-dimensional 4 ion ZigZag structure and a three-dimensional 6 ion structure. The results are in agreement with a simple one ion scattering model, as a requirement in the experiments was on average to only

scatter much less than one ion per cycle. At the same time it demonstrates that the localization effect is not inhibited by the crystal structural dimensions and the residual micromotion, even when the kinetic energy of the radial RF motion is much larger than the ion energy in the lattice potential. Consequently, this study is an important step towards the implementation of cold solid-state models with ions or the control of the crystalline structure of Coulomb crystals.

Chapter 8

Future aspects

In this chapter we consider some possible future aspects of the experimental projects described in the thesis. First (sec. 8.1) we will discuss how to implement the localizing lattice potential into experiments with large ion Coulomb crystals, and what will be needed in order to actually increase the strong coupling to an intra-cavity probe field. In sec. 8.2 we will describe how we intend to implement experiments with the quantum memory of light in the current experimental setup. In doing so, we describe an optical setup build to produce the probe and control field pulse-shapes, which has partly been tested to fulfill our requirements, and furthermore, we will introduce the expected limitations on our ability to detect any out-going photon states from the memory.

8.1 Enhancing the cavity coupling with localized ions in a Coulomb crystal

One of the most important future aspects for the localization of ions in a standing wave field is to apply the scheme to a large ion Coulomb crystal, in order to increase the coupling to a probe standing wave field. Doing so, the strong coupling could be increased further than possible for randomly positioned ions. By applying the lattice field along the axial direction as in the experiments described in this thesis, the ions in the crystal can localize in pancake-shaped slices in the radial direction, with a number of ions in each well.

Using the same lattice properties as for the localization of a few or single ions (in sec. 7.3-7.4) will not make this possible though. The length of the coulomb crystal ($>$ 1 mm) will cover an area that is typically bigger than the beating between the lattice standing wave and the probe standing wave (for $\Delta_l = 60$ FSR, $\lambda_{beat} \sim 200$ μm); see e.g. sec. 6.2. This dephasing effect is what we employ to find the center of the cavity using the ion crystal as an imaging medium. In this context though, if we assume that all ions in the crystal have been localized in the lattice potential along the cavity axis, the dephasing will smear out the probe field coupling as the field intensity seen by the ions will vary for the different lattice sites along the crystal length. On fig. 8.1 a lattice potential (red) is illustrated and we imagine that some ions (green) have been localized in each lattice well along the potential. On the top

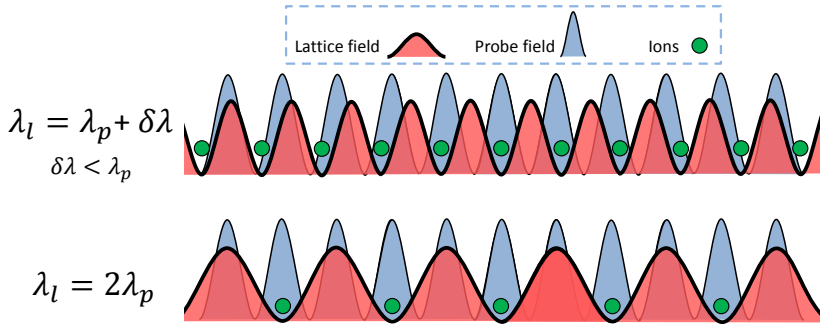

Figure 8.1: Illustration of localization for many ions (green), e.g. in an ion Coulomb crystal, in a lattice potential (red) and simultaneously interacting with a resonant probe field (blue). *Top*: a dephasing between the lattice potential and the probe field standing wave arises when the difference in wavelength is smaller than the probe wavelength. This will smear out the increase in probe coupling induced by the localizing effect on the ions. *Bottom*: When the lattice wavelength is exactly twice the probe wavelength, the localized ions will be situated at every second probe-field anti-node, always seeing a high probe field and the coupling will be significantly increased.

figure the lattice detuning is small compared to the wavelength of the probe field (like in the experiments described in this thesis), thus the two wavelengths only differ by a small $\delta\lambda$. This causes the dephasing to average out the increased probe coupling and the collective coupling to the whole ion crystal will be comparable to a completely delocalized situation. When increasing the detuning of the lattice field, the beating period gets smaller and smaller and hence, this issue gets destructive.

A possible solution to this dephasing effect is to apply a lattice standing wave field with a wavelength twice the wavelength of the probe field. In this way all the localized ions have a well-defined position that is correlated with every second anti-node of the probe field standing wave (see fig. 8.1 lower illustration). This will ideally increase the ion-cavity coupling to the probe field. For the single ion localization we found that the coupling could be increased from 50% (delocalised) to $\sim 81\%$ in the highest lattice potential. We can try to apply this result to the ion Coulomb case, assuming that each ion is localized as a single ion and is unaffected by Coulomb interactions. This results in an effective change in the single ion coupling rate as: $g^2 \to \xi g^2$, where $\xi = 80\%/50\% = 1.6$ is the increased coupling parameter. Hence, the cooperativity, $C = (Ng^2)/(2\kappa\gamma)$, will increase through the same factor. Related to the quantum storage process of chap. 4, the maximum combined write-read efficiency, $\eta = (2C/(1+2C))^2$, will hence grow. As found in e.g. [158, 159] the efficiencies can be expected in theory to exceed 90%

For the present storage scheme, where the $3D_{3/2} \leftrightarrow 4P_{1/2}$ transition at 866 nm is used, the double wavelength optical lattice should be produced by a 1732 nm laser field. This can be achieved e.g. using a commercial laser diode. In order to reach lattice depths comparable to what was studied in the current experiments (~ 30 mK), we need a Rabi frequency on the order of $> 2\pi \times 105$ GHz and thus, if we assume a focused beam-waist of ~ 40 μm the laser power needs to be > 500 W. It is hard to achieve this using free-running counter propagating beams and hence, in order to

create this standing wave lattice field the cavity mirrors would have to be exchanged to very high reflecting mirrors, coated for 1732 nm light.

As an alternative, we are at the moment building up a new cavity trap incorporating a high finesse optical cavity ($\mathcal{F} > 10^4$) resonating at the $4S_{1/2} \leftrightarrow 4P_{1/2}$ transition at 397 nm (see fig. 2.2). At the same time the coating on the cavity mirrors has been designed so as to also be resonant for the double frequency, 794 nm. The trap design is quite similar in terms of dimensions and geometry to the one described in this thesis. In this trap-cavity setup the optical lattice with twice the probe wavelength is directly applicable. One of the advantages in using the 397 nm transition for the cavity-ion coupling is the stronger achievable force as a result of the stronger dipole element of this transition. This results in a higher coupling strength g and unit cooperativity (C=1) should be achievable for ≤ 10 ions. Furthermore, when creating an optical lattice in this trap longer interaction times can be obtained as all scattering on the lattice field will bring the ions back into the ground $S_{1/2}$, which is exactly the state to which the lattice is applied. In fact, using Raman cooling processes in the lattice provides a way of lowering the temperature of the ions, and hence, enhance the localizing effect. This might make it possible to study simulations of solid-state systems such as the Frenkel-Kontorova model [98, 99]. Other interesting studies that are expected to be performed in this trap system is more precise investigations of thermodynamical properties of Coulomb crystals compared to sec. 6.1, optomechanical studies of the interaction between ion Coulomb crystals and the cavity field [37, 38, 199] and cavity assisted cooling of ion Coulomb crystals [200].

8.2 Considerations and future prospects for quantum storage

In this section we present some preparative steps and considerations for the future quantum storage experiments in the existing setup. In sec. 4.2.4 we introduced the general impedance matching conditions between the probe and control fields that constrain their temporal shapes and in sec. 4.3 we described the practical quantum memory implementation in the current ion-cavity trap system. As a typical choice for the probe pulse shape we use the *sech* function with width T [61, 158, 159]:

$$\Phi_{in}(t) = \sqrt{\frac{1}{T}}\mathrm{sech}\left(\frac{2t}{T}\right) \ . \tag{8.1}$$

The optimal control field shape that maximizes the mapping of the incoming probe photon-pulse into the atomic excitation during the writing phase (i.e. that maximizes the dark state amplitude) can be found using eq. (4.7), and gives

$$|\Omega_c(t)| = \sqrt{\gamma_{ab}(C+1)}\frac{|\Phi_{in}(t)|}{\sqrt{\int_{-\infty}^{t} \mathrm{d}t' \, |\Phi_{in}(t')|^2}} \tag{8.2}$$

$$= \sqrt{\frac{\gamma_{ab}(C+1)}{T}}\frac{2}{\sqrt{1+\mathrm{e}^{4t/T}}} \ , \tag{8.3}$$

where γ_{ab} is the atomic dipole decay rate of the probe field transition (see fig. 4.2). This is thus the control pulse-shape that theoretically gives the highest writing efficiency, if ground state decay is neglected during the writing phase. For an illustration

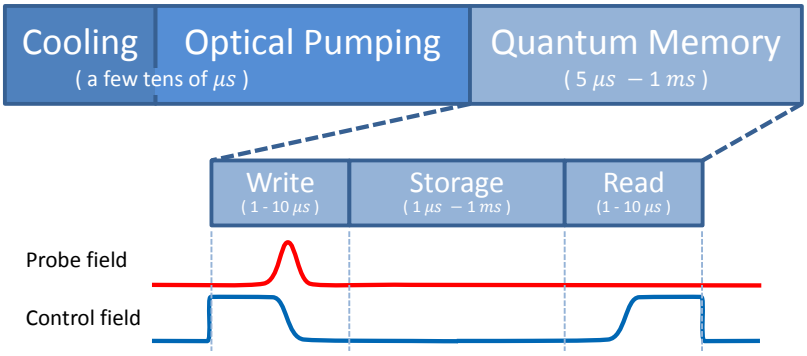

Figure 8.2: Expected experimental sequence for performing quantum storage of light pulses within our ion crystal-cavity system. Doppler cooling of the ions lasts ~ 5 μs followed by optical pumping for ~ 25 μs into the $3D_{3/2}, m_j = +3/2$ sub-state. The quantum memory part can have various lengths, mostly depending on the storage time (μs−ms). The lower lines show the temporal shapes of the probe field pulse (red) and the control field (blue) during all three parts of the storage process.

of the shapes see fig. 4.4 where the complete storage process is shown. During the read-out, the evolution of the control field is reversed, by letting $t \rightarrow -t$, and the stored photon is released with a similar shape as the incoming photon. Using a different control field shape during read-out would result in a different probe output shape related through the impedance matching condition (eq. (4.7)).

The expected experimental sequence for the quantum memory studies is illustrated on fig. 8.2. The medium is a large ion Coulomb crystal with as large a number of interacting ions as possible, eventually obtained by using a two-component ion Coulomb crystal. Similar to the experiments of sec. 6.1.2 and prior EIT studies [73], the cooling and optical pumping parts can be expected to have durations of a few tens of microseconds. After having pumped all ions into the $m_j = +3/2$ substate of $3D_{3/2}$ the quantum memory protocol is performed. The high control field amplitude is lowered with the chosen temporal shape at the same time as the probe pulse is injected into the cavity. During read-out the control field amplitude is increased again to the high level with the reversed temporal shape. Experiments should be performed as function of the length of the storage time, which we should ideally be able to vary from $\sim \mu$s to ∼ms, and hence observe how the efficiency of the total protocol depends on dephasing effects during storage.

8.2.1 Pulse-shaping setup

In order to produce the quantum memory pulses in a flexible way, we have built an optical setup with two fast switching AOMs[1], with the possibility of controlling the two fields independently in frequency and amplitude (see fig. 8.3). Due to the fact that EIT is achieved between Zeeman sublevels, the frequency difference between control and probe fields is small (∼MHz) and if one can use the same laser to generate them

[1]Produced by Brimrose, Model no: TEF-270-100-.800, see appendix G

it is easier to ensure a high relative phase stability. As seen on the figure an additional shutter AOM is placed just after the fiber that transfers light from the laser, in order to improve the extinction in the switch-off phase. This is especially important in the sensitive time between storage and retrieval where the collective excitation in the ion crystal should not be perturbed by stray light fields. Then the laser beam is split onto a PBS, and directed to each pulse shaping AOM. On the figure, AOM1 is used to produce the probe field pulse while AOM2 produces the control field pulse. To allow for scanning the frequencies of the probe and control fields independently, we place both pulse-shaping AOMs in a double-pass configuration, by which the beams can be stably coupled into SM fibers although the diffraction angle of the AOM is changed. After each AOM passage we isolate the -1st diffraction order using pinholes, and after the first passage the field polarization is rotated 90° by passing a $\lambda/4$-wave-plate twice through reflection on a flat mirror. This lets the fields pass the PBSs to the direction of two SM fibers transferring the light fields to the experiment. In addition, the probe field is overlapped with the cavity reference field at 894 nm and both fields are sent into the experimental cavity from the PT side (see fig. 5.4). The control field is coupled into the cavity from the HR side.

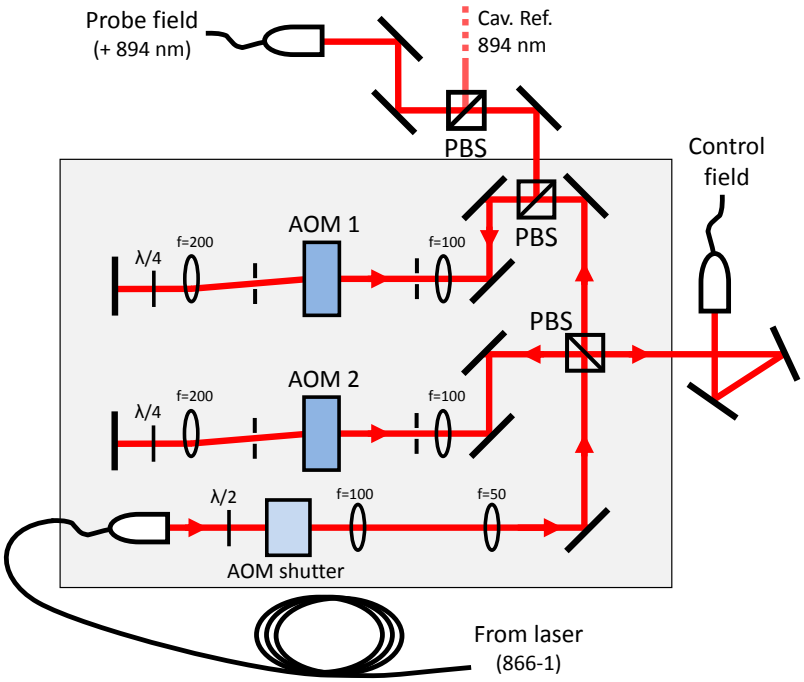

Figure 8.3: Schematics showing the pulse-shaping setup. The control and probe pulses are generated using two AOMs in double pass together with an additional shutter AOM that minimizes the any remaining field during the storage-time. Each beam is coupled into a fiber that transfers the light to the trap-table, where the pulses enters the cavity from opposite directions.

In the experiments the expected temporal pulse variations are on the μs scale and consequently the AOMs need to be able to shut much faster, by which we require their rise-times to be < 100 ns. The AOMs are connected to an RF-amplifying Direct Digital Synthesizer (DDS)[2] box on separate channels (DDS1 and DDS2) and through an input in this box the control voltage can be varied. DDS1 generates an RF-signal with a frequency between 215-265 MHz and is connected to the probe field AOM, while DDS2 (connected to the control field AOM) has frequencies between 200-255 MHz. The DDS has a linewidth < 10 Hz and a frequency resolution of $\simeq 1$ Hz and this is sufficiently smaller than the width of the EIT window (a few kHz) to employ the system in the quantum memory experiments. The exact frequency of the individual DDSs can be set from a computer (connected trough a RS232-port). The size of the amplification can be set manually on the DDS box using a dial while the control voltage is applied through an external BNC-input between 0V and 5V. To produce the pulse-shapes we connect to this input a function generator[3] connected to a computer interface, where the time-variation can be preset very accurately (1-2 ns between amplitude points). The same generator is used to control both pulse-shaping AOMs and the shutter AOM which receives a simple TTL signal. The whole pulse-shaping system can be triggered from the existing sequence used in prior experiments.

	Single pass [%]	Double pass [%]	Rise time [ns]
AOM1	44.0 ± 0.6	18.4 ± 0.4	43 ± 2
AOM2	51.8 ± 0.7	26.6 ± 0.5	45 ± 3
Shutter	51.7 ± 0.8	-	160 ± 11

Table 8.1: The AOM diffraction efficiency in single and double pass for the pulse-shaping setup, together with the rise-time of the individual AOMs. The values are an average of several measurements, which also accounts for the uncertainty.

All three AOMs were optimized and the resulting diffraction efficiencies are shown in table 8.1. The pulse-generating AOMs are specified to have optimal efficiencies for RF-powers of about 2 W, but unfortunately the DDS-box can only deliver a maximum power of 0.47 W (DDS1) and 0.57 W (DDS2), respectively. The diffraction efficiencies are thus not optimal, but as the laser intensities are well above what is required for the quantum storage experiments this is not a problem. The shutter AOM is driven with a 32 MHz driver with 4 W RF-output. Furthermore, the rise-time of each of the AOMs have been measured by applying a square pulse from the function generator, going from 0 to 5 V in ~ 19 ns. In table 8.1 the time from 10% to 90% of the maximum signal has been specified for each AOM. The results are obtained from several scans and the rise-time of the electric signal has been removed by fitting to a convolution of two rising-signals from error-functions. The response time of the detector[4] is small enough to be ignored (max 1 ns). From the data sheet of the pulse-shaping AOMs the rise-time is specified to 42 ns (see app. G), which is comparable to our measurements, and this will be sufficient to create experimental pulses on time-scales of $\gtrsim 0.5$ μs, for the quantum memory protocol. The rise-time of the shutter AOM is not as low as the

[2] A type of frequency synthesizer used for creating arbitrary waveforms from a single, fixed-frequency reference.

[3] TTi Arbitrary Waveform Generator - TGA1244.

[4] Thorlabs, DET10A

other AOMs, because the beam size inside it is relatively large (unfocused), but as it only needs to shut the beams on or off outside the pulse-period in order to ensure a good extinction, its rise time is not critical.

On fig. 8.4 a time scan of the whole pulse-shaping sequence, created using the AOM setup and measured optically using fast photo detectors, is shown. The blue curve shows the control field shape and the red curve shows the probe pulse, both created with the shapes defined above and with the width $T = 2$ μs. In the quantum memory experiments the timing between the probe and control field pulses needs to be optimized, by moving one pulse compared to the other in time. The green TTL signal shows the electric signal which is sent to the shutter AOM and the time between the rise of this signal to the rise of the optical control field signal shows the delay of the shutter AOM ($\sim$ 1.8 μs). Using a self-written software the function generator can be set to create the needed pulse widths of 0.1 μs$-$10 μs and vary the storage length between 1 μs and 1 ms. On the figure all the signals have been normalized to illustrate the shapes, but in the actual quantum memory experiments we can achieve the correct amplitudes of the pulses, by inserting ND-filters in the beam paths.

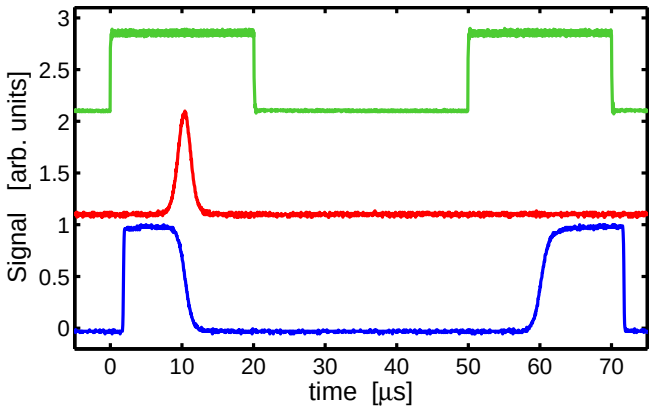

Figure 8.4: Optical measurement of the quantum memory pulse sequence as function of time. The pulse width was set to $T = 2$ μs and the storage time is 45 μs. *Blue curve*: Control field variation, *Red curve*: probe pulse shape, *Green curve*: electric signal sent to the AOM shutter. All signals has been normalized to unity amplitude.

To optimize the pulse-shaping and in order to determine the AOM's ability to reproduce the signals applied from the function generator we have performed some tests on the system. In a first test we measured the *sech*-pulse from the probe AOM as a function of the voltage input signal amplitude. On fig. 8.5 a number of scans can be seen. To the left, the electrical voltage signal is plotted as function of time, normalized to the maximum value. The corresponding amplitudes for each curve is plotted on the y-axis at the intersection with the low-point of the curves, with values between 0.5 V and 6 V. The red curves show the obtained optical time-variation of the AOM pulse-shape, normalized and placed in equivalence to the electrical curves. It is evident that the optical shape gets distorted if the voltage amplitude is set too high and consequently we choose the maximum voltage amplitude of 3.5 V. Having fixed

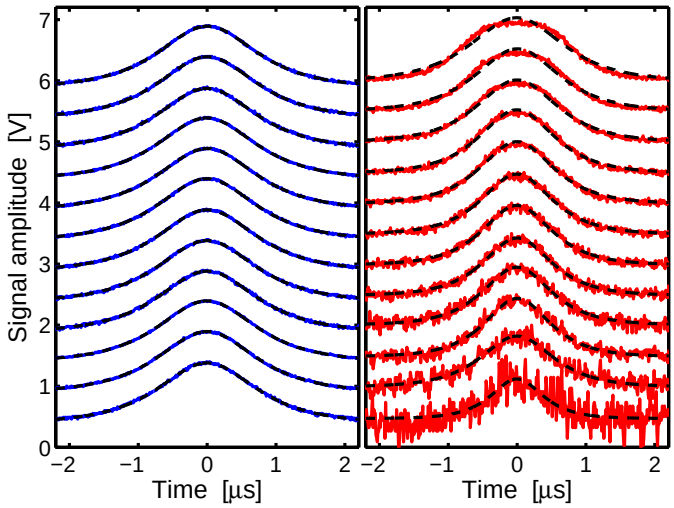

Figure 8.5: *Sech* pulse profiles for various input voltage amplitudes (0.5V to 6V). Left: the electrical signal. Right: the optical signal from the probe field AOM. Both are normalized to unity hight and the black dotted line is a fit to the applied *sech* shape. The optical pulse (red) is distorted for large voltage amplitudes.

this input voltage, the amplitudes of the optical signals can be varied using wave-plates followed by PBSs or by using various different ND-filters in the beam-paths.

In a second test we varied the AOM input laser power for a fixed pulse width and electronic voltage amplitude. Here we observed no deviation in the AOM output shape for input power up to 4 mW which will result in a laser field magnitude beyond what is required in the experiment.

Thirdly, through other tests we observed clear difference between the applied voltage signal width and the width of the actual optical signal. In order to know exactly the shape applied in the experiments we thus need to create a calibration of the shape set by the computer software. Hence, we created pulses using the function generator with widths T_{sig} and passed the voltage shape on to one of the AOMs. The optical output was measured with a fast photo-detector and the width (T_{opt}) could be found from a fit to the data. On fig. 8.6(a) a single pulse-scan of the probe AOM (through DDS1) is shown for an applied *sech* signal of width $T_{sig} = 5$ μs. The fit to the measurement gives the optical width of the pulse $T_{opt} = 3.6$ μs. This relative difference in width needs to be accounted for in order to reliably produce the correct shapes for the experimental studies. On fig. 8.6(b) T_{opt}, found from fits to the optical signal as the above, is plotted against T_{sig} for widths varying from 0.5 μs to 10 μs. The errorbars from the optical shape fits are within the markers. The blue line on the figure represents a linear fit to the data, that gives the connection $T_{sig} = 1.374(2)T_{opt} - 0.044(8)$, hence we have created a calibration that makes it possible to find the electrical voltage signal that should be sent to the AOM in order to obtain a certain optical signal width. Performing the same calibration on the control-field AOM (using DDS2) we found the calibration $T_{sig} = 1.417(4)T_{opt} - 0.052(9)$.

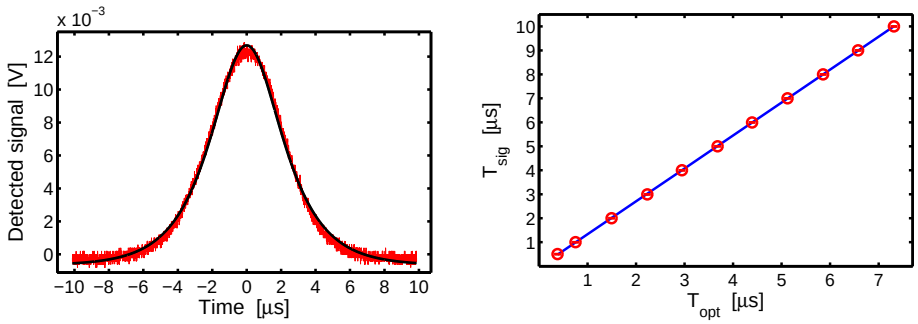

(a) (b)

Figure 8.6: (a) A single optical pulse scan from the probe AOM. The applied electrical signal has a width of $T_{sig} = 5$ μs while the fit to the optical signal (black line) gives a width of $T_{opt} = 3.6$ μs. (b) The connection between the applied electrical signal widths T_{sig} and the resulting optical width T_{opt} of the probe pulse. The blue line is a linear fit to the data that gives a calibration curve which is applicable for the quantum memory experiments.

In the final quantum memory experiments it is crucial that the pulses arrive at the medium with a well-defined temporal relation. Consequently, another important test is to determine the magnitude of the time jitter between pulses generated from the two AOMs. The function generator will be triggered using a single input and hence, the jitter in the optical signal is entirely due to the individual response time of the AOMs. Preliminary measurements have shown jitters on the order of $t_{jitter} = 0.6$-1.5 ns, depending on the pulse widths. These values are much smaller than the pulse widths and therefore they do not raise any concerns in achieving reliable pulses.

A last crucial test that needs to be performed on the system is a measurement of the extinction of the probe and control fields after the pulse-generating setup and subsequent fibers. This measurement should be performed carefully before starting the quantum memory experiments in order to ensure that the field intensities are low enough during the storage time.

8.2.2 Expected photon detection during read-out

To estimate the signal that we can obtain during the read-out process, we have to consider the expected field strengths of the probe and control fields. Ideally, we want the probe field to only contain one photon per pulse on average. This means that we can define the incoming temporal photon shape, proportional to the probe Rabi frequency squared (like in eq. 8.1), as

$$n_{p,in}(t) = n_{p,max}\frac{1}{T}\mathrm{sech}^2\left(\frac{2t}{T}\right) , \tag{8.4}$$

where we can choose $n_{p,max} = 1$ when the pulse contains only one photon on average. To get the total number of photons in the probe pulse for a time-interval $t_1 \rightarrow t_2$ we

integrate this:

$$N_{p,in} = n_{p,max}\frac{1}{T}\int_{t_1}^{t_2}\mathrm{sech}^2\left(\frac{2t'}{T}\right)\mathrm{d}t' \ . \tag{8.5}$$

Integrating over the complete pulse ($-\infty \to \infty$) we obtain $N_{p,in} = n_{p,max} \equiv 1$.

To give an estimate of the photon number in the control field we note here a result obtained by simulating the quantum memory protocol from [158, 159], where the optimal control field Rabi-frequency during read-out was found to have the temporal shape

$$\Omega_c(t) = A_\Omega\sqrt{\frac{\gamma_{ab}(1+2C)}{T}}\frac{2}{\sqrt{1+\mathrm{e}^{-4T_\Omega t/T}}} \ , \tag{8.6}$$

where $A_\Omega = 2.4$ and $T_\Omega = 1.2$ has been found trough the numerical optimizations [158]. The number of control field photons in the cavity can be found as the square of the Rabi frequency:

$$n_c(t) = n_{c,max}\frac{1}{1+\mathrm{e}^{-4T_\Omega t/T}} \ . \tag{8.7}$$

Here the number of control field photons when the field is at maximum can be found as $n_{c,max} = (\sqrt{6}\Omega_{c,max}/g)^2$, where the $\sqrt{6}$ comes from the Clebsch-Gordan coefficient of the considered $3D_{3/2}, m_j = -1/2$ sub-state. For the control field, the total number of intra-cavity photons in a time-interval is

$$N_c = \int_{t_1}^{t_2} n_c(t')\mathrm{d}t' \ . \tag{8.8}$$

For the future quantum memory experiments we can now estimate the expected detection efficiency and especially we are interested in comparing the number of photons exiting the cavity during read-out from the two fields. A sketch of the setup is shown on fig. 8.7. During read-out the probe field output exits the cavity trough the PT mirror, is reflected off the Glan polarizer and coupled to the APD using a single-mode fiber. If we assume to have stored a single probe photon in the quantum memory system we can take the efficiency of both the writing and reading process into account by multiplying the photon number with $\eta_{mem} = \left(\frac{2C}{1+2C}\right)^2$ and in addition we can include losses of the cavity field by multiplying with $\eta_{cav} = \left(\frac{\kappa_1}{\kappa}\right)^2$. Here, $\kappa_1 = 2\pi \times 1.5$ MHz is the decay rate through the PT mirror and $\kappa = 2\pi \times 2.2$ MHz is the total cavity field decay rate. Thus, the detected number of probe photons read out from the memory is

$$N_p^{det}(t_2) = \eta_{mem}\eta_{cav}n_{p,max}\frac{1}{T}\int_{t_1}^{t_2}\mathrm{sech}^2\left(\frac{2t'}{T}\right)\mathrm{d}t' \ . \tag{8.9}$$

Here, the start time of the integration t_1 is fixed, while the end-time t_2 can be varied.

The control field is coupled into the cavity trough the HR mirror with a σ^+ circular polarization. During read-out, ideally, the number of control field photons arriving at the detector (on the other side of the cavity) should be negligible because of the

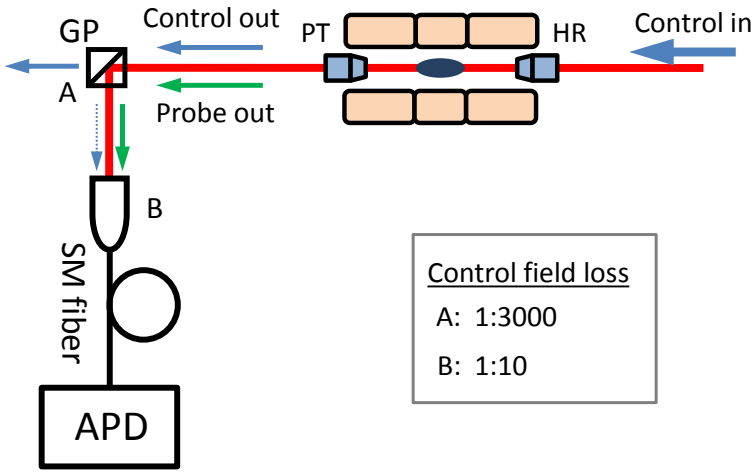

Figure 8.7: Sketch of the detection of the probe and control fields during the read-out phase of the quantum memory protocol. The control field enters the ion-cavity medium through the HR mirror and interacts with the medium by which the out-going probe pulse is created. We detect the photons exiting the cavity on the PT mirror side. The probe field is σ^- circularly polarized, while the control field is σ^+, and the Glan polarizer filters 1/3000 (A) of the control field photons away from the detector. Another 1/10 (B) loss of control field photons occurs at the coupling into the SM fiber transferring light to the APD detector.

Glan polarizer (see fig. 8.7). The polarization of the probe field is σ^- and the Glan polarizer should be able to filter the polarizations of the two fields better than $1:10^5$. In the experimental setup though, the extinction is only $1:3000$, which is attributed to birefringence effects in the mirror substrates that might lead to changes in the polarization of the fields. Furthermore, when the control field enters the SM fiber that goes to the APD detector there is an additional $1:10$ loss because of mismatching in size and direction of the control beam compared to the probe beam. In total, the number of control field photons arriving at the detector is 1/30000 smaller than the photons number exiting the cavity, and thus, the detected number of control field photons is

$$N_c^{det}(t_2) = \frac{2\kappa_1 n_{c,max}}{30000} \int_{t_1}^{t_2} \frac{1}{1+\mathrm{e}^{-4T_\Omega t/T}} \mathrm{d}t' \ . \tag{8.10}$$

Integrating over the whole pulse of both fields reveals that the number of detected control field photons is greater than the number of probe photons. Instead we can choose to end the detection before the pulses have ended and hence, hope to detect substantially more probe field photons than control field photons.

As an example we consider a crystal with an effective number of ions $N = 1500$ and a pulse-width of $T = 2\ \mu$s. From this the cooperativity is $C = (g^2 N)/(2\kappa\gamma_{23}) \approx 8.5$ which gives a maximum number of intracavity control field photons of $n_{c,max} \approx 4000$. On fig. 8.8 the integrated photon numbers (N_p^{det} and N_c^{det}) is shown as the shaded area under the graphs of $n_p(t/T)$ and $n_c(t/T)$ for $t_1 = -2.0T$ and $t_2 = 0.6T$. It is

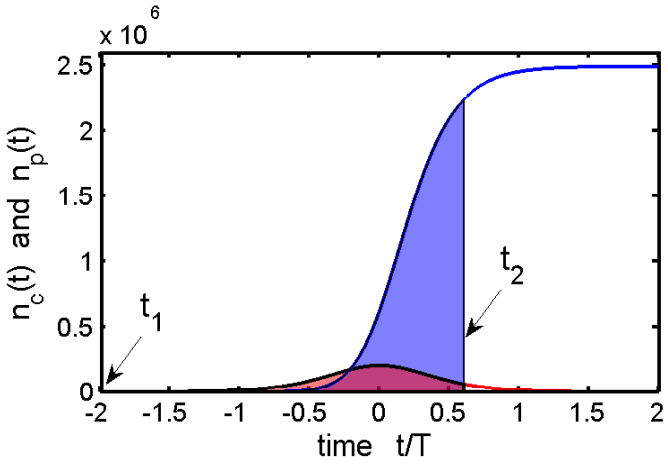

Figure 8.8: The outgoing photon number of the probe ($n_p(t)$) and control field ($n_c(t)$) are shown as function of time, from eq. (8.9) and (8.10) without the integral. The shaded area under the graphs represents the total number of photons in the time span from t_1 to t_2 for the two fields (N_p^{det} and N_c^{det}). All losses described in the text are included in the curves.

clear that the area under the control field curve is much bigger than that under the probe field curve, and hence the control field photons will dominate our detection. By keeping t_1 fixed while varying t_2 we can compare the total photon number of the two fields. In fig. 8.9 the signal-to-noise (S/N) corresponding to "probe-to-control field photon ratio" is shown, defined as

$$S/N = \frac{N_p^{det}}{N_p^{det} + N_c^{det} + N_{bg}} \ , \tag{8.11}$$

where we added a background detection noise N_{bg}, of 100 photons/s due to the APD dark count rate, essentially. Through the variation of the t_2 on fig. 8.9 we can see that the maximum signal-to-noise ratio can be obtained by stopping the measurement at $-0.9T$, and the S/N can be made almost unity. However, we have to take into account the finite efficiency of the detection system ($\sim$ 16%) that sets a limit to how low signals we can measure. Using $t_2 = -0.9T$ the average number of probe photons getting to the detection is only 0.01. If we put a bound on the S/N of 0.8 (only 20% of the detected photons come from the control field) the detection should stop at $t_2 = -0.3T$ which results in an average number of probe photons of 0.1. When starting up the experimental study of this quantum memory system, this quantity (S/N) should be measured in order to determine the best possible probe field detection.

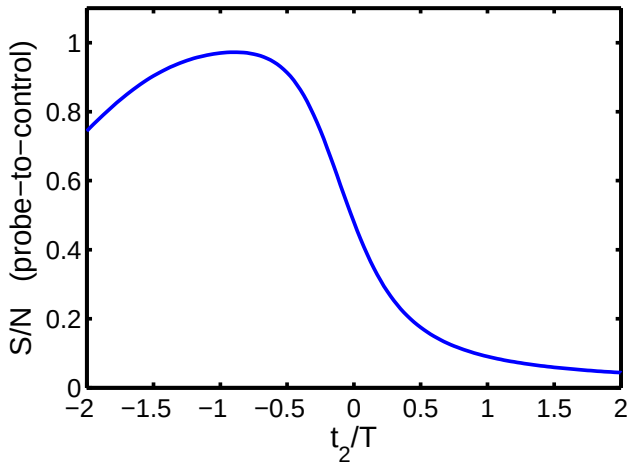

Figure 8.9: The signal-to-noise of eq. (8.11) is plotted as function of the end-time of the measurement (t_2) for a fixed start-time ($t_1 = -2T$). A background noise of 100 photons/s has furthermore been taken into account.

Chapter 9

Summary and outlook

This thesis contains the work that I have done on the CQED experiment with trapped ions during my time as a PhD student in the Ion Trap Group at Aarhus University. The content describes different methods for probing and controlling ion Coulomb crystals by using optical intra-cavity fields which should be applicable to many other experimental studies. My experimental work can be divided into three main subjects: measuring the temperature of ion Coulomb crystals using an optical cavity field at the single photon level, determining the absolute center of a linear Fabry-Pérot cavity using an atomic ensemble as an imaging medium, and localizing single ions and ion structures in a standing wave optical potential.

First, experiments with the purpose of determining the temperature of trapped laser cooled ion Coulomb crystals by coupling the ions to an optical cavity were described. This non-invasive probing method uses the strong coupling of the ions to a single mode cavity field at the single photon level [28]. The coupling scales with the number of ions and, therefore, the method benefits from operating with large ion Coulomb crystals. From changes observed in the cavity resonance spectra the coherent ion-cavity coupling can be determined and using a simple CQED model for the light-matter interaction including the effect of the thermal velocity distribution of the ions one can infer the temperature of the ions. By changing the cooling parameters of the system the ion temperature can be controlled and measured by this technique (see fig. 6.5). So far, we have performed extensive temperature measurements of various crystals with different thermodynamical properties from which we hope to gain knowledge about heating mechanisms in ion Coulomb crystals. A general study of crystal heating at different trapping parameters would be relevant e.g. for the implementation of photon storage in the ion-cavity system in order to determine the optimal crystal shape and size. Furthermore, ongoing studies of the temperatures of the same crystals obtained through independent molecular dynamics simulations should hopefully allow us to conclusively determine the accuracy of the method.

The second set of experiments uses the simultaneous interaction between two resonant intra-cavity fields and an ion Coulomb crystal trapped inside the cavity, to determine the absolute center of a linear Fabry-Pérot resonator. One field is intense and far detuned from an atomic resonance of the ions by which a spatially varying AC stark shift of the energy levels is imposed along the cavity axis. The second field is weaker and close-detuned to the bare atomic transition. In combination, the two

fields create a spatial beating pattern in the fluorescence of the crystal medium that depends on their relative detuning and which can be imaged on a CCD camera. Combining various sets of detunings, and thereby of beat patterns, we have shown that it is easily possible to find the absolute center with a precision of ± 135 nm. Comparing this to the length of the cavity (11.8 mm), the beating patterns (400-700 μm) or the periodicity of the two standing waves (433 nm) shows that this very simple approach is actually rather precise, and could be useful for CQED experiments with cold neutrals or ions.

Another set of experiments described in this thesis presents a method for localizing ions in a standing wave optical lattice potential inside the cavity. The lattice is produced by an intra-cavity field far detuned from atomic resonance, which produces a dipole force on the ions that confines them at nodes or anti-nodes of the standing wave. To find out whether the ions are localized in a lattice well we measured the scattering signal arising when the ions are excited from their internal state in the lattice to another state from which they can again decay down to the ground state. To obtain a clear localization signal, we compared the photon scattering probability for red- and blue-detuned lattices of equal depths. These produce identical potentials as seen from the ions, but a blue-detuned lattice localizes the ions at the nodes, where scattering is suppressed, while a red-detuned lattice localizes the ions at lattice anti-nodes, increasing the scattering. By considering the difference in scattering rates we could infer that a single ion was localized in lattice potentials of up to 34 mK depth, with a capture probability of $\sim 97\%$. By adding another, weaker standing wave field, close to atomic resonance, we were able to show an enhancement in the ion-cavity coupling of this field from the delocalized level coupling (50% of the maximal coupling strength) to $> 80\%$. Similarly, the procedure could be used to decrease the coupling strength between the field and the ions in order to control the interactions with additional potentials from e.g. optical fields, trapping fields, other ions or neutral atoms.

Furthermore, we investigated the possibility of localizing ions in small ion Coulomb crystal structures in the lattice potential. We verified that simultaneous sub-wavelength localization could be achieved for strings of up to 8 ions and have strong indication of localization of two- and three-dimensional structures of up to 6 ions. An interesting application of localizing ions in periodic optical potentials is in the simulation of cold, solid-state models, such as the Frenkel-Kontorova model of friction. Localized ions in an optical lattice could be used to study the sliding-to-pinning phase transition in this model [99, 194]. Another potential application of the ion localization could be to extend it to large ion Coulomb crystals in order to control their macroscopic structure. As proposed in [180] the interaction with the optical potential could be used to steer a phase-transition between various crystalline structures in the crystal, by continuously varying the trap frequencies for a fixed optical potential. So far, only simulations has been performed, but with the current localization tools at hand it might be possible to carry out these experiments in the near future.

The long-term goal of the project I have been working on is to construct a quantum memory for light and the experiments presented in this thesis can also be seen as steps to characterize and improve the ion-cavity system interactions in order to achieve this future goal. The storage of single photon fields in our system has been theoretically investigated initially by PhD student Anders Mortensen and more recently by masters

student Kasper Rothe Zangenberg. Based on the knowledge on the system acquired in past experiments [28,68,74] extensive numerical simulations were performed by Kasper in order to optimize the expected performance of such a quantum memory [158, 159]. The next step is to implement this protocol into the existing experiments. Previously obtained experimental results together with the simulations indicate that realizing a quantum memory with both high efficiency (high probability of retrieving an injected photon) and long storage time (∼ms), should be possible with our system. Moreover, due to the probability of coupling to different cavity modes [74], multi-mode storage could also be investigated.

A special application, proposed for the quantum memory system, is a photon number detector [75–77]. Related to our experiments the proposal of [77] is to use a Coulomb crystal of $^{40}Ca^{+}$ ions placed inside an optical cavity to study a high-efficiency photon number resolving detector, by converting a single stored photon into many fluorescence photons. First, the ions in the ensemble are prepared in their ground state, and a number of photons are subsequently converted into collective excitations in a metastable state of the ions, using EIT based light storage. Finally, the number of collective excitations (corresponding to the initial photon number) is probed by collecting resonance fluorescence on a closed transition to a fourth level. This leads to a noiseless detection with high efficiency and repetition rate.

Chapter 10

Acronyms

AOM	acousto-optic modulator
APD	avalanche photo detector
bcc	body-centered cubic
CCD	charge coupled device
DFB	distributed feedback
EIT	electromagnetically induced transparency
FSR	free spectral range
FWHM	full width at half the maximum
MD	molecular dynamics
PBS	polarizing beam splitter
PDH	Pound-Drever-Hall
PZT	piezo-electric transducer
RF	radio frequency
SHG	second harmonic generation
SM	single mode
CQED	Cavity Quantum Electrodynamics
RWA	rotating wave approximation
TC	Tavis-Cummings model
JC	Jaynes-Cummings model
GP	glan polarizer
STIRAP	Stimulated Raman Adiabatic Passage
DDS	Direct Digital Synthesizer

Appendices

Appendix A

The $^{40}Ca^{+}$ ion

A.1 Abundance of Ca-isotopes

Isotope	Abundance
40	96.941%
42	0.647%
43	0.135%
44	2.086%
46	0.004%
48	0.187%

Table A.1: Abundance of the stable isotopes of calcium [201].

A.2 Transition wavelengths and decay rates

Transition	Wavelength λ	$\Gamma = 2\gamma$	I_{sat} [mW/cm^2]
$4S_{1/2}$-$4P_{1/2}$	396.847 nm	$2\pi\times$ 20.7 MHz	43.3
$4S_{1/2}$-$4P_{3/2}$	393.366 nm	$2\pi\times$ 21.5 MHz	46.2
$3D_{3/2}$-$4P_{1/2}$	866.214 nm	$2\pi\times$ 1.69 MHz	0.34
$3D_{3/2}$-$4P_{3/2}$	849.802 nm	$2\pi\times$ 0.176 MHz	0.038
$3D_{5/2}$-$4P_{3/2}$	854.209 nm	$2\pi\times$ 1.56 MHz	0.33
$4S_{1/2}$-$3D_{3/2}$	732.389 nm	$2\pi\times$ 0.16 Hz	5.3×10^{-8}
$4S_{1/2}$-$3D_{5/2}$	729.147 nm	$2\pi\times$ 0.17 Hz	5.7×10^{-8}

Table A.2: Data for transitions in $^{40}Ca^{+}$, as shown in Fig. 2.2. The first five transitions are dipole-allowed while the last two are quadropole transitions. Transition wavelengths are measured in air [110, 202]. Γ is the transition rate [110, 202]. Saturation intensities are calculated according to $I_{\text{sat}} = \frac{\hbar\Gamma\omega^3}{12\pi c^2}$, using the relevant transition rate Γ and transition frequency ω.

A.3 Clebsch-Gordan coefficients

The coupling strengths for dipole-allowed transitions between the various sub-levels are characterized by the values of Γ given in Table A.2 and the Clebsch-Gordan coefficients (see, e.g., Ref. [147] for a definition), which are listed in Tables A.3–A.5.

	$4S_{1/2}, -1/2$	$4S_{1/2}, +1/2$
$4P_{1/2}, -1/2$	$-\sqrt{1/3}$	$\sqrt{2/3}$
$4P_{1/2}, +1/2$	$-\sqrt{2/3}$	$\sqrt{1/3}$
$4P_{3/2}, -3/2$	1	-
$4P_{3/2}, -1/2$	$\sqrt{2/3}$	$\sqrt{1/3}$
$4P_{3/2}, +1/2$	$\sqrt{1/3}$	$\sqrt{2/3}$
$4P_{3/2}, +3/2$	-	1

Table A.3: Clebsch-Gordan coefficients for transitions between the $4S_{1/2}$ state and the $4P_{1/2}$ and $4P_{3/2}$ states.

	$3D_{3/2}, -3/2$	$3D_{3/2}, -1/2$	$3D_{3/2}, +1/2$	$3D_{3/2}, +3/2$
$4P_{1/2}, -1/2$	$\sqrt{1/2}$	$-\sqrt{1/3}$	$\sqrt{1/6}$	-
$4P_{1/2}, +1/2$	-	$\sqrt{1/6}$	$-\sqrt{1/3}$	$\sqrt{1/2}$
$4P_{3/2}, -3/2$	$-\sqrt{3/5}$	$\sqrt{2/5}$	-	-
$4P_{3/2}, -1/2$	$-\sqrt{2/5}$	$-\sqrt{1/15}$	$\sqrt{8/15}$	-
$4P_{3/2}, +1/2$	-	$-\sqrt{8/15}$	$\sqrt{1/15}$	$\sqrt{2/5}$
$4P_{3/2}, +3/2$	-	-	$-\sqrt{2/5}$	$\sqrt{3/5}$

Table A.4: Clebsch-Gordan coefficients for transitions between the $3D_{3/2}$ state and the $4P_{1/2}$ and $4P_{3/2}$ states.

	$4P_{3/2}, -3/2$	$4P_{3/2}, -1/2$	$4P_{3/2}, +1/2$	$4P_{3/2}, +3/2$
$3D_{5/2}, -5/2$	$\sqrt{2/3}$	-	-	-
$3D_{5/2}, -3/2$	$-\sqrt{4/15}$	$\sqrt{2/5}$	-	-
$3D_{5/2}, -1/2$	$\sqrt{1/15}$	$-\sqrt{2/5}$	$\sqrt{1/5}$	-
$3D_{5/2}, +1/2$	-	$\sqrt{1/5}$	$-\sqrt{2/5}$	$\sqrt{1/15}$
$3D_{5/2}, +3/2$	-	-	$\sqrt{2/5}$	$-\sqrt{4/15}$
$3D_{5/2}, +5/2$	-	-	-	$\sqrt{2/3}$

Table A.5: Clebsch-Gordan coefficients for transitions between the $3D_{5/2}$ state and the $4P_{3/2}$ state.

A.4 Zeeman-splitting

Zeeman-substates will experience an energy shift, ΔE_B, when a magnetic field, B, is present, which is in general given by [193]:

$$\Delta E_B = m_j g_J \mu_B B \tag{A.1}$$

where m_J is the magnetic quantum number, μ_B is the Bohr magneton, B is the magnetic field strength and g_J is the Landé g-factor:

$$g_J = 1 + \frac{J(J+1) + S(S+1) - L(L+1)}{2J(J+1)} \tag{A.2}$$

where L, S and J are the quantum numbers corresponding to the angular momentum, the electric spin and the total angular momentum, respectively. Values of g_J are listed below for the relevant states of the $^{40}Ca^+$ ion.

State	L	S	J	g_J
$4S_{1/2}$	0	1/2	1/2	2
$4P_{1/2}$	1	1/2	1/2	2/3
$4P_{3/2}$	1	1/2	3/2	4/3
$3D_{3/2}$	2	1/2	3/2	4/5
$3D_{5/2}$	2	1/2	5/2	6/5

Table A.6: Values of g_J for the relevant levels of the $^{40}Ca^+$ ion.

Appendix B

Collective coupling strength

B.1 Single ion coupling strength

The coupling strength for a single ion at position $\mathbf{r}$ in the cavity is given by

$$g(\mathbf{r}) = g\Psi(\mathbf{r}) \ , \tag{B.1}$$

where $\Psi(\mathbf{r})$ is the modefunction of the standing wave TEM_{00} mode of the cavity field and where g is the coupling strength of a single ion at the waist and anti-node of this cavity field.

The coupling strength of a particular (dipole allowed) transition for a certain intensity I of the coupling field is characterized by the Rabi-Frequency, which for a transition between the Zeeman-substates $|g\rangle$ and $|e\rangle$ is given by [193]:

$$\Omega_{ge} = a_{ge}\frac{\Gamma}{2}\sqrt{\frac{I}{2I_{\mathrm{sat}}}} = a_{ge}\sqrt{\frac{3\pi c^2\Gamma}{2\hbar\omega^3}}\sqrt{I}, \tag{B.2}$$

where we have inserted the expression for the saturation intensity $I_{\mathrm{sat}} = \frac{\hbar\Gamma\omega_{eg}^3}{12\pi c^2}$ [147], Γ and ω are the transition rate and resonance frequency of the electronic transition (see tab. A.2), and a_{ge} is the Clebsch-Gordan coefficient for the considered Zeeman-substates.

For a single photon cavity field and a single atom the coupling rate g corresponds directly to the Rabi frequency. The single photon intensity in the cavity can be calculated using the normalization condition $IV = \hbar\omega_c$, where ω_c is the resonance frequency of the cavity, $V = \int |\Psi(\mathbf{r})| \, \mathrm{d}\mathbf{r} = \frac{\pi w_0^2}{4} L_c$ is the mode-volume of the cavity, w_0 is the waist of the TEM_{00} mode and L_c is the cavity length. Inserting this into eq. B.2 we find

$$g = a_{ge}\sqrt{\frac{6c^3\Gamma}{\omega^2 w_0^2 L_c}}. \tag{B.3}$$

In our experiments we will use the $\left|3D_{3/2}, m_j = +3/2\right\rangle \leftrightarrow \left|4P_{1/2}, m_J = +1/2\right\rangle$ transition at 866 nm as the probe transition. With the dipole decay rate ad wavelength given in tab. A.2, the Clebsch-Gordan coefficient in tab. A.4 and using the length and waist of the cavity in our experiment, $L_c = (11.8 \pm 0.3)$ mm and $w_0 = 37$ μm [27, 73],

we can calculate the expected single ion coupling rate of the probe transition for an ion located at the anti-node of the standing wave cavity field:

$$g = 2\pi \times (0.532 \pm 0.007) \text{ MHz}. \tag{B.4}$$

B.2 Collective coupling strength

The collective coupling for an ion crystal of uniform density ρ_0 and length L is found analogously to the modevolume

$$\begin{aligned} g^2 N &= \int g^2(\mathbf{r})\rho_0 d(\mathbf{r}) \\ &= g^2\rho_0 \int \Psi^2(\mathbf{r}) d\mathbf{r} \\ &= g^2\rho_0 \frac{\pi w_0^2}{2} \int_0^L \sin^2(kz) dz \\ &= g^2\rho_0 \frac{\pi w_0^2}{4} L \ . \end{aligned} \tag{B.5}$$

The effective number of ions is defined as the sum over all ions in the crystal weighted by the field mode function Ψ_{nm} of the TEM_{nm} mode considered (see sec. 3.2.1), $N_{eff} = \sum_{j=1}^{N_{tot}} \Psi_{nm}^2(\mathbf{r_j})$. Ion Coulomb crystals in a linear RF trap are to good approximation spheroids with length L and radius R and a constant ion density, ρ_0, throughout the whole ensemble (see sec. 2.3). Therefor, we can treat the system as a continuous medium and N_{eff} becomes an integral over the crystal volume V

$$N_{eff} = \rho_0 \int_V \Psi_{nm}^2(\mathbf{r}) \mathrm{d}\mathbf{r} \tag{B.6}$$

The exact expression of eq. B.6 can in general be evaluated numerically for an arbitrary TEM_{nm} mode, by knowing the crystal dimensions, its density and the cavity mode geometry. In most of our experiments we only consider the fundamental TEM_{00} Gaussian mode (see eq. (3.6)).

A typical crystal with large radial extension as compared to the cavity waist ($R \gg w_0$) and a length smaller than the Rayleigh range ($L \ll z_R$) the coupling to the TEM_{00} can be expressed in a simple way extracted directly from eq. (B.5):

$$N_{eff} \simeq \rho_0 \frac{\pi w_0^2}{4} L. \tag{B.7}$$

This definition can be used when estimating the number of ions in the cavity mode in e.g. chap. 6.

This definition does not, however, take the spheroidal shape of the crystal into account and, hence, overestimates the number of ions for very prolate crystals. The correct number of ions within the cavity modevolume is found from a convolution of the crystal shape and the cavity modefunction. For a crystal of length L and diameter

$2R$ the expression reads:

$$\begin{aligned} N_{eff} =& \rho_0 \int_{\text{crystal}} \Psi_{00}^2(\mathbf{r}-\mathbf{r}_0) d\mathbf{r} \\ =& \rho_0 \int_{-x'}^{x'} \int_{-y'}^{y'} \int_{-z'}^{z'} \frac{w_0^2}{w^2(z)} e^{-2((x-x_0)^2+(y-y_0)^2)/w^2(z)} \sin^2(kz)\, dx\, dy\, dz, \end{aligned} \quad \text{(B.8)}$$

where $x' = \sqrt{1-\frac{y^2}{R^2}-\frac{z^2}{R^2}}R$, $y' = \sqrt{1-\frac{z^2}{(L/2)^2}}R$ and $z' = L/2$. x_0 and y_0 are the offset between the center of the crystal and the cavity mode in the radial plane. This expression has been used when evaluating the number of ions interacting with the cavity field in sec. 6.1. For a more detailed description see [27, 73].

Appendix C

Laser systems

Laser	Purpose	Max power	Typical power	Linewidth
272	Photoionization	50 mW	5-30 mW	~ 35 kHz
397	Laser cooling / OP	10 mW	0.1-10 mW	~ 100 kHz
866-1	Laser cooling / Lattice	20 mW	1-6 mW	~ 100 kHz
866-2	Laser cooling / OP / Probe	20 mW	1-5 / 10^{-9} mW	~ 100 kHz
894	Cavity reference	20 mW	10^{-3} mW	~ 100 kHz

Table C.1: Data on various laser systems used in this work. The power level is that available for the experiment.

Appendix D

Complete elliptical integrals of first and second kind

Elliptic integrals originally emerged in integral calculus trough problems of determining the arc length of an ellipse. In modern mathematics an elliptic integral is defined as any function f which can be expressed on the form:

$$f(x) = \int_c^x R\left(t, \sqrt{P(t)}\right) \mathrm{d}t \ , \tag{D.1}$$

where P is a polynomial of degree 3 or 4 with no repeated roots, c is a constant and R is a rational function of two arguments in which both the numerator and the denominator are polynomials. For a comprehensive description see e.g. [203, 204].

Incomplete elliptic integrals are functions of two arguments, whereas, *complete* elliptic integrals are functions of a single argument. The arguments can be expressed in a variety of different but equivalent ways. Two arguments that are often used is ϕ and x, the so-called *amplitude*, which are connected through: $x = \sin(\phi)$. Specifying the value of one quantity determines the other. Elliptical integrals are said to be complete when the amplitude is $\phi = \pi/2$ and thus $x = 1$.

Complete elliptic integral of the first kind

This integral is in general defined as:

$$\mathcal{K}(k) = \int_0^{\pi/2} \frac{\mathrm{d}\theta}{\sqrt{1 - k^2 \sin^2\theta}} = \int_0^1 \frac{\mathrm{d}t}{\sqrt{(1-t^2)(1-k^2t^2)}} \ , \tag{D.2}$$

where $t = \sin\theta$. A special value used in this thesis is $\mathcal{K}(0) = \pi/2$ and the integral can be expressed as a power series like:

$$\mathcal{K}(k) = \frac{\pi}{2} \sum_{n=0}^{\infty} \left[\frac{(2n)!}{2^{2n}(n!)^2}\right]^2 \ k^{2n} \ . \tag{D.3}$$

The integral has the asymptotic expression to third power:

$$\mathcal{K}(k) \approx \frac{\pi}{2} + \frac{\pi}{8}\frac{k^2}{1-k^2} - \frac{\pi}{16}\frac{k^4}{1-k^2} \ , \tag{D.4}$$

for which the precision is better than 3×10^{-4} when $k < 1/2$.

Complete elliptic integral of the second kind

This integral has the form:

$$\mathcal{E}(k) = \int_0^{\pi/2} \sqrt{1 - k^2 \sin^2\theta}\ \mathrm{d}\theta = \int_0^1 \frac{\sqrt{1-k^2t^2}}{\sqrt{(1-t^2)}}\ \mathrm{d}t \ , \tag{D.5}$$

where two special values are $\mathcal{E}(0) = \pi/2$ and $\mathcal{E}(1) = 1$. The integral can also be expressed as a power series:

$$\mathcal{E}(k) = \frac{\pi}{2}\sum_{n=0}^{\infty}\left[\frac{(2n)!}{2^{2n}(n!)^2}\right]^2 \ \frac{k^{2n}}{1-2n} \ . \tag{D.6}$$

Appendix E

Correlation fluorescence measurement of excess micro-motion

To manipulate the interaction between micro-motion and ion localization we control the micro-motion amplitude by adjusting the phase of the RF-drive at the different electrodes (see sec. 7.3.5). In order to measure how micro-motion can influence the ion localization we needed to calibrate the external modification that was imposed on the system into a known micro-motion amplitude. This was done by conventional correlation fluorescence measurements of the excess micro-motion in the axial direction [113].

In our implementation, this was done by trapping a single $^{40}Ca^{+}$ ion and cooling it by mostly illuminating it with a single axial 397 nm cooling beam. A Doppler effect arises if the ion has excess micro-motion and modulates the signal measured by our imaging. Compared to the cooling beam the ion motion is driven by the RF-frequency giving rise to a modulation of the observed scattered during cooling. In order to resolve this fast ($4MHz$) modulation we gated our imaging system with a $\sim 100ns$ short pulses at a rate 0.5 Hz faster than the RF frequency. This pulsed observation aliases the 4 MHz Doppler modulation down to a 0.5 Hz fluorescence fluctuation easily detectable on our CCD camera, as illustrated on fig. E.1. From a Fourier transform of the signal the amplitude can be found, but because of noise non-vanishing Fourier components at the gate-trap offset frequency is expected even with perfect micromotion compensation.

With both random phase noise and a contrast-signal of unknown size, the resulting measure is a sum of the power of the two because the phase between the noise and the signal is random. Signal power scales with the contrast squared and the background can be estimated from Fourier-components different from the signal. The square of the contrast we measure is the square of the noise contrast (background) plus the square of the actual micromotion signal contrast. In this way we can estimate the noise-free signal by subtracting the background noise from the squared of the contrast signal.

By varying the specially designed capacitive loads on the trap electrodes [128] it is possible to add a phase difference between the two axial ends of the trap. This phase-

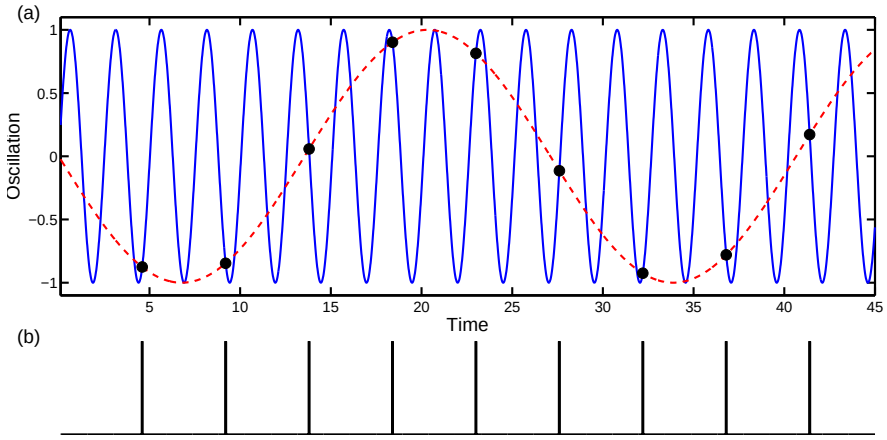

Figure E.1: (a) An ion experiences a fast RF-varying motion (blue curve) which is too fast for our imaging system to resolve. Therefor, we gate the imaging with short pulses ($\sim 100ns$) at a frequency close to the RF-frequency but with a known offset (here exaggerated for illustration), shown as the black vertical lines in (b). This detection aliases the Doppler modulation of the ions down to a slower fluctuating fluorescence signal (red dashed curve in (a)), whose amplitude is measurable trough Fourier transformation, and which resembles the actual RF-amplitude of the ion.

difference will give rise to excess micro-motion in the axial direction. In Fig. 7.13 the results are shown for a scan of end-cap electrode loads from one side of the trap giving rise to a beat-pattern of a certain amplitude. This amplitude is plotted as the squared contrast minus background. From the quadratic fit the load position can be related to the contrast signal. From simple considerations of the effect on the scattering signal obtained from a moving particle affected by an electrical field it is possible to estimate a connection between micro-motion amplitude and the contrast signal. In connection with the correlation fluorescence measurements we can, eventually, find the relation of excess micro-motion to be $3.4nm$ pr. load turn. With this calibration at hand the micro-motion effect on the localization signal can be estimated.

Appendix F

Acceptable signal levels in multi-ion localization experiments

One of the challenges of localizing multiple ions in the scheme presented in this thesis is that, in order to keep all ions in the lattice potential right up until the observation of a fluorescence photon, the total photon number scattered by all the ions in the lattice must be much less than one. To quantify how low this scattering should be we present here a simple calculation.

We assume that each of N ions in a lattice potential has equal probability p of scattering a photon in our experiment. From binomial statistics the average number of photons scattered in an experiment is Np and the probability of scattering no photons in an experiment is:

$$P_0 = (1-p)^N \ . \tag{F.1}$$

The average number of first scattered photons in their experiment is:

$$P_{first} = 1 - P_0 = 1 - (1-p)^N \ , \tag{F.2}$$

since any experiment where we scatter more than 0 photons produces 1 first-scattered photon. So the fraction of detected photons due to first-scattered photons is:

$$R_{first} = \frac{P_{first}}{Np} = \frac{1-(1-p)^N}{Np} \ . \tag{F.3}$$

We can now set a limit for how large a fraction of non-first-scattered photons $(1 - R_{first})$ is acceptable in the experiments and through eq. (F.3) the single ion scattering probability (p) can be determined. As an example, for $N = 4$ ions, if we want to keep the contamination of the signal from second and subsequent photons (after one ion has scattered) below $(1 - R_{first}) = 10\%$, then the single-ion scattering signal must be less than $p = 7\%$. This was exploited for the model fits presented in sec. 7.4.3.2 and 7.4.4.2.

Fig. F.1 shows the fraction of fluorescence due to second and subsequent photons $(1 - R_{first})$, as a function of single-ion scattering signal, p, for $N = 2, 3, 4, 5$ ions.

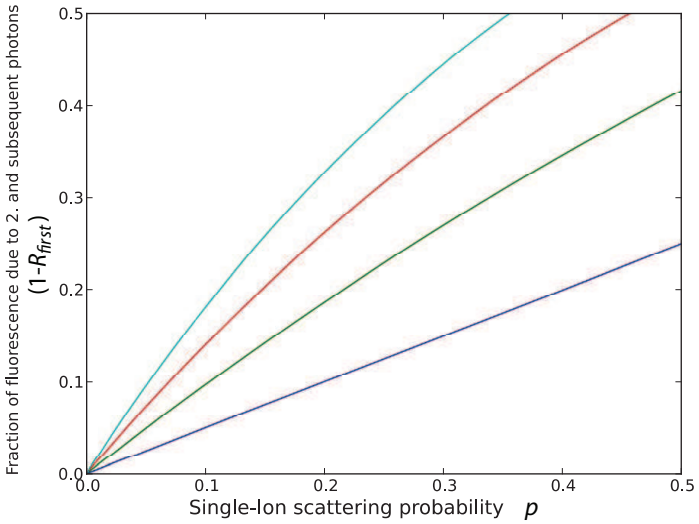

Figure F.1: $(1 - R_{first})$ as function of p for 2 (dark blue), 3 (green), 4(red), 5 (light blue) ions.

Appendix G

Brimrose Corporation of America - AOMs for pulse-shaping

ACOUSTO OPTIC FREQUENCY SHIFTER

MODEL NO.: TEF-270-100-.800

SERIAL NO.: 0903-AO-8862

	SPECIFICATIONS	TEST DATA
Wavelength of Operation	700 – 900 nm	792 nm
Substrate	TeO_2	TeO_2
Optical Power Density	5 W/mm^2	5 W/mm^2
Center Frequency	270 MHz	270 MHz
Bandwidth (3dB)	100 MHz	100 MHz
Active Aperture	0.3 mm	03 mm
Beam diameter inside crystal	0.2 mm	0.2 mm
Rise Time	42 ns	42ns
Optical Transmission	95 %	95%
Diffraction Efficiency	~ 70 %	70 %
Extinction Ratio	> 1000:1	> 1000:1
Wave Front Distortion	$\lambda/10$	$\lambda/10$
Bragg Angle	26 mrad	26 mrad
Separation Angle	51 mrad	51 mrad
Acoustic Velocity	4.2E+3 m/sec	4.2E+3 m/sec
Maximum RF Power	~ 2 Watts	2 Watts
Input Impedance	50 Ohms	50 Ohms
V.S.W.R.	2..1:1	2.1.:1
Optical Polarization	Linear, horizontal or	Vertical
RF Connector	SMA	SMA
Case Type	Air Cooled	Air Cooled

Bibliography

[1] S. Haroche and J. M. Raimond, *Exploring the quantum: atoms, cavities and photons* (Oxford University Press, Oxford; New York, 2006),
URL link.

[2] C. Cohen-Tannoudji, J. Dupont-Roc and G. Grynberg, *Atom-photon interactions : basic processes and applications*, A Wiley-Interscience publication (Wiley, Weinheim, 2004),
URL link.

[3] P. Berman, *Cavity quantum electrodynamics* (Academic Press, 1994),
URL link.

[4] G. Rempe, R. J. Thompson and H. J. Kimble, *Cavity quantum electrodynamics with strong coupling in the optical domain*, Physica Scripta **1994**, 67 (1994),
URL link.

[5] R. J. Thompson, G. Rempe and H. J. Kimble, *Observation of normal-mode splitting for an atom in an optical cavity*, Phys. Rev. Lett. **68**, 1132 (1992),
URL link.

[6] M. Brune, F. Schmidt-Kaler, A. Maali, J. Dreyer, E. Hagley, J. M. Raimond and S. Haroche, *Quantum Rabi Oscillation: A Direct Test of Field Quantization in a Cavity*, Phys. Rev. Lett. **76**, 1800 (1996),
URL link.

[7] A. Badolato, K. Hennessy, M. Atatüre, J. Dreiser, E. Hu, P. M. Petroff and A. Imamoglu, *Deterministic Coupling of Single Quantum Dots to Single Nanocavity Modes*, Science **308**, 1158 (2005),
URL link.

[8] G. Khitrova, H. M. Gibbs, M. Kira, S. W. Koch and A. Scherer, *Vacuum Rabi splitting in semiconductors*, Nat Phys **2**, 81 (2006),
URL link.

[9] A. Wallraff, D. I. Schuster, A. Blais, L. Frunzio, R. S. Huang, J. Majer, S. Kumar, S. M. Girvin and R. J. Schoelkopf, *Strong coupling of a single photon to a superconducting qubit using circuit quantum electrodynamics*, Nature **431**, 162 (2004),
URL link.

[10] I. Chiorescu, P. Bertet, K. Semba, Y. Nakamura, C. J. P. M. Harmans and J. E. Mooij, *Coherent dynamics of a flux qubit coupled to a harmonic oscillator*, Nature **431**, 159 (2004),
URL link.

[11] C. J. Hood, M. S. Chapman, T. W. Lynn and H. J. Kimble, *Real-Time Cavity QED with Single Atoms*, Phys. Rev. Lett. **80**, 4157 (1998),
URL link.

[12] P. Maunz, T. Puppe, I. Schuster, N. Syassen, P. W. H. Pinkse and G. Rempe, *Normal-Mode Spectroscopy of a Single-Bound-Atom-Cavity System*, Phys. Rev. Lett. **94**, 033002 (2005),
URL link.

[13] M. Harlander, M. Brownnutt, W. Hänsel and R. Blatt, *Trapped-ion probing of light-induced charging effects on dielectrics*, New Journal of Physics **12**, 093035 (2010),
URL link.

[14] A. Mortensen, *Aspects of ion Coulomb crystal based quantum memory for Light*, Ph.D. thesis, University of Aarhus (2005),
URL link.

[15] G. R. Guthohrlein, M. Keller, K. Hayasaka, W. Lange and H. Walther, *A single ion as a nanoscopic probe of an optical field*, Nature **414**, 49 (2001),
URL link.

[16] M. Keller, B. Lange, K. Hayasaka, W. Lange and H. Walther, *Continuous generation of single photons with controlled waveform in an ion-trap cavity system*, Nature **431**, 1075 (2004),
URL link.

[17] H. G. Barros, A. Stute, T. E. Northup, C. Russo, P. O. Schmidt and R. Blatt, *Deterministic single-photon source from a single ion*, New Journal of Physics **11**, 103004 (2009),
URL link.

[18] D. R. Leibrandt, J. Labaziewicz, V. Vuletić and I. L. Chuang, *Cavity Sideband Cooling of a Single Trapped Ion*, Phys. Rev. Lett. **103**, 103001 (2009),
URL link.

[19] A. Stute, B. Casabone, P. Schindler, T. Monz, P. O. Schmidt, B. Brandstatter, T. E. Northup and R. Blatt, *Tunable ion-photon entanglement in an optical cavity*, Nature **485**, 482 (2012),
URL link.

[20] M. Steiner, H. M. Meyer, C. Deutsch, J. Reichel and M. Kohl, *Single Ion Coupled to an Optical Fiber Cavity*, Physical Review Letters **110**, 043003 (2013),
URL link.

[21] B. Brandstatter, A. McClung, K. Schuppert, B. Casabone, K. Friebe, A. Stute, P. O. Schmidt, C. Deutsch, J. Reichel, R. Blatt and T. E. Northup, *Integrated fiber-mirror ion trap for strong ion-cavity coupling*, Review of Scientific Instruments **84**, 123104 (2013),
URL link.

[22] P. F. Herskind, S. X. Wang, M. Shi, Y. Ge, M. Cetina and I. L. Chuang, *Microfabricated surface ion trap on a high-finesse optical mirror*, Opt. Lett. **36**, 3045 (2011),
URL link.

[23] F. Dubin, C. Russo, H. G. Barros, A. Stute, C. Becher, P. O. Schmidt and R. Blatt, *Quantum to classical transition in a single-ion laser*, Nature Physics **6**, 350 (2010),
URL link.

[24] Y. Kaluzny, P. Goy, M. Gross, J. M. Raimond and S. Haroche, *Observation of Self-Induced Rabi Oscillations in Two-Level Atoms Excited Inside a Resonant Cavity: The Ringing Regime of Superradiance*, Phys. Rev. Lett. **51**, 1175 (1983),
URL link.

[25] F. Brennecke, T. Donner, S. Ritter, T. Bourdel, M. Kohl and T. Esslinger, *Cavity QED with a Bose-Einstein condensate*, Nature **450**, 268 (2007),
URL link.

[26] Y. Colombe, T. Steinmetz, G. Dubois, F. Linke, D. Hunger and J. Reichel, *Strong atom-field coupling for Bose-Einstein condensates in an optical cavity on a chip*, Nature **450**, 272 (2007),
URL link.

[27] P. Herskind, *Cavity Quantum Electrodynamics with Ion Coulomb Crystals*, Ph.D. thesis, University of Aarhus (2008),
URL link.

[28] P. F. Herskind, A. Dantan, J. P. Marler, M. Albert and M. Drewsen, *Realization of collective strong coupling with ion Coulomb crystals in an optical cavity*, Nature Physics **5**, 494 (2009),
URL link.

[29] A. Lambrecht, E. Giacobino and J. Courty, *Optical nonlinear dynamics with cold atoms in a cavity*, Optics Communications **115**, 199 (1995),
URL link.

[30] A. Lambrecht, T. Coudreau, A. M. Steinberg and E. Giacobino, *Squeezing with cold atoms*, EPL (Europhysics Letters) **36**, 93 (1996),
URL link.

[31] V. Josse, A. Dantan, L. Vernac, A. Bramati, M. Pinard and E. Giacobino, *Polarization Squeezing with Cold Atoms*, Phys. Rev. Lett. **91**, 103601 (2003),
URL link.

[32] V. Josse, A. Dantan, A. Bramati, M. Pinard and E. Giacobino, *Continuous Variable Entanglement using Cold Atoms*, Phys. Rev. Lett. **92**, 123601 (2004), URL link.

[33] J.-F. Roch, K. Vigneron, P. Grelu, A. Sinatra, J.-P. Poizat and P. Grangier, *Quantum Nondemolition Measurements using Cold Trapped Atoms*, Phys. Rev. Lett. **78**, 634 (1997), URL link.

[34] S. L. Mielke, G. T. Foster and L. A. Orozco, *Nonclassical Intensity Correlations in Cavity QED*, Phys. Rev. Lett. **80**, 3948 (1998), URL link.

[35] J. Klinner, M. Lindholdt, B. Nagorny and A. Hemmerich, *Normal Mode Splitting and Mechanical Effects of an Optical Lattice in a Ring Cavity*, Phys. Rev. Lett. **96**, 023002 (2006), URL link.

[36] K. W. Murch, K. L. Moore, S. Gupta and D. M. Stamper-Kurn, *Observation of quantum-measurement backaction with an ultracold atomic gas*, Nat Phys **4**, 561 (2008), URL link.

[37] F. Brennecke, S. Ritter, T. Donner and T. Esslinger, *Cavity Optomechanics with a Bose-Einstein Condensate*, Science **322**, 235 (2008), URL link.

[38] T. J. Kippenberg and K. J. Vahala, *Cavity Optomechanics: Back-Action at the Mesoscale*, Science **321**, 1172 (2008), URL link.

[39] H. W. Chan, A. T. Black and V. Vuletić, *Observation of Collective-Emission-Induced Cooling of Atoms in an Optical Cavity*, Phys. Rev. Lett. **90**, 063003 (2003), URL link.

[40] M. H. Schleier-Smith, I. D. Leroux, H. Zhang, M. A. Van Camp and V. Vuletić, *Optomechanical Cavity Cooling of an Atomic Ensemble*, Phys. Rev. Lett. **107**, 143005 (2011), URL link.

[41] M. A. Nielsen and I. L. Chuang, *Quantum computation and quantum information* (Cambridge University Press, Cambridge; New York, 2000), URL link.

[42] H. J. Kimble, *The quantum internet*, Nature **453**, 1023 (2008), URL link.

[43] D. Deutsch and R. Jozsa, *Rapid Solution of Problems by Quantum Computation*, Proceedings of the Royal Society of London Series a-Mathematical Physical and Engineering Sciences **439**, 553 (1992), URL link.

[44] P. W. Shor, *Polynomial-time algorithms for prime factorization and discrete logarithms on a quantum computer*, Siam Review **41**, 303 (1999),
URL link.

[45] J. I. Cirac, P. Zoller, H. J. Kimble and H. Mabuchi, *Quantum state transfer and entanglement distribution among distant nodes in a quantum network*, Physical Review Letters **78**, 3221 (1997),
URL link.

[46] D. Loss and D. P. DiVincenzo, *Quantum computation with quantum dots*, Physical Review A **57**, 120 (1998),
URL link.

[47] N. A. Gershenfeld and I. L. Chuang, *Bulk spin-resonance quantum computation*, Science **275**, 350 (1997),
URL link.

[48] Y. Makhlin, G. Schon and A. Shnirman, *Quantum-state engineering with Josephson-junction devices*, Reviews of Modern Physics **73**, 357 (2001),
URL link.

[49] D. Leibfried, R. Blatt, C. Monroe and D. Wineland, *Quantum dynamics of single trapped ions*, Reviews of Modern Physics **75**, 281 (2003),
URL link.

[50] J. I. Cirac and P. Zoller, *Quantum Computations with Cold Trapped Ions*, Physical Review Letters **74**, 4091 (1995),
URL link.

[51] A. Sorensen and K. Molmer, *Quantum computation with ions in thermal motion*, Physical Review Letters **82**, 1971 (1999),
URL link.

[52] H. Haffner, C. F. Roos and R. Blatt, *Quantum computing with trapped ions*, Physics Reports - Review Section of Physics Letters **469**, 155 (2008),
URL link.

[53] R. Blatt and D. Wineland, *Entangled states of trapped atomic ions*, Nature **453**, 1008 (2008),
URL link.

[54] J. Simon, H. Tanji, S. Ghosh and V. Vuletic, *Single-photon bus connecting spin-wave quantum memories*, Nat Phys **3**, 765 (2007),
URL link.

[55] C. Simon, M. Afzelius, J. Appel, A. B. de la Giroday, S. J. Dewhurst, N. Gisin, C. Y. Hu, F. Jelezko, S. Kroll, J. H. Muller, J. Nunn, E. S. Polzik, J. G. Rarity, H. De Riedmatten, W. Rosenfeld, A. J. Shields, N. Skold, R. M. Stevenson, R. Thew, I. A. Walmsley, M. C. Weber, H. Weinfurter, J. Wrachtrup and R. J. Young, *Quantum memories*, European Physical Journal D **58**, 1 (2010),
URL link.

[56] A. I. Lvovsky, B. C. Sanders and W. Tittel, *Optical quantum memory*, Nature Photonics **3**, 706 (2009),
URL link.

[57] T. Chaneliere, D. N. Matsukevich, S. D. Jenkins, S. Y. Lan, T. A. B. Kennedy and A. Kuzmich, *Storage and retrieval of single photons transmitted between remote quantum memories*, Nature **438**, 833 (2005),
URL link.

[58] R. Zhao, Y. O. Dudin, S. D. Jenkins, C. J. Campbell, D. N. Matsukevich, T. A. B. Kennedy and A. Kuzmich, *Long-lived quantum memory*, Nature Physics **5**, 100 (2009),
URL link.

[59] M. D. Eisaman, A. Andre, F. Massou, M. Fleischhauer, A. S. Zibrov and M. D. Lukin, *Electromagnetically induced transparency with tunable single-photon pulses*, Nature **438**, 837 (2005),
URL link.

[60] K. S. Choi, H. Deng, J. Laurat and H. J. Kimble, *Mapping photonic entanglement into and out of a quantum memory*, Nature **452**, 67 (2008),
URL link.

[61] M. Fleischhauer, S. F. Yelin and M. D. Lukin, *How to trap photons? Storing single-photon quantum states in collective atomic excitations*, Optics Communications **179**, 395 (2000),
URL link.

[62] A. V. Gorshkov, A. Andre, M. D. Lukin and A. S. Sorensen, *Photon storage in Lambda-type optically dense atomic media. I. Cavity model*, Physical Review A **76**, 033804 (2007),
URL link.

[63] A. Dantan and M. Pinard, *Quantum-state transfer between fields and atoms in electromagnetically induced transparency*, Physical Review A **69**, 043810 (2004),
URL link.

[64] M. Albert, J. P. Marler, P. F. Herskind, A. Dantan and M. Drewsen, *Collective strong coupling between ion Coulomb crystals and an optical cavity field: Theory and experiment*, Phys. Rev. A **85**, 023818 (2012),
URL link.

[65] A. Dantan, J. P. Marler, M. Albert, D. Guenot and M. Drewsen, *Noninvasive Vibrational Mode Spectroscopy of Ion Coulomb Crystals through Resonant Collective Coupling to an Optical Cavity Field*, Physical Review Letters **105** (2010),
URL link.

[66] M. Fleischhauer, A. Imamoglu and J. P. Marangos, *Electromagnetically induced transparency: Optics in coherent media*, Reviews of Modern Physics **77**, 633 (2005),
URL link.

[67] S. E. Harris, *Electromagnetically induced transparency*, Physics Today **50**, 36 (1997),
URL link.

[68] M. Albert, A. Dantan and M. Drewsen, *Cavity electromagnetically induced transparency and all-optical switching using ion Coulomb crystals*, Nature Photonics **5**, 633 (2011),
URL link.

[69] A. Dantan, M. Albert and M. Drewsen, *All-cavity electromagnetically induced transparency and optical switching: Semiclassical theory*, Phys. Rev. A **85**, 013840 (2012),
URL link.

[70] L. V. Hau, S. E. Harris, Z. Dutton and C. H. Behroozi, *Light speed reduction to 17 metres per second in an ultracold atomic gas*, Nature **397**, 594 (1999),
URL link.

[71] M. M. Kash, V. A. Sautenkov, A. S. Zibrov, L. Hollberg, G. R. Welch, M. D. Lukin, Y. Rostovtsev, E. S. Fry and M. O. Scully, *Ultraslow group velocity and enhanced nonlinear optical effects in a coherently driven hot atomic gas*, Physical Review Letters **82**, 5229 (1999),
URL link.

[72] C. Liu, Z. Dutton, C. H. Behroozi and L. V. Hau, *Observation of coherent optical information storage in an atomic medium using halted light pulses*, Nature **409**, 490 (2001),
URL link.

[73] M. Albert, *A light-matter interface based on ion Coulomb crystals in an optical cavity*, Ph.D. thesis, University of Aarhus (2010),
URL link.

[74] A. Dantan, M. Albert, J. P. Marler, P. F. Herskind and M. Drewsen, *Large ion Coulomb crystals: A near-ideal medium for coupling optical cavity modes to matter*, Physical Review A **80** (2009),
URL link.

[75] A. Imamoglu, *High Efficiency Photon Counting Using Stored Light*, Phys. Rev. Lett. **89**, 163602 (2002),
URL link.

[76] D. F. V. James and P. G. Kwiat, *Atomic-Vapor-Based High Efficiency Optical Detectors with Photon Number Resolution*, Phys. Rev. Lett. **89**, 183601 (2002),
URL link.

[77] C. Clausen, N. Sangouard and M. Drewsen, *Analysis of a photon number resolving detector based on fluorescence readout of an ion Coulomb crystal quantum memory inside an optical cavity*, New Journal of Physics **15**, 025021 (2013),
URL link.

[78] D. H. E. Dubin, *Theory of electrostatic fluid modes in a cold spheroidal non-neutral plasma*, Phys. Rev. Lett. **66**, 2076 (1991),
URL link.

[79] R. Linnet, I. Leroux, A. Dantan and M. Drewsen, *Sub-micron positioning of trapped ions with respect to the absolute center of a standing-wave cavity field*, Applied Physics B **114**, 295 (2014),
URL link.

[80] M. Enderlein, T. Huber, C. Schneider and T. Schaetz, *Single Ions Trapped in a One-Dimensional Optical Lattice*, Phys. Rev. Lett. **109**, 233004 (2012),
URL link.

[81] R. B. Linnet, I. D. Leroux, M. Marciante, A. Dantan and M. Drewsen, *Pinning an Ion with an Intracavity Optical Lattice*, Phys. Rev. Lett. **109**, 233005 (2012),
URL link.

[82] L. Karpa, A. Bylinskii, D. Gangloff, M. Cetina and V. Vuletić, *Suppression of Ion Transport due to Long-Lived Subwavelength Localization by an Optical Lattice*, Phys. Rev. Lett. **111**, 163002 (2013),
URL link.

[83] A. T. Grier, M. Cetina, F. Oručević and V. Vuletić, *Observation of Cold Collisions between Trapped Ions and Trapped Atoms*, Phys. Rev. Lett. **102**, 223201 (2009),
URL link.

[84] S. Schmid, A. Härter and J. H. Denschlag, *Dynamics of a Cold Trapped Ion in a Bose-Einstein Condensate*, Phys. Rev. Lett. **105**, 133202 (2010),
URL link.

[85] M. Cetina, A. T. Grier and V. Vuletić, *Micromotion-Induced Limit to Atom-Ion Sympathetic Cooling in Paul Traps*, Phys. Rev. Lett. **109**, 253201 (2012),
URL link.

[86] P. W. H. Pinkse, T. Fischer, P. Maunz and G. Rempe, *Trapping an atom with single photons*, Nature **404**, 365 (2000),
URL link.

[87] C. J. Hood, T. W. Lynn, A. C. Doherty, A. S. Parkins and H. J. Kimble, *The Atom-Cavity Microscope: Single Atoms Bound in Orbit by Single Photons*, Science **287**, 1447 (2000),
URL link.

[88] J. D. Thompson, T. G. Tiecke, N. P. de Leon, J. Feist, A. V. Akimov, M. Gullans, A. S. Zibrov, V. Vuletić and M. D. Lukin, *Coupling a Single Trapped Atom to a Nanoscale Optical Cavity*, Science **340**, 1202 (2013),
URL link.

[89] H. Ritsch, P. Domokos, F. Brennecke and T. Esslinger, *Cold atoms in cavity-generated dynamical optical potentials*, Rev. Mod. Phys. **85**, 553 (2013),
URL link.

[90] T. Botter, D. W. C. Brooks, S. Schreppler, N. Brahms and D. M. Stamper-Kurn, *Optical Readout of the Quantum Collective Motion of an Array of Atomic Ensembles*, Phys. Rev. Lett. **110**, 153001 (2013),
URL link.

[91] S. Chu, J. E. Bjorkholm, A. Ashkin and A. Cable, *Experimental-Observation of Optically Trapped Atoms*, Physical Review Letters **57**, 314 (1986),
URL link.

[92] J. Ye, D. W. Vernooy and H. J. Kimble, *Trapping of single atoms in cavity QED*, Physical Review Letters **83**, 4987 (1999),
URL link.

[93] P. K. Ghosh, *Ion traps* (Clarendon Press ; Oxford University Press, Oxford New York, 1995),
URL link.

[94] C. Schneider, M. Enderlein, T. Huber and T. Schaetz, *Optical trapping of an ion*, Nature Photonics **4**, 772 (2010),
URL link.

[95] A. Friedenauer, H. Schmitz, J. T. Glueckert, D. Porras and T. Schaetz, *Simulating a quantum magnet with trapped ions*, Nat Phys **4**, 757 (2008),
URL link.

[96] R. Schmied, T. Roscilde, V. Murg, D. Porras and J. I. Cirac, *Quantum phases of trapped ions in an optical lattice*, New Journal of Physics **10**, 045017 (2008),
URL link.

[97] C. Schneider, D. Porras and T. Schaetz, *Experimental quantum simulations of many-body physics with trapped ions*, Reports on Progress in Physics **75**, 024401 (2012),
URL link.

[98] I. Garcia-Mata, O. V. Zhirov and D. L. Shepelyansky, *Frenkel-Kontorova model with cold trapped ions*, The European Physical Journal D **41**, 325 (2007),
URL link.

[99] T. Pruttivarasin, M. Ramm, I. Talukdar, A. Kreuter and H. Häffner, *Trapped ions in optical lattices for probing oscillator chain models*, New Journal of Physics **13**, 075012 (2011),
URL link.

[100] J. D. Prestage, G. J. Dick and L. Maleki, *New Ion Trap For Frequency Standard Applications*, Journal Of Applied Physics **66**, 1013 (1989),
URL link.

[101] W. Paul, H. P. Reinhard and U. Vonzahn, *Das Elektrische Massenfilter Als Massenspektrometer Und Isotopentrenner*, Zeitschrift Fur Physik **152**, 143 (1958),
URL link.

[102] W. Paul, *Electromagnetic Traps for Charged and Neutral Particles*, Reviews of Modern Physics **62**, 531 (1990),
URL link.

[103] E. Fischer, *Die Dreidimensionale Stabilisierung Von Ladungstragern In Einem Vierpolfeld*, Zeitschrift Fur Physik **156**, 1 (1959),
URL link.

[104] D. A. Church, *Storage-Ring Ion Trap Derived From Linear Quadrupole Radio-Frequency Mass Filter*, Journal Of Applied Physics **40**, 3127 (1969),
URL link.

[105] M. Drewsen and A. Broner, *Harmonic linear Paul trap: Stability diagram and effective potentials*, Physical Review A **62** (2000),
URL link.

[106] L. Hornekær, N. Kjærgaard, A. M. Thommesen and M. Drewsen, *Structural properties of two-component Coulomb crystals in linear Paul traps*, Physical Review Letters **86**, 1994 (2001),
URL link.

[107] H. J. Metcalf and P. van der Straten, *Laser Cooling and Trapping* (Springer New York, 1999),
URL link.

[108] J. Eschner, G. Morigi, F. Schmidt-Kaler and R. Blatt, *Laser cooling of trapped ions*, Journal of the Optical Society of America B-Optical Physics **20**, 1003 (2003),
URL link.

[109] J. I. Cirac, L. J. Garay, R. Blatt, A. S. Parkins and P. Zoller, *Laser Cooling of Trapped Ions - the Influence of Micromotion*, Physical Review A **49**, 421 (1994),
URL link.

[110] D. F. V. James, *Quantum dynamics of cold trapped ions with application to quantum computation*, Applied Physics B-Lasers And Optics **66**, 181 (1998),
URL link.

[111] P. A. Barton, C. J. S. Donald, D. M. Lucas, D. A. Stevens, A. M. Steane and D. N. Stacey, *Measurement of the lifetime of the 3d 2D5/2 state in 40Ca+*, Physical Review A **62**, 032503 (2000),
URL link.

[112] R. Blatt, P. Gill and R. Thompson, *Current Perspectives on the Physics of Trapped Ions*, Journal of Modern Optics **39**, 193 (1992),
URL link.

[113] D. J. Berkeland, J. D. Miller, J. C. Bergquist, W. M. Itano and D. J. Wineland, *Minimization of ion micromotion in a Paul trap*, Journal of Applied Physics **83**, 5025 (1998),
URL link.

[114] D. H. Dubin, *Theory of structural phase transitions in a trapped Coulomb crystal*, Physical Review Letters **71**, 2753 (1993),
URL link.

[115] M. Block, A. Drakoudis, H. Leuthner, P. Seibert and G. Werth, *Crystalline ion structures in a Paul trap*, Journal of Physics B-Atomic Molecular and Optical Physics **33**, L375 (2000),
URL link.

[116] M. Drewsen, I. S. Jensen, N. Kjaergaard, J. Lindballe, A. Mortensen, K. Molhave and D. Voigt, *Non-stationary Coulomb crystals in linear Paul traps*, Journal of Physics B-Atomic Molecular and Optical Physics **36**, 525 (2003),
URL link.

[117] J. P. Hansen, *Statistical-Mechanics of Dense Ionized Matter .1. Equilibrium Properties of Classical One-Component Plasma*, Physical Review A **8**, 3096 (1973),
URL link.

[118] R. W. Hasse and J. P. Schiffer, *The Structure of the Cylindrically Confined Coulomb Lattice*, Annals of Physics **203**, 419 (1990),
URL link.

[119] L. Turner, *Collective Effects On Equilibria Of Trapped Charged Plasmas*, Physics Of Fluids **30**, 3196 (1987),
URL link.

[120] D. H. E. Dubin and T. M. O'Neil, *Trapped nonneutral plasmas, liquids, and crystals (the thermal equilibrium states)*, Reviews of Modern Physics **71**, 87 (1999),
URL link.

[121] E. L. Pollock and J. P. Hansen, *Statistical-Mechanics of Dense Ionized Matter .2. Equilibrium Properties and Melting Transition of Crystallized One-Component Plasma*, Physical Review A **8**, 3110 (1973),
URL link.

[122] W. L. Slattery, G. D. Doolen and H. E. Dewitt, *Improved Equation of State for the Classical One-Component Plasma*, Physical Review A **21**, 2087 (1980),
URL link.

[123] D. J. Wineland, J. C. Bergquist, W. M. Itano, J. J. Bollinger and C. H. Manney, *Atomic-Ion Coulomb Clusters in an Ion Trap*, Physical Review Letters **59**, 2935 (1987),
URL link.

[124] F. Diedrich, E. Peik, J. M. Chen, W. Quint and H. Walther, *Observation of a Phase-Transition of Stored Laser-Cooled Ions*, Physical Review Letters **59**, 2931 (1987),
URL link.

[125] M. Drewsen, C. Brodersen, L. Hornekær, J. S. Hangst and J. P. Schiffer, *Large Ion Crystals in a Linear Paul Trap*, Phys. Rev. Lett. **81**, 2878 (1998), URL link.

[126] R. Wuerker, H. Shelton and R. Langmuir, *Electrodynamic Containment of Charged Particles*, Journal of Applied Physics **30**, 342 (1959), URL link.

[127] S. L. Gilbert, J. J. Bollinger and D. J. Wineland, *Shell-Structure Phase of Magnetically Confined Strongly Coupled Plasmas*, Phys. Rev. Lett. **60**, 2022 (1988), URL link.

[128] P. F. Herskind, A. Dantan, M. Albert, J. P. Marler and M. Drewsen, *Positioning of the rf potential minimum line of a linear Paul trap with micrometer precision*, Journal of Physics B-Atomic Molecular and Optical Physics **42**, 154008 (2009), URL link.

[129] L. Hornekaer and M. Drewsen, *Formation process of large ion Coulomb crystals in linear Paul traps*, Physical Review A **66**, 013412 (2002), URL link.

[130] L. Hornekær, *Single- and Multi-Species Coulomb Ion Crystals: Structures, Dynamics and Sympathetic Cooling*, Ph.D. thesis, University of Aarhus (2000), URL link.

[131] J. P. Schiffer, *Phase transitions in anisotropically confined ionic crystals*, Phys. Rev. Lett. **70**, 818 (1993), URL link.

[132] R. Blumel, C. Kappler, W. Quint and H. Walther, *Chaos And Order Of Laser-Cooled Ions In A Paul Trap*, Physical Review A **40**, 808 (1989), URL link.

[133] J. P. Schiffer, M. Drewsen, J. S. Hangst and L. Hornekaer, *Temperature, ordering, and equilibrium with time-dependent confining forces*, Proceedings Of The National Academy Of Sciences Of The United States Of America **97**, 10697 (2000), URL link.

[134] J. M. Raimond, M. Brune and S. Haroche, *Colloquium: Manipulating quantum entanglement with atoms and photons in a cavity*, Reviews of Modern Physics **73**, 565 (2001), URL link.

[135] J. Stajic, *The Future of Quantum Information Processing*, Science **339**, 1163 (2013), URL link.

[136] V. Giovannetti, S. Lloyd and L. Maccone, *Advances in quantum metrology*, Nature Photonics **5**, 222 (2011), URL link.

[137] J. McKeever, A. Boca, A. D. Boozer, R. Miller, J. R. Buck, A. Kuzmich and H. J. Kimble, *Deterministic generation of single photons from one atom trapped in a cavity*, Science **303**, 1992 (2004),
URL link.

[138] F. L. Pedrotti, L. M. Pedrotti and L. S. Pedrotti, *Introduction to optics* (Pearson/Prentice Hall, Upper Saddle River, N.J., 2007),
URL link.

[139] P. Milonni and J. Eberly, *Lasers* (John Wiley & Sons, Inc., New York, 1988),
URL link.

[140] H. Kogelnik and T. Li, *Laser beams and resonators*, Appl Opt **5**, 1550 (1966),
URL link.

[141] E. Jaynes and F. W. Cummings, *Comparison of quantum and semiclassical radiation theories with application to the beam maser*, Proceedings of the IEEE **51**, 89 (1963),
URL link.

[142] B. W. Shore and P. L. Knight, *The Jaynes-Cummings Model*, Journal of Modern Optics **40**, 1195 (1993),
URL link.

[143] M. Tavis and F. W. Cummings, *Exact Solution for an N-Molecule-Radiation-Field Hamiltonian*, Phys. Rev. **170**, 379 (1968),
URL link.

[144] M. Tavis and F. W. Cummings, *Approximate Solutions for an N-Molecule-Radiation-Field Hamiltonian*, Phys. Rev. **188**, 692 (1969),
URL link.

[145] J. J. Sakurai and S. F. Tuan, *Modern quantum mechanics* (Addison-Wesley Pub. Co., Reading, Mass., 1994),
URL link.

[146] M. Scully and S. Zubairy, *Quantum Optics* (Cambridge University Press, 1997),
URL link.

[147] B. H. Bransden and C. J. Joachain, *Physics of Atoms and Molecules* (Prentice Hall, 2003), 2nd edition,
URL link.

[148] R. H. Dicke, *Coherence In Spontaneous Radiation Processes*, Physical Review **93**, 99 (1954),
URL link.

[149] R. J. Brecha, L. A. Orozco, M. G. Raizen, M. Xiao and H. J. Kimble, *Observation of oscillatory energy exchange in a coupled-atom-cavity system*, J. Opt. Soc. Am. B **12**, 2329 (1995),
URL link.

[150] J. D. Sterk, L. Luo, T. A. Manning, P. Maunz and C. Monroe, *Photon collection from a trapped ion-cavity system*, Phys. Rev. A **85**, 062308 (2012),
URL link.

[151] H. Takahashi, A. Wilson, A. Riley-Watson, F. Orucevic, N. Seymour-Smith, M. Keller and W. Lange, *An integrated fiber trap for single-ion photonics*, New Journal of Physics **15**, 053011 (2013),
URL link.

[152] H.-J. Briegel, W. Dür, J. I. Cirac and P. Zoller, *Quantum Repeaters: The Role of Imperfect Local Operations in Quantum Communication*, Phys. Rev. Lett. **81**, 5932 (1998),
URL link.

[153] E. Knill, R. Laflamme and G. J. Milburn, *A scheme for efficient quantum computation with linear optics*, Nature **409**, 46 (2001),
URL link.

[154] M. Fleischhauer and M. D. Lukin, *Quantum memory for photons: Dark-state polaritons*, Phys. Rev. A **65**, 022314 (2002),
URL link.

[155] M. D. Lukin, S. F. Yelin and M. Fleischhauer, *Entanglement of Atomic Ensembles by Trapping Correlated Photon States*, Phys. Rev. Lett. **84**, 4232 (2000),
URL link.

[156] A. Dantan, J. Cviklinski, M. Pinard and P. Grangier, *Dynamics of a pulsed continuous-variable quantum memory*, Phys. Rev. A **73**, 032338 (2006),
URL link.

[157] A. Dantan, A. Bramati and M. Pinard, *Entanglement storage in atomic ensembles*, EPL (Europhysics Letters) **67**, 881 (2004),
URL link.

[158] K. R. Zangenberg, *Rumlige Kavitetstilstandes Indvirkninger på en Kvantehukommelse Baseret på en Ion Coulomb Krystal*, Master's thesis, University of Aarhus (2011).

[159] K. R. Zangenberg, A. Dantan and M. Drewsen, *Spatial mode effects in a cavity EIT-based quantum memory with ion Coulomb crystals*, Journal of Physics B: Atomic, Molecular and Optical Physics **45**, 124011 (2012),
URL link.

[160] D. J. Larson, J. C. Bergquist, J. J. Bollinger, W. M. Itano and D. J. Wineland, *Sympathetic Cooling Of Trapped Ions - A Laser-Cooled 2-Species Nonneutral Ion Plasma*, Physical Review Letters **57**, 70 (1986),
URL link.

[161] P. Bowe, L. Hornekaer, C. Brodersen, M. Drewsen, J. S. Hangst and J. P. Schiffer, *Sympathetic crystallization of trapped ions*, Physical Review Letters **82**, 2071 (1999),
URL link.

[162] A. Mortensen, J. J. T. Lindballe, I. S. Jensen, P. Staanum, D. Voigt and M. Drewsen, *Isotope shifts of the* $4s^2\ ^1S_0 \rightarrow 4s5p\ ^1P_1$ *transition and hyperfine splitting of the* $4s5p\ ^1P_1$ *state in calcium*, Physical Review A **69**, 042502 (2004),
URL link.

[163] A. Mortensen, E. Nielsen, T. Matthey and M. Drewsen, *Observation of three-dimensional long-range order in small ion Coulomb crystals in an rf trap*, Physical Review Letters **96**, 103001 (2006),
URL link.

[164] R. W. P. Drever, J. L. Hall, F. V. Kowalski, J. Hough, G. M. Ford, A. J. Munley and H. Ward, *Laser Phase and Frequency Stabilization Using an Optical-Resonator*, Applied Physics B-Photophysics and Laser Chemistry **31**, 97 (1983),
URL link.

[165] E. D. Black, *An introduction to Pound-Drever-Hall laser frequency stabilization*, American Journal of Physics **69**, 79 (2001),
URL link.

[166] F. K. Jensen, *Laser frequency stabilization for use in stirap experiments*, Master's thesis, University of Aarhus (2004).

[167] C. E. Wieman and L. Hollberg, *Using Diode-Lasers for Atomic Physics*, Review of Scientific Instruments **62**, 1 (1991),
URL link.

[168] W. Happer, *Optical-Pumping*, Reviews of Modern Physics **44**, 169 (1972),
URL link.

[169] P. Herskind, A. Dantan, M. Langkilde-Lauesen, A. Mortensen, J. L. Sorensen and M. Drewsen, *Loading of large ion Coulomb crystals into a linear Paul trap incorporating an optical cavity*, Applied Physics B-Lasers and Optics **93**, 373 (2008),
URL link.

[170] A. Mortensen, E. Nielsen, T. Matthey and M. Drewsen, *Radio frequency field-induced persistent long-range ordered structures in two-species ion Coulomb crystals*, Journal Of Physics B-Atomic Molecular And Optical Physics **40**, F223 (2007),
URL link.

[171] J. E. Hansen, C. Laughlin, H. W. van der Hart and G. Verbockhaven, *Energy levels, wavefunction compositions and electric dipole transitions in neutral Ca*, Journal Of Physics B-Atomic Molecular And Optical Physics **32**, 2099 (1999),
URL link.

[172] N. Beverini, E. Maccioni, F. Sorrentino, V. Baraulia and M. Coca, *Measurementof the* $4s^2\ ^1S_0 \rightarrow 4s3d\ ^1D_2$ *transition probability in calcium*, European Physical Journal D **23**, 223 (2003),
URL link.

[173] P. Herskind, J. Lindballe, C. Clausen, J. L. Sorensen and M. Drewsen, *Second-harmonic generation of light at 544 and 272 nm from an ytterbium-doped distributed-feedback fiber laser*, Optics Letters **32**, 268 (2007),
URL link.

[174] B. G. Norton, E. W. Streed, M. J. Petrasiunas, A. Jechow and D. Kielpinski, *Millikelvin spatial thermometry of trapped ions*, New Journal of Physics **13**, 113022 (2011),
URL link.

[175] C. B. Zhang, D. Offenberg, B. Roth, M. A. Wilson and S. Schiller, *Molecular-dynamics simulations of cold single-species and multispecies ion ensembles in a linear Paul trap*, Phys. Rev. A **76**, 012719 (2007),
URL link.

[176] K. Okada, M. Wada, T. Takayanagi, S. Ohtani and H. A. Schuessler, *Characterization of ion Coulomb crystals in a linear Paul trap*, Physical Review A **81** (2010),
URL link.

[177] M. T. Bell, A. D. Gingell, J. M. Oldham, T. P. Softley and S. Willitsch, *Ion-molecule chemistry at very low temperatures: cold chemical reactions between Coulomb-crystallized ions and velocity-selected neutral molecules*, Faraday Discussions **142**, 73 (2009),
URL link.

[178] N. H. Nielsen, *Measuring the temperature of Coulomb crystals*, Master's thesis, University of Aarhus (2011).

[179] C. Cormick and G. Morigi, *Structural Transitions of Ion Strings in Quantum Potentials*, Phys. Rev. Lett. **109**, 053003 (2012),
URL link.

[180] P. Horak, A. Dantan and M. Drewsen, *Optically induced structural phase transitions in ion Coulomb crystals*, Phys. Rev. A **86**, 043435 (2012),
URL link.

[181] M. Drewsen, T. Matthey, A. Mortensen and J. Petter Hansen, *Direct imaging of thermally excited metastable structures of ion Coulomb clusters*, ArXiv e-prints (2012),
URL link.

[182] A. B. Mundt, A. Kreuter, C. Becher, D. Leibfried, J. Eschner, F. Schmidt-Kaler and R. Blatt, *Coupling a Single Atomic Quantum Bit to a High Finesse Optical Cavity*, Phys. Rev. Lett. **89**, 103001 (2002),
URL link.

[183] J. Eschner, C. Raab, F. Schmidt-Kaler and R. Blatt, *Light interference from single atoms and their mirror images*, Nature **413**, 495 (2001),
URL link.

[184] P. Maunz, T. Puppe, I. Schuster, N. Syassen, P. W. H. Pinkse and G. Rempe, *Cavity cooling of a single atom*, Nature **428**, 50 (2004),
URL link.

[185] S. Nuszmann, K. Murr, M. Hijlkema, B. Weber, A. Kuhn and G. Rempe, *Vacuum-stimulated cooling of single atoms in three dimensions*, Nat Phys **1**, 122 (2005),
URL link.

[186] D. Jaksch, C. Bruder, J. I. Cirac, C. W. Gardiner and P. Zoller, *Cold Bosonic Atoms in Optical Lattices*, Phys. Rev. Lett. **81**, 3108 (1998),
URL link.

[187] R. Grimm, M. Weidemüller and Y. B. Ovchinnikov, *Optical Dipole Traps for Neutral Atoms*, Advances In Atomic, Molecular, and Optical Physics **42**, 95 (2000),
URL link.

[188] M. Anderlini, P. J. Lee, B. L. Brown, J. Sebby-Strabley, W. D. Phillips and J. V. Porto, *Controlled exchange interaction between pairs of neutral atoms in an optical lattice*, Nature **448**, 452 (2007),
URL link.

[189] P. Hauke, R. J. Sewell, M. W. Mitchell and M. Lewenstein, *Quantum control of spin correlations in ultracold lattice gases*, Phys. Rev. A **87**, 021601 (2013),
URL link.

[190] T. Lauber, P. Massignan, G. Birkl and A. Sanpera, *Atomic wave packet dynamics in finite time-dependent optical lattices*, Journal of Physics B: Atomic, Molecular and Optical Physics **44**, 065301 (2011),
URL link.

[191] V. S. Letokhov, *Narrowing of Doppler Width in a Standing Light Wave*, Jetp Letters-Ussr **7**, 272 (1968),
URL link.

[192] J. P. Gordon and A. Ashkin, *Motion of Atoms in a Radiation Trap*, Physical Review A **21**, 1606 (1980),
URL link.

[193] C. Foot, *Atomic physics*, Oxford master series in physics (Oxford University Press, 2005),
URL link.

[194] A. Benassi, A. Vanossi and E. Tosatti, *Nanofriction in cold ion traps*, Nat Commun **2**, 236 (2011),
URL link.

[195] A. Stute, B. Casabone, B. Brandstatter, K. Friebe, T. E. Northup and R. Blatt, *Quantum-state transfer from an ion to a photon*, Nat Photon **7**, 219 (2013),
URL link.

[196] D. Porras and J. I. Cirac, *Effective Quantum Spin Systems with Trapped Ions*, Phys. Rev. Lett. **92**, 207901 (2004),
URL link.

[197] J. W. Britton, B. C. Sawyer, A. C. Keith, C. C. J. Wang, J. K. Freericks, H. Uys, M. J. Biercuk and J. J. Bollinger, *Engineered two-dimensional Ising interactions in a trapped-ion quantum simulator with hundreds of spins*, Nature **484**, 489 (2012),
URL link.

[198] S. Genway, W. Li, C. Ates, B. P. Lanyon and I. Lesanovsky, *Generalized Dicke Nonequilibrium Dynamics in Trapped Ions*, Phys. Rev. Lett. **112**, 023603 (2014),
URL link.

[199] K. Murch, *Cavity Quantum Optomechanics with Ultracold Atoms* (University of California, Berkeley, 2008),
URL link.

[200] V. Vuletić and S. Chu, *Laser Cooling of Atoms, Ions, or Molecules by Coherent Scattering*, Phys. Rev. Lett. **84**, 3787 (2000),
URL link.

[201] J. Emsley, *The Elements*, Oxford chemistry guides (Oxford University Press, New York, 1998),
URL link.

[202] NIST Atomic Spectra Database
URL link.

[203] H. Hancock, *Elliptic Integrals*, Mathematical monographs (John Wiley & Sons, Incorporated, 1917),
URL link.

[204] P. F. Byrd and M. D. Friedman, *Handbook of Elliptic Integrals for Engineers and Scientists*, volume 67 of *Die Grundlehren der mathematischen Wissenschaften* (Springer Berlin Heidelberg, 1971),
URL link.